Gas-phase Activation of CO_2 and CH_4 by Selected Transition-Metal Complexes: Ligand Effects and the Role of the Metal

vorgelegt von
M. Sc.
Marjan Firouzbakht
aus Karaj (Iran)

Von der Fakultät II – Mathematik und Naturwissenschaften
der Technischen Universität Berlin
zur Erlangung des akademischen Grades
Doktor der Naturwissenschaften

– Dr. rer. nat. –

genehmigte Dissertation

Promotionsausschuss:

Vorsitzender:	Prof. Dr. Arne Thomas
Gutachter:	Prof. Dr. Martin Kaupp
Gutachterin:	Prof. Dr. Jana Roithová

Tag der wissenschaftlichen Aussprache: 09. January 2018

Berlin 2018

Acknowledgment

First of all, I would like to thank my supervisors, Prof. Dr. Drs. h.c. Helmut Schwarz and Prof. Dr. Martin Kaupp, for giving me the chance to carry out my PhD Thesis in their groups. Due to this support, the last years were truly a unique experience. Furthermore, I am grateful to Prof. Dr. Jana Roithová for accepting my request to act as second examiner of this Thesis. Moreover, my thanks go to Prof. Dr. Arne Thomas for chairing the scientific discussion of the oral PhD examination.

I am very grateful to Dr. Maria Schlangen who has supervised my work and has always been available when I needed scientific or nonscientific advices. I will never forget your help and kindness Maria, and I am so glad that we have met. I am thankful to Dr. Thomas Weiske for his essential assistance concerning the technical maintenance of the machines, and to Andrea Beck and Nadine Rechenberg for their constant and kind assistance with any kind of problem.

I am particularly grateful to Dr. Shaodong Zhou, Dr. Patricio González-Navarrete, Dr. Nicole Rijs, Dr. Robert Kretschmer, Dr. Shadan Ghassemi Tabrizi, and Dr. Toni Maier for their countless supports and collaborations.

I am grateful to all my colleagues of both groups, past and present, specially Arobendo Mondal, Simon Gückel, and Oscar Aguilar-Cuevas who turned from distinguished colleagues to real friends.

Furthermore, I warmly express my gratitude to all of my friends specially Nastaran, Mahsa, Ludovica, and Marjan for their kind words and supports whenever I needed.

More personally, I am truly indebted to my family, especially my parents, as well as my siblings Mersede, Amin, and Ali for their infinite support along my study abroad. I Love you all. Finally, my last and special '*Thank You*' goes to Jost - you supported me throughout this stressful last year of my PhD. I could not have been through all of this without you. As I always say, you make my life beautiful!

Zusammenfassung

Die vorliegende Arbeit behandelt die Übergangsmetall-vermittelten Aktivierungen von CO_2 und CH_4, die mittels massenspektrometrischer Methoden und quantenchemischer Rechnungen untersucht wurden. Die Kationen der jeweiligen Übergangsmetalle wurden durch Elektrosprayionisation (ESI) erzeugt und anschließend mit der Tandem-Massenspektrometrie unter Quadrupol-Hexapol-Quadrupol Anordnung charakterisiert. Die quantenchemischen Rechnungen basieren sowohl auf der Dichtefunktionaltheorie (DFT) als auch auf *ab initio* Methoden.

Die Arbeit gliedert sich in drei Bereiche: i) O–CO Bindungsaktivierung durch Übergangsmetallkomplexe mit ausgewählten Liganden ($[Y(C_6D_5)]^+$ und $[CoX]^+$ (X = CN, F, Cl, Br, O und OH)), ii) Details der C–H Bindungsaktivierung von CH_4 durch $[OMoH]^+$ und $[NiL]^+$ (L= (C_6D_5), (NC_5D_4), (CN)), und iii) die gleichzeitige Aktivierung von CO_2 und CH_4 unter Verwendung der Niob- und Tantalkomplexe $[OMH]^+$ und $[M(OH)]^+$ (M = Nb, Ta) sowie durch die Rheniumcarbonylkomplexe $[Re(CO)_x]^+$ ($x = 0$–3).

Die Studien zur O-CO Bindungsaktivierung belegen, dass $[Y(C_6D_5)]^+$ zur Aktivierung von Kohlendioxid befähigt ist. Hierbei erfolgt entweder die Knüpfung einer C–C-Bindung unter Bildung eines Yttriumbenzoat-Komplexes, oder es wird die Übertragung eines Sauerstoffatoms beobachtet, für die die hohe Sauerstoffaffinität des frühen Übergangsmetalls die treibende Kraft darstellt. Auch $[Co(CN)]^+$ aktiviert CO_2 unter Bildung des flüchtigen Cyanoformations $[NC\text{-}CO_2Co]^+$ in der Gasphase, während die Komplexe $[CoX]^+$ (X = F, Cl, Br, O, and OH) wegen zu hoher kinetischer Barrieren, die überhalb des Eintrittskanals liegen, inert sind. Bei der thermischen Aktivierung von Methan konnte durch die Reaktivität von $[OMoH]^+$ im Vergleich zum unreaktiven Verhalten von $[MoH]^+$ ein bemerkenswerter Ligandeneffekt identifiziert werden. Während die thermischen Reaktionen von $[OMoH]^+$ mit Methan einige Gemeinsamkeiten mit $[OMH]^+$ aufweisen (M = Ti, V, Ta), existieren grundlegende Unterschiede im Hinblick auf die jeweiligen Reaktionsmechanismen. Ein weiteres Beispiel für einen Ligandeneffekt zeigt sich anhand der Reaktivität von $[Ni(C_6H_5)]^+$ und $[Ni(CN)]^+$ mit Methan im Vergleich zum unreaktiven $[Ni(NC_5H_4)]^+$. Auch bei der simultanen Aktivierung von CO_2 und CH_4 durch $[OMH]^+$ (M = Nb,Ta) und $[M(OH)]^+$ (M = Ta) wurden neue Erkenntnisse über die zugrundeliegenden Mechanismen gewonnen. Die Aktivierung von Methan verläuft in beiden Fällen unter H_2-Eliminierung, und bei der Aktivierung von CO_2 wird die Bildung von $[OM(OH)]^+$ (M = Nb, Ta) unter Abspaltung von CO beobachtet. Darüber hinaus stellen die Reaktionen von $[Re(CO)_x]^+$ ($x = 0$-3) mit CO_2 und CH_4 ein Beispiel dafür dar, dass die Anzahl der Liganden ebenfalls von Bedeutung für den Aktivierungsprozess ist. Während die Komplexe $[Re(CO)_x]^+$ ($x = 0$, 1, 3) unter thermischen Bedingungen gegenüber CO_2 unreaktiv sind, abstrahiert $[Re(CO)_2]^+$ ein Sauerstoffatom aus diesem Substrat. Der dabei erzeugte Oxokomplex $[ORe(CO)_2]^+$ reagiert mit CH_4 und bildet $[ORe(CO)(CH_2)(H)_2]^+$.

Abstract

The present Thesis presents studies on the transition metal-mediated CO_2 and CH_4 activation by means of mass spectrometric experiments in conjunction with quantum-chemical calculations. The transition metal cations were generated by electrospray ionization (ESI) and the subsequent investigations were performed by means of tandem mass spectrometry using a quadrupole-hexapole quadrupole arrangement. The quantum-chemical calculations were carried out using density functional theory (DFT) as well as *ab initio* methods.

The work is divided into three areas: i) O–CO bond activation by selected-ligated transition-metal cations i.e. $[Y(C_6D_5)]^+$ and $[CoX]^+$ (X = CN, F, Cl, Br, O, and OH), ii) fundamental details concerning C–H bond activation of CH_4 by $[OMoH]^+$ and $[NiL]^+$ (L= (C_6D_5), (NC_5D_4), (CN)), and iii) the ability of $[OMH]^+$ (M = Nb, Ta), $[M(OH)]^+$ (M = Nb, Ta), and rhenium carbonyl cations $[Re(CO)_x]^+$ (x = 0–3) with respect to the simultaneous activations of both CO_2 and CH_4.

In the O–CO bond activation studies, $[Y(C_6D_5)]^+$ showed the potency of carbon dioxide activation under carbon-carbon bond formation to generate an yttrium benzoate complex, as well as under O-atom transfer by taking the advantage of the high oxophilicity of early transition metals. Further, while $[Co(CN)]^+$ activates carbon dioxide to form the elusive cyanoformate ion $[NC–CO_2Co]^+$ in the gas phase, $[CoX]^+$ (X = F, Cl, Br, O, and OH) are inert toward CO_2 due to kinetic barriers located above the entrance asymptote. In the thermal activation of methane, the reactivity of $[OMoH]^+$ versus the inertness of $[MoH]^+$ reveals a remarkable ligand effect. While the thermal reactions of $[OMoH]^+$ with methane have some features in common with $[OMH]^+$ (M=Ti,V,Ta), fundamental mechanistic differences exist. Another example of a ligand effect is presented in case of the reactivity of $[Ni(C_6D_5)]^+$ and $[Ni(CN)]^+$ toward methane versus the inertness of $[Ni(NC_5D_4)]^+$. For the simultaneous activations of both CO_2 and CH_4 by $[OMH]^+$ (M = Nb, Ta) and $[M(OH)]^+$ (M = Ta), interesting insights into the underlying mechanisms have been gained and are discussed in detail. In both cases, the activation of methane proceeds by H_2 elimination, and the activation of CO_2 is observed to proceed via the formation of $[OM(OH)]^+$ (M = Nb, Ta) under the elimination of CO. Moreover, the reactions of $[Re(CO)_x]^+$ (x = 0-3) with CO_2 and CH_4 represent an example that the number of ligands also matters in the activation process. While the complexes $[Re(CO)_x]^+$ (x = 0, 1, 3) are thermally unreactive toward CO_2, $[Re(CO)_2]^+$ abstracts one oxygen atom from this substrate. The oxo complex $[ORe(CO)_2]^+$ reacts further with CH_4 to produce $[ORe(CO)(CH_2)(H)_2]^+$.

Unpublished Work

I) **M. Firouzbakht**, N. J. Rijs , M. Schlangen, M. Kaupp, and H. Schwarz, Ligand Effects on the Reactivity of $[CoX]^+$ (X = CN, F, Cl, Br, O, and OH) towards CO_2 in the Gas Phase: Generation of the Elusive Cyanoformate Ion.
This is a preprint version of a published paper. The final publication is available at Springer via http://dx.doi.org/10.1007/s11244-018-0903-8

II) **M. Firouzbakht**, M. Schlangen, H. Schwarz, and M. Kaupp, Thermal Carbon Dioxide and Methane Activation by $[Nb,O,H]^+$: A Combined Experimental/Theoretical Study.

List of Publications

III) **M. Firouzbakht**, S. Zhou, P. González-Navarrete, M. Schlangen, M. Kaupp, and H. Schwarz, Metal-Dependent Strengthening and Weakening of M−H and M−C Bonds by an Oxo Ligand: Thermal Gas-Phase Activation of Methane by $[OMH]^+$ and $[MH]^+$ (M = Mo, Ti). *Chem. Eur. J.* 23 (2017): 12346 – 12352.
DOI: 10.1002/chem.201701615

IV) S. Zhou, **M. Firouzbakht**, M. Schlangen, M. Kaupp, and H. Schwarz, On the Electronic Origin of Remarkable Ligand Effects on the Reactivities of $[NiL]^+$ Complexes (L = C_6H_5, C_5H_4N, CN) towards Methane. *Chem. Eur. J.* 23 (2017): 14430 – 14433.
DOI: 10.1002/chem.201702767

V) S. Zhou, J. Li, **M. Firouzbakht**, M. Schlangen, and H. Schwarz, "Sequential Gas-Phase Activation of Carbon Dioxide and Methane by $[Re(CO)_2]^+$: The Sequence of Events Matters!." *J. Am. Chem. Soc.* 139 (2017): 6169 – 6176.
DOI: 10.1021/jacs.7b01255

VI) **M. Firouzbakht**, N. J. Rijs, P. González-Navarrete, M. Schlangen, M. Kaupp, and H. Schwarz, On the Activation of Methane and Carbon Dioxide by $[OTaH]^+$ and $[TaOH]^+$ in the Gas Phase: A Mechanistic Study. *Chem. Eur. J.* 22 (2016): 10581 – 10589.
DOI: 10.1002/chem.201601339

VII) **M. Firouzbakht**, M. Schlangen, M. Kaupp, and H. Schwarz, Mechanistic aspects of CO_2 activation mediated by phenyl yttrium cation: A combined experimental/theoretical study. *J. Catal.* 343 (2016): 68 – 74.
DOI: 10.1016/j.jcat.2015.09.012

Table of Contents

1. Introduction 1
2. Experimental and Computational Methods 11
  2.1. Chemistry of ions in the gas phase 11
    2.1.1 Unimolecular reactions 11
    2.1.2 Theory of ion/molecule reactions 14
    2.1.3 Collision-induced dissociation 16
  2.2 Experimental setups 17
    2.2.1 The VG BioQ mass spectrometer 17
      2.2.1.1 Electrospray ionization 19
      2.2.1.2 Quadrupole analyzers 21
  2.3 Modeling ions in the gas phase 22
    2.3.1 Basic quantum mechanics and Schrödinger's equation 22
    2.3.2 Density-functional theory (DFT) 26
    2.3.3 The coupled-cluster method 30
    2.3.4 General considerations for the computations 30
3. Results 33
  3.1. C–O bond activation: reactions with carbon dioxide 33
  3.2. C–H bond activation: reactions with methane 35
  3.3. Simultaneous activation of C–H and C–O bonds 38
4. Conclusions and Outlook 42
References 45
A. Unpublished Work
B. Original Papers

1. Introduction

"We are running the most dangerous experiment in history right now, which is to see how much carbon dioxide the atmosphere can handle before there is an environmental catastrophe."[1]

– Elon Musk

Extensive research efforts have been focused on the utilization of *C1* chemistry as a future source for fuels and chemicals.[2] *C1* chemistry refers to the utilization of single carbon bearing molecules, such as carbon monoxide, carbon dioxide, and methane, for the production of valuable chemicals, high-purity hydrogen or premium chemicals from synthesis gas or from methanol.[3] The main resources of *C1* molecules are natural gas, coal, biomass, and organic wastes. Likewise, owing to human activities, the greenhouse gases CO_2 and CH_4 have dramatically increased in the atmosphere. Therefore, concentration of CH_4[4-7] and CO_2,[8-11] as well as the conversion of these *C1* building blocks to value-added chemicals and fuels have attracted worldwide attention.[10,12-18]

Natural gas is an abundant *C1* resource, in which methane forms the major component by volume (ca. 87%).[13] However, due to the inert nature of methane (as indicated by the high C–H bond dissociation energy, $BDE(H_3C\text{–}H) = 434\ \text{kJ mol}^{-1}$, the negative electron affinity, and an extremely high pK_a value), the development of large-scale conversion processes still constitutes a challenging issue.[19,20] A vast body of research has focused on transforming methane into more value-added commodity chemicals and fuels, while it is estimated that approximately 2×10^{14} cubic meters of methane remain uncaptured.[21]

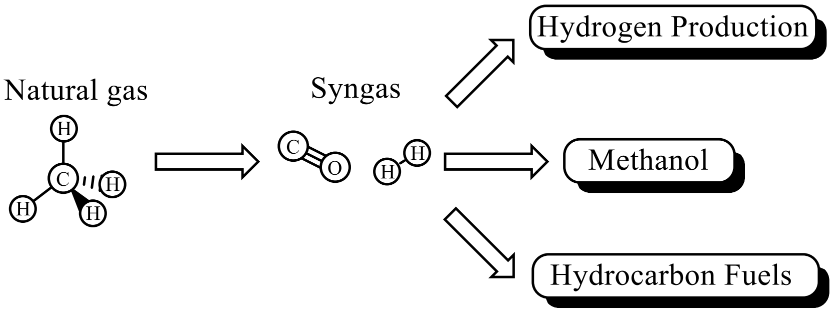

Scheme 1.1 Simplified scheme for the CH_4 transformation to syngas and its usage in industrial processes.

One of the most prominent uses of methane in the chemical industry is the production of synthesis gas by steam reforming (Reaction (1.1)).[21] Synthesis gas is a starting material for producing fuels and other valuable chemicals, e.g. methanol (Scheme1.1).[22] Steam reforming is highly endothermic and additionally needs to be catalyzed by transition metal complexes. According to many experimental and theoretical studies, Rh and Ru are the most active transition metals for steam reforming. However, due to the high cost of the latter, Ni catalysts with an intermediate activity are used in industry.[23] Instead of producing methanol from syngas via CH_4 oxidation and CO reduction (Reactions (1.1) and (1.2)), a direct transformation of methane into methanol (Reaction 1.3)) would be of much greater benefit. The problems associated with the direct conversion of methane are related to both kinetics and thermodynamics. High temperatures are required for the activation of methane. The strength of the C–H bond in methane is stronger than that of the C–H bond in the possible products, e.g. methanol (*BDE* (C–H) = 389 kJ mol^{-1}),[24] meaning that the products will be more reactive than methane. In order to circumvent these problems, several different approaches based on catalysis have been tested. However, proper catalysts for large-scale transformations are still missing.[21]

$$CH_4 + H_2O(g) \rightarrow CO(g) + 3H_2(g) \qquad (1.1)$$

$$\Delta H^0_{298K} = 206\ kJmol^{-1}$$

$$CO(g) + 2H_2(g) \rightarrow CH_3OH(l) \qquad (1.2)$$

$$\Delta H^0_{298K} = -91\ kJmol^{-1}$$

$$CH_4(g) + \tfrac{1}{2}\, O_2(g) \rightarrow CH_3OH(l) \qquad (1.3)$$

$$\Delta H^0_{298K} = -130\ kJmol^{-1}$$

There exist two main branches of studies for the activation of methane, i.e. I) coupling of methane, including oxidative coupling and pyrolysis, results in molecules containing C–C bonds, and II) partial oxidation reaction of methane including the generation of syngas, methanol, etc.[25] Regarding I), the oxidative coupling of methane (OCM) is a promising reaction for ethylene production. Since the yields of C_2 hydrocarbons never exceed 22%–25%, basic and applied research in order to find high-performance catalysts is still a highly active field.[26] Li-doped MgO is one of the most frequently studied catalysts for OCM due to its high catalytic activity in the low-temperature range.[27] Despite all of the vast studies, many aspects, e.g. the active center, the position of Li in MgO, the stability of the catalyst, etc, remain unclear.[20,27] For example, although Lunsford's assumption corresponds to an oxygen-centered radical as an active site, there exist several hypotheses about the possible formation of these radical sites.[27] A large amount of research has been devoted also to partial oxidation reactions. For instance, the selective oxidation of methane to methanol is of considerable interest for obtaining valuable chemicals directly from methane without the need of syngas production. Since methane monooxygenase enzymes, which contain di-iron or di-/tri-copper active clusters,[28-30] are able to perform this reaction under ambient conditions, to date many different bio-inspired catalysts for direct methanol formation from methane have been studied using these transition-metal complexes. According to several different studies on iron-, cobalt-, and copper-loaded zeolites, which can react with methane to produce methanol at low temperatures, Cu/zeolites have currently emerged as the best catalyst due to their most efficient performance.[31]

In addition to methane, carbon dioxide is also rightly viewed as potential *C1* source in organic synthesis, due to its high abundance and availability (e.g. as an industrial by-product of combustion and of respiration), low cost, and being practically nontoxic compared with alternative reagents.[32,33] However, CO_2 is also known for its kinetic inertness; moreover, with a standard enthalpy of formation of -394 kJ mol^{-1}, it is thermodynamically very stable.[19,34]

The use of CO_2 as chemical feedstock, however, is limited to a few industrial processes including: i) the chemical synthesis of urea from carbon dioxide and ammonia[35] (Scheme1.2, a), ii) the synthesis of salicylic acid from carbon dioxide and phenolates[36] (Scheme1.2, b), iii) producing cyclic carbonates by the reaction between carbon dioxide and epoxides[37,38] (Scheme1.2, c). In contrast to the chemical industry, the biotechnology industry is not a high-volume sales industry. However, there nevertheless exist some processes in which biocatalysts have been used to prepare a range of commercial products.[39] For example, acetogens produce over 10 trillion kilograms of acetic acid annually; they can grow autotrophically on the greenhouse gas CO_2, and they have the ability to anaerobically convert carbon dioxide and CO into acetyl-CoA by the Wood–Ljungdahl pathway.[40] One of the key enzymes in this pathway is the carbon monoxide dehydrogenase with $[NiFe_4S_4OH_x]$ as active site.[41] This enzyme is responsible for the reduction of CO_2 to CO and the subsequent assembly of acetyl-CoA.[42] While these processes are not likely to decrease CO_2 to a significant extent, fundamental research on new catalysts is needed in order to find more effective ways for CO_2 capture, storage and conversion.[43]

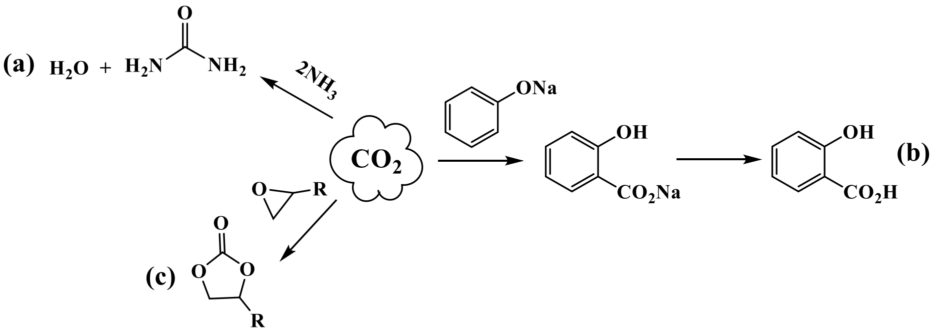

Scheme 1.2 Simplified Scheme of the CO_2 usage in industrial processes

According to their energy requirements, there exist two different groups of reactions for carbon dioxide: I) reactions that use the entire molecule, such as fixation onto an organic substrate which occur at lower temperatures, and II) reactions that convert CO_2 into other C_n $(n \geq 1)$ molecules. These reduction reactions require a large amount of energy.[19] The conversion of CO_2 has attracted much attention and, not surprisingly, became the subject of several studies.[35,44-46] Most of these studies have focused on using transition-metal complexes as catalyst due to their ability to activate the unreactive C–O bonds of carbon dioxide, and thus making them useful catalysts in many important chemical reactions.[47-50] Insertion of CO_2 into a metal−hydrogen bond constitutes a critical step in quite a few transition-metal-catalyzed reductions of CO_2 e.g. conversion of CO_2 to CH_3OH .[44,51]

One mechanism of CO_2 insertion into the M−H bond is shown in Scheme 1.3. The insertion proceeds via attack of the anionic hydride ligand (Lewis base), to the electrophile carbon atom of CO_2 and further continues by electron donation from the oxygen atom to the metal center which acts as Lewis acid.[52]

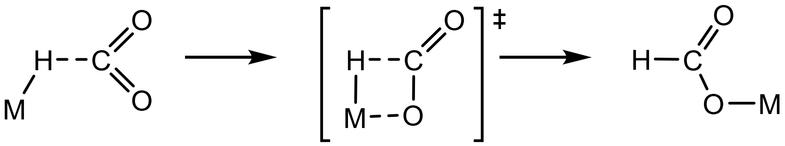

Scheme 1.3 Simplified scheme for the insersion prosses of CO_2 into to the M−H bond

The M−H unit can in general be considered as a Lewis acid−base pair. A frustrated Lewis acid-base pair (FLP) consists of a Lewis acid/base as well as bulky ligands that prevent these species from neutralizing each other,[53] and it has been shown that these systems are qualified for the reduction of CO_2 to CH_3OH.[54,55] A Lewis acid can activate CO_2 electrophilically to facilitate hydride transfer. As an example, Sasaki and co-workers showed that $[Ru_3(CO)_{12}]$/KI is able to activate CO_2 giving rise to the generation of a mixture of CO, CH_3OH, and CH_4.[56,57]

An alternative way to utilize both *C1* sources, CH_4 and CO_2, simultaneously is the dry reforming of CH_4 and CO_2 to syngas (Reaction (1.4)) or acetic acid (Reaction (1.5)). The former is of general interest to the chemical industry first of all due to yielding a lower H_2/CO ratio than steam reforming (Reaction (1.1)). However, this reaction is quite endothermic and thus rather energy intensive.[21] Nickel-based catalysts have been considered as the most suitable choice for the dry reforming in comparison with other transition metals, such as Ru, Rh, Pd, and Pt, due to their high turnover rates, long-term stabilities, and lower costs.[58,59] Furthermore, the direct coupling of CH_4 and CO_2 to CH_3CO_2H is much less endergonic (Reaction (1.5)) but apart from the effect of different solvents, nevertheless also energetically demanding.[60]

$$CH_4(g) + CO_2(g) \rightleftarrows 2H_2(g) + 2CO(g) \qquad (1.4)$$

$$\Delta H^0_{298K} = 247\ kJmol^{-1}$$

$$CH_4(g) + CO_2(g) \rightarrow CH_3CO_2H(g) \qquad (1.5)$$

$$\Delta G^0_{298K} = 16.98\ kJmol^{-1}$$

Producing acetic acid in a direct reaction of CH_4 and CO_2 is a way to decrease the production costs as well as environmental risks compared to the indirect route, and accordingly, there exist several studies on this topic.[60,61] The general idea of most of these studies is the generation of a methyl intermediate by C–H bond activation of CH_4 which then further reacts with CO_2 (Scheme 1.4).

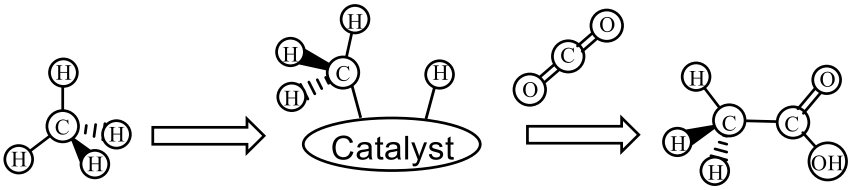

Scheme 1.4 Profile of direct synthesis of acetic acid from CO_2 and CH_4

For example, Ding et al. showed the feasibility of the direct conversion of CH_4 and CO_2 to acetic acid over Pd/SiO_2 and Rh/SiO_2 catalysts.[62] In their experiments, they confirmed the formation of M–CH_3 species (M = Pd, Rh) on the surface and the insertion of CO_2 into the M–C bond of the intermediate in two main steps. Additionally, they showed the significant role of the adsorption energy of the CH_3 species on the metal surface for the insertion of CO_2; this implies the importance of the nature of the metal for the direct coupling of CH_4 and CO_2. Likewise, zinc-modified H–ZSM-5 zeolite is able to activate CH_4 to form zinc-Me species (–Zn–CH_3) into which CO_2 insertion takes place to produce acetic acid species.[63] Recently, Rabie et al. introduced the bifunctional zeolite catalysts, Cu-M^+-ZSM-5e (M = Li, Na, K, and Ca), that were proven to activate both methane and carbon dioxide. While the activation of CO_2 results in the formation of surface carbonate species over alkali metal, the activation of CH_4 leads to the formation of (–Cu–CH_3) units, and the insertion of carbonate into the Cu–CH_3 bond to produce acetic acid.[64]

Despite several remarkable achievements regarding *C1* utilization, the catalytic activation of *C1* molecules constitutes still a highly active field of basic research because of the fundamental scientific challenges dealing with an economically viable direct conversion of methane and carbon dioxide through C–C bond formation at ambient conditions. In addition, progress in the utilization of CO_2 and CH_4 as reactants in chemical industry requires detailed knowledge of the mechanisms in terms of each of the elementary reaction steps and the different factors that govern each of the reaction steps. In this respect, understanding the reaction mechanisms is central to all research in this fast growing field.

As mentioned above, in order to design an efficient catalyst, much important information needs to be acquired, i.e. the unambiguous identification of the active sites and their intrinsic properties as well as the reaction mechanisms. Gas-phase experiments are extremely useful to study systematically catalytic reactions, since they are not obscured by ill-defined conditions such as the role of solvents, aggregation phenomena, or counter-ion effects.[7,65-68] To date, several studies on the activation of CH_4 and CO_2 mediated by transition-metal complexes in the gas phase have been performed.[7,69-76] A common and necessary step in all those studies is the coordination of CH_4 and CO_2 to a metal center. In case of carbon dioxide, there are four different coordination modes to the metal center (Scheme 1.5). Owing to the rather different electronegativities of oxygen and carbon, the oxygen atoms in free CO_2 are negatively polarized while a partial positive charge is located on the carbon atom. Therefore, in the reaction of CO_2 with cationic transition metal complexes, coordination modes i, ii, and iii (Scheme 1.5) are more probable.

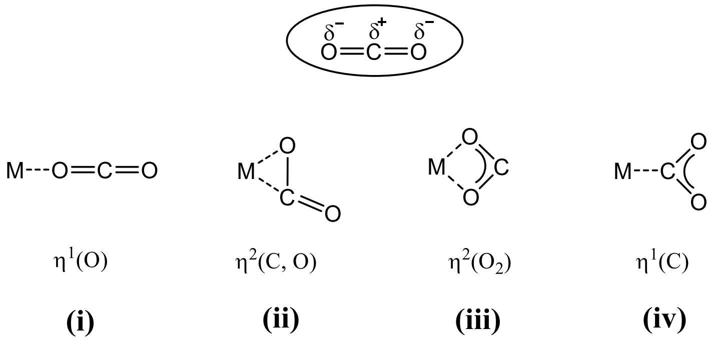

Scheme 1.5 Carbon dioxide and its possible coordination modes at a transition metal center.

In addition, the greater oxophilicity of early transition metals allows to accelerate this step by providing a stronger M–OCO interaction.[77] Furthermore, two different studies of Bohme and coworkers on the reaction of bare transition-metal cations with CO_2[78] and CH_4[79] showed a relatively different behavior of early and late transition metals regarding the activation of these two substrates.

In particular, metal-mediated dehydrogenation of methane was observed to occur only for some of the middle and late transition-metal ions of the third row at room temperature, according to reaction (1.6) (M = Ta, W, Os, Ir and Pt); none of the thermalized ground-state monoatomic 3d- and 4d-transition-metal (except Nb) cations were able to activate methane.[7,79-83]

$$[M]^+ + CH_4 \rightarrow [M,C,H_2]^+ + H_2 \qquad (1.6)$$

This dramatic difference in reactivity can be attributed to the significantly stronger M–CH_2 bonds of the 5d metals due to relativistic effects.[84,85] Likewise, regarding group 10 of the transition metals, the stabilization of the 6s orbital of Pt^+ is complemented by a significantly better overlap between the π orbitals of the carbene fragments with the $5d_\pi$ orbitals compared to the lighter $3d_\pi$ and $4d_\pi$ homologues, i.e. Ni and Pd, respectively.[84-87]

In contrast, but not really surprisingly, mainly oxygen-atom transfer (OAT) occurs from CO_2 to the early and some of the middle transition-metal cations, reflecting the higher oxophilicity of these species compared to late transition metals, as shown in reaction (1.7) (M = Sc, Ti, Y, Zr, Nb, La, Hf, Ta, and W).[78]

$$[M]^+ + CO_2 \rightarrow [MO]^+ + CO \qquad (1.7)$$

The oxygen-atom affinities (OA) of the transition-metal cations mentioned above that react according to reaction (1.7) exceed 665 kJ mol^{-1}, which is much larger than OA(CO) = 531 kJ mol^{-1}; this makes the reactions of these cationic atoms with CO_2 quite exothermic.[76]

Li et al. also showed that different properties of the metal center are required for the activation of CO_2 and CH_4 mediated by 3d transition-metal, doped magnesium oxide clusters $[MMgO]^{+/0/–}$ (M=Sc-Zn).[72] While the late-3d transition metal, doped metal oxide clusters are more promising for methane activation, cluster oxides containing early-3d transition metals are more suitable for CO_2 activation. All these studies somehow imply that finding a “simple” reagent to simultaneously mediate CO_2 and CH_4 activations can be extremely daunting due to fundamental differences in the molecular features of CO_2 and CH_4. Intriguingly, the stoichiometric coupling of methane to carbon dioxide by atomic Ta^+ has been observed. While the cationic oxide TaO^+, obtained by reduction of CO_2, is inert toward CH_4, $[Ta(CH_2)]^+$, generated in the reaction of $[Ta]^+$ with CH_4, can activate CO_2 resulting the complex $[Ta(CH_2)O]^+$ under elimination of CO. The further reaction of $[Ta(CH_2)O]^+$ with CO_2 finally results in the generation of $[TaO_2]^+$ and CH_2CO.[88,89] Other examples include the spin-allowed reactions of the oxo-ligated hydride complex $[OTiH]^+$ with methane[90] and carbon dioxide.[91]

In addition to the role of the transition metal for the activation of CO_2 and CH_4, the nature (e.g. H, O, OH, CH_2, CH_3, CH_2O, F, Cl…) as well as the number of ligands can directly control the reactivity and selectivity of ion/molecule reactions in the gas phase. For example, the gas-phase reactivities of diatomic transition-metal hydrides $[MH]^+$ with methane reveal the effects of a hydride ligand to the metal center. According to these studies, while naked atomic metal cations like e.g. Fe^+, Co^+, Ni^+, and Pd^+ do not afford thermal C–H bond activation of methane, the corresponding $[MH]^+$ ions give rise to an efficient H/CH_3 ligand exchange (reaction (1.8)).[92-95]

$$[MH]^+ + CH_4 \rightarrow [M(CH_3)]^+ + H_2 \tag{1.8}$$

Metal oxide cations, i.e. simple diatomic transition-metal or main-group element oxides, as well as larger cluster ions, are also capable to bring about C–H bond activation and abstract a hydrogen atom of methane.[20,96-103] Different mechanisms, e.g. hydrogen-atom transfer (HAT)[101,104,105] and proton-coupled electron transfer (PCET),[106-109] have been identified for this process; while HAT is favored for oxides that possess an unpaired electron located at a terminal oxygen atom, the ionic nature of the M–O bond plays an important role in PCET reactions.[110] However, also closed-shell species may react with hydrocarbons according to HAT, creating a radical species by electronic reorganization at the site of abstraction.[105,111,112] As an example for *open-shell* metal oxides, $[TiO_2]^{\bullet+}$ and $[ZrO_2]^{\bullet+}$ are capable of methane activation.[112] Instead of creating a methyl radical via HAT or PCET, some metal oxides activate methane under the elimination of closed-shell molecules like CH_2O or CH_3OH, or under the formation of an insertion product bearing a hydroxide and a methyl ligand. The latter has been observed by Zhou et al. in the reaction of $[TaO_2]^+$ with methane;[113] as example of the former type of reaction, formation of CH_2O, CH_3OH, and CH_2 occur in the thermal reactions of $[TaO_3]^+$ with methane.[114] In addition, some small diatomic metal oxides, such as $[MgO]^{\bullet+}$[115], $[PbO]^{\bullet+}$[99], and $[CuO]^+$[70] react with CH_4 by both a homolytic C−H bond scission as well as by $CH_4 \rightarrow CH_3OH$ conversion; in the case of $[CuO]^+$, the efficiency of inter-system crossing (ISC) from the triplet to the singlet PES together with the the thermodynamic properties of the reaction determine the branching ratio of methanol versus $CH_3^{\bullet}$ formation. The crucial intermediate of these reactions corresponds to $[H_3C\cdots M{-}OH]^+$ from which either the methyl radical is lost or the methyl group undergoes a rebound to the hydroxy ligand to generate $[M(CH_3OH)]^+$ and to eventually dissociate into $M^+ + CH_3OH$.

Furthermore, while there are many different gas-phase studies on the activation of CH_4,[4,7,20,83,96,100-102,116] only relatively few are available regarding CO_2 activation in the gas phase.[76] For instance, room-temperature CO_2 conversion mediated by $[LTiH]^+$ (L=Cp_2, O) was observed under CO elimination (L = O) and the generation of a formate complex (L = Cp_2), respectively.[91] In addition to OAT, an oxygen/sulfur ligand exchange is operative in the reactions of CO_2 with diatomic $[MS]^+$ (M = Y, Zr, Nb), leading to the formation of COS and MO^+.[117,118] Further, gas-phase studies on the activation of CO_2 using late transition-metal complexes are also relatively rare. Recently, He and co workers showed that while cationic Fe^+ is not able to activate CO_2, the products HCO_2^- and CO can be formed in the thermal reaction of CO_2 with the FeH^- anion.[119] Furthermore, the thermal activation of CO_2 has been achieved in the reaction with $[PtH_3]^-$, resulting in the generation of $[H_2Pt(HCO_2)]^-$.[120] Moreover, activation of CO_2 has also been observed in gas-phase model systems of carbonic anhydrase $[LZn(OH)]^+$ (L=imidazole or pyridine).[69] Apart from these examples, $OHMg(\eta^2\text{-}O_2C)^-$, i.e. η^2-coordinated CO_2 on $[MgOH]^-$, undergoes C–C bond forming S_N2 reactions with CH_3Cl to produce $OHMg(O_2CCH_3)$ and Cl^-.[121]

As mentioned above, the fact that no catalysts have been developed so far that can efficiently mediate, for example, the direct catalytic activation and coupling of CO_2 and CH_4 to hydrocarbons or alcohols, points to a fundamental problem in our current understanding. In the present work, mass spectrometry in conjunction with quantum-chemical calculations is employed to study transition-metal mediated activations of methane and carbon dioxide in the gas phase. The aim of this Thesis is to explore new metal-ligand systems which can bring about C–H bond activation of CH_4 and C–O bond activation of CO_2, respectively, as well as the possibility of coupling these two *C1* building blocks. Such model systems may provide information about the factors, like the nature and number of the ligands, substrates, and metal centers, which control the gas-phase reactivity. Likewise, combining the experiments with quantum-chemical calculations can complement the experimental information and provide insight into the reaction mechanisms.

2. Experimental and Computational Methods

"It does not matter how beautiful your theory is, it does not matter how smart you are. If it does not agree with experiment, it is wrong." [122]

– Richard P. Feynman

This chapter includes a description of the instrumental and computational methods of the present work. The reported studies have been performed using a tandem mass spectrometer with QHQ (Q: quadrupole, H: hexapole) configuration equipped with an electrospray-ionization (ESI) source; some features will be discussed in more details later in this chapter. After a brief overview of unimolecular reactions in the gas phase, the theory of ion/molecule reactions will be discussed as well. Following these subjects, fundamental aspects of collision-induced dissociation (CID) experiments are provided. The experimental part closes with technical details about the employed tandem-mass spectrometer. Finally, the theoretical and computational methods employed in this work are described briefly.

2.1. Chemistry of ions in the gas phase

In this section, those principles that are useful for the interpretation of the experimental data presented in this work using mass spectrometry are described. This includes unimolecular and ion/molecule reactions under ambient conditions as well as collision-induced dissociation.

2.1.1 Unimolecular reactions

Since the reactions in the mass spectrometer in the present work are investigated at a pressure range between 10^{-4} and 10^{-8} mbar (high vacuum conditions), single-collision conditions can be assumed. Note that the collision probability for single or double collisions, at a pressure of about $7\text{-}8\times10^{-2}$ mbar and a collision cross section of the ion of 5×10^{-16} cm^2 passing through a collision

region of 1 cm length, amounts to 10%; this implies having 95% of single collisions and 5% of double collisions.[123] The collision cell in this study is filled with xenon at a pressure of circa 10^{-4} mbar, and the probability for more than two successive collisions is thus equal to zero.
According to the Rice-Ramsperger-Marcus-Kassel (RRKM) theory,[124-128] ions isolated in the gas phase are not in thermal equilibrium with their surroundings. Thus, if we neglect the emission of internal energy (E_{int}) by radiation,[129] this energy is conserved in the isolated system during a unimolecular reaction, i.e dissociation and/or rearrangement.

One of the most important approaches for describing an unimolecular decomposition is the quasi-equilibrium theory (QET)[130] which is an extension of RRKM. There are different prerequisites in QET theory. For instance: i) energy release by radiation is neglected, and ii) in ergodically-behaved systems, the distribution of the initial energy between all possible energy states is more rapid in comparison to the dissociation processes. Note that in some cases, non-ergodic behavior has been observed.[131-136] Unimolecular decomposition will only occur if the internal energy E_{int} of the ion $[AB]^+$ is high enough to overcome the activation-energy barrier E_0 that leads to the formation of $[A]^+$ and neutral B (see Figure 2.1). Likewise, a certain amount of excess energy E_{ex} is needed to detect the fragmentation of polyatomic ions; this phenomenon is known as kinetic shift.[137] Without this extra energy the activated ion does not dissociate before it reaches the detector, thus no fragments are detected.

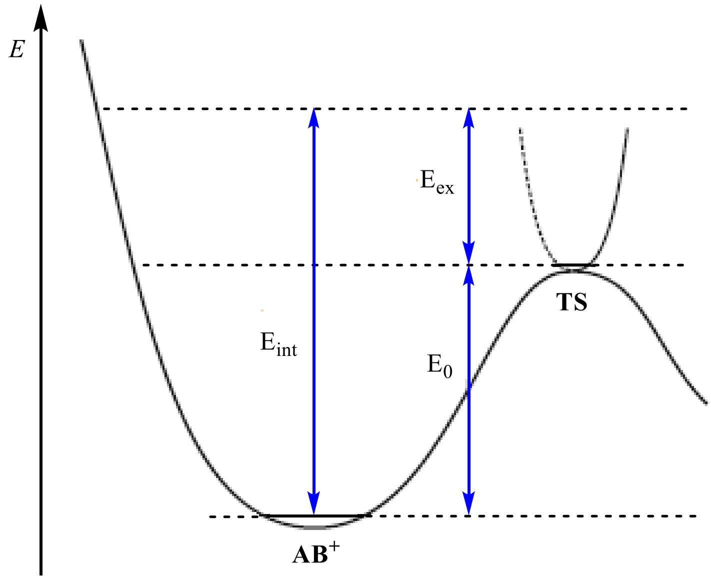

Figure 2.1 Schematic representation of the key values that are relevant for the calculation of unimolecular rate constants $K(E_{int})$.

The rate of the unimolecular dissociation of the ion is given by Equation (2.1).[138]

$$k(E_{int}) = \sigma N_{vr}(E_{int} - E_0)/h\rho_{vr}(E_{int}) \tag{2.1}$$

Here, σ denotes the degeneracy of the reaction path, E_{int} is the total internal energy of the system, and E_0 represents the activation energy. $N_{vr}(E_{int} - E_0)$ stands for the number of states available between E_0 and E_{int} in the transition state (TS), $\rho_{vr}(E_{int})$ is the density of states of the energized ion, and h is the Planck constant. According to QET and RRKM theory, the rate constant $k(E_{int})$ for dissociation is proportional to the probability that at least the amount of E_0 out of the randomly distributed energy is accumulated in the reaction coordinate. There are two different processes for fragmentation: i) simple bond-cleavage reactions, generally occurring via loose transition states, and ii) rearrangement/fragmentation reactions, resulting from transition states often with a rigid structure (tight TS) (Figure 2.2).

While rearrangement reactions, $[A–B–C–D]^+ \rightarrow [A–C–B–D]^+ \rightarrow [A–C]^+ + [B–D]$, usually lead to more stable products and are thus thermodynamically favored, these processes are kinetically disfavored due to the tight transition structures possessing a small density of states. Unlike rearrangement processes, simple bond dissociation processes, $[A–B–C–D]^+ \rightarrow [A–B]^+ + [C–D]$ are kinetically favored by nature of their loose transition structures. However, these reactions often are thermodynamically less favorable.

Furthermore, there may exist different fragmentation pathways in parallel which lead to different $k(E)$ functions, for instance two homolytic bond cleavages with different activation energies (Figure 2.2, a) or one homolytic bond cleavage and one rearrangement fragmentation (Figure 2.2, b) in competition. In the latter case, when $E_{int} < E_{tight}$, no fragmentation takes place; increasing the energy such that $E_{tight} < E_{int} < E_{loose}$, the favored pathways would be the rearrangement fragmentation; going further, with $E_{tight} < E_{loose} < E_{int}$, both pathways are possible to occur. Finally, with an internal energy E', both channels have the same rate constant, and a faster reaction rate for the rearrangement than for the direct bond cleavage is observed with $E_{int} < E'$, while in the case of $E_{int} > E'$, the reaction rate is larger for the direct bond cleavage than for the rearrangement fragmentation.

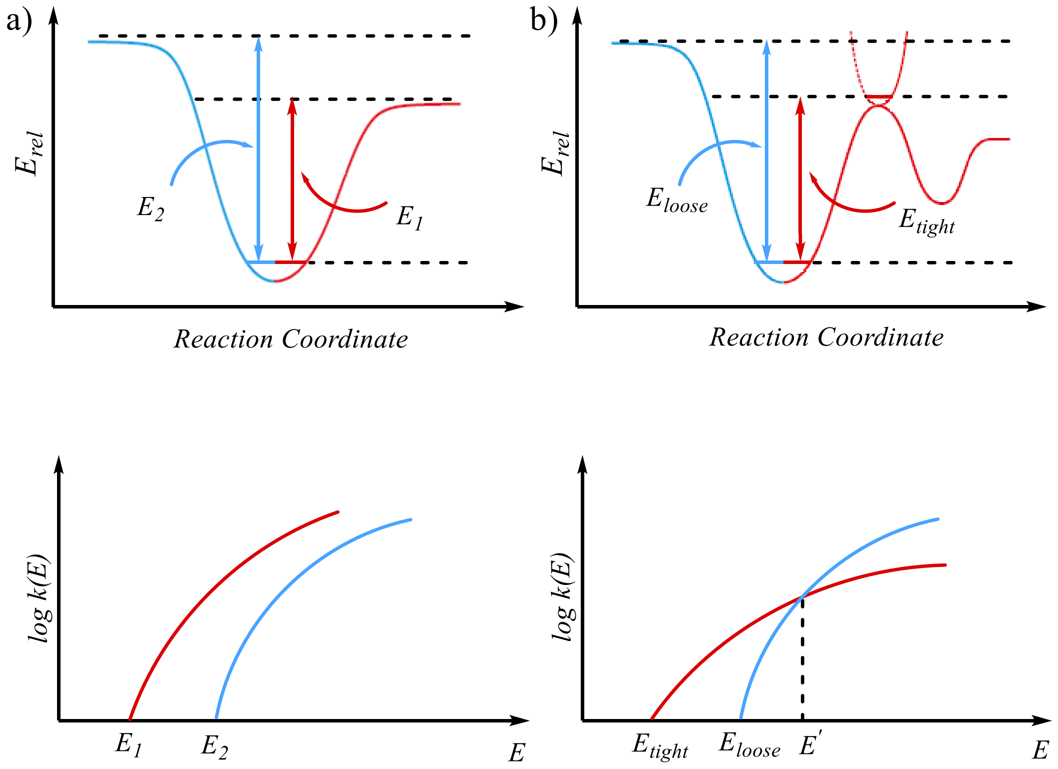

Figure 2.2 Energy dependencies of rate constants *k(E)* for different unimolecular reactions: a) direct bond cleavage involving loose transition states with different appearance energies, E_1 and E_2; b) direct bond cleavage (E_{loose}) versus rearrangement fragmentation (E_{tight}).

2.1.2 Theory of ion/molecule reactions

According to many studies published during the middle of the last century, every reaction between a mass-selected ion $[A]^+$ and a neutral molecule B has its own story from, e.g., a complicated rearrangement/fragmentation to a simple direct decomposition after formation of an encounter complex. These kinds of processes are referred to as ion/molecule reactions.[139-142]

The first step in the ion/molecule reaction corresponds to the formation of an encounter complex $[AB]^+$ from the separated reactants $[A]^+$ and B. Owing to the ion-dipole force between an ion and a neutral molecule, the formation of the encounter complex is exothermic. In the absence of heat loss, the complex stores this energy as an internal energy via statistical distribution among the ro-vibrational degrees of freedom (ergodic behavior). This energy can then be used further to overcome the barriers for intramolecular rearrangement processes and fragmentations.

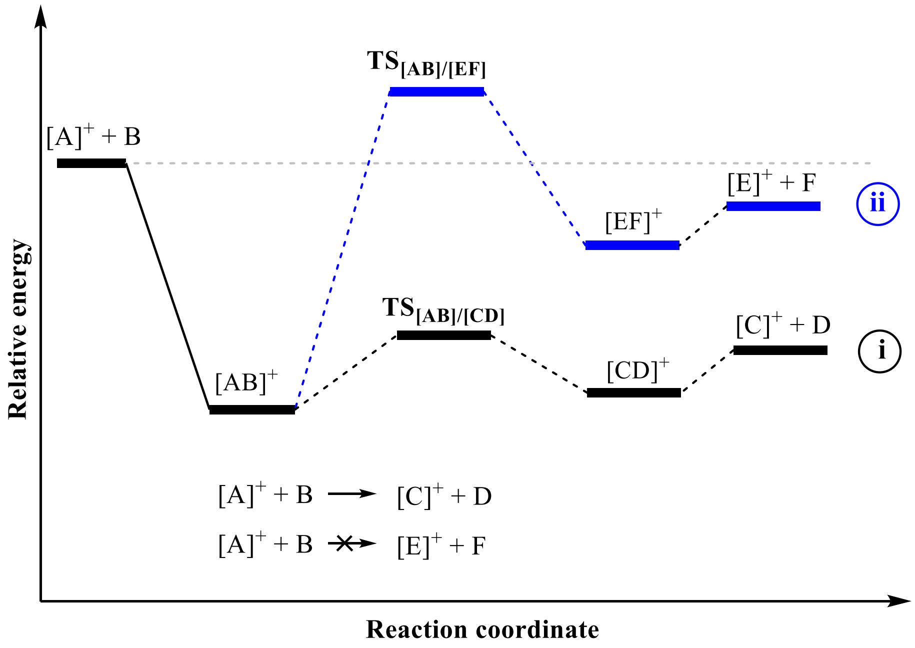

Figure 2.3 Schematic potential-energy surface for a thermally accessible (i), and a non-accessible (ii) bimolecular ion/molecule reaction in the gas phase.

There are two alternative fates for the encounter complex: 1) back-dissociation to $[A]^+$ and B, and 2) overcoming the barriers for rearrangement/fragmentation. In the current study, reactions take place under thermal conditions, thus only those reactions can be probed which are exothermic and the respective transition state is energetically located below the entrance channel. This implies that for example, path (ii) in Figure 2.3, $[A]^+ + B \rightarrow [AB]^+ \rightarrow TS_{[AB]/[EF]} \rightarrow [EF]^+ \rightarrow E^+ + F$ is not accessible due to the existence of a transition state, $TS_{[AB]/[EF]}$, which is higher in energy than the entrance channel.

The absolute rate coefficient *k* for a quantitative description of a bimolecular ion/molecule reaction cannot be measured directly in the multipole setup VG Bio-Q.[143] However, it can be determined relative to the coefficient of a reference reaction, ideally with the same neutral substrate, for which the bimolecular rate constant is known,[144] i.e. the absolute rate constant of the reaction of interest can be derived by calibration.

The rate equation for the reaction between precursor $[A]^+$ and neutral B is given by Equation (2.2). Since the number of ions $[A]^+$ is orders of magnitudes smaller compared to the number of neutral molecules, the concentration of the B can be considered as constant. Thus, the kinetic parameter of this reaction can be determined in terms of a pseudo first-order reaction (Equation (2.2)) in which the measured pseudo first-order rate constant (k_{pseudo}) corresponds to the product of the actual rate constant (k_{exp}) and the pressure $\rho(B)$ of reactant B.

$$-\frac{d([A]^+)}{dt} = k_{exp} \cdot [A]^+ \cdot \rho(B) = k_{pseudo} \cdot [A]^+ \qquad (2.2)$$

By considering the initial concentration of ions, $[A]_0^+$, at the beginning of the reaction ($t = 0$), the differential equation can be solved as shown in Equation (2.3).

$$[A]^+ = [A]_0^+ \cdot e^{-k_{exp} \cdot \rho(B) \cdot t} = [A]_0^+ \cdot e^{-k_{pseudo} \cdot t} \qquad (2.3)$$

Regarding the measurement of reaction rates in a tandem mass spectrometer, the pressure of the neutral reactant is the only variable while the reaction time *t*, i.e. the time of passing the collision cell, is considered to be constant for every mass-selected ion. Therefore, the measured rate constant $k_{m(\rho)}$ can be derived according to Equation (2.4).

$$\ln\left(\frac{I[A]^+}{I_0[A]^+}\right) = k_{m(\rho)} . \rho(B) \qquad (2.4)$$

Further, by plotting $\ln\left(\frac{I[A]^+}{I_0[A]^+}\right)$ as a function of the pressure provides a line with the slope equal to $k_{m(\rho)}$.

2.1.3 Collision-induced dissociation

In the present work, collision-induced dissociation (CID)[145-147] experiments are used to probe the structural assignment of the ion of interest and to elucidate its ionic precursors (see also the scan modes of the VG Bio-Q mass spectrometer described in chapter 2.2.1). A CID process is an ion/neutral gas reaction, $AB^+ + N \rightarrow A^+ + B + N$, under external energy supply, which leads to the fragmentation of the respective ion. After acceleration of the ions, their kinetic energy is converted into internal energy by a collision with an unreactive neutral gas (like Ar, Xe, or N_2), consequently leading to the fragmentation of the ion. The degree of fragmentation depends decisively on the kinetic energy of the collision partners and can be varied by a voltage applied to the collision cell. In this work, collision energies in the range of E_{lab} = 1 - 30 eV were applied. This range of energies indicates that CID experiments are performed by low-energy collisions. In low-energy collisions, the direct excitation of vibrational modes occurs.[148]

During the collision incidence of ion AB^+ with the neutral gas N, a given amount of energy can be transferred; the latter is defined as center of mass energy, E_{CM}. This maximum amount of transferred energy is a function of the mass of the neutral gas m_N, the mass of the ion m_{AB^+}, the charge of the ion z, as well as the kinetic energy of the ion in the laboratory frame of reference E_{lab} (Equation 2.5).

$$E_{CM} = E_{lab} \frac{z \cdot m_N}{m_N + m_{AB^+}} \tag{2.5}$$

The efficiency of energy transfer depends on the various factors, including the polarizability of the neutral collision partner. For instance, xenon is more efficient than argon due to its more polarizable nature, which causes a longer-lived collision complex and thus a more complete energy transfer.[149] After redistribution of the internal energy, the internal energy cannot be dissipated to the surroundings due to the single-collision conditions mentioned above. Therefore, dissociation processes may occur with potentially different fragmentation pathways according to the internal energy available.

2.2 Experimental setups

2.2.1 The VG Bio-Q mass spectrometer

The experiments were performed using a VG BIO-Q (Figure 2.4) tandem mass spectrometer of QHQ configuration (Q: quadrupole, H: hexapole) equipped with an electrospray-ionization source (see Section 2.2.1.1). Millimolar solutions of different precursors in appropriate solvents are introduced via a syringe pump through a fused-silica capillary to the ESI source in order to produce the ions under investigation (note that the preparation details have been discussed separately in each article in the experimental sections).

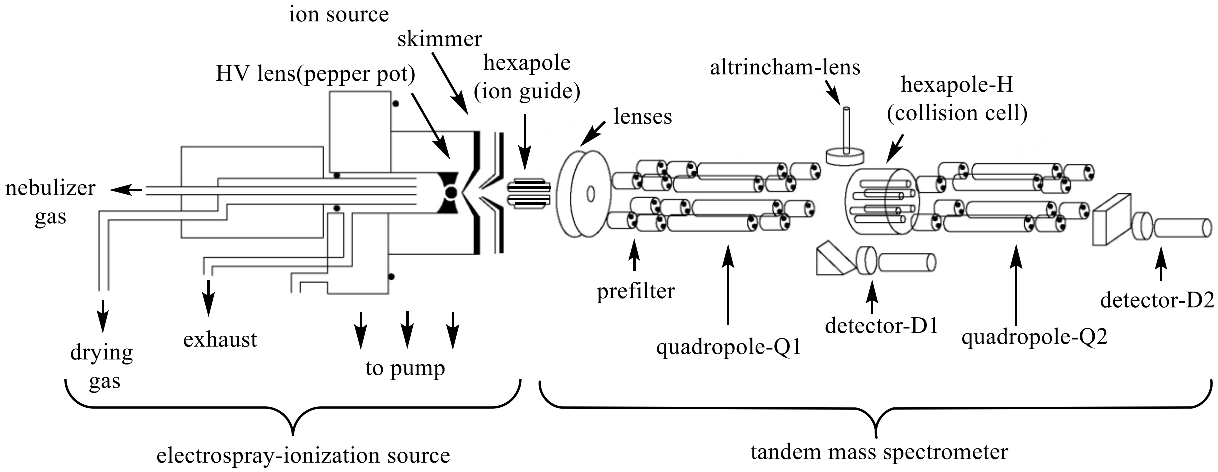
ion source
skimmer
HV lens(pepper pot)
hexapole
(ion guide)
altrincham-lens
hexapole-H
(collision cell)
lenses
nebulizer
gas
prefilter
detector-D2
drying
gas
exhaust
to pump
quadropole-Q1
detector-D1
quadropole-Q2
electrospray-ionization source
tandem mass spectrometer

Figure 2.4 Technical draft of the commercial VG Bio-Q tandem mass spectrometer with QHQ configuration (Q: Quadrupole; H: Hexapole).

Nitrogen is used as a nebulizing and drying gas at a source temperature of 80 °C. The cone voltage (Uc) that determines the degree of collisional activation of the incident ions in the transfer from the ESI source to the mass spectrometer can be tuned between 0 and 200 V. The larger the cone voltage, the more excessive fragmentations occur.[143]

In the present studies, different modes of the VG Bio-Q have been utilized that are shown in Scheme (2.1). A general overview of the ions formed in the ion source can be obtained from the "MS" mode by scanning Q1. Ion/molecule reactions (see Section 2.1.2) as well as CID experiments (see Section 2.1.3) are probed in the "daughter"-ion mode, in which Q1 is fixed on the mass of a parent ion. The fragment or product ions resulting from collisions or from thermal reactions of the mass-selected ion with a neutral gas in the hexapole are scanned in Q2. CID experiments can be performed by accelerating the ions in the hexapole and using an inert collision gas. The same mode but at a nominal collision energy of $E_{lab} = 0$ eV is used for the ion molecule reactions. For the parent-ion mode, Q2 is fixed to the mass of a fragment ion, while in Q1 all m/z values are scanned to determine which parent-masses generate that particular daughter. During the neutral loss/gain scan mode, Q1 and Q2 are scanned synchronously with a chosen value of Δm.

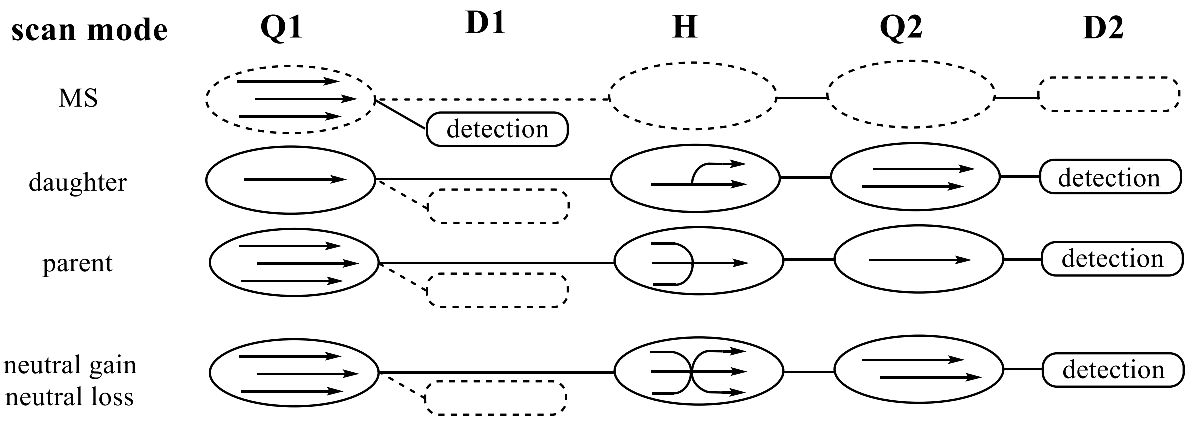
scan mode
Q1
D1
H
Q2
D2
MS
detection
daughter
detection
parent
detection
neutral gain
neutral loss
detection

Scheme 2.1 Schematic overview of the different operation modes of the VG Bio-Q mass spectrometer.

2.2.1.1 Electrospray ionization

Electrospray ionization (ESI) (Figure 2.5) is used in this work, which allows transferring organometallic compounds directly from solution to the gas phase under rather soft conditions.[150-153] ESI became revolutionary due to its ability to allow the measurement of the molecular mass of biologically important, high-molecular weight analytes such as proteins.[154] Furthermore, as a requirement for ESI, the analyte has to be soluble in an appropriate solvent, e.g. methanol, acetonitrile, or water.[155,156] Highly dilute solutions of the species of interest, in the concentration range of 10^{-3} to 10^{-6} moles L^{-1}, are introduced into the ESI source by means of a syringe pump.

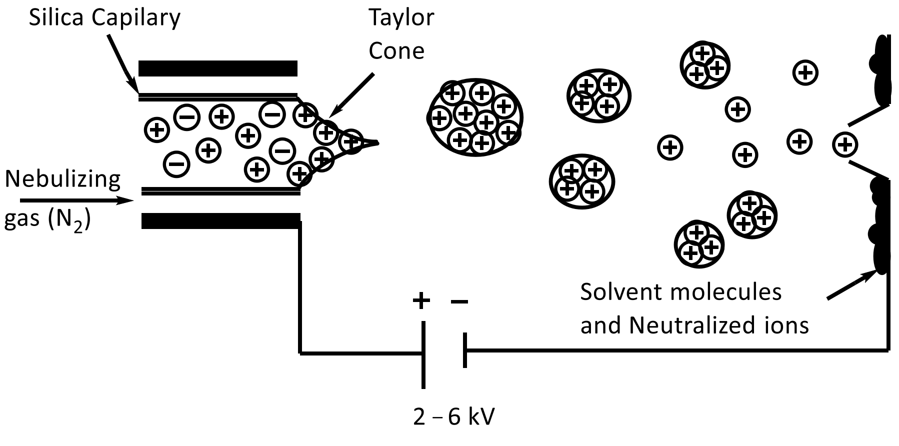
Silica Capilary
Taylor Cone
Nebulizing gas (N₂)
+ –
Solvent molecules and Neutralized ions
2 – 6 kV

Figure 2.5 Schematic representation of the ejection/liberation processes during ESI of the sample when operated in the positive-ion mode.

The sample solution is pumped through a silica capillary that is surrounded by a stainless-steel capillary. A positive or negative electrical potential of 2 - 6 keV is applied to the latter relative to the counter electrode, the skimmer.[157] Due to the interaction of the solvent molecules with the produced electric field, a Taylor cone is formed at the tip of the capillary, from which small droplets are ejected.[158,159] The droplet surface is enriched with either positive or negative ions depending on the operation mode. Solvent evaporation using drying gas, e.g. dinitrogen, reduces the volume of the droplets that bear a constant charge, thus leading to the fission of the droplets.

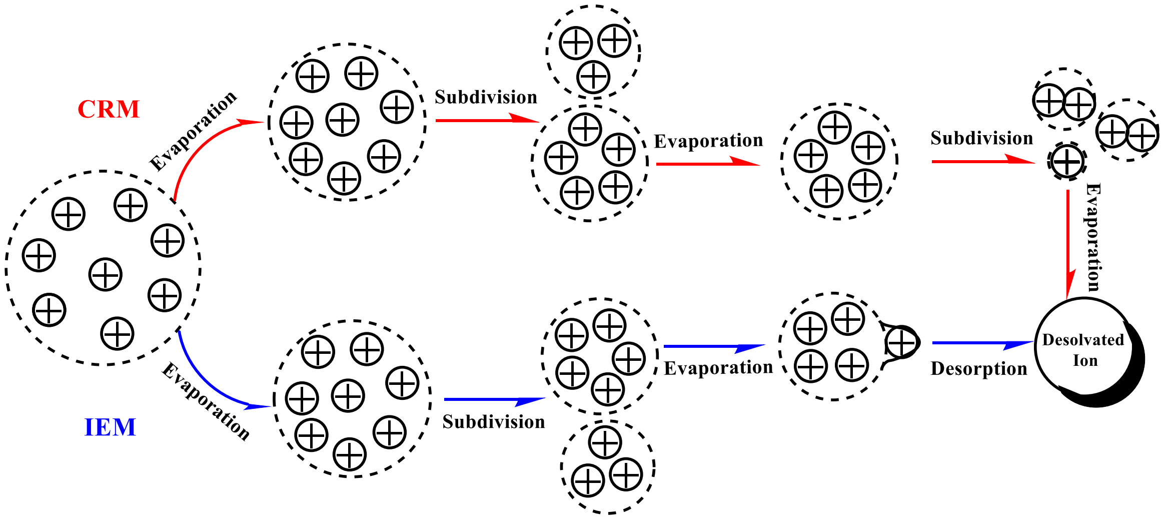

Figure 2.6 Schematic representation of possible pathways for the desolvated ion formation from a charged liquid droplet. The upper part of the diagram illustrates the CRM mechanism (marked in red) and the lower part illustrates the IEM mechanism (marked in blue).

The charge-residue model (CRM)[160-162] and the ion-evaporation model (IEM)[163,164] are two models that has been suggested to explain the formation of ions from charged droplets (Figure 2.6).[165,166] According to the CRM model, as the droplet shrank by evaporation of the solvent, the surface ions get closer together until the coulomb repulsion forces between them exceeds the integral of surface tension. At this point which is called the ‘‘Rayleigh limit’’,[167-169] the droplet increases the available surface area by breaking up into smaller droplets. These new droplets undergo the same process again until they reach again the Rayleigh limit, and Coulomb explosions happen until droplets remain that contain exclusively one analyte molecule. In contrast, the IEM assumes that when the droplet size reaches less than 10 nm, the electric field owing to the charges at the surface of the droplet is strong enough to cause direct emission of the solvated ions.[157,166] According to different studies, the actual mechanism most likely depends very much on the mass of the analyte. For instance, in the case of very large proteins, CRM is more likely to be valid, while for the smaller species such as metal ions, IEM is more probable to occur.[159,170-172] Details on the actual precursors employed in this study will be given in the respective sections.

2.2.1.2 Quadrupole analyzers

The VG Bio-Q contains two quadrupole-mass filters, Q1 and Q2. The quadrupole mass analyzer separates charged particles according to their mass-to-charge ratio (m/z) via electric fields. In the early 1950's it was realized by W. Paul (who was awarded the Nobel Prize in Physics in 1989 together with Hans Dehmelt and Norman Ramsey) that the use of magnetic fields can be replaced by electric fields in ion trap techniques.[173,174] Since then, quadrupole devices have been developed and became one of the most widely used types of mass analyzers. A quadrupole analyzer consists of four metal rods that are arranged parallel to the z-axis (Figure 2.7).

A DC voltage (U) and a radiofrequency (RF) voltage (V) are applied to opposite rods which are electrically connected to each other. This leads to an electric potential Φ_0 and thus to the oscillation of the ions (Equation 2.6). [175,176]

$$\Phi_0 = U + V\cos(\omega t) \tag{2.6}$$

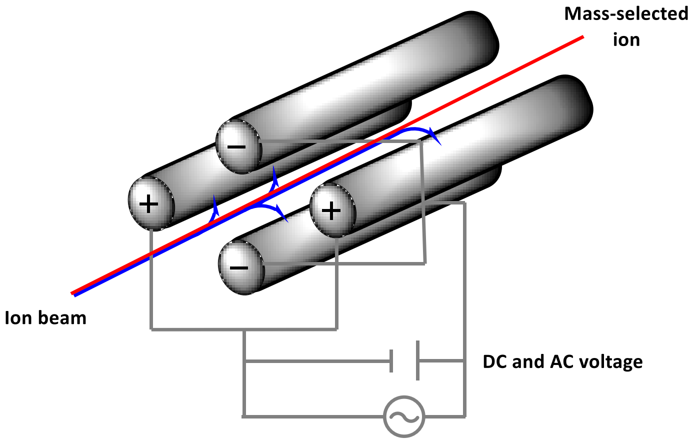

Figure 2.7 Schematic model of a quadrupole analyzer and simplified representation of the trajectories of resonant (red line) and non-resonant ions (blue lines).

According to the *U/V* ratio at a constant frequency *ω*, ions with a certain *m/z* value or an *m/z* range move on a stable path through the analyzer or collide with the rods. The latter case leads to the neutralization and thus to the elimination of the ions. Therefore, the modulation of the DC and AC voltage allows the analysis of broad *m/z* ranges as well as the isolation of individual ions for conducting ion/molecule reactions.

2.3 Modeling ions in the gas phase

Quantum-chemical calculations provide an essential complementary tool for mass-spectrometric studies.[7,96,99,100,102,103,177-181] They help to understand experimental results associated with gas-phase reactions in a mass spectrometer, and allow to determine quantities which are not easily available experimentally. For instance, structural details, energetic information, and the electronic state(s) of the reactants, products, intermediates, and even transition states can be calculated. More generally, with the aid of computational chemistry, in favorable cases it becomes even possible to predict the results of experiments.

In most cases, calculations on the basis of density functional theory (DFT) provide sufficiently accurate results. Compared to *ab initio* ('post Hartree-Fock') methods (the CCSD(T) coupled-cluster method often represents a gold standard for single-reference cases), DFT has the advantage of a significantly lower computational cost. However, in the usually employed Kohn-Sham realization with currently available standard functionals, DFT is generally not suitable for systems with multi-reference character, and more demanding methods that account for both dynamic and static correlation are needed; the N-Electron Valence-State Perturbation Theory (NEVPT2)[182,183] represents one example that has been used in this thesis.

This chapter introduces the central concepts of quantum-chemical calculations with a focus on the methods and basis sets employed in this work. More details on specific methods are elucidated in each published article presented in the last chapter.

2.3.1 Basic quantum mechanics and Schrödinger's equation

Modern quantum mechanics was developed in 1925 and 1926. There were initially two versions, one formulated by Heisenberg, Born, and Jordan,[184,185] and another one by

Schrödinger.[186,187] Shortly afterwards, Schrödinger could show that the two formulations are equivalent in terms of their physical interpretation and are mathematically transformable.

Starting from the classical expression for the energy of a particle, which is the sum of the kinetic and potential energies, as well as de Broglie's conjecture that all particles can be represented as waves with frequency ω and wave number k, the equation of the total energy of a particle turns into Equation (2.7).

$$\hbar\omega = K + V = \frac{1}{2}mv^2 + V(x) = \frac{p^2}{2m} + V(x) = \frac{\hbar^2 k^2}{2m} + V(x) \qquad (2.7),$$

while

$$E = \hbar\omega \text{ and } p = \hbar k.$$

By multiplying Equation (2.7) with $\psi(x,t)$ and considering that $\omega\psi(x,t) = i\frac{\partial\psi(x,t)}{\partial t}$ and $k^2\psi(x,t) = -\frac{\partial^2\psi(x,t)}{\partial x^2}$ (derived from $\psi(x,t) = Ae^{i(kx-\omega t)}$), the time-dependent Schrödinger equation (Schrödinger wave equation), Equation (2.8), is obtained.

$$i\hbar\frac{\partial\psi(x,t)}{\partial t} = \frac{-\hbar^2}{2m}\frac{\partial^2\psi(x,t)}{\partial x^2} + V(x)\psi(x,t) \qquad (2.8)$$

When the external potential $V = V(x)$ (electrostatic potential of clamped nuclei acting on the electrons, see below) is not time dependent, solutions to the time-independent Schrödinger equation are needed:

$$E\psi(x) = \frac{-\hbar^2}{2m}\frac{\partial^2\psi(x)}{\partial x^2} + V(x)\psi(x) \qquad (2.9)$$

Going from one to three dimensions, the $\frac{\partial^2\psi(x)}{\partial x^2}$ term becomes $\nabla^2\psi(x,y,z)$ (the sum of the second spatial derivatives).

By summarizing the kinetic and potential energy operators into the Hamilton operator, $\hat{H}$, which represents the total energy of the system, the time-independent Schrödinger equation is given by Equation (2.10) in more general form.

$$E\psi = \hat{H}\psi \tag{2.10}$$

Unfortunately, the Schrödinger equation can be solved in closed form only for very simple cases, such as the hydrogen atom. For more complicated systems (many-electron systems, atoms and molecules) approximations have to be applied. The molecular Hamiltonian operator comprises terms representing the nuclear kinetic energy T_n, the inter-nuclear potential V_{nn}, and an electronic Hamilton operator H_{el} (Equations (2.11) and (2.12))

$$\hat{H} = \hat{T}_n + \hat{V}_{nn} + \hat{H}_{el} \qquad (2.11),$$

where

$$\hat{H}_{el} = \hat{T}_e + \hat{V}_{ee} + \hat{V}_{ne} \qquad . \tag{2.12}$$

The Born-Oppenheimer approximation[188] represents an often crucial first step of simplification. Due to their lower mass, the electrons move much faster than the nuclei, and rapidly adjust to any structural change. Thus assuming the nuclei fixed, the contributions of the nuclei and the electrons of the Schrödinger equation can be factorized, giving rise to an equation for an electronic wave function that depends only parametrically on the nuclear positions (Equation (2.13)):

$$\left(\hat{H}_{el} + V_{nn}\right)\psi_{el} = U\psi_{el} \tag{2.13}$$

We can define an electronic energy E_{el} by subtracting the constant nucleus-nucleus repulsion V_{nn}.

$$U = E_{el} + V_{nn} \tag{2.14}$$

The solution of Equation (2.14) is still difficult, because the wave function of a system with N electrons depends on 3*N* spatial and *N* spin coordinates. In the Hartree-Fock (HF) method,[189-191] the N-particle wave function is approximated by an antisymmetrized product of one-electron functions (spin orbitals), written as a single Slater determinant (Equation (2.15)).

$$\psi_{HF} = \frac{1}{\sqrt{N!}}\begin{vmatrix} \varphi_1(x_1) & \varphi_2(x_1) & \dots & \varphi_N(x_1) \\ \varphi_1(x_2) & \varphi_2(x_2) & \dots & \varphi_N(x_2) \\ \vdots & \vdots & \ddots & \vdots \\ \varphi_1(x_N) & \varphi_2(x_N) & \dots & \varphi_N(x_N) \end{vmatrix} \quad (2.15)$$

The $\varphi_i(x)$ are determined so that the HF wave function minimizes the energy, under the constraint of their orthonormality. Each spin-orbital $\varphi_i(x)$ is a product of a spatial orbital ($\phi(x)$) and a spin function ($\sigma(s)$). Following the variational principle the exact ground state energy is a lower bound to the resulting energy. The Hartree-Fock energy (E_{HF}) is obtained by Equation (2.16)

$$E_{HF} = \langle\psi_{HF}|\hat{H}|\psi_{HF}\rangle = \sum_{i=1}^{N} h_i + \frac{1}{2}\sum_{ij=1}^{N}(J_{ij} - K_{ij}) \quad (2.16),$$

where

$$h_i = \int \varphi_i^*(x_1)\left[-\frac{1}{2}\nabla_1^2 - \sum_{K=1}^{M}\frac{Z_K}{\vec{R}_{1K}}\right]\varphi_i(x_1)dx_1 \,,$$

$$J_{ij} = \iint \varphi_i^*(x_1)\,\varphi_i(x_1)\frac{1}{\vec{r}_{12}}\varphi_j^*(x_2)\varphi_j(x_2)dx_1dx_2 \,,$$

$$K_{ij} = \iint \varphi_i^*(x_1)\,\varphi_j(x_1)\frac{1}{\vec{r}_{12}}\varphi_j^*(x_2)\varphi_i(x_2)dx_1dx_2 \,.$$

The h_i accounts for the kinetic energy of an electron and the potential energy of this electron i interacting with the nucleus. The Coulomb, J_{ij}, and exchange integrals, K_{ij}, result from the electron-electron repulsion terms in the full Hamiltonian for a multi-electron system.

In general, the basic approximation of HF is the use of a single Slater determinant as we mentioned before; all other aspects derive from this fact. Additionally, there is also the approximation of a finite set of basis functions. In general the HF method captures a large fraction of the total energy. The remaining difference between E_{HF} and the true ground state energy E_0 is defined as the correlation energy E_C:[192]

$$E_C = E_0 - E_{HF} \tag{2.17}$$

The correlation of electrons is not covered by the HF method, it is often divided into dynamical and non-dynamical (static) correlation, at least conceptually. Dynamical correlation is a short-range effect and comes from the actual motions of the individual electrons. Post-HF methods like Configuration Interaction (CI), Møller-Plesset perturbation or Coupled-Cluster (CC) theories are appropriate to recover dynamical correlation. Static correlation is important for molecules where more than one determinant is needed for a qualitatively correct description of the ground state. The multi-configurational self-consistent field (MCSCF) methods take account of non-dynamical correlation. However, all these wave-function based methods become computationally rather expensive for large systems, since the wave function for an N electron system depends on $3N$ coordinates ($4N$ if the spin is included).

2.3.2 Density-functional theory (DFT)

While the HF method is based on the concept of a wave function, density functional theory (DFT) is founded on a probability density $\rho(r)$, the electron density. The two theorems by Hohenberg and Kohn laid the theoretical foundation for DFT and state that the total energy is a functional of the electron density.[193] The Kohn-Sham (KS) approach, developed only a year later, is essential for a large fraction of today's practical DFT calculations.[194]

In DFT, the total energy is written as a functional of the electron density, with three contributions: the kinetic energy $T[\rho]$ of the electrons, the electron-nuclear attraction $V_{ne}[\rho]$, and the electron-electron repulsion $V_{ee}[\rho]$ (Equation (2.18)). The exact form of the Hohenberg-Kohn functional $F[\rho]$, comprising $T[\rho]$ and $V_{ee}[\rho]$, is unknown.

$$E[\rho] = T[\rho] + V_{ne}[\rho] + V_{ee}[\rho] = \int \hat{V}_{ne}\rho(r)dr + F[\rho] \tag{2.18}$$

DFT would be an exact theory, if the explicit form of $F[\rho]$ was known. The quality of a DFT calculation thus crucially depends on the quality of the approximation to $F[\rho]$. The breakthrough for practical DFT was initiated by Kohn and Sham. They showed that via the introduction of a fictitious non-interacting reference system yielding the same $\rho(r)$ as the (interacting) system of interest, a large part $T_S[\rho]$ of the kinetic energy $T[\rho]$ can be calculated exactly.[195] The density simply represents a sum of occupied orbitals (Equation (2.19)). The Kohn-Sham determinant built from these orbitals (analogous to the Slater determinant introduced above) represents the ground state of the non-interacting reference system; its kinetic energy $T_S[\rho]$, is exactly given by Equation (2.20). Note that for T_s, the density may not enter explicitly; the KS orbitals and not the density ρ appear in the equation related to this functional.

$$\rho(r) = \sum_i^N |\varphi_i(r)|^2 \tag{2.19}$$

$$T_s[\rho] = -\frac{1}{2}\sum_{i=1}^N \int \varphi_i^*(r)\nabla^2\varphi_i(r) \tag{2.20}$$

As we noted above, while $T_S[\rho]$ recovers a large fraction of the kinetic energy, it naturally is not equal to the kinetic energy of a real system with interacting electrons $T[\rho]$. The difference in kinetic energy due to the correlation of electrons thus gives rise to a new term $T_C[\rho]$.

In addition a major fraction of the electron-electron interaction $V_{ee}[\rho]$ is captured by classical Coulomb repulsion of the density (Equation (2.21)).

$$J[\rho] = \frac{1}{2}\iint \frac{\rho(r_1)\rho(r_2)}{r_{12}} dr_1 dr_2 \tag{2.21}$$

The remaining unknown parts of the electronic energy, the non-classical term of the repulsion, $E_{ncl}[\rho]$, and the kinetic correlation energy $T_C[\rho]$, are gathered in the exchange-correlation functional, $E_{XC}[\rho]$:

$$E_{XC}[\rho] = (T[\rho] - T_s[\rho]) + (V_{ee}[\rho] - J[\rho]) = T_c[\rho] + E_{ncl}[\rho] \tag{2.22}$$

In KS-DFT the choice of a specific approximate expression for $E_{XC}[\rho]$ is crucial.[196] The exchange-correlation energy $E_{XC}[\rho]$ can be divided into exchange and correlation contributions. There are four widely used approaches for approximating the exchange-correlation energy functional: 1) the local density approximation (LDA), 2) the generalized gradient approximation (GGA), 3) meta-GGAs, and 4) hybrid functionals.

In the LDA, it is assumed that the density varies very slowly and the local density is treated like a uniform electron gas. The exact analytical form of the exchange energy functional for the uniform electron gas is known (Slater exchange) and the correlation energy can be determined virtually exactly by quantum Monte Carlo methods, which may be fitted by interpolation.[197,198] The Vosko, Wilk and Nusair (VWN) interpolation formula for LDA correlation is regarded as relatively exact.[199] Later this formula has been updated by Perdew and Wang.[200] One of the major deficiencies of the LDA approximation is its poor performance for the calculation of molecular energetic properties.[201] Despite some successful structure prediction, in particular for some transition-metal complexes[202] and for solid-state systems,[203] the LDA proved inaccurate for the thermochemistry or kinetics of most relevant molecules. Further, in 1988, Becke introduced the generalized gradient approximation (GGA). GGA is expressed using the LDA exchange energy density and a gradient correction. The first gradient corrected functionals were developed by Becke, Perdew and Wang.[204,205] The most popular GGA functionals are the exchange part of Becke, and the correlation part of Perdew or Lee, Yang and Parr (LYP);[206] these functionals include dynamical correlation and the combination of such semi-local functionals for exchange and correlation provides on average good results in thermochemistry. However, while bond lengths can be reproduced quite reasonably, barriers are often underestimated. Furthermore, Perdew and co-workers developed so-called meta-GGA functionals;[207,208] the TPSS functional is a widely used example.[209] Hybrid functionals are among the most popular functionals. They replace a certain amount of semi-local DFT exchange by the exact-exchange energy (E_{XX}) computed from KS orbitals; in contrast to DFT exchange, exact (Hartree-Fock-type) exchange is self-interaction free. One of the most popular hybrid exchange-correlation functionals which is mainly used in this Thesis, is the B3LYP functional (Equation (2.23)) with 20% exact-exchange contributions (Table 2.1). This functional sees widespread use and often affords good results for thermochemistry and structures of transition metal compounds.

$$E_{XC}^{\mathrm{B3LYP}} = aE_X^0 + (1-a)E_X^{\mathrm{Dirac}} + b\Delta E_X^{\mathrm{B88}} + (1-c)E_C^{\mathrm{VWN}} + cE_C^{\mathrm{LYP}} \qquad (2.23),$$

where

$$a = 0.20, b = 0.72, \text{and } c = 0.81.$$

Concerning the analysis of reaction pathways which is the main part of the computational work of the current Thesis, it is worth mentioning that the DFT spin-state energetics are very sensitive to the exchange-correlation functional, particularly to the exact-exchange admixture in hybrid functionals.[210-212] For instance, pure gradient-corrected exchange functionals tend to stabilize the lower spin states,[213] while hybrid functionals tend to favor higher spin states with increasing exact-exchange admixture.[214,215] Furthermore, the LDA has a notorious tendency to overbind, which is particularly severe for molecules.[216] While the GGA has been shown to improve agreement with experiments for molecules, it frequently overcorrects LDA's overbinding, leading to even worse agreement with experiment for structures than LDA in some cases.[217] Although hybrid functionals can improve the results regarding bond energies, in most of the cases, i.e metal-metal and metal-ligand bonding, they are extremely sensitive to the amount of Hartree-Fock exchange; increasing the Hartree-Fock exchange contribution too much can cause significant errors.[218-221] In addition, the influence of exact-exchange admixture has usually major effects on the spin density distribution of transition-metal complexes.[222] For example, a metal-ligand bond can become more ionic (self-interaction errors tend to render the bonds too covalent at the LDA or GGA level).[223,224]

The conclusion according to some benchmark studies is that DFT generally gives more reliable descriptions of the structures and relative energies for transition-metal systems than HF and MP2 methods.[225] Among different types of DFT functionals, hybrid methods are favored to treat the energetics for transition metal−ligand complexes.[225,226] For example, a review by Harrison confirms in particular that the hybrid B3LYP functional can be the most promising functional for transition metal diatomics.[227] However, there is no specific exchange-correlation functional that represents a best choice across all conceivable systems and properties. Hence, users of DFT approaches should consider their results carefully and test them against experimental data or high-level *ab initio* results, where available. In addition, considering different diagnostic tools, i.e. T_1[228] and TAE%[229] is an alternative way to judge the multi-reference character of the species studied and thus the likely accuracy of DFT methods.

2.3.3 The coupled-cluster method

In the HF approximation, the Coulomb correlation energy of the electrons is not considered, resulting in higher calculated energies than the exact solution to the Schrödinger equation. In order to approximately include the correlation energy, various post-Hartree-Fock methods like Coupled Cluster theory were developed. In Coupled Cluster (CC) theory the (exact) wave function is expressed by applying the operator $e^{\hat{T}}$ to the HF wave function, Equation (2.24).

$$\psi = e^{\hat{T}}\psi_{HF} \quad , \qquad (2.24),$$

where

$$e^{\hat{T}} = 1 + \hat{T} + \frac{\hat{T}^2}{2!} + \frac{\hat{T}^3}{3!} + \cdots$$

and

$$\hat{T} = \hat{T}_1 + \hat{T}_2 + \cdots + \hat{T}_N \quad .$$

In the expression of the cluster operator $\hat{T}$, N corresponds to the number of electrons in the molecule and $\hat{T}_n$ to the n-particle excitation operator, i.e. the one-particle excitation operator $\hat{T}_1$, the two-particle excitation operator $\hat{T}_2$, etc. For a two-electron system, the CC-formalism with single and double excitations (CCSD) gives the exact solution.[230] When more electrons are present, however, improving the calculation by adding triple excitations increases the computing cost dramatically, making CCSDT hard to apply to large systems. This issue can be moderated by estimating the effects of triple excitations in a perturbative manner, defining the CCSD(T) method.[231,232] The CCSD(T) method is used in the present study for a few selected systems in order to calculate the PES. It also provides us with two diagnostic tools, i.e. T_1[228] and TAE%[229] diagnostics, to judge the multi-reference character of the wave function.

2.3.4 General considerations for the computations

For the computational studies we employed the Gaussian 09 program package,[233] using unrestricted DFT calculations with different basis sets and functionals which are listed in Table

2.1. In case of the Turbomole basis sets by Weigend and Ahlrichs et al., i.e. def2-TZVP,[234] def2-TZVPD,[235] def2-TZVPP,[234] and def2-QZVP,[234] for the 4d and 5d metals molybdenum, niobium, tantalum, and rhenium, quasi-relativistic, energy-adjusted effective core potentials (ECPs) and associated valence basis sets for the metal atoms have been utilized.[236] Furthermore, an energy-consistent, small-core pseudopotential adjusted in multi-configuration Dirac-Hartree-Fock calculations is included when using the aug-cc-pvtz-pp valence basis set for Mo (paper III).[237]

All energies (given in kJ mol^{-1}) are corrected for (unscaled) zero-point vibrational energy contributions. We utilized ΔH values for the PES. The allowance for entropy in the PES may be inaccurate due to significant errors that can result from the harmonic oscillator approximation used to calculate the partition function for low-frequency modes, causing significant error in the derived vibrational entropy which in turn affects the final free-energy value.[238-240]

Table 2.1 DFT functionals together with the respective amount of exact-exchange admixture and basis sets employed in the present work.

NUMBER OF PAPER	**FUNCTIONAL/ AMOUNT OF EXACT EXCHANGE (%)**	**BASIS SET**
I	B3LYP/20	def2-TZVP
II	B3LYP/20	def2-QZVP
^{1}III	TPSSH/10, B3LYP/20, M06/27, and BHLYP/50	def2-TZVPD
^{2}IV	B3LYP/20, B97-1/21, and PBE0/25	def2-TZVP
^{3}V	B2GP-PLYP/65 (double hybrid with MP2 correlation)	def2-TZVP
VI	B3LYP/20	def2-QZVP
VII	B3LYP/20	def2-QZVP

^{1} For comparison, additional calculations with CCSD(T)/aug-cc-pvtz(pp)//B3LYP/def2-TZVPD have been done.

^{2} Data reported in the publication correspond to the B3LYP-D3BJ/def2-QZVPP//def2-TZVP level of theory.

^{3} Data reported in the publication correspond to the CCSD(T)/def2-TZVPP//B2GP-PLYP/def2-TZVP level of theory.

Moreover, ΔG values are appropriate to describe species in thermal equilibrium with the environment, which does not hold for the hot micro-canonical encounter complex in the mass-spectra experiments. In order to find and locate the transition state, we manually build a guess structure and optimize it using the classical Berny algorithm.[241] If the starting structure exhibits a single negative second derivative of the energy with respect to nuclear displacements (force constant) then the search will converge to the closest saddle point. Starting with a guess transition-state structure is often successful for reactions in which chemical intuition provides reasonable transition-state guesses. The nature of local minima and transition states has been verified by harmonic vibrational frequency analysis of the respective optimized structures. Intrinsic reaction coordinate (IRC) calculations were performed to link transition-state structures with the corresponding minima.[242-244] For those reactions that involve more than a single spin surface, the two-state reactivity (TSR) paradigm[245-249] has been considered. In these cases, the minimum-energy crossing points (MECPs) were calculated using the algorithm developed by Harvey et al.[250]

3. Results

“A detective with his murder mystery, a chemist seeking the structure of a new compound, use little of the formal and logical modes of reasoning. Through a series of intuitions, surmises, fancies, they stumble upon the right explanation, and have a knack of seizing it when it once comes within reach.”[251]

– Gilbert Newton Lewis

The present Dissertation is based on research articles published during the time as a PhD student in the groups of Prof. Dr. Martin Kaupp and Prof. Dr. Helmut Schwarz and is conceptually divided into four Chapters plus two separate parts, A, ‘*Unpublished work*’, and B, ‘*original papers*’ at the end of the Thesis. The ‘*original papers*’ part of the current Thesis corresponds to the original versions of the published articles. The author performed all the experiments and quantum chemical calculations included in articles III, VI, VII, and also those included in part A. Likewise, the author has performed the experimental part of article IV and has participated in the data analysis of article V. Finally, all the articles as well as unpublished drafts have been finalized as teamwork of all co-authors.

This Chapter includes a brief overview of the reactions studied in this paper-based doctoral Thesis.

3.1. C–O bond activation: reactions with carbon dioxide

A prominent strategy for CO_2 activation involves the insertion of CO_2 into a metal–hydrogen or metal–carbon bond,[77,252-259] The greater oxophilicity of early transition metals allows to accelerate this type of reactions providing a stronger M–OCO interaction.[77] Therefore, mechanistic aspects of the thermal reaction of $[Y(C_6D_5)]^+$ with CO_2 are analyzed in detail in article (VII). To generate the $[Y(C_6D_5)]^+$ cation, in which the yttrium atom is η^1-coordinated to the phenyl ring, a millimolar solution of yttrium(III) acetate hydrate and per-deuterated benzoic acid in a methanol/water mixture was used for ESI. The reaction of $[Y(C_6D_5)]^+$ with CO_2 proceeds by generation of two ionic products; see Equations. (3.1) and (3.2).

$$[Y(C_6D_5)]^+ + CO_2 \longrightarrow [Y,C_7,D_5,O_2]^+ \quad 71\% \qquad (3.1)$$

$$[Y(C_6D_5)]^+ + CO_2 \longrightarrow [Y,C_6,D_5,O]^+ + CO \quad 29\% \qquad (3.2)$$

The main reaction channel (Equation (3.1)) may correspond to the generation of a simple adduct or of insertion intermediates; the latter may be accessible via either C–O or C–C bond formation. According to DFT calculations, the most stable structure of the product ion corresponds to a benzoate complex in which the yttrium atom is coordinated to both oxygen atoms of the carboxylate group (**3**, Scheme 3.1). Subsequently, the decarbonylation process from **3** (Scheme 3.1) is hampered by a kinetic barrier of 54.4 kJ mol^{-1} located above the entrance channel and, thus not accessible under thermal conditions. Likewise, if loss of CO were to take place from the encounter complex (Scheme 3.1), formation of high-valent $[(C_6D_5)YO]^+$ would be hampered by kinetic barriers that are too high in energy to be accessible under thermal conditions. In contrast, CO can be eliminated from other intermediates **1** and **2** (Scheme 3.1), which are formed in the course of insertion of CO_2 into the Y–C bond of $[YC_6D_5]^+$. This decarbonylation results in the generation of $[(C_6D_5)OY]^+$ (**4**, Scheme 3.1).

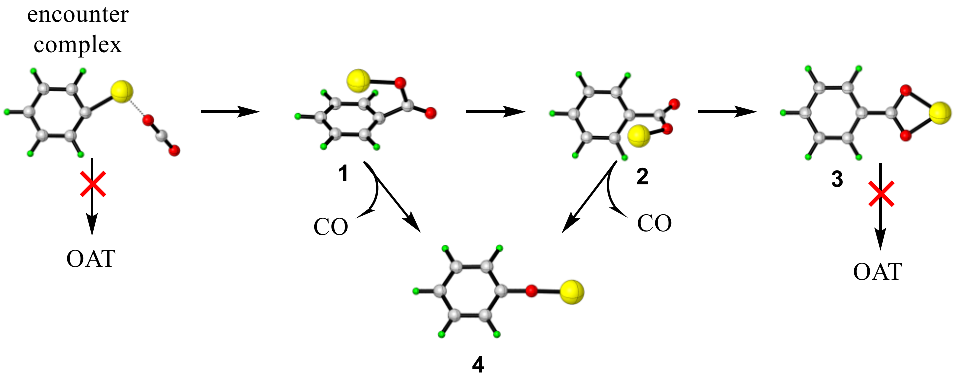

Scheme 3.1 Plausible intermediates for decarbonylation process resulting from the reaction of $[Y(C_6D_5)]^+$ with CO_2. Color code: Y = yellow, C = gray, H = green, O = red.

We then explored the possibility of activating a C–O bond of CO_2 mediated by $[CoX]^+$ (X=CN, F, Cl, Br, O, and OH) (unpublished article (I)). The mass-selected $[CoX]^+$ (X=CN, F, Cl, Br, O, and OH) cations are generated by ESI, transferred into the mass spectrometer and exposed to CO_2

(see the original article for details). The $[CoX]^+$ (X= F, Cl, Br, O, and OH) ions are non-reactive at the detection limit of the product ions; however, $[CoCN]^+$ reacts with CO_2 generating $[Co,O_2,C_2,N]^+$ as the only product, according to Equation (3.3).

$$[Co(CN)]^+ + CO_2 \quad \rightarrow \quad [Co,O_2,C_2,N]^+ \qquad (3.3)$$

According to DFT calculations, the product ion of Reaction (3.3) corresponds to a complex in which the cobalt atom is η^2 coordinated to both oxygen atoms of the carboxylate group. This ionic product is predicted 113.8 kJ mol^{-1} below the separated reactants. Several reaction pathways have been considered for the decarbonylation process, starting from different encounter complexes and intermediates; nevertheless, loss of CO from all of these complexes is hampered by kinetic barriers that are too high in energy to be accessible under thermal conditions. In contrast to the reaction profile of $[Co(CN)]^+/CO_2$, according to the DFT description, insertions of CO_2 into the Co–X bonds of $[CoX]^+$, (X = O, OH, F, Cl, and Br) are hindered by kinetic barriers higher than the entrance channel. In the case of $[CoO]^+/CO_2$ and $[CoBr]^+/CO_2$, the insertion process is also thermodynamically not accessible; the reactions $[CoO]^+ + CO_2 \rightarrow [Co(CO_3)]^+$ and $[CoBr]^+ + CO_2 \rightarrow [Co(BrCO_2)]^+$ are endothermic by 43.1 and 20.0 kJ mol^{-1}, respectively. Further, OAT is not possible for any of the systems investigated in this Thesis due to high kinetic barriers. Therefore, weak-field ligands (F, Cl, Br, O, and OH)[260] do not result in the conversion of CO_2 under thermal conditions, while the strong ligand field exerted by CN,[261] allows activation of CO_2 under ambient conditions.

3.2. C–H bond activation: reactions with methane

Next, we considered the generation of the $[OMoH]^+$ cation as well as its gas-phase reaction with CH_4 (Article (III)). The ions of interest have been generated by ESI from a methanolic solution of $MoCl_5$. In addition to the ion of interest, i.e. $[OMoH]^+$, the formation of a hydroxide cation $[Mo(OH)]^+$ is also conceivable. Thus, we have carried out gas-phase hydrogen-deuterium (H/D) exchange reactions[262] with D_2, as well as hydroxide-ligand exchange[263] via ion/molecule reactions with $H_2{}^{18}O$ in order to identify the structure(s) of $[Mo,O,H]^+$. While an H/D exchange is expected in the reactions of $[OMoH]^+$, an $^{16}O/^{18}O$ exchange with water points to the presence of

$[Mo(OH)]^+$. These combined experimental/computational investigations predict that when using a methanolic solution of $MoCl_5$, only a single isomer, most likely $[OMoH]^+$, is generated (for details, see article (III) "Generation and structural identification of $[Mo,O,H]^{+}$"). Further, the present study shows that the diatomic $[MoH]^+$ cation does not react with CH_4 under thermal conditions; the introduction of an oxygen atom as a ligand to form $[OMoH]^+$ results in the generation of an active species which is able to activate methane via Equation (3.4).

$$[OMoH]^+ + CH_4 \quad \rightarrow \quad [Mo,O,C,H_3]^+ + H_2 \qquad (3.4)$$

The different reactivities of $[MoH]^+$ and $[OMoH]^+$ are caused by the differential strengthening of the Mo–C bond in the product ion compared to that of the Mo–H bond in the precursor ion upon oxo substitution. In contrast to the oxo-ligand effect in $[OTiH]^+$ reported previously,[90] the addition of an oxygen atom to the molybdenum-hydride species follows an opposite trend. Thus, while the presence of this ligand *weakens* both the Ti–H and the Ti–CH_3 bonds, it *strengthens* the Mo–H and Mo–CH_3 bonds in the analogous Mo systems. Such differential strengthening can be explained partially by different amounts of exchange energy that are lost upon binding due to the decreasing number of unpaired nonbonding electrons; therefore, the $Mo–H^+$ and $Mo–C^+$ bonds are stronger in the case of $[OMoX]^+$ (X = H, CH_3) as compared to $[MoX]^+$ (X = H, CH_3).[264] Additionally, natural localized molecular orbital (NLMO) analyses[265,266] indicate that the Mo(5s)-contributions to the α-spin-channel Mo-X bonding NLMO are substantially enhanced by oxo substitution (Table S1 in Supporting Information; note that the trend for $[OTiX]^+$ vs. $[TiX]^+$ is just the reverse[93]). This "spin-polarized rehybridization" appears to contribute to the strengthening of the Mo–X bonds by oxo substitution, and it is apparent also in the shapes of the relevant canonical MOs. Thus, while the thermal reactions of $[OMoH]^+$ with methane have some features in common with $[OTiH]^+$, e.g. σ-bond metathesis,[90] fundamental mechanistic differences exist with regard to the operation of a multi-state reactivity scenario[245-249] for the molybdenum system.

Furthermore, by exploring the gas-phase reactions of $[NiL]^+$ (L = (C_6H_5), (C_5H_5N), (CN)) with methane, unexpected ligand effects were encountered; due to their versatile reactivities towards small molecules, e.g. methane, nickel-containing species attract wide interest in gas-phase chemistry.[267] According to our findings, while $[Ni(C_6H_5)]^+$ exclusively abstracts one hydrogen atom from methane (Equation (3.5)), $[Ni(CN)]^+$ brings about both H-atom abstraction and the ligand exchange to release HCN (Equation (3.6 a and b)); in contrast, $[\mathrm{Ni(C_5H_4N)}]^+$ is inert towards this substrate under the same conditions.

$$[\mathrm{Ni(C_6H_5)}]^{\bullet+} + \mathrm{CH_4} \longrightarrow [\mathrm{Ni,C_6,H_6}]^{+} + \mathrm{CH_3^{\bullet}} \qquad (3.5)$$

$$[\mathrm{Ni(CN)}]^{\bullet+} + \mathrm{CH_4} \left\{ \begin{array}{lll} \longrightarrow [\mathrm{Ni(NCH)}]^{+} + \mathrm{CH_3^{\bullet}} & 68\% & (3.6\ a) \\ \longrightarrow [\mathrm{Ni(CH_3)}]^{+} + \mathrm{HCN} & 32\% & (3.6\ b) \end{array} \right.$$

The most stable structure of $[\mathrm{Ni(C_6H_5)}]^+$ is located on the triplet-state surface, in which only the C_{ipso} of the phenyl ligand is bound to the nickel atom (**5**, Scheme 3.2). The energetically most favorable pathway for the reaction of $[\mathrm{Ni(C_6H_5)}]^+$ with $\mathrm{CH_4}$ proceeds via a two-state reactivity scenario (see article (IV) for details), and in the final product, $[\mathrm{Ni(C_6H_6)}]^+$, the nickel atom is η^6 coordinated to the benzene ring (**6**, Scheme 3.2). Further, the most stable structure of $[\mathrm{Ni(C_5H_4N)}]^+$ corresponds to an η^2-coordinated, planar complex that is located on the singlet-state surface (**7**, Scheme 3.2). Without exception, all explored pathways for the $[\mathrm{Ni(C_5H_4N)}]^+/\mathrm{CH_4}$ couple involve at one stage transition states that are not accessible at ambient condition. In contrast to the Ni(η^2-NC) coordination of $[\mathrm{Ni(C_5H_4N)}]^+$, the complex $[\mathrm{Ni(CN)}]^+$ exhibits a quasi-linear (**8**, Scheme 3.2), triplet ground-state structure. A thermally available TSR scenario is also operative for $[\mathrm{Ni(CN)}]^+/\mathrm{CH_4}$ to generate both $[\mathrm{Ni(CH_3)}]^+$ and $[\mathrm{Ni(NCH)}]^+$ (**9** and **10**, Scheme 3.2).

To obtain a better understanding of the respective C–H bond activation steps, the deformation energy (ΔE_{def}), and its comparison with the respective reaction barrier ($\Delta E^{\ddagger}$) were examined. As described before,[268] the barriers which correspond by and large to the deformation energy, i.e. $\Delta E_{\mathrm{def}} \approx \Delta E^{\ddagger}$, are indicative for H-atom transfer (HAT); for other C–H bond activation steps, however, the TSs benefit from large stabilizing interactions that lower the barriers well below the corresponding deformation energies, i.e. $\Delta E_{\mathrm{def}} >> \Delta E^{\ddagger}$ representing a proton-coupled electron transfer (PCET).[108,268,269] According to this classification, a PCET pathway involving a two-state reactivity scenario, prevails for both $[\mathrm{Ni(C_6H_5)}]^+/\mathrm{CH_4}$ and $[\mathrm{Ni(CN)}]^+/\mathrm{CH_4}$. In addition, an alternative, single-state HAT pathway is also thermally available for $[\mathrm{Ni(CN)}]^+/\mathrm{CH_4}$. The presence of the empty *4s*(Ni) orbital is essential for the investigated PCET pathways, while the HAT pathway for $[\mathrm{Ni(CN)}]^+/\mathrm{CH_4}$ benefits from the excessive energy released when forming the encounter complex.

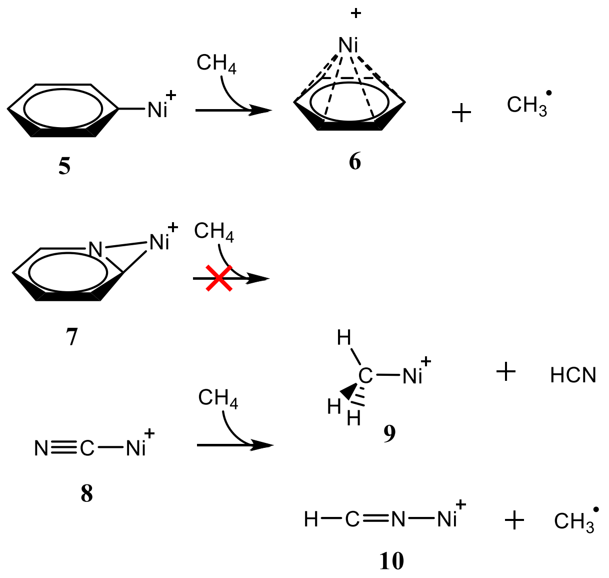

Scheme 3.2 Schematic presentation of the reactions for $[Ni(C_6H_5)]^+/CH_4$, $[Ni(C_5H_4N)]^+/CH_4$, and $[Ni(CN)]^+/CH_4$.

3.3. Simultaneous activation of C–H and C–O bonds

In the last part of the work we have investigated mechanistic aspects of the “joint” activation of both methane and carbon dioxide by some transition metal complexes. In the first part (Article (VI)), we investigated the reactions of these two *C1* sources with two isomers of $[Ta,O,H]^+$, i.e. $[OTaH]^+$ and $[TaOH]^+$. These experiments revealed that $[Ta,O,H]^+$, reacting with CH_4 and CO_2, resulted in the ionic products $[Ta,O,C,H_3]^+$ and $[Ta,O_2,H]^+$, respectively. Isotopic labeling experiments with CD_4 revealed the formations of $[Ta,O,C,D_3]^+$ and $[Ta,O,C,D_2H]^+$, and a clean reaction in the case of reaction with $C^{18}O_2$ under the exclusive formation of $[Ta,^{16}O,^{18}O,H]^+$. The calculated PESs indicate that both isomers are able to thermally activate a C–H bond of methane. In the spin-allowed activation of CH_4 by $[OTaH]^+$, the rate-limiting step proceeds through a transition state located only 3.6 kJ mol^{-1} below the entrance channel, and the final product corresponds to the methyl-oxo tantalum complex (**12**, Scheme 3.3). In contrast, the activation of a C–H bond in case of the $[Ta(OH)]^+$ complex requires an ISC from the quartet to the doublet spin state PES, and this is associated with a rate-limiting barrier located 20 kJ mol^{-1} below the entrance channel. Here, two different reaction pathways toward the elimination of H_2 are possible on the doublet PES; either via σ-bond metathesis to generate a genuine H_2 intermediate $[H_2Ta(OH)(CH_2)]^+$, from which H_2 is eliminated under the formation of methylene-hydroxo complex (**11**, Scheme 3.3), or alternatively through the generation of the complex $[(H)_2Ta(O)(CH_3)]^+$ and eventually elimination of H_2 under the production of a methyl-oxo tantalum complex (**12**, Scheme 3.3).

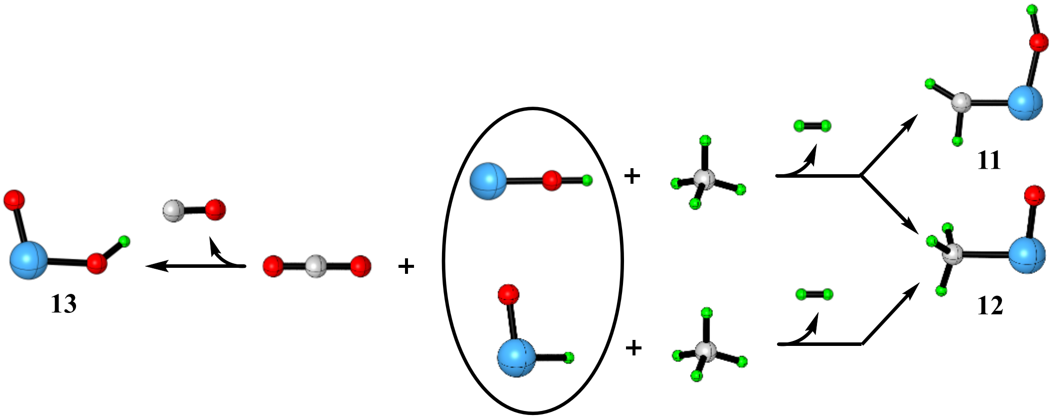

Scheme 3.3 Possible products resulting from the reactions of $[Ta,O,H]^+$ with CH_4 (**11** and **12**) and CO_2 (**13**). Color code: Ta = blue, C = gray, H = green, O = red.

The activation of CO_2 follows a similar trend: the rate-limiting transition structure of the spin-allowed C–O activation mediated by $[OTaH]^+$ is -9.0 kJ mol^{-1} below the separated reactants, while for the $[Ta(OH)]^+$ system a spin crossing is necessary to access the transition structure of C–O bond activation with a relative energy of -57.4 kJ mol^{-1}. In both cases an oxo-hydroxo complex (c, Figure 3.1) is generated concomitantly with elimination of CO.

We further aimed to understand the activation of CH_4 and CO_2 promoted by $[Nb,O,H]^+$ and compared these findings with the previously investigated $[Ta,O,H]^+$ systems (see unpublished article (II)). Our experiments revealed that $[Nb,O,H]^+$ reacts with CH_4 and CO_2 under the formation of the ionic products $[Nb,O,C,H_3]^+$ (Equation (3.7)) and $[Nb,O_2,H]^+$ (Equation (3.8)) and the concomitant elimination of H_2 and CO, respectively.

$$[Nb,O,H]^+ + CH_4 \rightarrow [Nb,O,C,H_3]^+ + H_2 \quad (3.7)$$

$$[Nb,O,H]^+ + CO_2 \rightarrow [Nb,O_2,H]^+ + CO \quad (3.8)$$

Isotopic labelling experiments with $C^{18}O_2$ showed a clean reaction similar to that observed for tantalum. In contrast to the scrambling processes observed for the tantalum complex in the reaction with CD_4, the exclusive formation of $[Nb,O,C,D_3]^+$ has been observed in the case of the Nb system. DFT calculations indicate that, while $[ONbH]^+$ is able to thermally activate a C–H bond of methane in a similar fashion like the oxo-hydride tantalum complex, a kinetic barrier for the activation of methane by $[Nb(OH)]^+$ has been located on the PES. In the spin-allowed activation of CH_4 by $[ONbH]^+$, the rate-limiting step proceeds through a transition state located 29.0 kJ mol^{-1} below the entrance channel. Furthermore, in the case of CO_2 activation, the relative energy of the transition structure for the spin-allowed C–O activation mediated by $[ONbH]^+$ is similar to that of the entrance channel (0.3 kJ mol^{-1}) but still plausible to occur considering the error bars of the calculation. Note also that the ions of the high-energy tail of the kinetic-energy distribution of the precursor ion might be responsible for the observed reactions; the kinetic energy width of the parent ions at half peak height has been determined to 0.4 eV.[69,270,271] Likewise, for the $[Nb(OH)]^+/CO_2$ system a spin crossing is necessary to access the transition structure of C–O bond activation with a relative energy of -11.2 kJ mol^{-1}. These findings may indicate a similar product structure as the Ta-complexes ($[Ta(OH)]^+$ and $[OTaH]^+$) for the reaction with CO_2.

Finally, in order to investigate a simultaneous activation of CO_2 and CH_4, in article (V), the potential of carbonyl rhenium complexes in activating and coupling carbon dioxide and methane has been explored by a combination of gas-phase experiments (using Fourier-Transform Ion-Cyclotron-Resonance (FT-ICR) mass spectrometry, see experimental details in article (V)) and high-level quantum chemical calculations.

In the thermal interaction of $[Re(CO)_x]^+$ ($x = 0–3$) with CO_2, only $[Re(CO)_2]^+$ is able to abstract one oxygen atom from this substrate according to Equation (3.9).

$$[Re(CO)_2]^+ + CO_2 \quad \rightarrow \quad [Re,C_2,O_3]^+ + CO \qquad (3.9)$$

According to the calculation at the CCSD(T)/def2-TZVPP//B2GP-PLYP/def2-TZVP level of theory, the final product for the reaction of $[Re(CO)_2]^+$ with CO_2 corresponds to an oxo-dicarbonyl complex of rhenium, $[ORe(CO)_2]^+$ (**14**, Scheme 3.4). Furthermore, regarding the reaction of CO_2 with $[Re]^+$, $[Re(CO)]^+$ and $[Re(CO)_3]^+$, while the overall O-atom processes are exothermic, these paths are hampered by kinetic barriers amounting to 106.5, 13.3, and 56.1 kJ mol^{-1}, respectively, above the entrance channel. The unique reactivity of $[Re(CO)_2]^+$ toward CO_2 among all investigated rhenium complexes may be traced back to the relatively low excitation energy necessary for promotion of the triplet ground state to the singlet state (42 kJ mol^{-1}), such that a spin-crossing for $[Re(CO)_2]^+/CO_2$ is energetically accessible under thermal conditions. One of the 5d orbitals of the excited $^1[Re(CO)_2]^+$ is empty, resulting in a lower HOMO(CO_2)–LUMO($^1[Re(CO)_2]^+$) gap of 5.1 eV in compared to the ground state HOMO(CO_2)–LUMO($^1[Re(CO)_x]^+$) (X =0-3) which is between 6.2–6.4 eV. Thus, CO_2 activation via such a donor-acceptor interaction is facilitated.

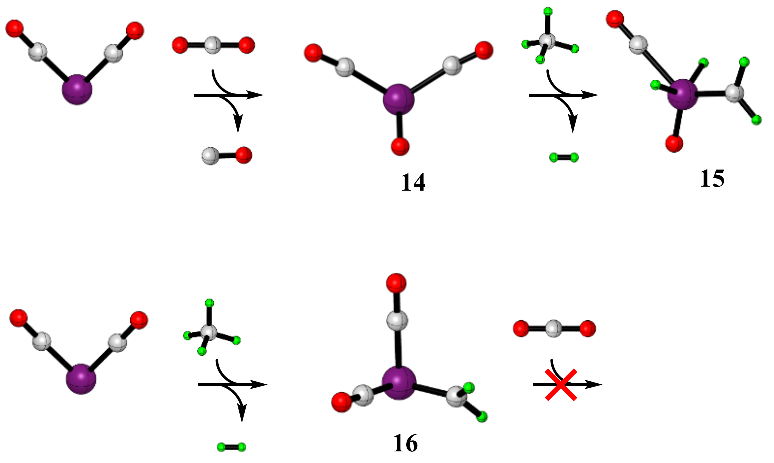

Scheme 3.4 Schematic reaction pathways for the activation of carbon dioxide and methane by $[Re(CO)_2]^+$ as a starting species. Color code: Re = purple, C = gray, H = green, O = red.

Next, the ionic product $[ORe(CO)_2]^+$ activates two C–H bonds of methane to produce a dihydrido methylene complex $[ORe(CO)(CH_2)(H)_2]^+$ (**15**, Scheme 3.4). However, coupling of the C1 fragments CO and CH_2 to form CH_2CO does not take place. For the activation of CH_4 by $[ORe(CO)_2]^+$, both the Lewis base and acid characters of the rhenium center are crucial in the initial insertion of the rhenium atom into the H_3C–H bond via PECT. Thus, it is the amphoteric character of rhenium, enhanced by ligation, which enables the thermal reactivities of this complex toward both CO_2 and CH_4. Furthermore, reversing the activation steps, i.e., sequential activation of first CH_4 and then CO_2, is not possible under thermal conditions. While the activation of methane by $[Re(CO)_2]^+$ is plausible under H_2 elimination and methylene complexes $[Re(CO)_2(CH_2)]^+$ generation (**16**, Scheme 3.4),[272] $[Re(CO)_2(CH_2)]^+$ is unreactive toward CO_2 .

4. Conclusions and Outlook

"The greatest ideas are the simplest."[273]

– William Golding

Since entering the 21st century the issue of a global climate change has caused increasing concern of the international community. There has been growing interest in the creation of a recycling process in which greenhouse gases, e.g. CO_2, CH_4, that are typically emitted from large sources such as power plants, steel plants, etc., are steadily captured and used as a *C1* source to produce useful chemicals. It is believed that more scientific research in this area is needed to understand what is lacking for the fruitful development of more effective catalysts to convert hydrocarbons into chemical feedstock by consuming these two hazardous greenhouse gases. Since gas-phase experiments are extremely useful to systematically study catalytic reactions, in this work mass spectrometric experiments in conjunction with quantum-chemical calculations were employed to explore new metal-ligand systems which can bring about C–H and C–O bond activation of CH_4 and CO_2, respectively, as well as the possibility of simultaneous activation of these two buildings blocks. Further, the factors, like the nature and number of the ligands, substrates, and metal centers, which control the gas-phase reactivity, have been explored. Since this study covers a broad range of chemical reactions, the Thesis is made up from three parts as summarized below.

In the work on CO_2 activation, several complex ions, such as $[Y(C_6D_6)]^+$ and $[CoX]^+/CO_2$ (X = CN, F, Cl, Br, O and OH), have been generated in the gas phase and, in some cases, proven to be reactive with CO_2 under thermal conditions. Various mechanisms have been addressed. For example, the reaction of the phenyl yttrium cation with CO_2 proceeds by migratory insertion under C–C bond formation followed by decarbonylation. Furthermore, ligand effects on the reactivity of ionic complexes towards CO_2 have been derived. Thus, we found that carbon dioxide activation by $[CoX]^+$ (X = CN, F, Cl, Br, O and OH) is feasible under thermal conditions only for X = CN. DFT calculations showed that activation of CO_2 either by insertion into the Co–X bond of $[CoX]^+$, (X = O, OH, F, Cl, and Br) or by O-atom transfer from CO_2 to the metal center are hindered by kinetic barriers located above the reactant asymptote. In the case of $[CoO]^+/CO_2$ and $[CoBr]^+/CO_2$, the insertion process is also thermodynamically inaccessible. Further, the final insertion products for both $[Y(C_6D_5)]^+$ and $[Co(CN)]^+$ correspond to complexes in which the metal center is η^2-coordinated to both oxygen atoms of the carboxylate group.

As to the work on CH_4 activation, various aspects of ligand effects on the reactivity of ionic metal complexes were studied. For example, while atomic Mo^+ and Ni^+ in their ground states are inert towards CH_4, adding ligands like O, H, CN, C_6H_5 may result in active complexes. Further, the oxo-hydride complex of molybdenum $[OMoH]^+$ activates methane spontaneously at ambient conditions, while its hydride complex $[MoH]^+$ does not; this has been attributed to the differential strengthening of the Mo–C compared to the Mo–H bond upon oxo substitution. This contrasts to the results obtained for the Ti analogues ($[TiH]^+$ and $[HTiO]^+$); here, unlike the oxo-ligand effect in $[OMoX]^+$ (X = H, CH_3), the presence of this ligand weakens both the Ti–H and the Ti–CH_3 bonds. The strengthening of the Mo–X bond by oxo substitution, versus the weakening of Ti–X bonding, are substantially related to the enhancement of Mo(5s)-contributions to the α-spin-channel. When ligating Ni^+ with CN and C_6H_5 to form $[Ni(CN)]^+$ and $[Ni(C_6H_5)]^+$, the reactivity towards CH_4 is switched on; however, the complex $[Ni(C_5H_4N)]^+$ is inert towards this substrate. Here, the presence of an empty *4s*(Ni) orbital is essential. Various mechanisms have been considered with the aim of DFT calculations. While methane activation by $[Ni(C_6H_5)]^+$ proceeds via a PCET pathway, both PCET and HAT pathways are feasible in case of $[Ni(CN)]^+/CH_4$ under thermal conditions. Finally, a two-state reactivity scenario prevails for the $[OMoH]^+/CH_4$, $[Ni(C_6H_5)]^+/CH_4$, and $[Ni(CN)]^+/CH_4$ couples.

We also investigated the possibility of both CO_2 and CH_4 activations by one reactive species. Interestingly, the ionic complexes $[X,O,H]^+$ (M = Ta, Nb) and $[Re(CO)_2]^+$ were found to be reactive with both substrates under ambient conditions. While the thermal reactions of $[Ta,O,H]^+$ with both CO_2 and CH_4 have some features in common with $[Nb,O,H]^+$, fundamental differences exist. For example, as shown computationally, while $[Ta(OH)]^+$ is able to thermally activate methane, a kinetic barrier above the entrance channel hinders the activation of methane by $[Nb(OH)]^+$. In general, the higher reactivity as well as the bifunctionality of $[Ta,O,H]^+$ compared to $[Nb,O,H]^+$ originates from the relativistic strengthening of certain bonds for the heavier 5d element. This includes a higher oxygen-atom affinity (OA) of Ta compared to Nb, a stronger M–C interaction in the reaction with CH_4 and a stronger M–OCO interaction in the reaction with CO_2.

For the $[Re(CO)_2]^+$/CH_4&CO_2 systems, interestingly, the precursor ion is not only reactive with both substrates, but also able to sequentially activate CO_2 and CH_4; by contrast, the inverse feed-in of the two substrates does not help; here, the product ion of methane activation, $[Re(CO)_2(CH_2)]^+$, is unreactive toward CO_2. It could also be shown in this work that the number of ligands matters for the reactivity of ionic complexes towards CO_2. Thus, in contrast to the bis-carbonyl complex of rhenium, the bare Re^+ cation as well as the complexes $[Re(CO)_x]^+$ ($x = 1, 3$) are thermally unreactive toward CO_2. The root cause of the versatile reactivity of $[Re(CO)_2]^+$ corresponds to the amphoteric feature of the rhenium center in that it serves as both Lewis base and acid. Finally, in none of the above systems the coupling of the *C1* fragments CO and CH_2 to form CH_2CO takes place.

The present work aims at a better and more fundamental understanding of the nature of processes in homogeneous, heterogeneous and enzymatic catalysis for the activation of CO_2 and CH_4; yet, the knowledge presented in this Thesis provides just a very small step in order to find a more effective utilization of natural resources. Many factors such as variations in terms of the oxidation state of the transition metal, the nature of the ligands and substrates, and a comparison with related transition metal complexes are all helpful in understanding the correlation between reactivity and the electronic characteristics and structural properties. Possible extensions of this work might address the questions remaining in some of the respective topics. For example, more comparative gas-phase studies on the nature of metal and ligand effects in transition-metal mediated direct C–C bond coupling of CH_4 and CO_2 are necessary. Moreover, since there are very few ion molecule reactions in case of activation of CO_2 with ligated *late* transition metal complexes as well as CH_4 with ligated *early* transition metal complexes, finding the accessible thermal reaction and its fundamental mechanistic information can be a new target. Likewise, by changing the transition metals and ligands, and examining alterations of the electronic structures of the precursor and of the reaction mechanism, one can explore the factors that contribute to the chemical reactivity and selectivity. Besides this goal, gas-phase models of the active sites of enzymes e.g. methyl-coenzyme M reductase (MCR) which catalyzes the key step in converting CO_2 to methane, constitute a challenging target. In addition, further mass-spectrometric studies in conjunction with quantum-chemical calculations can address questions regarding the mechanism of bio-catalytic reactions by gas-phase models. For instance, mechanistic studies on Cytochrome P450 revealed that the concept of TSR[245-249] accounts for the reactions of this enzyme.[274,275]

References

[1] E. Musk, https://twitter.com/elonmusknewsorg/status/760920726564134912.

[2] C. B. Roberts, N. O. Elbashir, *Fuel Process. Technol.* **2003**, 83, 1-9.

[3] J. Fierro, *Catal. lett.* **1993**, 22, 67-91.

[4] H. Schwarz, *Angew. Chem. Int. Ed.* **2011**, 50, 10096-10115.

[5] V. N. Cavaliere, D. J. Mindiola, *Chem. Sci.* **2012**, 3, 3356-3365.

[6] P. Tang, Q. Zhu, Z. Wu, D. Ma, *Energy Environ. Sci.* **2014**, 7, 2580-2591.

[7] H. Schwarz, *Isr. J. Chem.* **2014**, 54, 1413-1431.

[8] A. J. Morris, G. J. Meyer, E. Fujita, *Acc. Chem. Res.* **2009**, 42, 1983-1994.

[9] M. Mikkelsen, M. Jørgensen, F. C. Krebs, *Energy Environ. Sci.* **2010**, 3, 43-81.

[10] W. Wang, S. Wang, X. Ma, J. Gong, *Chem. Soc. Rev.* **2011**, 40, 3703-3727.

[11] G. Fiorani, W. Guo, A. W. Kleij, *Green Chem.* **2015**, 17, 1375-1389.

[12] G. A. Olah, *Angew. Chem. Int. Ed.* **2005**, 44, 2636-2639.

[13] J. R. Webb, T. Bolaño, T. B. Gunnoe, *ChemSusChem*. **2011**, 4, 37-49.

[14] M. Cokoja, C. Bruckmeier, B. Rieger, W. A. Herrmann, F. E. Kühn, *Angew. Chem. Int. Ed.* **2011**, 50, 8510-8537.

[15] G. A. Olah, *Angew. Chem. Int. Ed.* **2013**, 52, 104-107.

[16] P. V. L. Reddy, K.-H. Kim, H. Song, *Renew. Sustainable Energy Rev.* **2013**, 24, 578-585.

[17] M. Aresta, A. Dibenedetto, A. Angelini, *Chem. Rev.* **2014**, 114, 1709-1742.

[18] J. M. Weber, *Int. Rev. Phys. Chem.* **2014**, 33, 489-519.

[19] V. Havran, M. P. Duduković, C. S. Lo, *Ind. Eng. Chem. Res.* **2011**, 50, 7089-7100.

[20] H. Schwarz, *Chem. Phys. Lett.* **2015**, 629, 91-101.

[21] R. Horn, R. Schlögl, *Catal. Lett.* **2015**, 145, 23-39.

[22] M. J. da Silva, *Fuel Process. Technol.* **2016**, 145, 42-61.

[23] G. Jones, J. G. Jakobsen, S. S. Shim, J. Kleis, M. P. Andersson, J. Rossmeisl, F. Abild-Pedersen, T. Bligaard, S. Helveg, B. Hinnemann, *J. Catal.* **2008**, 259, 147-160.

[24] A. Holmen, *Catal. Today*. **2009**, 142, 2-8.

[25] C. Mesters, *Annu. Rev. Chem. Biomol. Eng.* **2016**, 7, 223-238.

[26] Y. S. Su, J. Y. Ying, W. H. Green, *J. Catal.* **2003**, 218, 321-333.

[27] S. Arndt, G. Laugel, S. Levchenko, R. Horn, M. Baerns, M. Scheffler, R. Schlögl, R. Schomäcker, *Catal. Rev.* **2011**, 53, 424-514.

[28] R. Balasubramanian, S. M. Smith, S. Rawat, L. A. Yatsunyk, T. L. Stemmler, A. C. Rosenzweig, *Nature*. **2010**, 465, 115-119.

[29] M. Bordeaux, A. Galarneau, J. Drone, *Angew. Chem. Int. Ed.* **2012**, 51, 10712-10723.

[30] R. Banerjee, Y. Proshlyakov, J. D. Lipscomb, D. A. Proshlyakov, *Nature*. **2015**, 518, 431-434.

[31] H. V. Le, S. Parishan, A. Sagaltchik, C. Göbel, C. Schlesiger, W. Malzer, A. Trunschke, R. Schomäcker, A. Thomas, *ACS Catal.* **2017**, 7, 1403-1412.

[32] H. Arakawa, M. Aresta, J. N. Armor, M. A. Barteau, E. J. Beckman, A. T. Bell, J. E. Bercaw, C. Creutz, E. Dinjus, D. A. Dixon, K. Domen, D. L. DuBois, J. Eckert, E. Fujita, D. H. Gibson, W. A. Goddard, D. W. Goodman, J. Keller, G. J. Kubas, H. H. Kung, J. E. Lyons, L. E. Manzer, T. J. Marks, K. Morokuma, K. M. Nicholas, R. Periana, L. Que, J. Rostrup-Nielson, W. M. H. Sachtler, L. D. Schmidt, A. Sen, G. A. Somorjai, P. C. Stair, B. R. Stults, W. Tumas, *Chem. Rev.* **2001**, 101, 953-996.

[33] M. Aresta, A. Dibenedetto, *Dalton Trans.* **2007**, 2975-2992.

[34] C. Maeda, Y. Miyazaki, T. Ema, *Catal. Sci. Tech.* **2014**, 4, 1482-1497.

[35] I. Omae, *Coord. Chem. Rev.* **2012**, 256, 1384-1405.

[36] C. Federsel, R. Jackstell, M. Beller, *Angew. Chem. Int. Ed.* **2010**, 49, 6254-6257.

[37] C. Martín, G. Fiorani, A. W. Kleij, *ACS Catal.* **2015**, 5, 1353-1370.

[38] J. W. Comerford, I. D. V. Ingram, M. North, X. Wu, *Green Chem.* **2015**, 17, 1966-1987.

[39] S. M. Thomas, R. DiCosimo, V. Nagarajan, *Trends Biotechnol.* **2002**, 20, 238-242.

[40] S. W. Ragsdale, *Ann. N. Y. Acad. Sci.* **2008**, 1125, 129-136.

[41] A. Ciaccafava, D. Tombolelli, L. Domnik, J.-H. Jeoung, H. Dobbek, M.-A. Mroginski, I. Zebger, P. Hildebrandt, *Angew. Chem. Int. Ed.* **2017**, 56, 7398-7401.

[42] T. I. Doukov, T. M. Iverson, J. Seravalli, S. W. Ragsdale, C. L. Drennan, *Science*. **2002**, 298, 567-572.

[43] K. M. K. Yu, I. Curcic, J. Gabriel, S. C. E. Tsang, *ChemSusChem*. **2008**, 1, 893-899.

[44] P. G. Jessop, F. Joó, C.-C. Tai, *Coord. Chem. Rev.* **2004**, 248, 2425-2442.

[45] T. Sakakura, J.-C. Choi, H. Yasuda, *Chem. Rev.* **2007**, 107, 2365-2387.

[46] T. C. Johnson, D. J. Morris, M. Wills, *Chem. Soc. Rev.* **2010**, 39, 81-88.

[47] I. Hermans, *Angew. Chem. Int. Ed.* **2013**, 52, 4522-4523.

[48] W. B. Tolman, Activation of Small Molecules: Organometallic and Bioinorganic Perspectives, Wiley, **2006**.

[49] M. Aresta, A. Dibenedetto, E. Quaranta, *J. Catal.* **2016**, 343, 2-45.

[50] B. Wang, S. Albarracín-Suazo, Y. Pagán-Torres, E. Nikolla, *Catal. Today*. **2017**, 285, 147-158.

[51] S. Chakraborty, J. Zhang, J. A. Krause, H. Guan, *J. Am. Chem. Soc.* **2010**, 132, 8872-8873.

[52] P. G. Jessop, T. Ikariya, R. Noyori, *Chem. Rev.* **1995**, 95, 259-272.

[53] D. W. Stephan, G. Erker, *Angew. Chem. Int. Ed.* **2010**, 49, 46-76.

[54] C.-H. Lim, A. M. Holder, J. T. Hynes, C. B. Musgrave, *Inorg. Chem.* **2013**, 52, 10062-10066.

[55] D. W. Stephan, *J. Am. Chem. Soc.* **2015**, 137, 10018-10032.

[56] K.-i. Tominaga, Y. Sasaki, M. Kawai, T. Watanabe, M. Saito, *J. Chem. Soc., Chem. Commun.* **1993**, 629-631.

[57] T. Ken-ichi, S. Yoshiyuki, W. Taiki, S. Masahiro, *Bull. Chem. Soc. Jpn.* **1995**, 68, 2837-2842.

[58] A. P. E. York, T. c. Xiao, M. L. H. Green, J. B. Claridge, *Catal. Rev.* **2007**, 49, 511-560.

[59] D. J. Moon, *Catal. Surv. Asia*. **2008**, 12, 188-202.

[60] E. M. Wilcox, G. W. Roberts, J. J. Spivey, *Catal. Today*. **2003**, 88, 83-90.

[61] W. Huang, K. C. Xie, J. P. Wang, Z. H. Gao, L. H. Yin, Q. M. Zhu, *J. Catal.* **2001**, 201, 100-104.

[62] Y.-H. Ding, W. Huang, Y.-G. Wang, *Fuel Process. Technol.* **2007**, 88, 319-324.

[63] J.-F. Wu, S.-M. Yu, W. D. Wang, Y.-X. Fan, S. Bai, C.-W. Zhang, Q. Gao, J. Huang, W. Wang, *J. Am. Chem. Soc.* **2013**, 135, 13567-13573.

[64] A. M. Rabie, M. A. Betiha, S.-E. Park, *App. Catal. B*. **2017**, 215, 50-59.

[65] K. Eller, H. Schwarz, *Chem. Rev.* **1991**, 91, 1121-1177.

[66] D. Schröder, C. Heinemann, W. Koch, H. Schwarz, *Pure Appl. Chem.* **1997**, 69, 273-280.

[67] D. K. Böhme, H. Schwarz, *Angew. Chem. Int. Ed.* **2005**, 44, 2336-2354.

[68] M. Schlangen, H. Schwarz, *Catal. Lett.* **2012**, 142, 1265-1278.

[69] D. Schröder, H. Schwarz, S. Schenk, E. Anders, *Angew. Chem. Int. Ed.* **2003**, 42, 5087-5090.

[70] N. Dietl, C. van der Linde, M. Schlangen, M. K. Beyer, H. Schwarz, *Angew. Chem. Int. Ed.* **2011**, 50, 4966-4969.

[71] N. Dietl, M. Schlangen, H. Schwarz, *Chem. Eur. J.* **2011**, 17, 1783-1788.

[72] J. Li, P. González-Navarrete, M. Schlangen, H. Schwarz, *Chem. Eur. J.* **2015**, 21, 7780-7789.

[73] S. Zhou, J. Li, X.-N. Wu, M. Schlangen, H. Schwarz, *Angew. Chem. Int. Ed.* **2016**, 55, 441-444.

[74] S. Ramakrishnan, K. M. Waldie, I. Warnke, A. G. De Crisci, V. S. Batista, R. M. Waymouth, C. E. D. Chidsey, *Inorg. Chem.* **2016**, 55, 1623-1632.

[75] P. D. Dau, P. B. Armentrout, M. C. Michelini, J. K. Gibson, *Phys. Chem. Chem. Phys.* **2016**, 18, 7334-7340.

[76] H. Schwarz, *Coord. Chem. Rev.* **2017**, 334, 112-123.

[77] K.-C. Lau, B. J. Petro, S. Bontemps, R. F. Jordan, *Organometallics*. **2013**, 32, 6895-6898.

[78] G. K. Koyanagi, D. K. Bohme, *J. Phys. Chem. A*. **2006**, 110, 1232-1241.

[79] A. Shayesteh, V. V. Lavrov, G. K. Koyanagi, D. K. Bohme, *J. Phys. Chem. A*. **2009**, 113, 5602-5611.

[80] K. K. Irikura, J. L. Beauchamp, *J. Am. Chem. Soc.* **1991**, 113, 2769-2770.

[81] K. K. Irikura, J. L. Beauchamp, *J. Phys. Chem.* **1991**, 95, 8344-8351.

[82] X.-G. Zhang, R. Liyanage, P. B. Armentrout, *J. Am. Chem. Soc.* **2001**, 123, 5563-5575.

[83] P. B. Armentrout, *Chem. Eur. J.* **2017**, 23, 10-18.

[84] C. Heinemann, R. H. Hertwig, R. Wesendrup, W. Koch, H. Schwarz, *J. Am. Chem. Soc.* **1995**, 117, 495-500.

[85] H. Schwarz, *Angew. Chem. Int. Ed.* **2003**, 42, 4442-4454.

[86] C. Heinemann, H. Schwarz, W. Koch, K. G. Dyall, *J. Chem. Phys.* **1996**, 104, 4642-4651.

[87] F. Rakowitz, C. M. Marian, B. Schimmelpfennig, *Phys. Chem. Chem. Phys.* **2000**, 2, 2481-2488.

[88] R. Wesendrup, H. Schwarz, *Angew. Chem. Int. Ed.* **1995**, 34, 2033-2035.

[89] N. Sändig, W. Koch, *Organometallics*. **1998**, 17, 2344-2351.

[90] R. Kretschmer, M. Schlangen, H. Schwarz, *Angew. Chem. Int. Ed.* **2013**, 52, 6097-6101.

[91] S.-Y. Tang, N. J. Rijs, J. Li, M. Schlangen, H. Schwarz, *Chem. Eur. J.* **2015**, 21, 8483-8490.

[92] T. J. Carlin, L. Sallans, C. J. Cassady, D. B. Jacobson, B. S. Freiser, *J. Am. Chem. Soc.* **1983**, 105, 6320-6321.

[93] Q. Zhang, M. T. Bowers, *J. Phys. Chem. A*. **2004**, 108, 9755-9761.

[94] M. Schlangen, D. Schröder, H. Schwarz, *Angew. Chem. Int. Ed.* **2007**, 46, 1641-1644.

[95] M. Schlangen, H. Schwarz, *Angew. Chem. Int. Ed.* **2007**, 46, 5614-5617.

[96] D. Schröder, H. Schwarz, *Angew. Chem. Int. Ed.* **1995**, 34, 1973-1995.

[97] J. Roithová, D. Schröder, *J. Am. Chem. Soc.* **2007**, 129, 15311-15318.

[98] M. Engeser, M. Schlangen, D. Schröder, H. Schwarz, T. Yumura, K. Yoshizawa, *Organometallics*. **2003**, 22, 3933-3943.

[99] D. Schröder, H. Schwarz, *Proc. Natl. Acad. Sci. U.S.A.* **2008**, 105, 18114-18119.

[100] M. Schlangen, H. Schwarz, *Dalton Trans.* **2009**, 10155-10165.

[101] N. Dietl, M. Schlangen, H. Schwarz, *Angew. Chem. Int. Ed.* **2012**, 51, 5544-5555.

[102] H. Schwarz, *Angew. Chem. Int. Ed.* **2015**, 54, 10090-10100.

[103] H. Schwarz, P. González-Navarrete, J. Li, M. Schlangen, X. Sun, T. Weiske, S. Zhou, *Organometallics*. **2017**, 36, 8-17.

[104] J. M. Mayer, *J. Phys. Chem. Lett.* **2011**, 2, 1481-1489.

[105] W. Lai, C. Li, H. Chen, S. Shaik, *Angew. Chem. Int. Ed.* **2012**, 51, 5556-5578.

[106] D. R. Weinberg, C. J. Gagliardi, J. F. Hull, C. F. Murphy, C. A. Kent, B. C. Westlake, A. Paul, D. H. Ess, D. G. McCafferty, T. J. Meyer, *Chem. rev.* **2012**, 112, 4016-4093.

[107] J.-M. Savéant, *Annu. Rev. Anal. Chem.* **2014**, 7, 537-560.

[108] A. Migliore, N. F. Polizzi, M. J. Therien, D. N. Beratan, *Chem. Rev.* **2014**, 114, 3381-3465.

[109] S. Hammes-Schiffer, *J. Am. Chem. Soc.* **2015**, 137, 8860-8871.

[110] J. Li, S. Zhou, J. Zhang, M. Schlangen, T. Weiske, D. Usharani, S. Shaik, H. Schwarz, *J. Am. Chem. Soc.* **2016**, 138, 7973-7981.

[111] C. Li, D. Danovich, S. Shaik, *Chem. Sci.* **2012**, 3, 1903-1918.

[112] J. N. Harvey, M. Diefenbach, D. Schröder, H. Schwarz, *Int. J. Mass Spectrom.* **1999**, 182, 85-97.

[113] S. Zhou, J. Li, M. Schlangen, H. Schwarz, *Chem. Eur. J.* **2016**, 22, 7225-7228.

[114] S. Zhou, J. Li, M. Schlangen, H. Schwarz, *Angew. Chem. Int. Ed*. **2016**, 55, 7257-7260.

[115] D. Schröder, J. Roithová, *Angew. Chem. Int. Ed.* **2006**, 45, 5705-5708.

[116] D. Schröder, *Angew. Chem. Int. Ed.* **2010**, 49, 850-851.

[117] I. Kretzschmar, D. Schröder, H. Schwarz, C. Rue, P. B. Armentrout, *J. Phys. Chem. A*. **1998**, 102, 10060-10073.

[118] I. Kretzschmar, D. Schröder, H. Schwarz, P. B. Armentrout, *Int. J. Mass Spectrom.* **2006**, 249, 263-278.

[119] L.-X. Jiang, C. Zhao, X.-N. Li, H. Chen, S.-G. He, *Angew. Chem. Int. Ed.* **2017**, 56, 4187-4191.

[120] X. Zhang, G. Liu, K.-H. Meiwes-Broer, G. Ganteför, K. Bowen, *Angew. Chem. Int. Ed.* **2016**, 55, 9644-9647.

[121] H. Dossmann , C. Afonso, D. Lesage, J.-C. Tabet, E. Uggerud, *Angew. Chem. Int. Ed.* **2012**, 51, 6938-6941.

[122] R. P. Feynman. **1965**, Lecture 7, Seeking New Laws.

[123] J. L. Holmes, *Org. Mass Spectrom.* **1985**, 20, 169-183.

[124] O. K. Rice, H. C. Ramsperger, *J. Am. Chem. Soc.* . **1927**, 49, 1617–1629.

[125] O. K. Rice, H. C. Ramsperger, *J. Am. Chem. Soc.* **1928**, 50, 617–620.

[126] L. S. Kassel, *J. Phys. Chem.* **1928**, 32, 1065–1079.

[127] R. A. Marcus, O. K. Rice, *J. Phys. Colloid Chem.* **1951**, 55, 894–908.

[128] R. A. Marcus, *J. Chem. Phys.* **1952**, 20, 359–364.

[129] R. C. Dunbar, *Mass Spectrom. Rev.* **1992**, 11, 309-339.

[130] H. M. Rosenstock, M. B. Wallenstein, A. L. Wahrhaftig, H. Eyring, *Proc. Natl. Acad. Sci. U. S. A.* **1952**, 38, 667-678.

[131] G. Depke, C. Lifshitz, H. Schwarz, E. Tzidony, *Angew. Chem. Int. Ed.* **1981**, 20, 792-793.

[132] F. Turecek, F. W. McLafferty, *J. Am. Chem. Soc.* **1984**, 106, 2525-2528.

[133] R. C. Dunbar, *Mass spectrom. rev.* **1992**, 11, 309-339.

[134] S. Anand, H. B. Schlegel, *Phys. Chem. Chem. Phys.* **2004**, 6, 5166-5171.

[135] R. D. Leib, W. A. Donald, M. F. Bush, J. T. O'Brien, E. R. Williams, *J. Am. Soc. Mass Spectrom.* **2007**, 18, 1217-1231.

[136] A. K. Shukla, *Int. J. Mass Spectrom.* **2017**.

[137] C. Lifshitz, *Mass Spectrom. Rev.* **1982**, 1, 309-348.

[138] T. Baer, P. M. Mayer, *J. Am. Soc. Mass Spectrom.* **1997**, 8, 103-115.

[139] G. Gioumousis, D. P. Stevenson, *J. Chem. Phys.* **1958**, 29, 294-299.

[140] D. P. Stevenson, D. O. Schissler, *J. Chem. Phys.* **1958**, 29, 282-294.

[141] E. Uggerud, *Mass Spectrom. Rev.* **1992**, 11, 389-430.

[142] R. Zahradnik, *Acc. Chem. Res.* **1995**, 28, 306-312.

[143] D. Schröder, T. Weiske, H. Schwarz, *Int. J. Mass Spectrom.* **2002**, 219, 729-738.

[144] D. Schröder, H. Schwarz, *Can. J. Chem.* **2005**, 83, 1936-1940.

[145] F. W. McLafferty, P. F. Bente, R. Kornfeld, S.-C. Tsai, I. Howe, *J. Am. Chem. Soc.* **1973**, 95, 2120-2129.

[146] K. Levsen, H. Schwarz, *Mass Spectrom. Rev.* **1983**, 2, 77-148.

[147] S. A. McLuckey, *J. Am. Soc. Mass Spectrom.* **1992**, 3, 599-614.

[148] R. A. Yost, C. G. Enke, D. C. McGilvery, D. Smith, J. D. Morrison, *Int. J. Mass Spectrom. Ion Phys.* **1979**, 30, 127-136.

[149] D. A. Hales, P. B. Armentrout, *J. Cluster Sci.* **1990**, 1, 127-142.

[150] P. Chen, *Angew. Chem. Int. Ed.* **2003**, 42, 2832-2847.

[151] D. A. Plattner, *Top. Curr. Chem.* . **2003**, 225, 153-203.

[152] M. N. Eberlin, *Eur. J. Mass Spectrom.* **2007**, 13, 19.

[153] D. Schröder, *Acc. Chem. Res.* **2012**, 45, 1521-1532.

[154] J. B. Fenn, *Angew. Chem. Int. Ed.* **2003**, 42, 3871-3894.

[155] W. Henderson, B. K. Nickleson, L. J. McCaffrey, *Polyhedron*. **1998**, 17, 4291-4313.

[156] N. B. Cech, C. G. Enke, *Mass Spectrom. Rev.* **2001**, 20, 362-387.

[157] S. Banerjee, S. Mazumdar, *Int. J. Anal. Chem.* **2012**, 2012, 40.

[158] G. Taylor, *Proc. R. Soc. Lond. A*. **1964**, 280, 383-397.

[159] P. Kebarle, L. Tang, *Anal. Chem.* **1993**, 65, 972A-986A.

[160] M. Dole, L. L. Mack, R. L. Hines, R. C. Mobley, L. D. Ferguson, M. B. Alice, *J. Chem. Phys.* **1968**, 49, 2240-2249.

[161] M. Dole, R. L. Hines, L. L. Mack, R. C. Mobley, L. D. Ferguson, M. B. Alice, *Macromolecules*. **1968**, 1, 96-97.

[162] G. Schmelzeisen-Redeker, L. Bütfering, F. W. Röllgen, *Int. J. Mass Spectrom. Ion Processes*. **1989**, 90, 139-150.

[163] J. V. Iribarne, B. A. Thomson, *J. Chem. Phys.* **1976**, 64, 2287-2294.

[164] B. A. Thomson, J. V. Iribarne, *J. Chem. Phys.* **1979**, 71, 4451-4463.

[165] S. Nguyen, J. B. Fenn, *Proc. Natl. Acad. Sci.* **2007**, 104, 1111-1117.

[166] P. Kebarle, U. H. Verkerk, *Mass Spectrom. Rev.* **2009**, 28, 898-917.

[167] L. Rayleigh, *Philos. Mag.* **1882**, 14, 184–186.

[168] D. C. Taflin, T. L. Ward, E. J. Davis, *Langmuir*. **1989**, 5, 376–384.

[169] D. Duft, T. Achtzehn, R. Muller, B. A. Huber, T. Leisner, *Nature*. **2003**, 421, 128.

[170] J. Fernandez de la Mora, *Anal. Chim. Acta*. **2000**, 406, 93-104.

[171] M. Gamero-Castaño, J. F. d. l. Mora, *J. Mass Spectrom.* **2000**, 35, 790-803.

[172] P. Kebarle, *J. Mass Spectrom.* **2000**, 35, 804-817.

[173] W. Paul, H. Steinwedel, *Zeit. f. Naturf.* **1953**, 8a, 448–450.

[174] W. Paul, *Angew. Chem. Int. Ed.* **1990**, 29, 739-748.

[175] W. Paul, M. Raether, *Z. Phys.* **1955**, 140, 262–273.

[176] J. H. Gross, Mass Spectrometry 1st ed., Springer, **2004**.

[177] H. Schwarz, D. Schröder, *Pure. Appl. Chem.* **2000**, 72, 2319-2332.

[178] D. Schröder, H. Schwarz, *Top. Organomet. Chem.* **2007**, 22, 1-15.

[179] G. E. Johnson, E. C. Tyo, A. W. Castleman, Jr., *Proc Natl Acad Sci U S A*. **2008**, 105, 18108-18113.

[180] J. Roithová, D. Schröder, *Chem. Rev.* **2010**, 110, 1170-1211.

[181] H. Schwarz, *Catal. Sci. Technol.* **2017**.

[182] C. Angeli, R. Cimiraglia, S. Evangelisti, T. Leininger, J.-P. Malrieu, *J. Chem. Phys.* **2001**, 114, 10252-10264.

[183] C. Angeli, R. Cimiraglia, J.-P. Malrieu, *J. Chem. Phys.* **2002**, 117, 9138-9153.

[184] M. Born, P. Jordan, *Z. Phys.* **1925**, 34, 858.

[185] M. Born, W. Heisenberg, P. Jordan, *Z. Phys.* **1926**, 35, 557.

[186] E. Schrödinger, *Ann. Phys.* **1926**, 79, 361.

[187] E. Schrödinger, *Ann. Phys.* **1926**, 79, 489.
[188] M. Born, R. Oppenheimer, *Ann. Phys.* **1927**, 389, 457-484.
[189] D. R. Hartree, *Proc. Camb. Philos. Soc.* **1928**, 24, 89.
[190] V. Fock, *Z. Physik*. **1930**, 61, 126-148.
[191] J. C. Slater, *Phys. Rev.* **1930**, 35, 210-211.
[192] P.-O. Löwdin, *Adv. Chem. Phys.* **1959**, 2, 207.
[193] P. Hohenberg, W. Kohn, *Phys. Rev.* **1964**, 136, B864-B871.
[194] W. Kohn, L. J. Sham, *Phys. Rev.* **1965**, 140, A1133-A1138.
[195] F. Neese, *Coord. Chem. Rev.* **2009**, 253, 526-563.
[196] D. Rappoport, N. R. M. Crawford, F. Furche, K. Burke, *Approximate Density Functionals: Which Should I Choose?, Vol.*, John Wiley & Sons, Ltd, **2006**.
[197] J. C. Slater, *Phys. Rev.* **1951**, 81, 385.
[198] D. Ceperley, B. Alder, *Phys. Rev. Lett.* **1980**, 45, 567-581.
[199] S. H. Vosko, L. Wilk, M. Nusair, *Can. J. phys.* **1980**, 58, 1200-1211.
[200] J. P. Perdew, Y. Wang, *Phys. Rev. B*. **1992**, 45, 13244.
[201] W. Koch, M. C. Holthausen, A chemist's guide to density functional theory, Wiley-VCH: Weinheim, Germany, **2000**.
[202] T. Ziegler, *Chem. Rev.* **1991**, 91, 651-667.
[203] R. O. Jones, O. Gunnarsson, *Rev. Mod. Phys.* **1989**, 61, 689.
[204] A. Becke, *Phys. Rev. A*. **1986**, 33, 2786.
[205] J. P. Perdew, *Phys. Rev. B*. **1986**, 33, 8822.
[206] C. Lee, W. Yang, R. G. Parr, *Phys. rev. B*. **1988**, 37, 785.
[207] J. P. Perdew, A. Ruzsinszky, J. Tao, V. N. Staroverov, G. E. Scuseria, G. I. Csonka, *J. chem. phys.* **2005**, 123, 062201.
[208] J. P. Perdew, A. Ruzsinszky, L. A. Constantin, J. Sun, G. I. Csonka, *J. Chem. Theory Comput.* **2009**, 5, 902-908.
[209] J. Tao, J. P. Perdew, V. N. Staroverov, G. E. Scuseria, *Phys. Rev. Lett.* **2003**, 91, 146401.
[210] J. N. Harvey, *Annu. Rep. Prog. Chem., Sect. C: Phys. Chem.* **2006**, 102, 203-226.
[211] A. Ghosh, *JBIC, J. Biol. Inorg. Chem.* **2006**, 11, 712-724.
[212] J. Conradie, A. Ghosh, *J. Phys. Chem. B*. **2007**, 111, 12621-12624.
[213] G. Ganzenmüller, N. Berkaïne, A. Fouqueau, M. E. Casida, M. Reiher, *J. chem. phys.* **2005**, 122, 234321.
[214] M. Reiher, O. Salomon, B. Artur Hess, *Theor. Chem. Acc.* **2001**, 107, 48-55.
[215] J. N. Harvey, *Struct. Bond.* **2004**, 112, 81-102.
[216] W. Kohn, A. D. Becke, R. G. Parr, *J. Phys. Chem.* **1996**, 100, 12974-12980.
[217] A. Van de Walle, G. Ceder, *Phys. Rev. B*. **1999**, 59, 14992.
[218] Y. Zhao, N. E. Schultz, D. G. Truhlar, *J. Chem. Phys.* **2005**, 123, 161103.
[219] I. J. Kobylianskii, F. J. Widner, B. Kräutler, P. Chen, *J. Am. Chem. Soc.* **2013**, 135, 13648-13651.
[220] N. E. Schultz, Y. Zhao, D. G. Truhlar, *J. Phys. Chem. A*. **2005**, 109, 4388-4403.

[221] N. E. Schultz, Y. Zhao, D. G. Truhlar, *J. Phys. Chem. A*. **2005**, 109, 11127-11143.
[222] M. Munzarová, M. Kaupp, *J. Phys. Chem. A*. **1999**, 103, 9966-9983.
[223] M. Kaupp, R. Reviakine, O. L. Malkina, A. Arbuznikov, B. Schimmelpfennig, V. G. Malkin, *J. Comp. Chem.* **2002**, 23, 794-803.
[224] C. Remenyi, M. Kaupp, *J. Am. Chem. Soc.* **2005**, 127, 11399-11413.
[225] S. Niu, M. B. Hall, *Chem. Rev.* **2000**, 100, 353-406.
[226] J. Baker, P. Pulay, *J. Comput. Chem.* **2003**, 24, 1184-1191.
[227] J. F. Harrison, *Chem. Rev.* **2000**, 100, 679-716.
[228] T. J. Lee, P. R. Taylor, *Int. J. Quantum Chem.* **1989**, 36, 199-207.
[229] A. Karton, *WIREs Comput. Mol. Sci.* . **2016**, 6, 292-310.
[230] M. Alcami, O. Mo, M. Yáñez, *Mass Spectrom. Rev.* **2001**, 20, 195-245.
[231] J. A. Pople, M. Head-Gordon, K. Raghavachari, *J. chem. phys.* **1987**, 87, 5968-5975.
[232] K. Raghavachari, G. W. Trucks, J. A. Pople, M. Head-Gordon, *Chem. Phys. Lett.* **1989**, 157, 479-483.
[233] M. J. T. Frisch, G. W.; Schlegel, H. B.; Scuseria, G. E.; Robb, M. A.; Cheeseman, J. R.; Scalmani, G.; Barone, V.; Mennucci, B.; Petersson, G. A.; Nakatsuji, H.; Caricato, M.; Li, X.; Hratchian, H. P.; Izmaylov, A. F.; Bloino, J.; Zheng, G.; Sonnenberg, J. L.; Hada, M.; Ehara, M.; Toyota, K.; Fukuda, R.; Hasegawa, J.; Ishida, M.; Nakajima, T.; Honda, Y.; Kitao, O.; Nakai, H.; Vreven, T.; Montgomery, J. A., Jr.; Peralta, J. E.; Ogliaro, F.; Bearpark, M.; Heyd, J. J.; Brothers, E.; Kudin, K. N.; Staroverov, V. N.; Kobayashi, R.; Normand, J.; Raghavachari, K.; Rendell, A.; Burant, J. C.; Iyengar, S. S.; Tomasi, J.; Cossi, M.; Rega, N.; Millam, J. M.; Klene, M.; Knox, J. E.; Cross, J. B.; Bakken, V.; Adamo, C.; Jaramillo, J.; Gomperts, R.; Stratmann, R. E.; Yazyev, O.; Austin, A. J.; Cammi, R.; Pomelli, C.; Ochterski, J. W.; Martin, R. L.; Morokuma, K.; Zakrzewski, V. G.; Voth, G. A.; Salvador, P.; Dannenberg, J. J.; Dapprich, S.; Daniels, A. D.; Farkas, Ö.; Foresman, J. B.; Ortiz, J. V.; Cioslowski, J.; Fox, D. J. Gaussian, Inc., Wallingford CT. **2009**.
[234] F. Weigend, R. Ahlrichs, *Phys. Chem. Chem. Phys.* **2005**, 7, 3297-3305.
[235] D. Rappoport, F. Furche, *J. Chem. Phys.* **2010**, 133, 134105.
[236] D. Andrae, U. Häußermann, M. Dolg, H. Stoll, H. Preuß, *Theor. Chim. Acta*. **1990**, 77, 123-141.
[237] K. A. Peterson, D. Figgen, M. Dolg, H. Stoll, *J. Chem. Phys.* **2007**, 126, 124101.
[238] P. Y. Ayala, H. B. Schlegel, *J. Chem. Phys.* **1998**, 108, 2314-2325.
[239] N. Iché-Tarrat, J.-C. Barthelat, D. Rinaldi, A. Vigroux, *J. Phys. Chem. B*. **2005**, 109, 22570-22580.
[240] R. E. Plata, D. A. Singleton, *J. Am. Chem. Soc.* **2015**, 137, 3811-3826.
[241] H. B. Schlegel, *J. Comput. Chem.* **1982**, 3, 214-218.
[242] K. Fukui, *Acc. Chem. Res.* **1981**, 14, 363-368.
[243] D. G. Truhlar, N. J. Kilpatrick, B. C. Garrett, *J. Chem. Phys.* **1983**, 78, 2438-2442.
[244] C. Gonzalez, H. B. Schlegel, *J. Chem. Phys.* **1989**, 90, 2154-2161.
[245] P. B. Armentrout, *Science*. **1991**, 251, 175-179.

[246] D. Schröder, S. Shaik, H. Schwarz, *Acc. Chem. Res.* **2000**, 33, 139-145.
[247] J. N. Harvey, R. Poli, K. M. Smith, *Coord. Chem. Rev.* **2003**, 238–239, 347-361.
[248] H. Schwarz, *Int. J. Mass Spectrom.* **2004**, 237, 75-105.
[249] S. Shaik, *Int. J. Mass Spectrom.* **2013**, 354–355, 5-14.
[250] J. N. Harvey, M. Aschi, H. Schwarz, W. Koch, *Theor. Chem. Acc.* **1998**, 99, 95-99.
[251] G. N. Lewis, *The anatomy of science, Vol. 1*, **1926**, pp.6.
[252] W. J. Evans, D. B. Rego, J. W. Ziller, A. G. DiPasquale, A. L. Rheingold, *Organometallics*. **2007**, 26, 4737-4745.
[253] C. Federsel, A. Boddien, R. Jackstell, R. Jennerjahn, P. J. Dyson, R. Scopelliti, G. Laurenczy, M. Beller, *Angew. Chem. Int. Ed.* **2010**, 49, 9777-9780.
[254] L. Dang, Z. Lin, T. B. Marder, *Organometallics*. **2010**, 29, 917-927.
[255] W. Sattler, G. Parkin, *J. Am. Chem. Soc.* **2012**, 134, 17462-17465.
[256] R. Zhang, L. Song, H. Liu, B. Wang, *Appl. Catal., A*. **2012**, 443–444, 50-58.
[257] Y. Jiang, O. Blacque, T. Fox, H. Berke, *J. Am. Chem. Soc.* **2013**, 135, 7751-7760.
[258] C. Dong, X. Yang, J. Yao, H. Chen, *Organometallics*. **2015**, 34, 121-126.
[259] H. Fong, J. C. Peters, *Inorg. Chem.* **2015**, 54, 5124-5135.
[260] T. Ryutaro, *Bull. Chem. Soc. Jpn.* **1938**, 13, 388-400.
[261] J. S. Griffith, L. E. Orgel, *Q. Rev. Chem. Soc.* **1957**, 11, 381-393.
[262] D. B. Jacobson, B. S. Freiser, *J. Am. Chem. Soc.* **1985**, 107, 72-80.
[263] J. R. Khusnutdinova, P. Y. Zavalij, A. N. Vedernikov, *Organometallics*. **2007**, 26, 3466-3483.
[264] G. Ohanessian, W. A. Goddard, *Acc. Chem. Res.* **1990**, 23, 386-392.
[265] A. E. Reed, F. Weinhold, *J. Chem. Phys.* **1985**, 83, 1736-1740.
[266] A. E. Reed, L. A. Curtiss, F. Weinhold, *Chem. Rev.* **1988**, 88, 899-926.
[267] M. Schlangen, Nickel-mediated bond activation of small alkanesand of molecular oxygen –Ligand effects and the role of the metal's formaloxidation state, Technischen Universität Berlin, Berlin, **2008**.
[268] D. Usharani, D. C. Lacy, A. Borovik, S. Shaik, *J. Am. Chem. Soc.* **2013**, 135, 17090-17104.
[269] J. J. Warren, T. A. Tronic, J. M. Mayer, *Chem. Rev.* **2010**, 110, 6961-7001.
[270] D. Schröder, M. Engeser, H. Schwarz, E. C. E. Rosenthal, J. Döbler, J. Sauer, *Inorg. Chem.* **2006**, 45, 6235-6245.
[271] N. Dietl, T. Wende, K. Chen, L. Jiang, M. Schlangen, X. Zhang, K. R. Asmis, H. Schwarz, *J. Am. Chem. Soc.* **2013**, 135, 3711-3721.
[272] S. Zhou, J. Li, M. Schlangen, H. Schwarz, *Angew. Chem. Int. Ed.* **2017**, 56, 2951-2954.
[273] W. Golding, *Lord of the Flies*, **1954**, pp.143.
[274] H. Hirao, D. Kumar, W. Thiel, S. Shaik, *J. Am. Chem. Soc.* **2005**, 127, 13007-13018.
[275] S. Shaik, H. Hirao, D. Kumar, *Nat. Prod. Rep.* **2007**, 24, 533-552.

A. Unpublished Work

Unpublished paper I

Ligand Effects on the Reactivity of $[CoX]^+$ (X = CN, F, Cl, Br, O, and OH) towards CO_2 in the Gas Phase: Generation of the Elusive Cyanoformate Ion.

***Abstract**: The thermal reactions of $[CoX]^+$ (X = CN, F, Cl, Br, O, and OH) with carbon dioxide have been investigated experimentally and theoretically by using electrospray ionization mass spectrometry (ESI-MS) and density functional theory. Surprisingly, in contrast to the inertness of $[CoX]^+$ (X = F, Cl, Br, O, and OH) toward carbon dioxide, $[Co(CN)]^+$ activates carbon dioxide to form the elusive cyanoformate ion $[NC–CO_2Co]^+$ in the gas phase. Mechanistic investigation into this ligand-controlled CO_2 activation via C–C bond formation, mediated by a first-row late transition-metal complex, reveals that the inertness of $[CoX]^+$ (X = F, Cl, Br, O, and OH) is due to kinetic barriers located above the entrance asymptote. The exception is the $[Co(CN)]^+/CO_2$ couple, for which the thermal reaction is both thermodynamically and kinetically accessible.*

Keywords: bond activation • carbon dioxide • Cobalt complexes • C–C bond formation • Ligand effect • ESI-MS • cyano ligand

1. Introduction

Carbon dioxide continues to make headlines in the media as a potent green-house gas with its many detrimental side effects.[1] While even its excessive use as an abundant and cheap C(1) building block is not likely to reduce significantly its presence in the atmosphere and the oceans, chemical transformations of CO_2 are nevertheless considered attractive,[2] provided the thermodynamic and kinetic impediments can be mitigated.[3] In fact, catalytic reduction of CO_2 is possible by either biological systems, e.g. enzymes,[4] or metal complexes.[2a,5] In case of the latter, high temperatures and pressures are often required for an efficient chemical activation of CO_2.[6] Recently, cobalt-based catalysts, e.g. $Co(dmpe)_2H$ in THF, have shown the potential to activate CO_2 at ambient conditions.[7] In general, cobalt macrocyclic catalysts in the condensed phase are well known for their activity in mediating the reduction of CO_2 to CO.[8] Likewise, catalytic CO_2 activation can be carried out by homogeneous cobalt complexes such as e.g. $[Co(H_2)(PP_3)]^+$ (PP_3

= $P(CH_2CH_2PPh_2)_3$) species in water with $NaHCO_3$,[9] and water-soluble Cp*Co(III) complexes, which bear dihydroxyl-substituted bipyridine (DHBP) ligands, [Cp*Co(DHBP–2H$^+$)(OH_2)], with strong electron-donating properties.[10]

An alternative approach to carrying out CO_2 capture and conversion with inorganic metal complexes is to employ biological systems, such as bacteria[11] and enzymes.[4] Unfortunately, relatively little is known about the mechanisms whereby enzymes catalyze the capture and reduction of CO_2. One capturing process in nature involves the formation of cyanoformate, $[NCCOO]^-$; the latter is involved in the generation of ethylene,[12] which serves as a plant hormone for biological processes such as seed germination, fruit ripening, and leaf senescence.[13] The generation of cyanoformate plays a vital "shuttling" role, removing cyanide from the enzymatic active site, thus avoiding the poisoning and deactivation of the enzyme for metabolism.[14] The stability of cyanoformate depends crucially on the dielectric constant of its local surrounding. It has been proposed that it is formed in the low-dielectric site of the enzyme, while it decomposes into CN^- and CO_2 in higher dielectric media.[14] Surprisingly, there is not much information about CO_2 coordination chemistry with small ligands such as halides or pseudo-halides (e.g. OH^-, CN^-, Cl^- etc). Currently, there are only few studies on complexes of CO_2 with small anionic donors.[15] In addition to hydrogen carbonate $[HO\text{-}CO_2]^-$[16] and cyanoformate $[NC\text{-}CO_2]^-$[14-15], Zhang et al. isolated and characterized the adduct of carbon dioxide and fluoride.[17]

Gas-phase studies, where mass-selected metal ions and complexes are reacted under well-defined conditions with inert substrates, serve as valuable models for understanding the more complex processes taking place in the condensed phase. With regard to CO_2 activation, although these studies give valuable insight into the required properties of potential metal catalysts, they are relatively rare.[18] For instance, O-atom abstraction has been observed under thermal conditions in the gas phase by early transition metal cations as a consequence of their high oxophilicity.[18-19] Likewise, ligated early transition metal cations are capable of activating carbon dioxide.[18,20] For example, room-temperature CO_2 conversion mediated by $[LTiH]^+$ (L=Cp_2, O) was observed under CO elimination (L = O) and the generation of a formate complex (L = Cp_2), respectively.[20a] Gas phase studies on the activation of CO_2 using late transition-metal cation complexes are also relatively rare. Recently, He et.al. showed that, while cationic Fe^+ is not able to activate CO_2, the products HCO_2^- and CO can be formed in the thermal reaction of CO_2 with the FeH^- anion.[21] Furthermore, thermal activation of CO_2 has been achieved in the reaction with $[PtH_3]^-$, resulting in the generation of $[H_2Pt(HCO_2)]^-$.[22] Recently, Zhou et al. showed that $[Re(CO)_2]^+$ abstracts one oxygen atom to form $[ORe(CO)_2]^+$, concurrent with the elimination of carbon monoxide, while the complexes $[Re(CO)_x]^+$ ($x = 0, 1, 3$) are thermally unreactive toward CO_2.[23] Finally, imidazole and pyridine complexes of zinc, $[L_nZnOH]^+$ (n = 1, 2), are capable of activating carbon dioxide under thermal conditions, as indicated by O-atom exchange.[24]

To date there is no study that addresses the thermal activation of CO_2 by cobalt containing complexes in the gas phase. Thus, we aimed at understanding the effect of halide or pseudo-halide ligands on the reactivity of cobalt complexes, in order to better tailor cobalt catalysts for this task. Herein, we describe the mechanistic details of the reaction of carbon dioxide and $[CoX]^+$ (X = CN, F, Cl, Br, O and OH). The combination of gas-phase experiments and quantum mechanical calculations provides insight into the fundamental steps of carbon dioxide activation mediated by cobalt complexes at a molecular level.

2. Experimental Section and Computational Details

The experiments were performed using a VG Bio-Q mass spectrometer of QHQ configuration (Q: quadrupole; H: hexapole) equipped with an electrospray-ionization (ESI) source, as described in detail elsewhere.[25] CH_3CN, CH_3OH, $CoF_2•4H_2O$, $CoCl_2•6H_2O$, $CoBr_2$, $Co(NO_3)_2•6H_2O$, CO_2, and $C^{18}O_2$ were obtained from Sigma-Aldrich and utilized without further purification. To generate $[Co(CN)]^+$, a millimolar solution of cobalt(II) chloride and acetonitrile has been used. Further, in the case of $[CoO]^+$ as well as $[Co(OH)]^+$, a millimolar solution of $Co(NO_3)_2•6H_2O$ in a methanol/water mixture was utilized.[26] Finally, the halogen complexes of cobalt are generated by electrospray of a methanolic solution of CoX_2 (X = F, Cl, and Br). All samples were introduced into the mass spectrometer via a syringe pump and a fused-silica capillary connected to the ESI source with a pump rate of 4µl/min. Nitrogen was used as a nebulizing and drying gas, at a source temperature of 80 ºC. The maximum intensity of the desired complex was achieved by adjusting the cone voltage (U_c) to around 80-100 V. When appropriate, the isotope patterns of the ions of interest have been compared with the calculated isotope patterns to confirm the identity of the ions.[27] The reactions of the respective mass-selected precursor ions with carbon dioxide have been probed at a collision energy (E_{lab}) nominally set to 0 eV, which, in conjunction with the ca. 0.4 eV kinetic energy width of the parent ion at peak half height, allows the investigation of quasi-thermal reactions, as described previously.[24,28] The pressure of carbon dioxide in the hexapole was varied between ca. 1.02×10^{-3} to 1.32×10^{-3} mbar. Cationic products are recorded by scanning Q2. Travelling wave ion-mobility spectrometry (TWIMS) experiments were attempted with the same cobalt solutions as described above on a Synapt G2 mass spectrometer (Waters, Manchester) fitted with a standard ESI source in order to get structural information about the product ion.[29] However, despite extensive tuning of the instrument parameters, it was not possible to obtain a signal intensity sufficient for measuring an arrival time distribution or to conduct further experiments.

For the computational studies we employed the Gaussian 09 program package[30] using unrestricted calculations with the B3LYP functional[31] and the def2-TZVP basis sets of Weigend and Ahlrichs.[32] The satisfying performance of the B3LYP functional for energetic and structural aspects of cobalt containing systems has been reported previously.[33] The nature of local minima and transition states (TSs) were verified by harmonic vibrational frequency analysis of the respective optimized structures. Intrinsic reaction coordinate (IRC) calculations[34] were performed in order to confirm the connection between TSs and minima. All energies (given in kJ mol^{-1}) are corrected for (unscaled) zero-point vibrational energy contributions.

3. Results and Discussion

In the reaction of mass-selected $[CoX]^+$ ions (X = CN, F, Cl, Br, O, and OH) with carbon dioxide, no product ions are observed for $[CoX]^+$ (X = F, Cl, Br, O, and OH) above the detection limit; however, $[Co(CN)]^+$ (*m/z* 85) reacts under the generation of $[Co,O_2,C_2,N]^+$ (*m/z* 129) as the only product, according to Eq. (1a). Note that in all the mass spectra in which the precursor ion, $[Co(CN)]^+$ (*m/z* 85), has been isolated for ion/molecule reactions, a signal at *m/z* 76 is present (See Figure S1). This ion arises from a CN/OH ligand exchange between the $[Co(CN)]^+$ precursor and water; the latter is present as background gas in the mass spectrometer. Since only exothermic reactions can take place in the isolated gas phase, the occurrence of this process implies *BDE*(Co^+-CN) ≤ *BDE*(Co^+-OH) (297±25 kJ mol^{-1}).[35]

Figure 1 details the mass spectra for the ion/molecule reaction of $[Co(CN)]^+$ (*m/z* 85) with carbon dioxide. The relative rate constant for this reaction amounts to 1.9×10^{-10} cm^{-3} s^{-1} $molecule^{-1}$;[36] this value corresponds to an efficiency of 19% relative to the gas-kinetic collision limit.[37]

$$[Co(CN)]^+ + CO_2 \rightarrow [Co,O_2,C_2,N]^+ \tag{1a}$$

$$[Co(CN)]^+ + C^{18}O_2 \rightarrow [Co,^{18}O_2,C_2,N]^+ \tag{1b}$$

Furthermore, labeling experiments with $C^{18}O_2$ result in a clean mass shift *m*/*z* 129 → *m*/*z* 133 due to ^{18}O incorporation in the reaction product, as shown in Figure (1b) and Eq. (1b). The product ions at *m*/*z* 129 (and *m*/*z* 133) may correspond to a simple adduct or to insertion intermediates; the latter may be accessible via either C–C or C–N bond formation.

DFT calculations were performed in order to reveal the possibility of, and to obtain mechanistic insight into, the activation of CO_2 with $[Co(CN)]^+$ as the reactive species. According to the calculations, the most stable structure of $[Co(CN)]^+$ species has a triangular shape (i, Scheme 1) and possesses a quartet ground state (with the doublet and sextet electronic states being 33.1 and 281.4 kJ mol^{-1} higher in energy). Note that the cyanide and isocyanide isomers (structures ii and iii, respectively, Scheme 1) in their quartet ground state are 28.3 and 30.4 kJ mol^{-1} higher in energy, respectively (See Table S1 for more details).

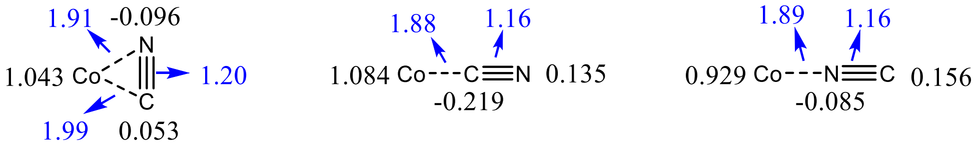

i ii iii

Scheme 1 Bond distances (in Å and marked in blue) and calculated charge distributions (marked in black) of the cationic cobalt complex

Starting from $[Co(CN)]^+$, the incoming carbon dioxide ligand coordinates initially to the metal center of the precursor leading to the complex **1** (Figure 2 and path A of Scheme 2). This step is barrier free. The ligand-exchange process via path C (Scheme 2) is endothermic by 582.6 kJ mol^{-1} relative to the entrance channel and thus not accessible under thermal conditions. We further examined the possibility of oxygen-atom transfer (paths D, Scheme 2) via DFT calculations.

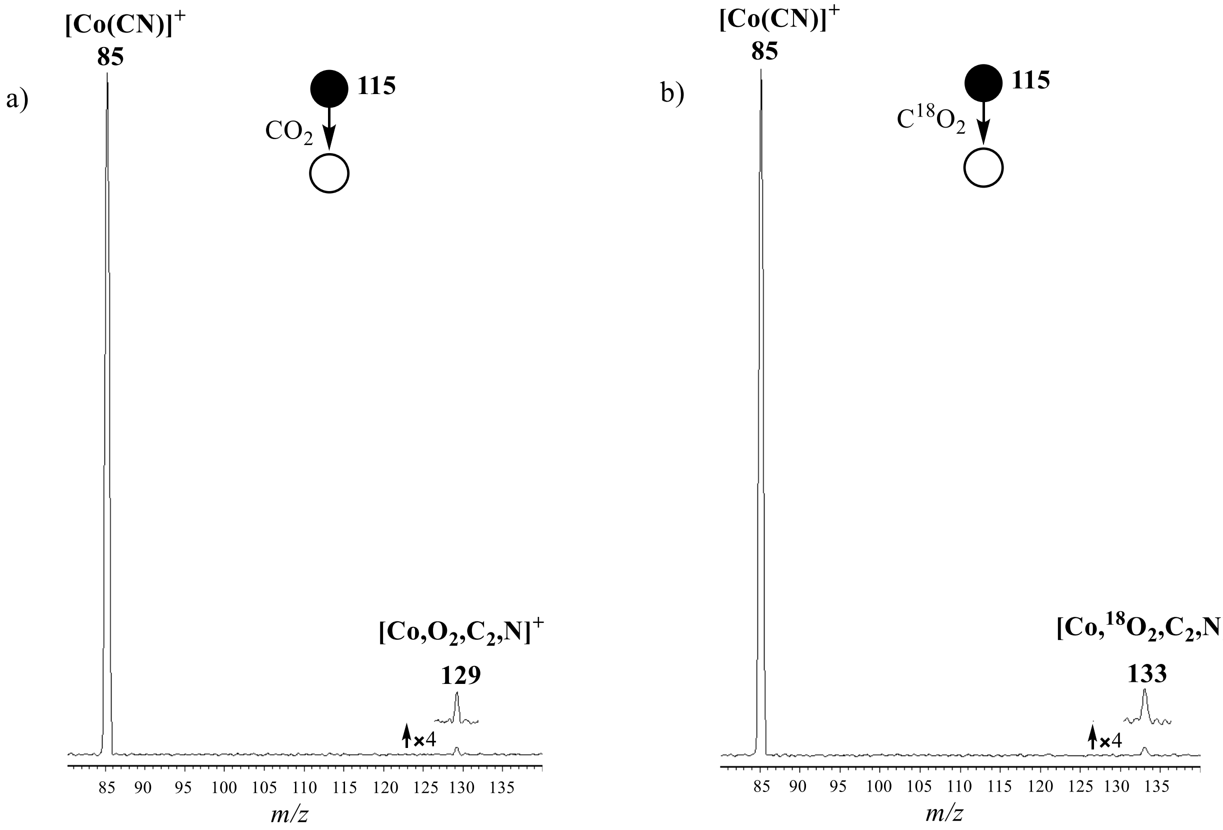

Figure 1 Mass spectra resulting from the thermal ion/molecule reaction of mass-selected $[Co(CN)]^+$ a) with CO_2 at a pressure of 1.24×10^{-3} mbar, b) with $C^{18}O_2$ at a pressure of 1.32×10^{-3} mbar.

Regarding the oxygen-atom transfer (OAT) from CO_2 to the metal center of $[Co(CN)]^+$, path D (Scheme 2), three alternative ways starting from complex **1**, **2**, and **3** have been located on the potential-energy surface (PES); however, they are all hindered by barriers higher than 200 kJ mol^{-1} in both the doublet and quartet spin states (see Figure S2). Thus, C–O bond activation of CO_2 with concomitant loss of CO is also inaccessible under ambient conditions. For the insertion resulting in C–N bond formation, i.e. path E in Scheme 2, a transition structure has been located starting from the NC–M–OCO intermediate ^{4}**2** (see Figure S2); however, the kinetic barrier ^{4}**TS$_{2/3s}$** amounting to 18.4 kJ mol^{-1} above the entrance channel is prohibitively high. Therefore, only path B (Scheme 2) constitutes a probable alternative, as described in the following. Starting from the encounter complex ^{4}**1**, interconversions via ^{4}**1** ⇆ ^{4}**TS$_{1/2}$** ⇆ ^{4}**2** and ^{4}**1** ⇆ ^{4}**TS$_{1/3}$** ⇆ ^{4}**3** are facile as both transition states are located below the entrance channel and are essentially iso-energetic (^{4}**TS$_{1/2}$** = 166.6 kJ mol^{-1} and ^{4}**TS$_{1/3}$** = 166.2 kJ mol^{-1}). In both processes, linear arrangements are achieved for both N-C-Co (^{4}**2**) and C-N-Co (^{4}**3**), respectively. The existence of interconverting M–

CN versus M–NC isomers has been shown for both the condensed[38] and the gas phase.[39] In fact, the rearrangement between different structures from cyanide (linear → bent → side-on → bent) to isocyanide has been known for quite some time.[40] For example, the stable isocyanide product $[Co(NC)(NH_3)_5]^{2+}$ which results from the selenium elimination reaction of $[Co(NCSe)(NH_3)_5]^{2+}$, can rearrange, although only sluggishly, to the cyanide form $[Co(CN)(NH_3)_5]^{2+}$.[40d]

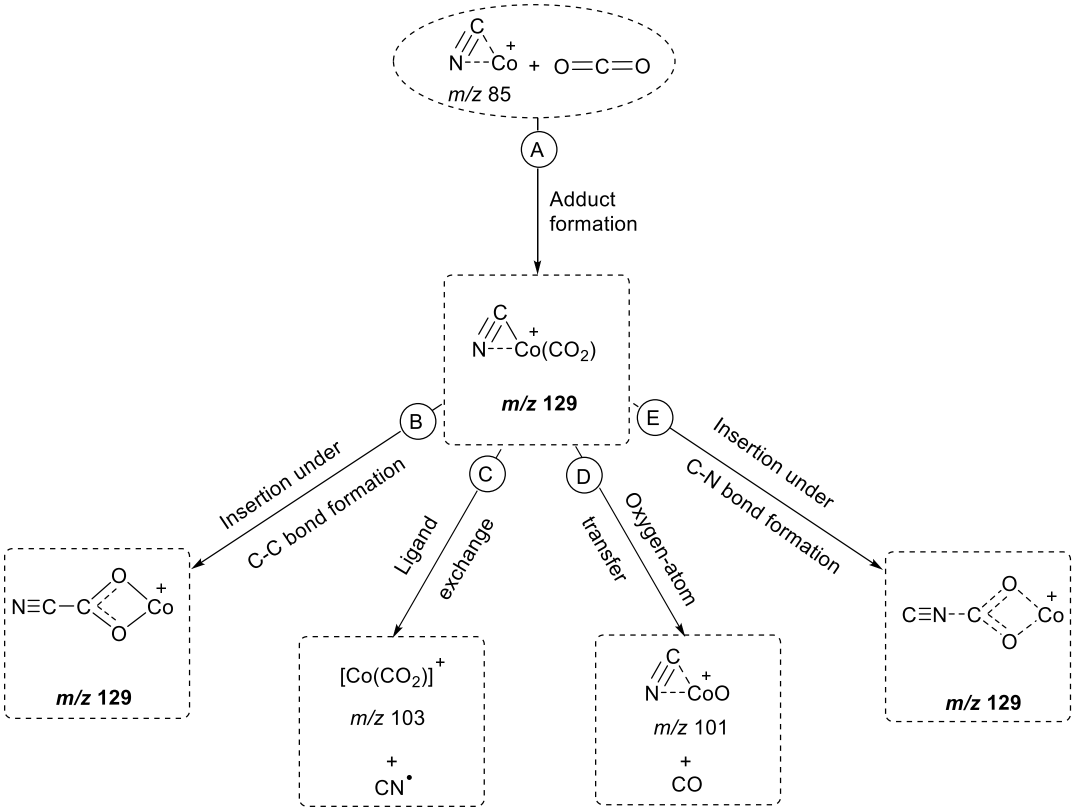

m/z 85
A
Adduct formation
m/z 129
B
Insertion under C-C bond formation
C
Ligand exchange
D
Oxygen-atom transfer
E
Insertion under C-N bond formation
m/z 129
[Co(CO2)]+
m/z 103
CN•
m/z 101
CO
m/z 129

Scheme 2 Possible routes for the reactions of $[Co(CN)]^+$ with carbon dioxide

The reactive species for C-C bond formation corresponds to the CN–M–OCO intermediate ^{4}**3**. CO_2 insertion may occur via the four-centered transition state ^{4}**TS3/4**, eventually generating the η^3 N,C,O coordinated cyanoformate complex ^{4}**4**. This step is kinetically and thermodynamically possible, as all transition states and intermediates are located below the entrance channel. In the following step, ^{4}**4** → ^{4}**TS4/5** → ^{4}**5**, the coordination changes to a η^2 coordination of Co to both oxygen atoms of the carboxylate group. Note that despite several efforts, it was not possible to locate a direct transition state starting from encounter complex ^{4}**2** to intermediate ^{4}**4**. Finally, CO elimination from complex ^{4}**4** has been considered via two different paths. However, barriers of

138.6 and 87.4 kJ mol^{-1} above the entrance channel prevent this reaction from occurring (see Figure S3).

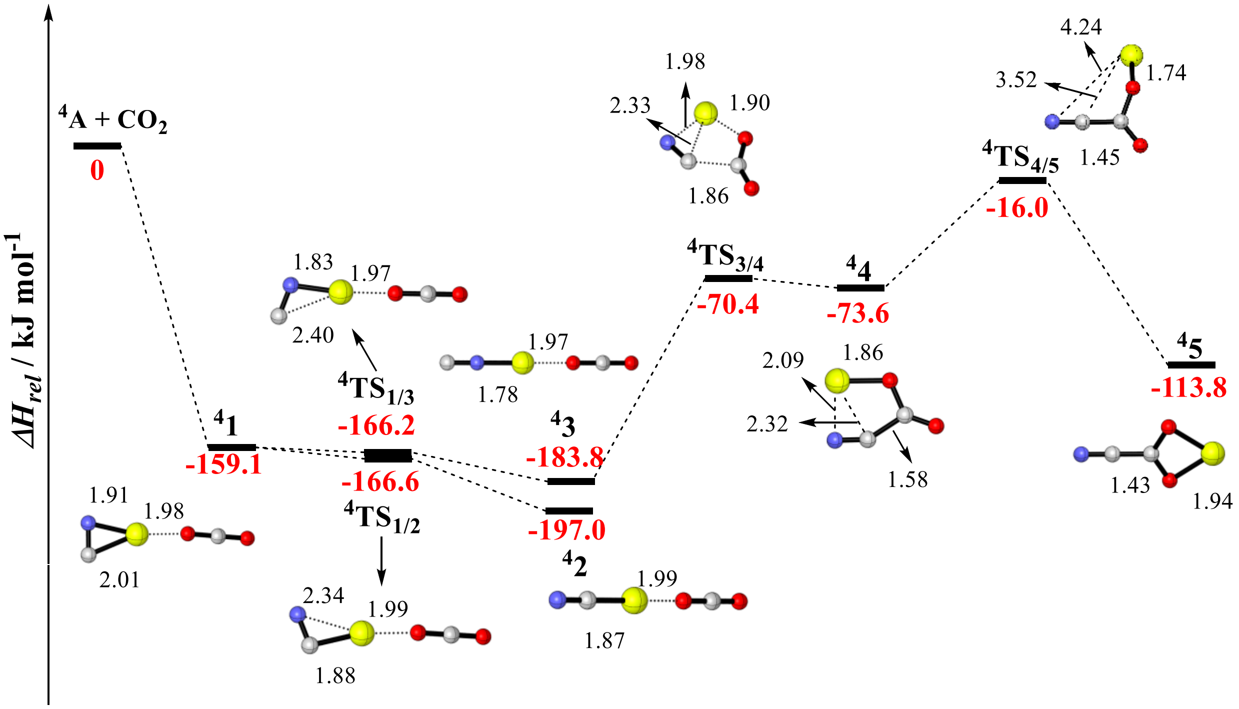
ΔH$_{rel}$ / kJ mol^{-1}
^{4}A + CO$_2$
0
^{4}1
-159.1
1.91
1.98
2.01
^{4}TS$_{1/3}$
-166.2
1.83
1.97
2.40
-166.6
^{4}TS$_{1/2}$
2.34
1.99
1.88
^{4}3
-183.8
1.97
1.78
-197.0
^{4}2
1.99
1.87
^{4}TS$_{3/4}$
-70.4
1.98
2.33
1.90
1.86
^{4}4
-73.6
2.09
1.86
2.32
1.58
^{4}TS$_{4/5}$
-16.0
4.24
3.52
1.74
1.45
^{4}5
-113.8
1.43
1.94

Figure 2 PES for the reaction of [Co(CN)]$^+$ with CO$_2$ as calculated by B3LYP/def2-TZVP. All energies, corrected for zero-point vibrational energy (ZPVE) contributions, are given in kJ mol^{-1} and marked in red; bond lengths are given in Å. Charges are omitted for the sake of brevity. Color code: C = grey, N = blue, O = red, Co = yellow.

A widely employed type of C–C bond formation using cyano groups in the condensed phase corresponds to the transition-metal catalyzed reaction of cyano or isocyano groups with alkyl or aryl substrates. These types of C–C bond formation result in the generations of e.g. α-hydroxy carbonyl, α-amino nitriles, aryl nitriles, etc.[41] The reaction sequence shown in Figure 2 constitutes a new mechanistic example for C–C bond formation, through the reaction between a metal-cyanide complex and carbon dioxide in the gas phase.

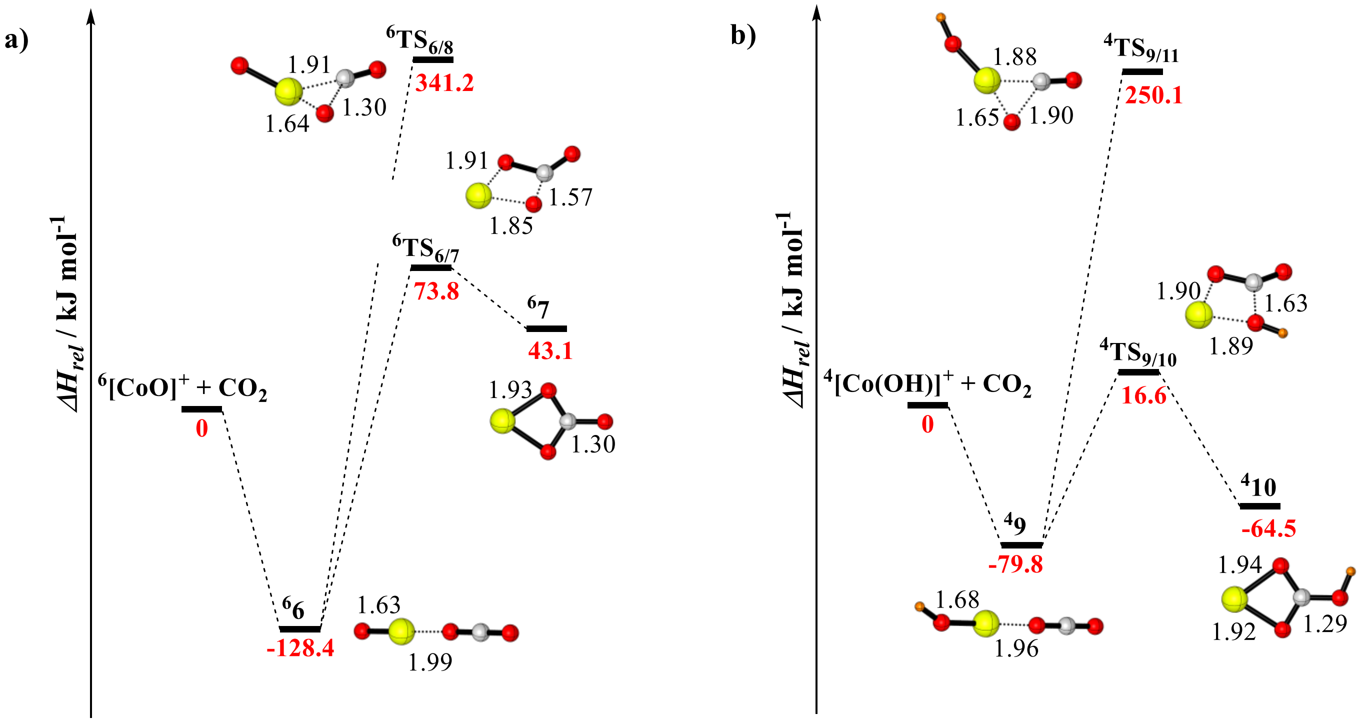

Figure 3 Simplified PESs for the reaction of a) $[CoO]^+$, and b) $[Co(OH)]^+$ with CO_2 as calculated by B3LYP/def2-TZVP. All energies, corrected for zero-point vibrational energy (ZPVE) contributions, are given in kJ mol^{-1} and marked in red, and bond lengths in Å. Charges are omitted for the sake of brevity. Color code: C = grey, O = red, Co = yellow, H = orange.

We further calculated some of the relevant stationary points on the PESs for the reaction of $[CoX]^+$ (X=F, Cl, Br, O, and OH) in their respective ground state (sextet for $[CoO]^+$ and quartet for the remaining complexes) with carbon dioxide (Figures 3 and 4); for these ion-molecule pairs, no reaction has been observed in the experiments. In all cases, after having formed an encounter complex, barriers significantly higher than the reactant asymptote inhibit the insertion reactions to occur at ambient conditions (Figure S4). Note that in the case of $[CoO]^+/CO_2$ and $[CoBr]^+/CO_2$ (Figures 3a and 4c), the insertion process is also thermodynamically not accessible; the reactions $[CoO]^+ + CO_2 \rightarrow [Co(CO_3)]^+$ and $[CoBr]^+ + CO_2 \rightarrow [Co(BrCO_2)]^+$ are endothermic by 43.1 and 20.0 kJ mol^{-1}, respectively. Furthermore, DFT calculations predict barriers higher than 200 kJ mol^{-1} for the direct OAT for all of the species (Figures 3 and 4). Therefore, none of the species shown in Figures 3 and 4 is able to activate carbon dioxide. This is in line with the experimental findings that no reactions take place for the $[CoX]^+$ (X=F, Cl, Br, O, and OH)/CO_2 couples (Figure S4).

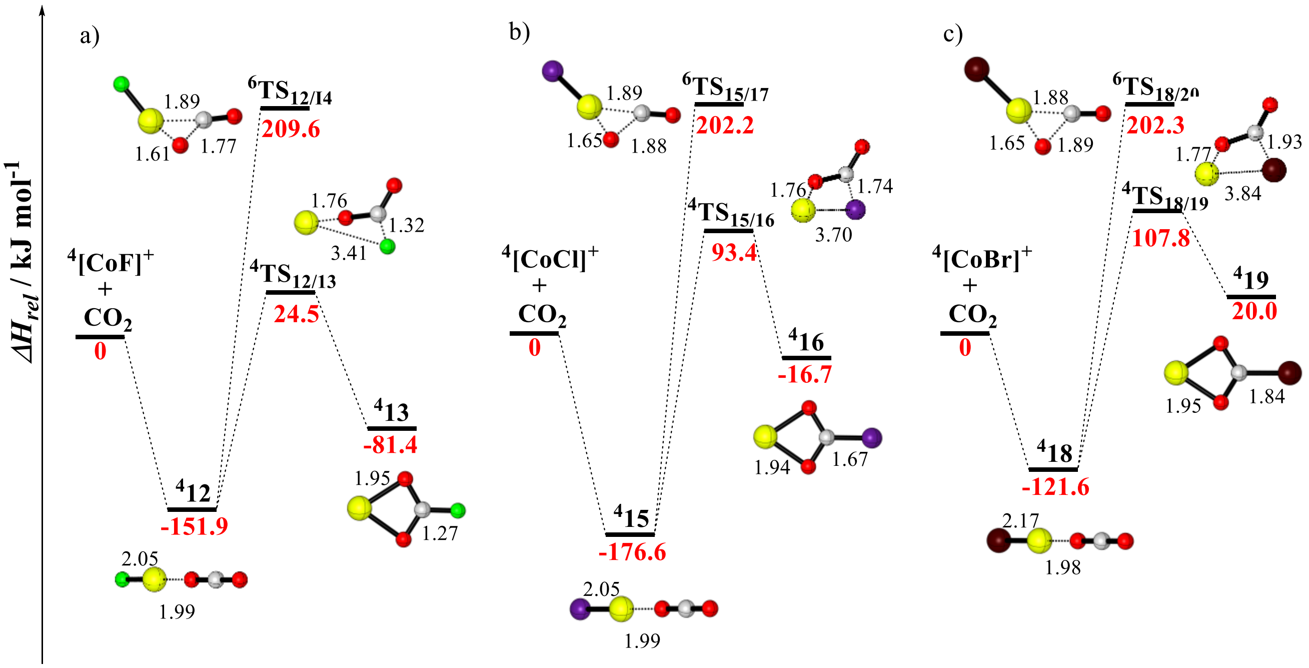

Figure 4 Simplified PESs for the reaction of a) $[CoF]^+$, b) $[CoCl]^+$, and c) $[CoBr]^+$ with CO_2 as calculated by B3LYP/def2-TZVP. All energies, corrected for zero-point vibrational energy (ZPVE) contributions, are given in kJ mol^{-1} and marked in red, and bond lengths in Å. Superscripts indicate spin state. Charges are omitted for the sake of brevity. Color code: C = grey, O = red, Co = yellow, F = green, Cl = purple, Br = brown.

An intriguing observation from our calculations is that, while the concerted insertion processes for the reaction of $[CoF]^+$, $[CoCl]^+$ and $[Co(OH)]^+$ with carbon dioxide are thermodynamically favored, the respective barriers are significantly higher in energy as compared to both ^{4}**TS**$_{3/4}$ and ^{4}**TS**$_{4/5}$ in the stepwise $[Co(CN)]^+/CO_2$ insertion reaction. The cyanide ligand in ^{4}**TS**$_{3/4}$ is still closely bound to the metal center, and the side-on coordination might have a stabilizing effect. Furthermore, the differences in the energies of the barriers can be attributed to the formation of different C–X bonds (X = F, Cl, OH, and CN) in the final products. In ^{4}**TS**$_{4/5}$, the C–C bond length is very close to that of the product (^{4}**TS**$_{4/5}$: 1.45 Å, ^{4}**5**: 1.43 Å); thus, ^{4}**TS**$_{4/5}$ corresponds to a late transition structure. In comparison, the newly generated C–F, C–Cl, and C–OH bonds in ^{4}**TS**$_{12/13}$, ^{4}**TS**$_{15/16}$, and ^{4}**TS**$_{9/10}$ are developed to a much smaller extent compared to the subsequent intermediates (the difference between the bond lengths in the transition state and the respective intermediate are 0.05 Å for the C–F, 0.07 Å for the C–Cl, and 0.34 Å for the C–OH). The higher degree of C–X bond formation with X = C implies a higher stabilization of the corresponding transition state.

These experimental and computational evidences for a reactive $[Co(CN)]^+/CO_2$ couple suggest the combination of cyanide or isocyanide ligands and cobalt metal centers as the preferred ligand[42] to bring about metal-mediated activation of CO_2. According to the calculations, the CN ligand actively takes part in the reaction resulting in the formation of $[Co(\eta\text{-}O)_2C(CN)]^+$. Further, in contrast to the concerted CO_2 insertion into the Co–X (X = F, Cl, Br, O and OH) bonds, the insertion process in the case of $[Co(CN)]^+$ proceeds in a stepwise manner. The change from a concerted reaction path to a multi-step sequence has been suggested as a strategy in order to utilize C(1) building blocks, e.g. CO_2, in synthesis.[43]

4. Conclusions

In a combined experimental/computational study, we have investigated mechanistic aspects of the thermal gas-phase reactions of the cobalt complexes $[CoX]^+$ (X = CN, F, Cl, Br, O, and OH) with carbon dioxide. We demonstrate the feasibility of carbon dioxide activation under carbon-carbon bond formation for X = CN by $[Co(CN)]^+$. According to the DFT calculations, the observed signal in the mass spectrum is assigned to a complex in which the cobalt atom is η^2 coordinated to both oxygen atoms of the cyanoformate group. This product ion is energetically 113.8 kJ mol^{-1} lower compared to the separated reactants. In addition, various pathways have been considered for the decarbonylation process, starting from different encounter complexes and intermediates. Loss of CO from all of these complexes is hampered by kinetic barriers that are ways too high in energy to be accessible under thermal conditions. Likewise, according to the DFT calculations, activation of CO_2 via insertion of CO_2 into the M-X bond of $[CoO]^+$ (X = O) and $[CoBr]^+$ (X = Br) is not only endothermic, but is also hindered by kinetic barriers higher than the entrance asymptote. Furthermore, regarding the insertion processes for $[CoF]^+$, $[CoCl]^+$ and $[Co(OH)]^+$, while the overall reactions are exothermic, these paths are hampered by kinetic barriers amounting to 79.0, 93.4, and 16.6 kJ mol^{-1}, respectively, above the entrance channel. Moreover, the OAT is not accessible in any of mentioned cases due to high kinetic barriers. Therefore, weak- and middle-field ligands (F, Cl, Br, O, and OH)[44] do not result in the conversion of CO_2 under thermal conditions, while the strong-field CN ligand[45] allows activation of CO_2 under ambient conditions. These computational results are all in line with the experimental findings. This is the first example of CO_2 activation through C–C bond formation in the gas phase by a first-row late transition metal complex.

References

[1] a) P. L. Munday, *Biol. Lett.* **2017**, *13*, DOI: 10.1098/rsbl.2017.0438 ; b) K. Zickfeld, S. Solomon, D. M. Gilford, *Proc. Natl. Acad. Sci. U.S.A.* **2017**, *114*, 657-662.

[2] a) M. Cokoja, C. Bruckmeier, B. Rieger, W. A. Herrmann, F. E. Kühn, *Angew. Chem. Int. Ed.* **2011**, *50*, 8510-8537; b) A. M. Appel, J. E. Bercaw, A. B. Bocarsly, H. Dobbek, D. L. DuBois, M. Dupuis, J. G. Ferry, E. Fujita, R. Hille, P. J. Kenis, *Chem. Rev.* **2013**, *113*, 6621-6658; c) M. Aresta, A. Dibenedetto, A. Angelini, *Chem. Rev.* **2014**, *114*, 1709-1742; d) K. A. Grice, *Coord. Chem. Rev.* **2017**, *336*, 78-95.

[3] a) V. Havran, M. P. Duduković, C. S. Lo, *Ind. Eng. Chem. Res.* **2011**, *50*, 7089-7100; b) M.-Y. Wang, Y. Cao, X. Liu, N. Wang, L.-N. He, S.-H. Li, *Green Chem.* **2017**, *19*, 1240-1244.

[4] K. Schuchmann, V. Müller, *Science* **2013**, *342*, 1382-1385.

[5] a) X. Yin, J. R. Moss, *Coord. Chem. Rev.* **1999**, *181*, 27-59; b) Q. Liu, L. Wu, R. Jackstell, M. Beller, *Nat. Commun.* **2015**, *6*, 5933; c) Q.-W. Song, Z.-H. Zhou, L.-N. He, *Green Chem.* **2017**, DOI: 10.1039/C1037GC00199A.

[6] a) J. F. Hull, Y. Himeda, W.-H. Wang, B. Hashiguchi, R. Periana, D. J. Szalda, J. T. Muckerman, E. Fujita, *Nat. Chem.* **2012**, *4*, 383-388; b) K. Sumida, D. L. Rogow, J. A. Mason, T. M. McDonald, E. D. Bloch, Z. R. Herm, T.-H. Bae, J. R. Long, *Chem. Rev.* **2012**, *112*, 724-781; c) W.-H. Wang, Y. Himeda, J. T. Muckerman, G. F. Manbeck, E. Fujita, *Chem. Rev.* **2015**, *115*, 12936-12973; d) M. Aresta, A. Dibenedetto, E. Quaranta, *J. Catal.* **2016**, *343*, 2-45; e) E. Alper, O. Yuksel Orhan, *Petroleum* **2017**, *3*, 109-126.

[7] M. S. Jeletic, M. T. Mock, A. M. Appel, J. C. Linehan, *J. Am. Chem. Soc.* **2013**, *135*, 11533-11536.

[8] J. Schneider, H. Jia, J. T. Muckerman, E. Fujita, *Chem. Soc. Rev.* **2012**, *41*, 2036-2051.

[9] C. Federsel, C. Ziebart, R. Jackstell, W. Baumann, M. Beller, *Chem. Eur. J.* **2012**, *18*, 72-75.

[10] Y. M. Badiei, W.-H. Wang, J. F. Hull, D. J. Szalda, J. T. Muckerman, Y. Himeda, E. Fujita, *Inorg. Chem.* **2013**, *52*, 12576-12586.

[11] J. Zeikus, R. Kerby, J. Krzycki, *Science* **1985**, *227*, 1167-1173.

[12] M. C. Pirrung, *Acc. Chem. Res.* **1999**, *32*, 711-718.

[13] a) S. P. Burg, E. A. Burg, *Science* **1965**, *148*, 1190-1196; b) H. Qiao, Z. Shen, S.-s. C. Huang, R. J. Schmitz, M. A. Urich, S. P. Briggs, J. R. Ecker, *Science* **2012**, *338*, 390-393.

[14] L. J. Murphy, K. N. Robertson, S. G. Harroun, C. L. Brosseau, U. Werner-Zwanziger, J. Moilanen, H. M. Tuononen, J. A. C. Clyburne, *Science* **2014**, *344*, 75-78.

[15] C. Hering, J. von Langermann, A. Schulz, *Angew. Chem. Int. Ed.* **2014**, *53*, 8282-8284.

[16] D. Braga, E. D'Oria, F. Grepioni, F. Mota, J. J. Novoa, C. Rovira, *Chem. Eur. J.* **2002**, *8*, 1173-1180.

[17] X. Zhang, U. Gross, K. Seppelt, *Angew. Chem. Int. Ed. Engl.* **1995**, *34*, 1858-1860.

[18] H. Schwarz, *Coord. Chem. Rev.* **2017**, *334*, 112-123.

[19] G. K. Koyanagi, D. K. Bohme, *J. Phys. Chem. A* **2006**, *110*, 1232-1241.

[20] a) S.-Y. Tang, N. J. Rijs, J. Li, M. Schlangen, H. Schwarz, *Chem. Eur. J.* **2015**, *21*, 8483-8490; b) J. Li, P. González-Navarrete, M. Schlangen, H. Schwarz, *Chem. Eur. J.* **2015**, *21*, 7780-7789; c) M. Firouzbakht, N. J. Rijs, P. González-Navarrete, M. Schlangen, M. Kaupp, H. Schwarz, *Chem. Eur. J.* **2016**, *22*, 10581-10589; d) M. Firouzbakht, M. Schlangen, M. Kaupp, H. Schwarz, *J. Catal.* **2016**, *343*, 68-74.

[21] L.-X. Jiang, C. Zhao, X.-N. Li, H. Chen, S.-G. He, *Angew. Chem. Int. Ed.* **2017**, *56*, 4187-4191.

[22] X. Zhang, G. Liu, K.-H. Meiwes-Broer, G. Ganteför, K. Bowen, *Angew. Chem. Int. Ed.* **2016**, *55*, 9644-9647.

[23] S. Zhou, J. Li, M. Firouzbakht, M. Schlangen, H. Schwarz, *J. Am. Chem. Soc.* **2017**, *139*, 6169-6176.

[24] D. Schröder, H. Schwarz, S. Schenk, E. Anders, *Angew. Chem. Int. Ed.* **2003**, *42*, 5087-5090.

[25] C. Trage, D. Schröder, H. Schwarz, *Chem. Eur. J.* **2005**, *11*, 619-627.

[26] D. Schröder, J. Roithová, H. Schwarz, *Int. J. Mass Spectrom.* **2006**, *254*, 197-201.

[27] Scientific Instrument Service, Isotope Distribution Calculator and Mass Spec Plotter: http://www.sisweb.com/mstools/isotope.htm.

[28] a) D. Schröder, M. Engeser, H. Schwarz, E. C. E. Rosenthal, J. Döbler, J. Sauer, *Inorg. Chem.* **2006**, *45*, 6235-6245; b) N. Dietl, T. Wende, K. Chen, L. Jiang, M. Schlangen, X. Zhang, K. R. Asmis, H. Schwarz, *J. Am. Chem. Soc.* **2013**, *135*, 3711-3721.

[29] a) N. J. Rijs, T. Weiske, M. Schlangen, H. Schwarz, *Chem. Phys. Lett.* **2014**, *608*, 408-424; b) N. J. Rijs, T. Weiske, M. Schlangen, H. Schwarz, *Anal. Chem.* **2015**, *87*, 11601-11601.

[30] M. J. Frisch, G. W. Trucks, H. B. Schlegel, G. E. Scuseria, M. A. Robb, J. R. Cheeseman, G. Scalmani, V. Barone, B. Mennucci, G. A. Petersson, H. Nakatsuji, M. Caricato, X. Li, H. P. Hratchian, A. F. Izmaylov, J. Bloino, G. Zheng, J. L. Sonnenberg, M. Hada, M. Ehara, K. Toyota, R. Fukuda, J. Hasegawa, M. Ishida, T. Nakajima, Y. Honda, O. Kitao, H. Nakai, T. Vreven, J. A. J. Montgomery, J. E. Peralta, F. Ogliaro, M. Bearpark, J. J. Heyd, E. Brothers, K. N. Kudin, V. N. Staroverov, R. Kobayashi, J. Normand, K. Raghavachari, A. Rendell, J. C. Burant, S. S. Iyengar, J. Tomasi, M. Cossi, N. Rega, J. M. Millam, M. Klene, J. E. Knox, J. B. Cross, V. Bakken, C. Adamo, J. Jaramillo, R. Gomperts, R. E. Stratmann, O. Yazyev, A. J. Austin, R. Cammi, C. Pomelli, J. W. Ochterski, R. L. Martin, K. Morokuma, V. G. Zakrzewski, G. A. Voth, P. Salvador, J. J.

Dannenberg, S. Dapprich, A. D. Daniels, Ö. Farkas, J. B. Foresman, J. V. Ortiz, J. Cioslowski, Fox, I. D. J. Gaussian, Wallingford CT, **2009**.

[31] a) A. D. Becke, *J. Chem. Phys.* **1993**, *98*, 5648-5652; b) C. Lee, W. Yang, R. G. Parr, *Phys. Rev. B* **1988**, *37*, 785-789.

[32] a) F. Weigend, R. Ahlrichs, *Phys. Chem. Chem. Phys.* **2005**, *7*, 3297-3305; b) D. Andrae, U. Häußermann, M. Dolg, H. Stoll, H. Preuß, *Theor. Chem. Acc.* **1990**, *77*, 123-141.

[33] a) C.-F. Huo, Y.-W. Li, G.-S. Wu, M. Beller, H. Jiao, *J. Phys. Chem. A* **2002**, *106*, 12161-12169; b) C.-F. Huo, T. Zeng, Y.-W. Li, M. Beller, H. Jiao, *Organometallics* **2005**, *24*, 6037-6042; c) V. M. Rayón, P. Redondo, H. Valdés, C. Barrientos, A. Largo, *J. Phys. Chem. A* **2007**, *111*, 6334-6344; d) J. Yuan, S. Wang, Y. Si, B. Yang, H. Chen, *Dalton Trans.* **2014**, *43*, 5516-5525.

[34] a) K. Fukui, *Acc. Chem. Res.* **1981**, *14*, 363-368; b) D. G. Truhlar, N. J. Kilpatrick, B. C. Garrett, *J. Chem. Phys.* **1983**, *78*, 2438-2442; c) C. Gonzalez, H. B. Schlegel, *J. Chem. Phys.* **1989**, *90*, 2154-2161.

[35] C. J. Cassady, B. S. Freiser, *J. Am. Chem. Soc.* **1984**, *106*, 6176-6179.

[36] Note that the absolute rate coefficient for the reaction cannot be measured directly in our multipole setup; rather, the rate coefficient was determined by using the $[Y]^+/CO_2$ system as a reference: a) C. Heinemann, R. Wesendrup, H. Schwarz, *Chem. Phys. Lett.* **1995**, *239*, 75-83; b) M. Pavlov, M. R. A. Blomberg, P. E. M. Siegbahn, R. Wesendrup, C. Heinemann, H. Schwarz, *J. Phys. Chem. A* **1997**, *101*, 1567-1579; c) X.-G. Zhang, R. Liyanage, P. B. Armentrout, *J. Am. Chem. Soc.* **2001**, *123*, 5563-5575; d) D. Schröder, H. Schwarz, *Can. J. Chem.* **2005**, *83*, 1936-1940.

[37] a) M. P. Langevin, *Ann. Chim. Phys* **1905**, *8*, 245–288; b) G. Gioumousis, D. P. Stevenson, *J. Chem. Phys.* **1958**, *29*, 294-299.

[38] W. P. Griffith, *Q. Rev. Chem. Soc.* **1962**, *16*, 188-207.

[39] a) T. Naota, A. Tannna, S. Kamuro, M. Hieda, K. Ogata, S.-I. Murahashi, H. Takaya, *Chem. Eur. J.* **2008**, *14*, 2482-2498; b) J. Li, G. N. Khairallah, V. Steinmetz, P. Maitre, R. A. J. O'Hair, *Dalton Trans.* **2015**, *44*, 9230-9240.

[40] a) F. Schneider, B. Rabinovitch, *J. Am. Chem. Soc.* **1962**, *84*, 4215-4230; b) G. W. Van Dine, R. Hoffmann, *J. Am. Chem. Soc.* **1968**, *90*, 3227-3232; c) S. Alvarez, C. Lopez, *Inorg. Chim. Acta* **1982**, *64*, L99-L100; d) W. P. Fehlhammer, M. Fritz, *Chem. Rev.* **1993**, *93*, 1243-1280; e) N. Zhu, H. Vahrenkamp, *Angew. Chem. Int. Ed.* **1994**, *33*, 2090-2091; f) A. Coppola, P. Sánchez-Alonso, D. Sucunza, C. Burgos, R. Alajarín, J. Alvarez-Builla, M. E. G. Mosquera, J. J. Vaquero, *Org. Lett.* **2013**, *15*, 3388-3391.

[41] a) S.-I. Murahashi, N. Komiya, H. Terai, T. Nakae, *J. Am. Chem. Soc.* **2003**, *125*, 15312-15313; b) S.-I. Murahashi, N. Komiya, H. Terai, *Angew. Chem. Int. Ed.* **2005**, *44*, 6931-6933; c) S.-I. Murahashi, T. Nakae, H. Terai, N. Komiya, *J. Am. Chem. Soc.* **2008**, *130*, 11005-11012; d) W. Han, A. R. Ofial, *Chem. Commun.* **2009**, 5024-5026; e) S. Singhal, S. L. Jain, B. Sain, *Chem. Commun.* **2009**, 2371-2372; f) P. Anbarasan, H. Neumann, M. Beller, *Angew. Chem. Int. Ed.* **2011**, *50*, 519-522; g) H. Pellissier, *Adv. Synth. Catal.* **2015**, *357*, 857-882; h) X.-P. Zeng, Z.-Y. Cao, X. Wang, L. Chen, F. Zhou, F. Zhu, C.-H. Wang, J. Zhou, *J. Am. Chem. Soc.* **2016**, *138*, 416-425; i) W. Jiang, J. Yang, Y.-Y. Liu, S.-Y. Song, J.-F. Ma, *Inorg. Chem.* **2017**, *56*, 3036-3043; j) B. Song, B. Xu, *Chem. Soc. Rev.* **2017**, *46*, 1103-1123.

[42] D. Schröder, H. Schwarz, *Proc. Natl. Acad. Sci.* **2008**, *105*, 18114-18119.

[43] V. K. K. Praneeth, M. R. Ringenberg, T. R. Ward, *Angew. Chem. Int. Ed.* **2012**, *51*, 10228-10234.

[44] T. Ryutaro, *Bull. Chem. Soc. Jpn.* **1938**, *13*, 388-400.

[45] J. S. Griffith, L. E. Orgel, *Q. Rev. Chem. Soc.* **1957**, *11*, 381-393.

Supporting Information

Ligand Effects on the Reactivity of $[CoX]^+$ (X = CN, F, Cl, Br, O, and OH) towards CO_2 in the Gas Phase: Generation of the Elusive Cyanoformate Ion.

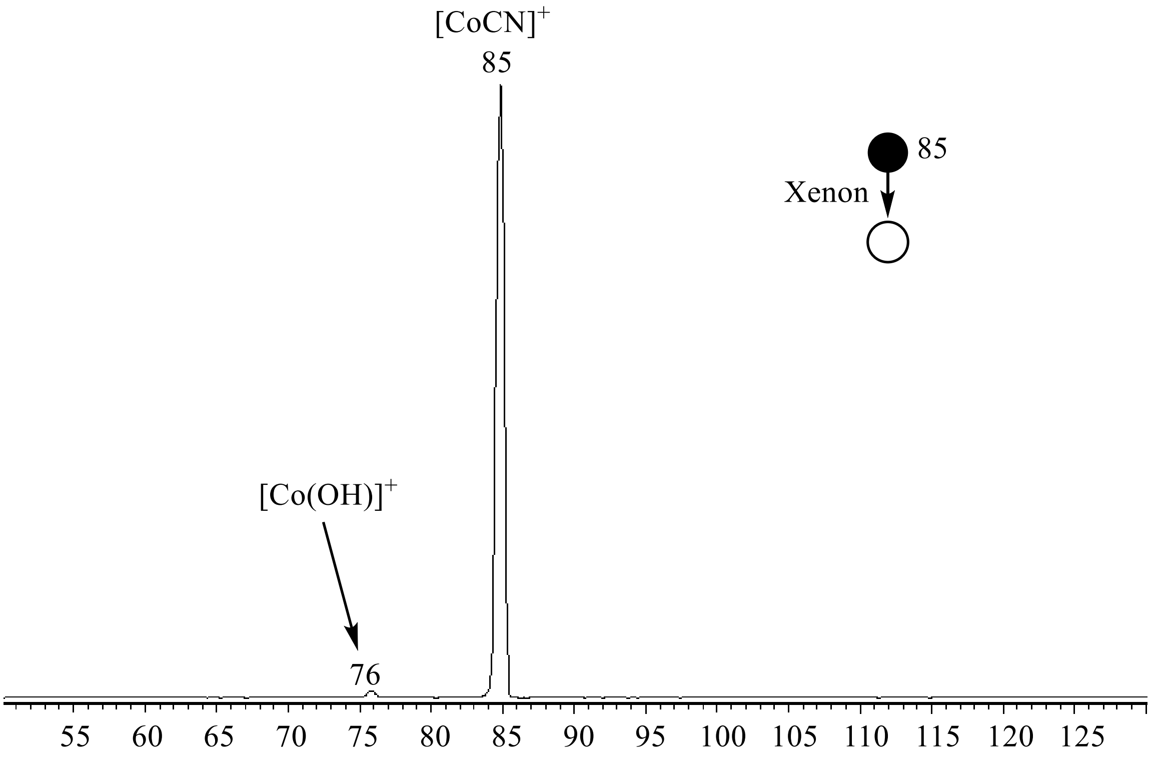

Figure S1 Mass spectra resulting from the thermal ion/molecule reaction of mass-selected [CoCN]$^+$ with xenon.

Table S1 The relative energies (in kJ mol^{-1}) of different isomers of $[Co,C,N]^+$ in various spin states.

	Spin state		
Structure	doublet	quartet	sextet
A	57.3	0	281.4
B	61.4	28.3	309.7
C	34.0	30.4	193.9

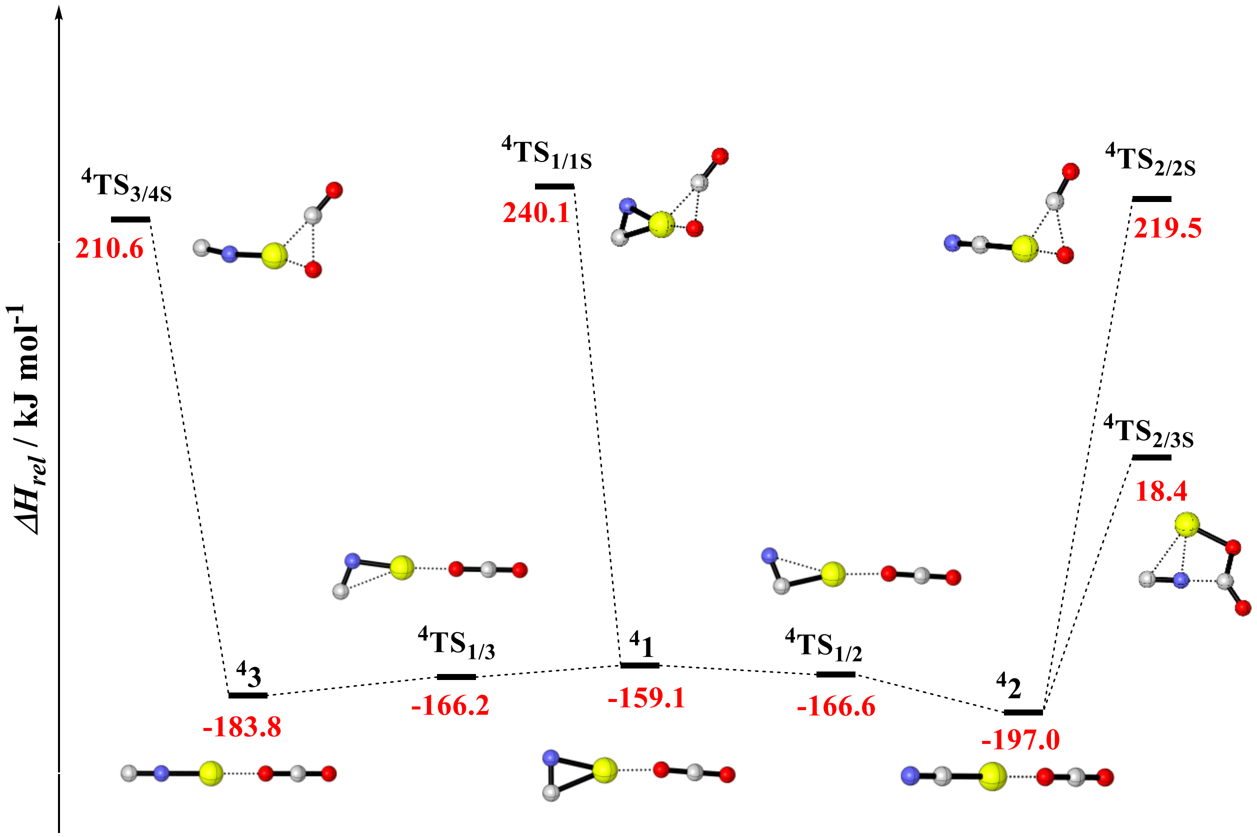

Figure S2 PESs for the oxygen-atom transfer in the reaction of $[CoCN]^+$ with carbon dioxide (B3LYP/def2-TZVP). All ZPVE-corrected energies are given in kJ mol^{-1} and marked in red. Note that all corresponding structures shown here in their doublet-spin states are less favorable than quartet-spin states; therefore, TSR is not probable for these pathways. Color code: N = blue, O = red, C = grey, and Co = yellow.

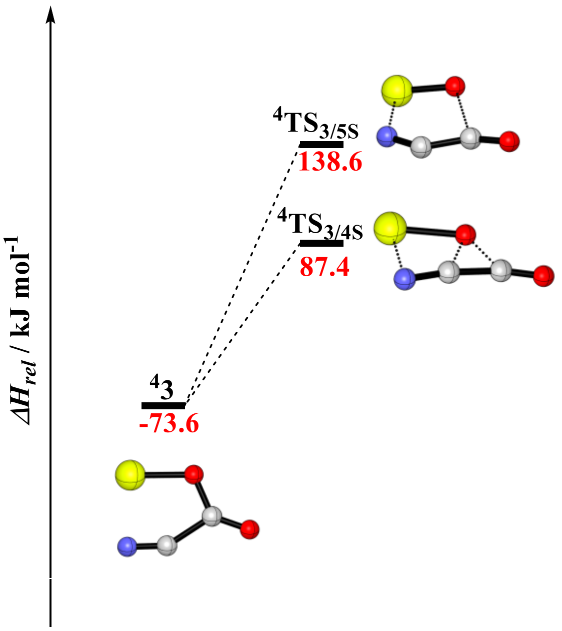

Figure S3 Simplified PESs for the oxygen-atom transfer starting from intermediate ^{4}**3** (B3LYP/def2-TZVP). All ZPVE-corrected energies are given in kJ mol^{-1} and marked in red. Note that all corresponding structures shown here in their doublet-spin states are less favorable than quartet-spin states; therefore, TSR is not probable for these pathways. Color code: N = blue, O = red, C = grey, and Co = yellow.

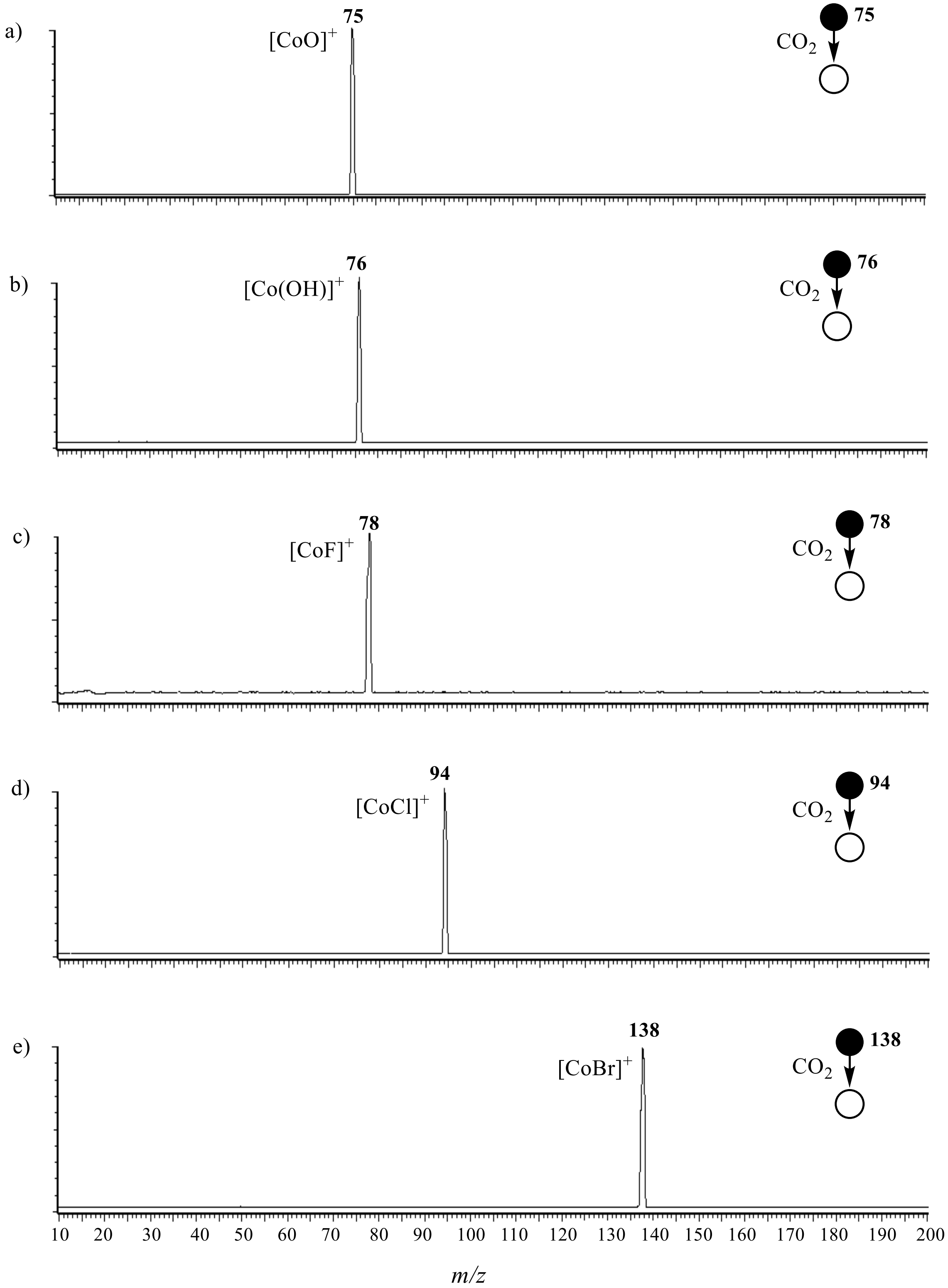

Figure S4 Mass spectra resulting from the thermal ion/molecule reactions of mass-selected a) $[CoO]^+$, b) $[Co(OH)]^+$, c) $[CoF]^+$, d) $[CoCl]^+$, and e) $[CoBr]^+$ with CO_2.

Unpublished paper II

Thermal Carbon Dioxide and Methane Gas-Phase Activation by $[Nb,O,H]^+$: A Combined Experimental/Theoretical Study.

Abstract: *The ion/molecule reactions of* $[Nb,O,H]^+$ *with methane and carbon dioxide have been studied using electrospray-ionization mass spectrometry (ESI-MS) and density functional theory (DFT). In the experiments, the liberation of* H_2 *has been observed in the reaction with methane, while the formation of* $[Nb,O_2,H]^+$ *under CO elimination takes place in the reaction with carbon dioxide. According to the calculations, both the hydroxide complex,* $[Nb(OH)]^+$*, as well as the oxo-hydride species,* $[ONbH]^+$*, are able to activate* CO_2 *resulting in decarbonylation. In contrast, while theory predicts that the reaction of* $[ONbH]^+$ *with methane yields the ionic product* $[ONb(CH_3)]^+$*, concomitant with the elimination of* H_2*, for the hydroxide complex activation of methane is not possible under thermal conditions.*

Keywords: Bond Activation, Methane, Carbon Dioxide, Niobium Complexes, H_2 Liberation, Decarbonylation, Two-State Reactivity

1. Introduction

In recent years, utilization of CO_2 and CH_4 as *C1* source for the efficient transformations of these small molecules into value-added chemicals have gained relevance due to environmental and industrial reasons.[1] However, the chemical transformations of both carbon dioxide and methane represent substantial challenges due to the inert nature of these two greenhouse gases (as indicated, for example, by a standard enthalpy of formation of -394 kJ mol^{-1} for CO_2, and a high C–H bond dissociation energy *BDE*(H_3C–H) of 434 kJ mol^{-1} [2] for methane). Despite the rather unreactive nature of the C–H and the C–O bonds of these two substrates activation processes can still be achieved when reactive reagents, e.g. some transition-metal complexes, are employed.[3] The high oxophilicity of early transition metals makes them proper candidates for the activation of CO_2 by providing a stronger metal-oxygen interaction.[4] In contrast, the physico-chemical properties that are required to promote C–H bond activation of CH_4 are quite different. As a consequence, late transition-metal complexes are preferable.[3h,5] Despite this general trend, we recently showed that the tantalum complexes $[Ta,O,H]^+$ can activate both carbon dioxide and methane in an ion molecule reaction in the gas phase under thermal conditions.[6] Further, tantalum and niobium complexes have been used as catalysts to activate CO_2 resulting in oxygen-atom transfer (OAT) with concomitant CO elimination.[7] Likewise, the activation of carbon dioxide by niobium-hydride complexes via the migratory insertion of carbon dioxide into the Nb–H bond has been reported.[8] In addition, in a recent study Etienne and co-workers provided mechanistic insights of methane activation by a η^2-cyclopropene complex of niobium via a 1,3-C-H bond addition mechanisms.[9] Further, the use of gas-phase ion/molecule experiments in conjunction with computational studies represents an extremely useful approach to investigate important details of related condensed-phase reactions.[3f,3i,10] The gas-phase reactions of $[Nb]^+$ and $[NbO]^+$ give rise to the decarbonylation of carbon dioxide and the formation of $[NbO]^+$ and $[NbO_2]^+$, respectively; both reactions occur under thermal conditions according to Equations (1) and (2).[11]

$$[Nb]^+ + CO_2 \rightarrow [NbO]^+ + CO \qquad (1)$$

$$[NbO]^+ + CO_2 \rightarrow [NbO_2]^+ + CO \qquad (2)$$

Furthermore, adduct formation with methane, Equation (3a), as well as the metal-mediated dehydrogenation, Equation (3b), have been observed to occur in the thermal reaction of $[Nb]^+$ with methane.[12]

$$[Nb]^+ + CH_4 \longrightarrow \begin{cases} [Nb(CH_4)]^+ & 25\% \qquad (3a) \\ [Nb(CH_2)]^+ + H_2 & 75\% \qquad (3b) \end{cases}$$

In addition to the abovementioned processes, dissociative addition of CH_4 in the gas phase was also observed in some cases.[13] As an example for a niobium complex, recently He and co-workers reported the oxidative addition of CH_4 to $[HNbN]^-$ resulting in the adsorption product $[(H)_2NbN(CH_3)]^-$, Eq. (4).[14]

$$[HNbN]^- + CH_4 \rightarrow [(H)_2NbN(CH_3)]^- \qquad (4)$$

Hence, niobium complexes can be viewed as promising candidates to carry out both C–O and C–H bond activations similar to its group homologue tantalum. The only example of stoichiometric coupling of methane to carbon dioxide in the gas phase has been observed in the case of Ta^+.[15] Schwarz and co-workers showed that, while the cationic oxide TaO+, obtained by reduction of CO_2, is inert toward CH_4, $[Ta(CH_2)]^+$ generated in the reaction of $[Ta]^+$ with CH_4, can activate CO_2 resulting in the complex $[Ta(CH_2)O]^+$ under elimination of CO. The further reaction of $[Ta(CH_2)O]^+$ with CO_2 finally results in the generation of $[TaO_2]^+$ and CH_2CO.[15]

Here we aim to understand in more details the activation of CH_4 and CO_2 promoted by $[Nb,O,H]^+$ at a strictly molecular level and compare these findings with the previously investigated $[Ta,O,H]^+$ system.[6]

2. Results and Discussion

ESI of a methanolic solution of $NbCl_5$ results in the formation of ions at *m/z* 110 which contain niobium, and may correspond to $[Nb,O,H]^+$. The $[Nb,O,H]^+$ species can contain two isomers, $[ONbH]^+$ (**1**) and $[Nb(OH)]^+$ (**2**) (Chart 1). It is worth noting that the ground state of species **1** is predicted to be a doublet, whereas the ground state of **2** corresponds to the quartet state (the latter being 9.1 kJ mol^{-1} higher in energy than ^{2}**1**).

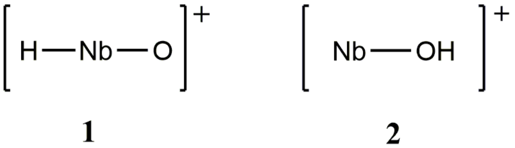

Chart 1 Isomers of the niobium complex at *m/z* 110.

As has been previously achieved for the separation of isomeric copper species formed in ESI via traveling wave ion mobility (TWIMS),[16] we tried to explore the feasibility of separating the species via ion mobility experiments. However, despite several efforts, it was not possible to generate sufficient intensity of $[Nb,O,H]^+$ to perform this analysis. Likewise, an experimental distinction of these two isomers by collision-induced dissociation (CID)[17] is not instructive, and hydrogen-deuterium (H/D) exchange reactions with D_2 (identifying the structure directly via its reactivity)[18] indicates the formation of $[ONbH]^+$ (**1**) but cannot rule out the co-generation of $[Nb(OH)]^+$ (**2**) (see “Supporting Information” for more details). Therefore, owing to the probability of having produced a mixture of two isomers, we considered the reactivities toward CH_4 and CO_2 of both isomers.

Figure 1 details the mass spectra for the thermal ion/molecule reactions of the mass-selected ions $[Nb,O,H]^+$ (*m/z* 110) with CO_2 and CH_4. The relative rate constant for the reaction of $[Nb,O,H]^+$ (*m/z* 110) with CO_2 amounts to 4.6×10^{-10} cm^{-3} s^{-1} $molecule^{-1}$.[11,19] This value corresponds to an efficiency of 64% relative to the gas-kinetic collision limit.[20] In case of the reaction with CH_4, the relative rate constant amounts to 2.4×10^{-10} cm^{-3} s^{-1} $molecule^{-1}$,[11,19] which corresponds to an efficiency of 24% relative to the gas-kinetic collision limit.[20]

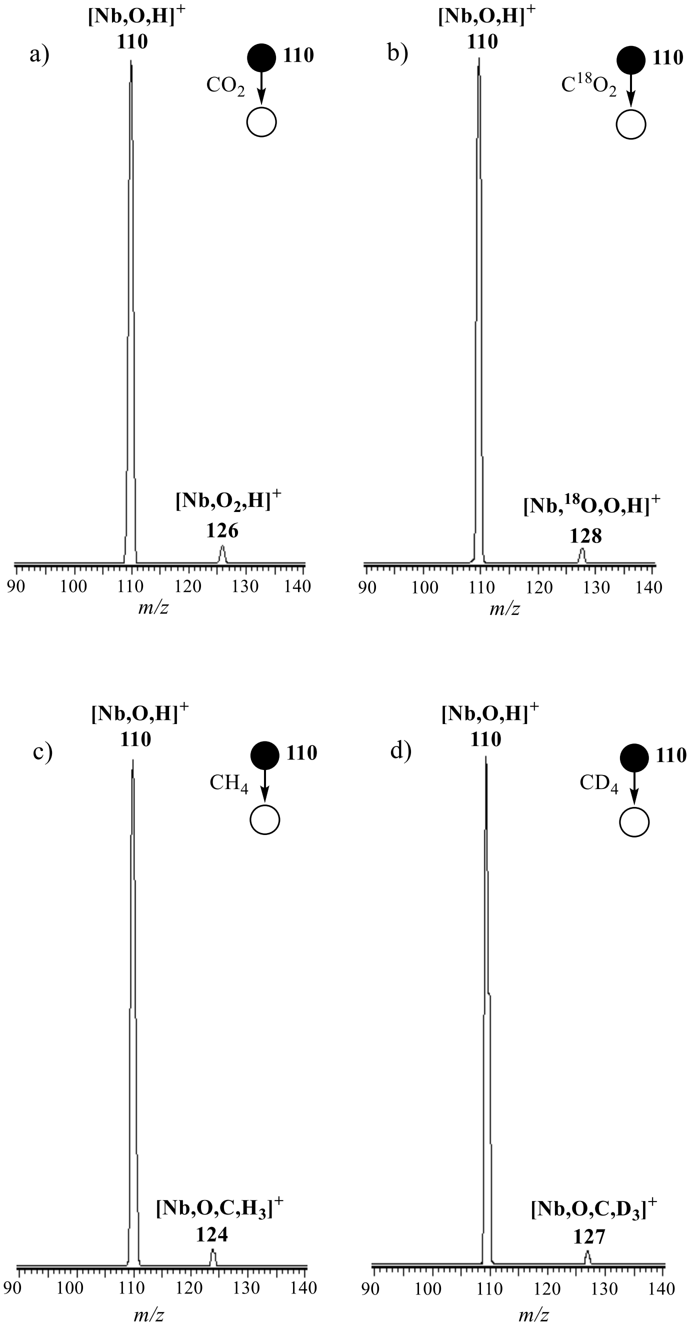

Figure 1 Mass spectra resulting from the thermal ion/molecule reaction of mass-selected $[Nb,O,H]^+$ with a) CO_2 at a pressure of 10.6×10^{-4} mbar, b) $C^{18}O_2$ at a pressure of 9.4×10^{-4} mbar, c) CH_4 at a pressure of 5.3×10^{-4} mbar, and d) CD_4 at a pressure of 4.1×10^{-4} mbar. The tandem-MS experiments are described with mass-selected $[Nb,O,H]^+$ species as indicated.

The reaction with CO_2 results in oxygen-atom transfer (OAT), yielding the complex $[Nb,O_2,H]^+$ (*m/z* 126) concomitant with the elimination of carbon monoxide (Figure 1a, Equation 5). Experiments with $C^{18}O_2$ result in a quantitative shift, i.e. *m/z* 126 → 128 (Figure 1b, Equation 6). Thus, the oxygen atom that is transferred to the ionic product originates exclusively from carbon dioxide.

$$[ONbH]^{+} + CO_2 \quad \rightarrow \quad [Nb,O_2,H]^{+} + CO \qquad (5)$$

$$[ONbH]^{+} + C^{18}O_2 \quad \rightarrow \quad [Nb,^{18}O,O,H]^{+} + CO \qquad (6)$$

Further, we tested the ability of the $[Nb,O,H]^+$ ions to activate the C–H bond of methane. In the ion/molecule reaction of *m/z* 110 ions with methane, a fragment ion $[Nb,O,C,H_3]^+$ (*m/z* 124) is generated concomitant with the elimination of H_2 (Figure 1c and Equation 7); labeling experiments with CD_4 result in a clean mass shift *m/z* 124 → *m/z* 127 (Figure 1d and Equation 8), thus pointing to a ligand switch.

$$[Nb,O,H]^{+} + CH_4 \quad \rightarrow \quad [Nb,O,C,H_3]^{+} + H_2 \qquad (7)$$

$$[Nb,O,H]^{+} + CD_4 \quad \rightarrow \quad [Nb,O,C,D_3]^{+} + HD \qquad (8)$$

Next, the reaction mechanisms were interrogated by quantum-chemical calculations. The DFT-based potential energy surfaces (PESs) and selected structural information for the reactions of the two isomers $[ONbH]^+$ (**1**) and $[Nb(OH)]^+$ (**2**) are shown in Figure 2 (with CO_2) and in Figures 3 and Figure S4 in "Supporting Information" (with CH_4).

We first explored the possibility of activating a C–O bond of CO_2 mediated by species ^{2}**1** (Figure 2a). Starting from ^{2}**1**, the incoming carbon dioxide coordinates to the metal center leading to the complex ^{2}**3**. A CO_2 insertion process into the Nb–H bond occurs via a four-centered transition state, $^{2}\mathbf{TS_{3/4}}$, generating the carboxylated intermediate ^{2}**4**. This step may correspond to a σ-bond metathesis process as it is already discussed in case of insertion reaction of CO_2 with transition-metal complexes.[21] From ^{2}**4**, H-atom migration from the carbon atom to the Nb-bound oxygen atom takes place via ^{2}**TS$_{4/5}$** resulting in complex ^{2}**5**, in which CO is loosely coordinated to the hydrogen atom of the newly formed OH ligand. The transition state ^{2}**TS$_{4/5}$** is almost isoenergetic to the entrance channel to occur under thermal conditions. Moreover, the ions of the high-energy tail of the kinetic energy distribution might be responsible for the observed reaction; as determined in previous studies;[22] the width of the kinetic energy distribution amounts to 0.4 eV. A barrierless evaporation of carbon monoxide from ^{2}**5** gives rise to ^{2}**6**. Since the efficiency of the reaction of [Nb,O,H]$^{+}$ with CO_2 is rather high, another reaction channel should exist, which is more efficient than the [ONbH]$^{+}$/CO_2 couple. Therefore, we further considered the CO_2 activation mediated by species ^{4}**2** (Figure 2b).

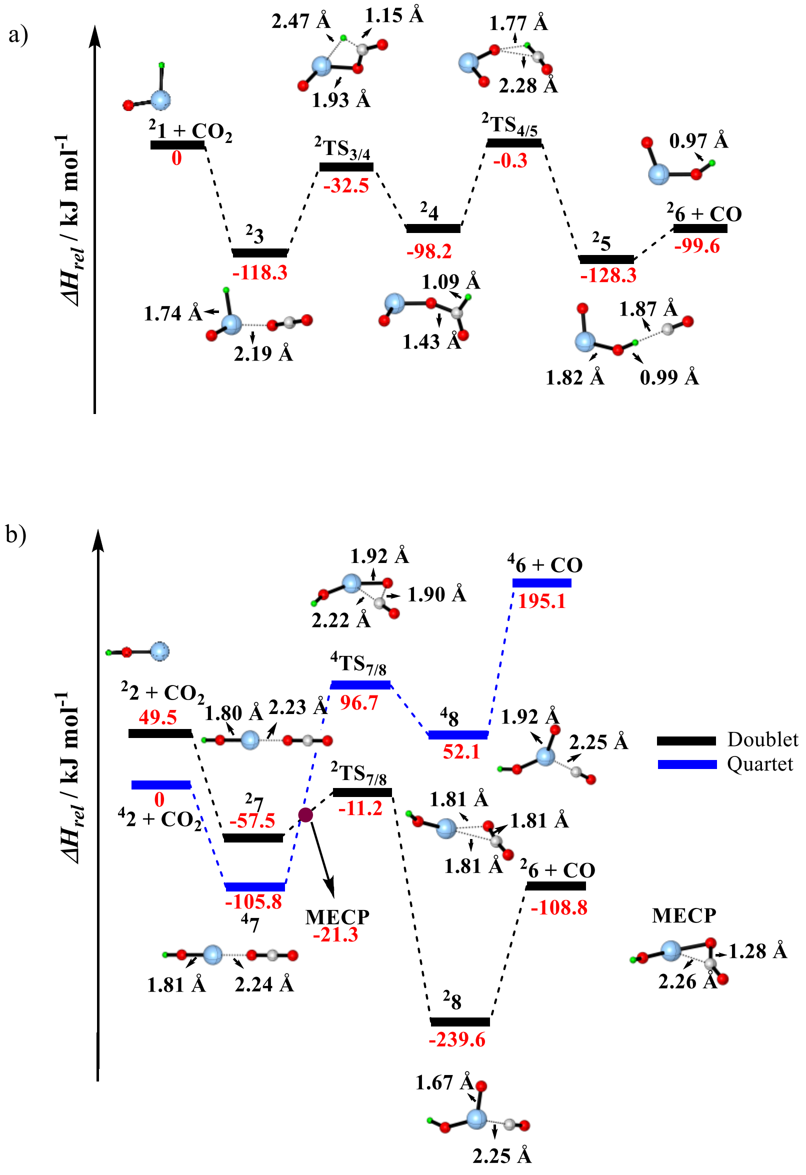
a)
ΔH_rel / kJ mol⁻¹
²1 + CO₂
0
²3
-118.3
²TS3/4
-32.5
²4
-98.2
²TS4/5
-0.3
²5
-128.3
²6 + CO
-99.6
2.47 Å
1.15 Å
1.93 Å
1.77 Å
2.28 Å
0.97 Å
1.74 Å
2.19 Å
1.09 Å
1.43 Å
1.87 Å
1.82 Å
0.99 Å
b)
ΔH_rel / kJ mol⁻¹
²2 + CO₂
49.5
0
⁴2 + CO₂
²7
-57.5
-105.8
⁴7
⁴TS7/8
96.7
²TS7/8
-11.2
MECP
-21.3
⁴8
52.1
²8
-239.6
⁴6 + CO
195.1
²6 + CO
-108.8
1.92 Å
1.90 Å
2.22 Å
1.80 Å
2.23 Å
1.92 Å
2.25 Å
1.81 Å
1.81 Å
1.81 Å
1.81 Å
2.24 Å
1.67 Å
2.25 Å
MECP
1.28 Å
2.26 Å
Doublet
Quartet

Figure 2 Potential-energy profile for the reaction of a) $[ONbH]^+$ and b) $[Nb(OH)]^+$ with CO_2. All energies, corrected for zero-point vibrational energy (ZPVE) contributions, are given in kJ mol^{-1} and marked in red. Color code: C = gray, H = green, O = red, Nb = blue.

In contrast to the doublet ground state of complex **1**, the reactive species **2** possesses a quartet ground state (with the doublet electronic state being 49.5 kJ mol^{-1} higher in energy). After having formed the quartet adduct ^{4}**7**, proceeding on the ground state quartet surface of ^{4}**7** is prohibited by a high barrier that is 96.7 kJ mol^{-1} above the entrance channel ($^4\mathbf{TS_{7/8}}$). Therefore, in order to allow for a thermal process the system must undergo an intersystem crossing (ISC) to access the doublet surface. Thus, after spin crossing at a minimum energy crossing point (MECP) in the vicinity of transition structure $^2\mathbf{TS_{7/8}}$, the migration of an oxygen atom of CO_2 to the metal center via $^2\mathbf{TS_{7/8}}$ eventually leads, under the elimination of CO, to the exothermic formation of $[ONb(OH)]^+$ (^{2}**6**).

Thus, two plausible pathways were found for the activation of CO_2, revealing that both ^{2}**1** and ^{4}**2** are able to activate a C–O bond of CO_2. While ^{2}**1** mediates the reaction on a spin-allowed doublet surface via a step-wise carboxylation/decarbonylation mechanism, in the reaction of ^{4}**2** with CO_2, ISC from the quartet to the doublet surface according to a two-state reactivity (TSR) scenario [23] enables the OAT from CO_2 to $[Nb(OH)]^+$ under the generation of $[ONb(OH)]^+$.

To obtain a better understanding of the reactivity of $[Nb,O,H]^+$ towards CO_2, we have also compared the current system with the related couple $[Ta,O,H]^+/CO_2$.[6] In the experiments, both Ta and Nb complexes show similar reactivity towards carbon dioxide, and also the calculated PESs of the reaction profiles are qualitatively similar. Further, the calculated binding energies of CO_2 to the niobium complexes $^2[ONbH]^+$ (118.3 kJ mol^{-1}) and $^{2,4}[Nb(OH)]^+$ (57.5 kJ mol^{-1} and 105.8 kJ mol^{-1}, respectively) are slightly smaller than that for the respective tantalum complexes ($^2[HTaO]^+$ 123.0 kJ mol^{-1}, $^2[Ta(OH)]^+$ 94.2 kJ mol^{-1}, and $^4[Ta(OH)]^+$ 109.6 kJ mol^{-1}). These trends can in general be explained by the higher oxygen-atom affinity (OA) of Ta compared to Nb (OA(Ta) = 188 ± 15 kcal mol^{-1}, OA(Nb) = 164.4 ± 2.5 kcal mol^{-1}).[24] Moreover, the reaction is expected to be faster for the $[Ta(OH)]^+/CO_2$ couple, since the rate-determining transition state is much lower in energy compared to the niobium system (-57.5 kJ mol^{-1} versus -11.2 kJ mol^{-1}). This is line with the experimentally determined rate constant of the $[Ta,O,H]^+/CO_2$ system, 5.8×10^{-10} cm^{-3} s^{-1} $molecule^{-1}$ (Φ = 87%), which is higher than that of $[Nb,O,H]^+/CO_2$,4.6×10^{-10} cm^{-3} s^{-1} $molecule^{-1}$ (Φ = 64%).[17]

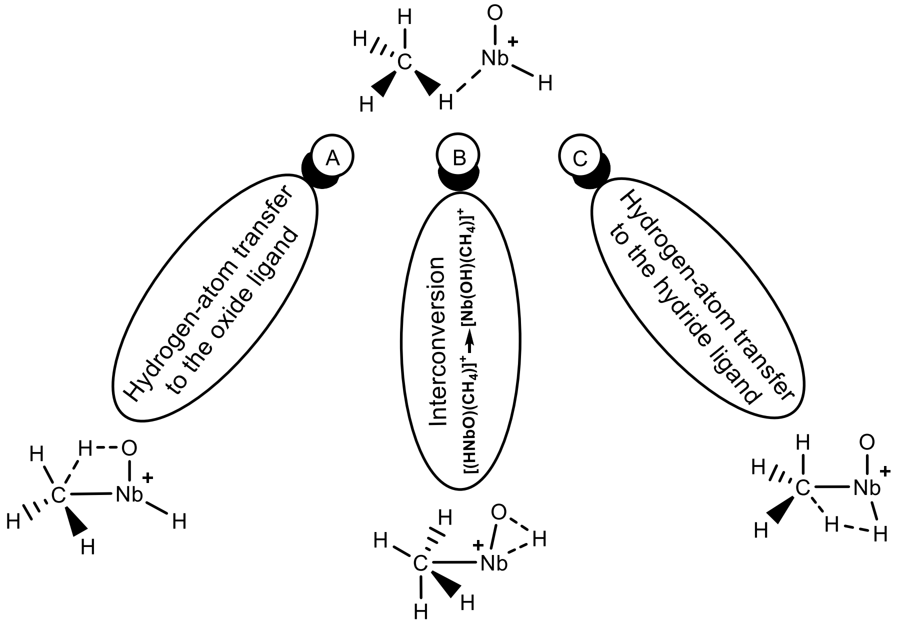
A
Hydrogen-atom transfer to the oxide ligand
B
Interconversion [(HNbO)(CH4)]+ → [Nb(OH)(CH4)]+
C
Hydrogen-atom transfer to the hydride ligand
Nb
+

Scheme 1 Possible routes and respective transition states for the reaction of $[ONbH]^+$ with methane.

In the next step, quantum chemical calculations have been performed to obtain a refined mechanistic insight into the reactions of $[ONbH]^+$ (Figures 3) as well as $[Nb(OH)]^+$ (Figure S5 in "Supporting Information") with CH_4. In the former case, starting from ^{2}**1**, the incoming methane coordinates to the metal center leading to the exothermic and barrier-free formation of complex ^{2}**9**. After having formed the doublet adduct ^{2}**9**, three different scenarios were considered (A-C, Scheme 1).

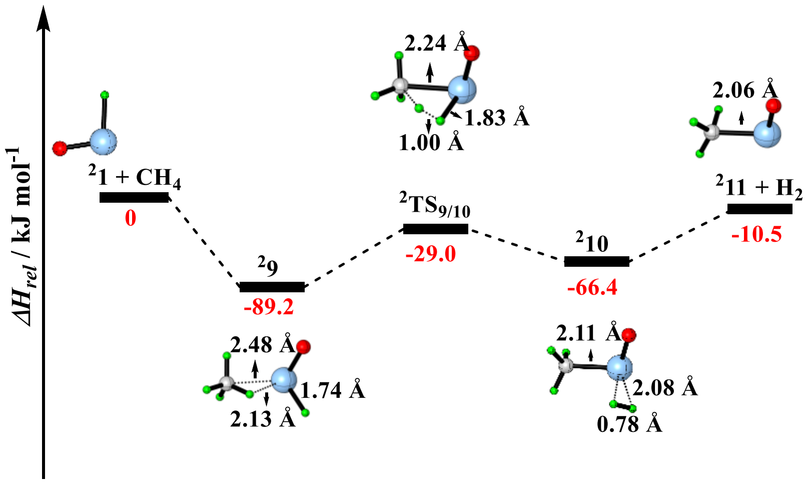

Figure 3 Potential-energy profile for the reaction of $[ONbH]^+$ with CH_4 on the doublet spin state surface. All energies, corrected for zero-point vibrational energy (ZPVE) contributions, are given in kJ mol^{-1} and marked in red. Charges are omitted for the sake of brevity. Color code: C= gray, H = green, O = red, Nb = blue.

All reaction pathways have been considered in the calculations. The spin-preserving formation of a hydroxide ligand (path A) is hindered by a barrier of 54.7 kJ mol^{-1} (Figure S4, ^{2}**TS$_{9/8S}$**) above the entrance channel (the relative energy of the respective transition-state structure in the quartet spin state amounts to 249.7 kJ mol^{-1}), therefore, path A is not accessible under thermal conditions. Likewise, the interconversion $[HNbO(CH_4)]^+ \rightleftharpoons [Nb(OH)(CH_4)]^+$ (path B) is hampered by a kinetic barrier amounting to 118.5 kJ mol^{-1} (Figure S4, ^{2}**TS$_{9/9S}$**) on the doublet spin surface (the relative energy of the respective transition-state structure is 133.9 kJ mol^{-1} on the quartet PES). Hence, only pathway C constitutes a plausible alternative (Figure 3). From ^{2}**9**, a hydrogen atom from methane is transferred to the hydride ligand in a concerted manner via ^{2}**TS$_{9/10}$**, giving rise to intermediate $[(CH_3)NbO(H_2)]^+$ (^{2}**10**). As previously demonstrated for the reaction of $[OTiH]^+$, $[OTaH]^+$, and $[OMoH]^+$ with CH_4, this corresponds to a σ-bond metathesis process,[6,25] with a coplanar arrangement of the two hydrogen, the carbon, and the niobium atoms. Regarding the reaction of $[Nb(OH)]^+$ (**2**) with methane (Figure S5), after the barrier-free formation of the encounter complex ^{4}**9S**, which is exothermic by -87.1 kJ mol^{-1}, the subsequent steps on the quartet surface are all considerably higher in energy compared to the entrance channel. In addition, a spin crossing from the quartet to the doublet state is not of benefit in order to allow the reaction to proceed via a thermally accessible pathway, since the transition state ^{2}**TS$_{9S/10S}$** is located 9.2 kJ mol^{-1} above the reactants (Figure S5). Consequently, the dehydrogenation of methane by $[Nb(OH)]^+$ leading to the formation of $[Nb(O)(CH_3)]^+$ and $[Nb(OH)(CH_2)]^+$ is not accessible under thermal conditions due to both kinetic barriers and endothermicity of some of the exit channels (see Figure S5 in "Supporting Information" for more details). This is in contrast to the tantalum system, for which the formation of both $[Ta(O)(CH_3)]^+$ and $[Ta(OH)(CH_2)]^+$ is accessible under thermal conditions according to the calculations, and this theoretical finding has been used to explain the elimination of D_2 in the labeling experiments of this system.[6] Therefore, the exclusive elimination of HD in the labeling experiment of $[Nb,O,H]^+$ with CD_4 might indicate that the reaction of the hydroxide complex does not occur under thermal conditions (in line with the DFT results shown in Figure S5). Alternatively, only the hydride complex $[ONbH]^+$ and not the hydroxo complex $[Nb(OH)]^+$ is generated in the ESI source. In general, the stronger M–C interaction for Ta than for the lighter Nb congener can be responsible for the higher reactivity of $[Ta(OH)]^+$ towards CH_4. The strong interaction results from lanthanide contraction, which leads to a tightening of the valence s orbitals, resulting in a stabilization of the 6s orbital energy relative to that of 5d,[26] thus leading to higher bond dissociation energies of the M–C bonds for 5d metals.[27] These features traced back to the operation of a relativistic effect,[28] which is much more significant for 5d elements than for their lighter congeners.

To summarize, labeling experiments together with theoretical investigations indicate that while the activation of methane is not possible for the hydroxide complex of niobium under thermal conditions, the oxo-hydride complexes $[HMO]^+$ (M = Nb, Ta) as well as $[Ta(OH)]^+$ are able to activate a C–H bond of CH_4.

3. Conclusions

In this combined experimental/computational study, we have investigated mechanistic aspects of the reaction of $[Nb,O,H]^+$ (*m/z* 110) with both methane and carbon dioxide. Our experiments revealed that the reactions of $[Nb,O,H]^+$ (*m/z* 110) with CH_4 and CO_2 result in the ionic products $[Nb,O,C,H_3]^+$ (*m/z* 124) and $[Nb,O_2,H]^+$ (*m/z* 126) with the concomitant elimination of H_2 and CO, respectively. Isotopic labeling experiments with $C^{18}O_2$ showed a clean reaction similar to the corresponding tantalum system in our previous study. However, in contrast to the reaction of $[Ta,O,H]^+$ with CD_4 in which the formations of both $[Ta,O,C,D_3]^+$ and $[Ta,O,C,D_2,H]^+$ are observed with concomitant elimination of HD and D_2, respectively, only the formation of $[Nb,O,C,D_3]^+$ under HD loss has been observed for the corresponding Nb system.

DFT calculations indicate that $[ONbH]^+$ is able to thermally activate a C–H bond of methane, while a kinetic barrier above the entrance channel hinders the activation of methane by $[Nb(OH)]^+$. In the spin-allowed activation of CH_4 by $[ONbH]^+$, the rate-limiting step proceeds through a transition state located 29.0 kJ mol^{-1} below the entrance channel; thus, the reaction takes place via a two-state reactivity scenario. The same is true for the reaction of $[Nb(OH)]^+$ with CO_2; a spin crossing is necessary to access the transition structure of C–O bond activation with a relative energy of -11.2 kJ mol^{-1}. In the case of CO_2 activation mediated by $[ONbH]^+$, the rate-limiting transition structure of the spin-allowed C–O activation is almost zero but still plausible to occur under the thermal conditions applied in the experiments. These findings may represent a quantitatively similar behavior as for the reactions of Ta complexes with CO_2. However, due to the lower relative energy of the rate-determining step, the reaction proceeds faster in the tantalum system than with niobium, in line with the experiments.

4. Experimental Section and Computational Details

The experiments were performed using a VG Bio-Q mass spectrometer of QHQ configuration (Q: quadrupole; H: hexapole) equipped with an electrospray-ionization (ESI) source, as described in detail elsewhere.[29] Methanol and niobium(V) chloride, CH_4, CD_4, CO_2, and $C^{18}O_2$ were obtained from Sigma-Aldrich and utilized without further purification. To generate $[Nb,O,H]^+$, a millimolar methanolic solution of niobium(V) chloride was introduced into the mass spectrometer via a syringe pump and a fused-silica capillary connected to the ESI source with a pump rate of 4µl/min. Nitrogen was used as a nebulizing and drying gas, at a source temperature of 80 ºC. The maximum intensity of the desired complex was achieved by adjusting the cone voltage (U_c) to around 80-90 V. The reactions of $[Nb,O,H]^+$ with methane and carbon dioxide have been probed at a collision energy (E_{lab}) nominally set to 0 eV, which, in conjunction with the ca. 0.4 eV kinetic energy width of the parent ion at peak half height, allows the investigation of quasi-thermal reactions, as described previously.[22] The pressure of hydrogen, water, methane, and carbon dioxide were varied between ca. 3.9×10^{-4} to 12.4×10^{-4} mbar in the hexapole. Cationic products are recorded by scanning of Q2. The travelling-wave ion-mobility spectrometry (TWIMS) experiments were carried out with the same solutions described above, on a Synapt G2 mass spectrometer (Waters, Manchester) fitted with a standard ESI source, as previously described.[16] In spite of extensive tuning of the instrument parameters it was not possible to obtain a signal satisfactory for measuring arrival time distributions.

For the computational studies we employed the Gaussian 09 program package[30] using unrestricted Kohn-Sham calculations with the B3LYP functional[31] and the def2-QZVP basis sets of Weigend and Ahlrichs, including a quasirelativistic, energy-adjusted effective core potential (ECP) and an associated valence basis set for the niobium atom.[32] The satisfying performance of the B3LYP functional for energetic and structural aspects of 5d-block transition metals has been confirmed previously in benchmark studies.[33]The nature of local minima and transition states (TSs) was verified by harmonic vibrational frequency analysis of the respective optimized structures. IRC calculations[34] were performed in order to confirm the connection between transition states and minima. All energies (given in kJ mol^{-1}) are corrected for (unscaled) zero-point vibrational energy contributions. For those reactions that involve more than a single spin-state surface, the TSR paradigm has been considered.[23] It was thus necessary to not only locate and characterize the stationary points on each potential-energy surface (PES), but to also identify the MECPs where the relevant spin states lie close in energy. We located MECPs via the structures having identical structure and energy in the doublet and quartet states. The MECPs were calculated using the algorithm developed by Harvey et al.[35]

References

[1] a) M. Aresta, A. Dibenedetto, *Dalton Trans.* **2007**, 2975-2992; b) D. J. Darensbourg, *Chem. Rev.* **2007**, *107*, 2388-2410; c) M. Aresta, A. Dibenedetto, A. Angelini, *Chem. Rev.* **2014**, *114*, 1709-1742; d) J. M. Weber, *Int. Rev. Phys. Chem.* **2014**, *33*, 489-519.

[2] a) K. Huang, C.-L. Sun, Z.-J. Shi, *Chem. Soc. Rev.* **2011**, *40*, 2435-2452; b) V. Havran, M. P. Duduković, C. S. Lo, *Ind. Eng. Chem. Res.* **2011**, *50*, 7089-7100; c) C. Maeda, Y. Miyazaki, T. Ema, *Catal. Sci. Tech.* **2014**, *4*, 1482-1497; d) H. Schwarz, *Chem. Phys. Lett.* **2015**, *629*, 91-101.

[3] a) R. Wesendrup, H. Schwarz, *Angew. Chem. Int. Ed.* **1995**, *34*, 2033-2035; b) D. Schröder, H. Schwarz, S. Schenk, E. Anders, *Angew. Chem. Int. Ed.* **2003**, *42*, 5087-5090; c) T. Sakakura, J.-C. Choi, H. Yasuda, *Chem. Rev.* **2007**, *107*, 2365-2387; d) W. Wang, S. Wang, X. Ma, J. Gong, *Chem. Soc. Rev.* **2011**, *40*, 3703-3727; e) N. Dietl, M. Schlangen, H. Schwarz, *Chem. Eur. J.* **2011**, *17*, 1783-1788; f) H. Schwarz, *Isr. J. Chem.* **2014**, *54*, 1413-1431; g) S.-Y. Tang, N. J. Rijs, J. Li, M. Schlangen, H. Schwarz, *Chem. Eur. J.* **2015**, *21*, 8483-8490; h) J. Li, P. González-Navarrete, M. Schlangen, H. Schwarz, *Chem. Eur. J.* **2015**, *21*, 7780-7789; i) H. Schwarz, *Coord. Chem. Rev.* **2017**, *334*, 112-123; j) S. Zhou, J. Li, M. Firouzbakht, M. Schlangen, H. Schwarz, *J. Am. Chem. Soc.* **2017**, *139*, 6169-6176; k) S. Zhou, M. Firouzbakht, M. Schlangen, M. Kaupp, H. Schwarz, *Chem. Eur. J.*, *In press*, DOI: 10.1002/chem.201703767.

[4] K.-C. Lau, B. J. Petro, S. Bontemps, R. F. Jordan, *Organometallics* **2013**, *32*, 6895-6898.

[5] a) D. Schröder, H. Schwarz, *Angew. Chem. Int. Ed.* **1995**, *34*, 1973-1995; b) Y. Shiota, K. Yoshizawa, *J. Am. Chem. Soc.* **2000**, *122*, 12317-12326.

[6] M. Firouzbakht, N. J. Rijs, P. González-Navarrete, M. Schlangen, M. Kaupp, H. Schwarz, *Chem. Eur. J.* **2016**, *22*, 10581-10589.

[7] V. A. Williams, D. R. Manke, P. T. Wolczanski, T. R. Cundari, *Inorg. Chim. Acta* **2011**, *369*, 203-214.

[8] A. Antiñolo, S. García-Yuste, A. Otero, E. Villaseñor, *J. Organomet. Chem.* **2007**, *692*, 4436-4447.

[9] C. Li, C. Dinoi, Y. Coppel, M. Etienne, *J. Am. Chem. Soc.* **2015**, *137*, 12450-12453.

[10] a) F.-X. Li, X.-G. Zhang, P. B. Armentrout, *Int. J. Mass Spectrom* **2006**, *255–256*, 279-300; b) J. Roithová, D. Schröder, *Chem. Rev.* **2010**, *110*, 1170-1211; c) H. Schwarz, *Angew. Chem. Int. Ed.* **2011**, *50*, 10096-10115.

[11] G. K. Koyanagi, D. K. Bohme, *J. Phys. Chem. A* **2006**, *110*, 1232-1241.

[12] a) A. Shayesteh, V. V. Lavrov, G. K. Koyanagi, D. K. Bohme, *J. Phys. Chem. A* **2009**, *113*, 5602-5611; b) P. B. Armentrout, *Chem. Eur. J.* **2017**, *23*, 10-18.

[13] a) S. Zhou, J. Li, M. Schlangen, H. Schwarz, *Angew. Chem. Int. Ed.* **2016**, *55*, 7685-7688; b) S. Zhou, J. Li, M. Schlangen, H. Schwarz, *Chem. Eur. J.* **2016**, *22*, 7225-7228; c) S. Zhou, J. Li, M. Schlangen, H. Schwarz, *Angew. Chem. Int. Ed.* **2016**, *55*, 14867-14871.

[14] J.-B. Ma, L.-L. Xu, Q.-Y. Liu, S.-G. He, *Angew. Chem. Int. Ed.* **2016**, *55*, 4947-4951.

[15] a) R. Wesendrup, H. Schwarz, *Angew. Chem. Int. Ed. Engl.* **1995**, *34*, 2033-2035; b) N. Sändig, W. Koch, *Organometallics* **1998**, *17*, 2344-2351.

[16] a) N. J. Rijs, T. Weiske, M. Schlangen, H. Schwarz, *Chem. Phys. Lett.* **2014**, *608*, 408-424; b) N. J. Rijs, T. Weiske, M. Schlangen, H. Schwarz, *Anal. Chem.* **2015**, *87*, 9769-9776.

[17] K. Levsen, H. Schwarz, *Mass Spectrometry Reviews* **1983**, *2*, 77-148.

[18] D. B. Jacobson, B. S. Freiser, *J. Am. Chem. Soc.* **1985**, *107*, 72-80.

[19] Note that the absolute rate coefficients for the reactions cannot be measured directly in our multipole setup; rather, the rate coefficient was determined by using the $[Pt]^+/CH_4$ system (in case of methane activation) and $[Y]^+/CO_2$ system (in case of carbon dioxide activation) as a reference: a) C. Heinemann, R. Wesendrup, H. Schwarz, *Chem. Phys. Lett.* **1995**, *239*, 75-83; b) M. Pavlov, M. R. A. Blomberg, P. E. M. Siegbahn, R. Wesendrup, C. Heinemann, H. Schwarz, *J. Phys. Chem. A* **1997**, *101*, 1567-1579; c) X.-G. Zhang, R. Liyanage, P. B. Armentrout, *J. Am. Chem. Soc.* **2001**, *123*, 5563-5575; d) D. Schröder, H. Schwarz, *Can. J. Chem.* **2005**, *83*, 1936-1940.

[20] a) M. P. Langevin, *Ann. Chim. Phys* **1905**, *8*, 245–288; b) G. Gioumousis, D. Stevenson, *J. Chem. Phys.* **1958**, *29*, 294-299.

[21] T. Fan, X. Chen, Z. Lin, *Chem. Commun.* **2012**, *48*, 10808-10828.

[22] a) D. Schröder, T. Weiske, H. Schwarz, *Int. J. Mass Spectrom.* **2002**, *219*, 729-738; b) D. Schröder, M. Engeser, H. Schwarz, E. C. E. Rosenthal, J. Döbler, J. Sauer, *Inorg. Chem.* **2006**, *45*, 6235-6245; c) P. Gruene, C. Trage, D. Schröder, H. Schwarz, *Eur. J. Inorg. Chem.* **2006**, *2006*, 4546-4552; d) N. Dietl, T. Wende, K. Chen, L. Jiang, M. Schlangen, X. Zhang, K. R. Asmis, H. Schwarz, *J. Am. Chem. Soc.* **2013**, *135*, 3711-3721.

[23] a) P. B. Armentrout, *Science* **1991**, *251*, 175-179; b) D. Schröder, S. Shaik, H. Schwarz, *Acc. Chem. Res.* **2000**, *33*, 139-145; c) J. N. Harvey, R. Poli, K. M. Smith, *Coord. Chem. Rev.* **2003**, *238–239*, 347-361; d) H. Schwarz, *Int. J. Mass Spectrom.* **2004**, *237*, 75-105; e) S. Shaik, *Int. J. Mass Spectrom.* **2013**, *354–355*, 5-14.

[24] a) M. Sievers, Y. M. Chen, P. B. Armentrout, *J. chem. phys.* **1996**, *105*, 6322-6333; b) D. Schröder, H. Schwarz, S. Shaik, in *Metal-Oxo and Metal-Peroxo Species in Catalytic Oxidations* (Ed.: B. Meunier), Springer Berlin Heidelberg, Berlin, Heidelberg, **2000**, pp. 91-123.

[25] a) R. Kretschmer, M. Schlangen, H. Schwarz, *Angew. Chem. Int. Ed.* **2013**, *52*, 6097-6101; b) M. Firouzbakht, S. Zhou, P. González-Navarrete, M. Schlangen, M. Kaupp, H. Schwarz, *Chem. Eur. J.* **2017**, *23*, 12346-12352.

[26] J. J. Carroll, J. C. Weisshaar, *J. Phys. Chem.* **1996**, *100*, 12355-12363.

[27] a) K. K. Irikura, J. Beauchamp, *J. Phys. Chem.* **1991**, *95*, 8344-8351; b) J. M. Simoes, J. Beauchamp, *Chem. Rev.* **1990**, *90*, 629-688.

[28] a) H. Schwarz, *Angew. Chem. Int. Ed.* **2003**, *42*, 4442-4454; b) K. K. Irikura, J. Beauchamp, *J. Am. Chem. Soc.* **1991**, *113*, 2769-2770.

[29] C. Trage, D. Schröder, H. Schwarz, *Chem. Eur. J.* **2005**, *11*, 619-627.

[30] M. J. T. Frisch, G. W.; Schlegel, H. B.; Scuseria, G. E.; Robb, M. A.; Cheeseman, J. R.; Scalmani, G.; Barone, V.; Mennucci, B.; Petersson, G. A.; Nakatsuji, H.; Caricato, M.; Li, X.; Hratchian, H. P.; Izmaylov, A. F.; Bloino, J.; Zheng, G.; Sonnenberg, J. L.; Hada, M.; Ehara, M.; Toyota, K.; Fukuda, R.; Hasegawa, J.; Ishida, M.; Nakajima, T.; Honda, Y.; Kitao, O.; Nakai, H.; Vreven, T.; Montgomery, J. A., Jr.; Peralta, J. E.; Ogliaro, F.; Bearpark, M.; Heyd, J. J.; Brothers, E.; Kudin, K. N.; Staroverov, V. N.; Kobayashi, R.; Normand, J.; Raghavachari, K.; Rendell, A.; Burant, J. C.; Iyengar, S. S.; Tomasi, J.; Cossi, M.; Rega, N.; Millam, J. M.; Klene, M.; Knox, J. E.; Cross, J. B.; Bakken, V.; Adamo, C.; Jaramillo, J.; Gomperts, R.; Stratmann, R. E.; Yazyev, O.; Austin, A. J.; Cammi, R.; Pomelli, C.; Ochterski, J. W.; Martin, R. L.; Morokuma, K.; Zakrzewski, V. G.; Voth, G. A.; Salvador, P.; Dannenberg, J. J.; Dapprich, S.; Daniels, A. D.; Farkas, Ö.; Foresman, J. B.; Ortiz, J. V.; Cioslowski, J.; Fox, D. J. Gaussian, Inc., Wallingford CT, **2009**.

[31] a) A. D. Becke, *J. Chem. Phys.* **1993**, *98*, 5648-5652; b) C. Lee, W. Yang, R. G. Parr, *Phys. Rev. B* **1988**, *37*, 785-789.

[32] a) F. Weigend, R. Ahlrichs, *Phys. Chem. Chem. Phys.* **2005**, *7*, 3297-3305; b) D. Andrae, U. Häußermann, M. Dolg, H. Stoll, H. Preuß, *Theor. Chem. Acc.* **1990**, *77*, 123-141.

[33] a) X. Zhang, H. Schwarz, *Chem. Eur. J.* **2010**, *16*, 5882-5888; b) X. Zhang, H. Schwarz, *Theor. Chem. Acc.* **2011**, *129*, 389-399.

[34] a) K. Fukui, *Acc. Chem. Res.* **1981**, *14*, 363-368; b) D. G. Truhlar, N. J. Kilpatrick, B. C. Garrett, *J. Chem. Phys.* **1983**, *78*, 2438-2442; c) C. Gonzalez, H. B. Schlegel, *J. Chem. Phys.* **1989**, *90*, 2154-2161.

[35] J. N. Harvey, M. Aschi, H. Schwarz, W. Koch, *Theor. Chem. Acc.* **1998**, *99*, 95-99.

Supporting Information

Thermal Carbon Dioxide and Methane Activation by $[Nb,O,H]^+$: A Combined Experimental/Theoretical Study.

ESI of a methanolic solution of $NbCl_5$ results in the formation of ions at *m/z* 110 which contain niobium, and which correspond to $[Nb,O,H]^+$ according to the mass-to-charge ratio. An experimental distinction of the two possible isomers $[ONbH]^+$ (**1**) and $[Nb(OH)]^+$ (**2**) by collision-induced dissociation (CID) is not instructive since in both cases hydrogen-atom loss is expected due to the strong Nb^+–O bond dissociation energy BDE(Nb^+–O) = 688 kJ mol^{-1}.[1] We have also carried out hydrogen-deuterium (H/D) exchange reactions with D_2 in order to identify the structure of $[Nb,O,H]^+$ generated by ESI directly via its reactivity.[2] Thus, mass-selected $[Nb,O,H]^+$ reacts with D_2 according to Equation S1 (Figure S1).

$$[Nb,O,H]^+ + D_2 \rightarrow [Nb,O,D]^+ + HD \qquad (S1)$$

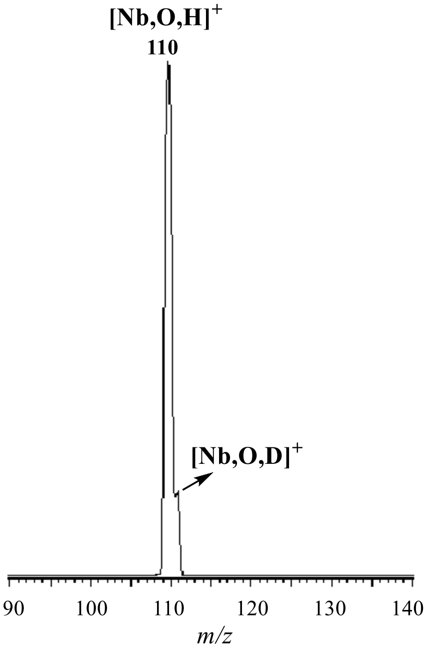

Figure S1. Mass spectra resulting from the thermal ion/molecule reaction of mass-selected $[Nb,O,H]^+$ with D_2 at a pressure of 5.8×10^{-4} mbar.

DFT calculations predict that the transition states associated with the lowest energy barriers for the H/D exchange in the case of $[ONbH]^+$ and $[Nb(OH)]^+$ are located 50.2 kJ mol^1 below and 86.8 kJ mol^{-1} above the entrance channel, respectively (Figures S2 and S3, respectively). Thus, while the H/D exchange is kinetically not possible for the $[Nb(OH)]^+$ isomer ^{2}**2**, the observed reactivity (Equation S1) provides circumstantial evidence that ^{2}**1** is generated by ESI. However, this conclusion does not rule out the co-generation and presence of unreactive isomer ^{2}**2**, similar to our previous study on the related Ta system.[3] Therefore, owing to the probability of having produced a mixture of two isomers, we considered the reactivities toward CH_4 and CO_2 of both isomers.

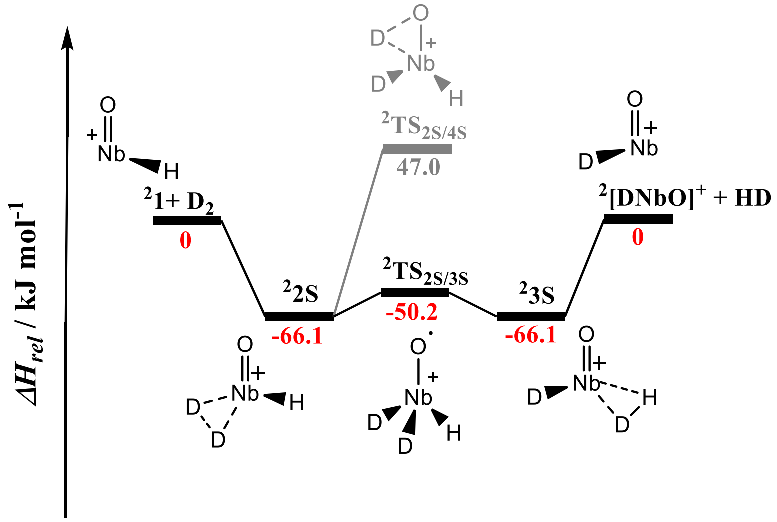
ΔH_rel / kJ mol⁻¹
²1+ D₂
0
²2S
-66.1
²TS2S/4S
47.0
²TS2S/3S
-50.2
²3S
-66.1
²[DNbO]⁺ + HD
0
O
Nb
H
D
+

Figure S2. Potential-energy profile for the reaction of ^{2}**1** with D_2 on the doublet spin-state surface. All energies, corrected for zero-point vibrational energy (ZPVE) contributions, are given in kJ mol^{-1} and marked in red (B3LYP/def2-QZVP).

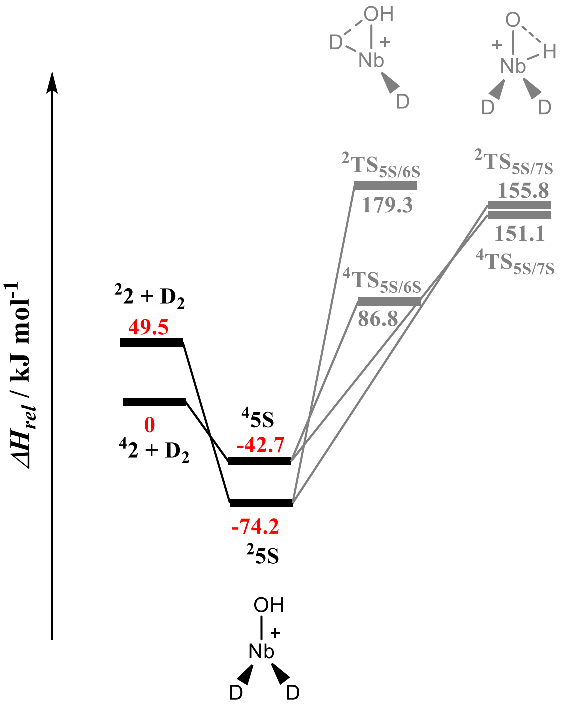
ΔH_rel / kJ mol⁻¹
²2 + D₂
49.5
0
⁴2 + D₂
⁴5S
-42.7
-74.2
²5S
²TS5S/6S
179.3
⁴TS5S/6S
86.8
²TS5S/7S
155.8
151.1
⁴TS5S/7S
OH
O
Nb
H
D
+

Figure S3. PESs of the reaction of $[Nb(OH)]^+$ with D_2. All energies, corrected for ZPVE contributions, are given in kJ mol^{-1} and marked in red (B3LYP/def2-QZVP).

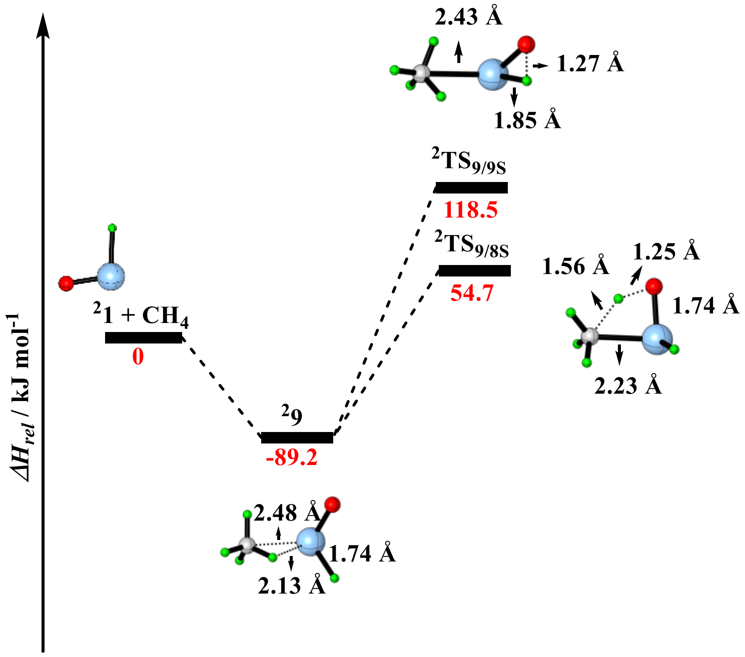
ΔH_rel / kJ mol⁻¹
²1 + CH₄
0
²9
-89.2
2.48 Å
1.74 Å
2.13 Å
²TS₉/₉S
118.5
2.43 Å
1.27 Å
1.85 Å
²TS₉/₈S
54.7
1.56 Å
1.25 Å
1.74 Å
2.23 Å

Figure S4. PES for the reaction of $[ONbH]^+$ with methane for the doublet-spin states. All energies, corrected for ZPVE contributions, are given in kJ mol^{-1} and marked in red. Note that all corresponding transition-state structures shown here in their quartet-spin states are located well above the entrance channel; therefore, TSR is not probable for these pathways. Color code: C = gray, H = green, O = red, Nb = blue.

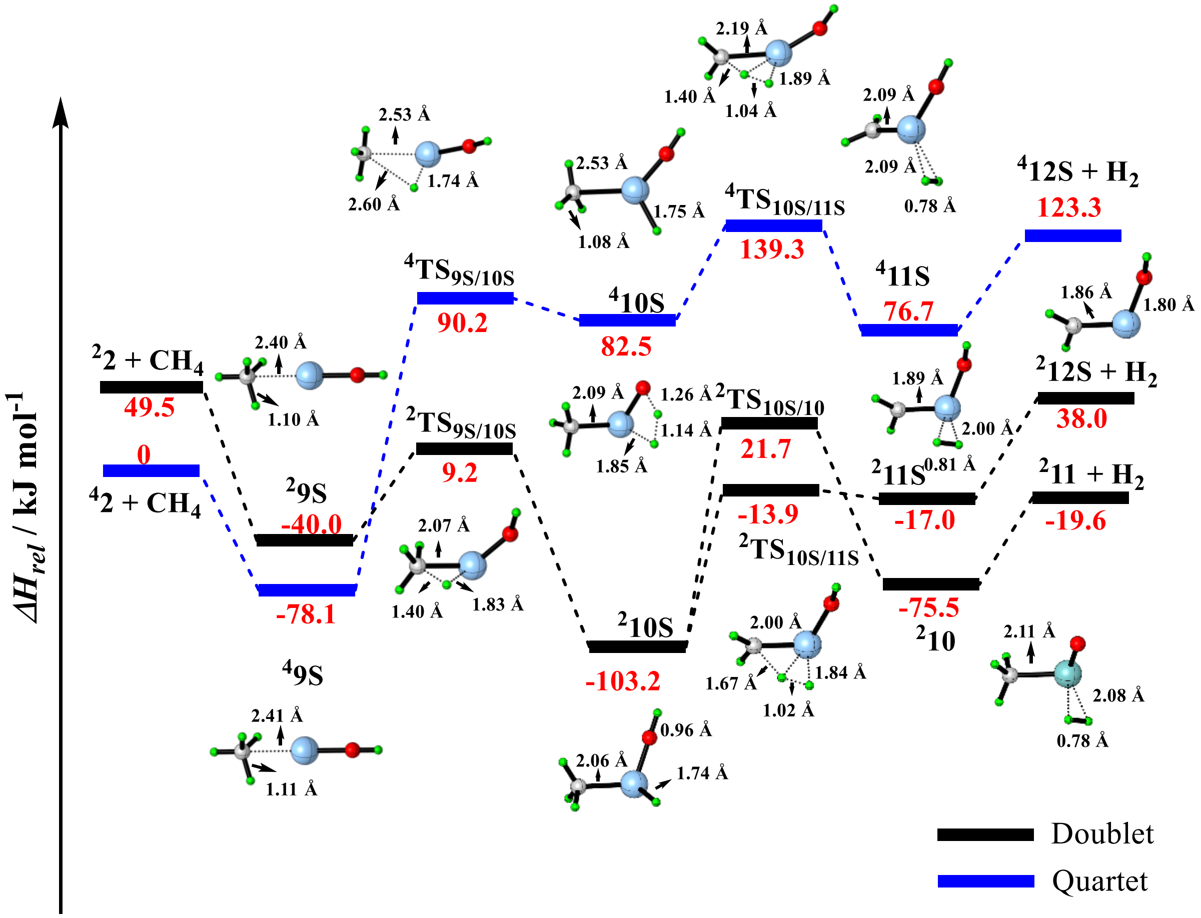

ΔH_rel / kJ mol-1
2.53 Å
1.74 Å
2.60 Å
2.19 Å
1.89 Å
1.40 Å
1.04 Å
2.09 Å
2.09 Å
0.78 Å
2.53 Å
1.75 Å
1.08 Å
4TS10S/11S
139.3
412S + H2
123.3
4TS9S/10S
90.2
410S
82.5
411S
76.7
1.86 Å
1.80 Å
22 + CH4
49.5
2.40 Å
1.10 Å
2.09 Å
1.26 Å
1.14 Å
1.85 Å
2TS10S/10
21.7
1.89 Å
2.00 Å
0.81 Å
212S + H2
38.0
0
42 + CH4
29S
-40.0
2TS9S/10S
9.2
-13.9
2TS10S/11S
211S
-17.0
211 + H2
-19.6
-78.1
2.07 Å
1.40 Å
1.83 Å
-75.5
210
49S
210S
-103.2
2.00 Å
1.67 Å
1.84 Å
1.02 Å
2.11 Å
2.08 Å
0.78 Å
2.41 Å
1.11 Å
0.96 Å
2.06 Å
1.74 Å
Doublet
Quartet

Figure S5. Potential-energy surfaces for the reaction of $[Nb(OH)]^+$ with methane for the low-spin (black) and high-spin (blue) states. All energies, corrected for ZPVE contributions, are given in kJ mol^{-1} and marked in red. Charges are omitted for the sake of clarity. Color code: C = gray, H = green, O = red, Nb = blue.

References

[1] M. R. Sievers, Y. M. Chen, P. B. Armentrout, *J. Chem. Phys.* **1996**, *105*, 6322-6333.

[2] D. B. Jacobson, B. S. Freiser, *J. Am. Chem. Soc.* **1985**, *107*, 72-80.

[3] M. Firouzbakht, N. J. Rijs, P. González-Navarrete, M. Schlangen, M. Kaupp, H. Schwarz, *Chem. Eur. J.* **2016**, *22*, 10581-10589.

Reproduced with permission from Chem. Eur. J., 2017, 23, 12346 – 12352 Copyright 1999-2018 Wiley-VCH Verlag GmbH&Co. KGaA

Reproduced with permission from Chem. Eur. J., 2017, 23, 14430 – 14433 Copyright 1999-2018 Wiley-VCH Verlag GmbH&Co. KGaA

Reproduced with permission from J. Am. Chem. Soc., 2017, 139, 6169 – 6176 Copyright 2017 American Chemical Society.

Reproduced with permission from Chem. Eur. J., 2016, 22, 10581 – 10589 Copyright 1999-2018 Wiley-VCH Verlag GmbH&Co. KGaA

Reproduced with permission from J. Catal., 2016, 343, 68 – 74 Copyright 2018 Elsevier

B. Original Papers

Paper III

ChemPubSoc Europe
DOI: 10.1002/chem.201701615
CHEMISTRY
A European Journal
Full Paper

Bond Activation

Metal-Dependent Strengthening and Weakening of M—H and M—C Bonds by an Oxo Ligand: Thermal Gas-Phase Activation of Methane by $[OMH]^+$ and $[MH]^+$ (M = Mo, Ti)

Marjan Firouzbakht, Shaodong Zhou, Patricio González-Navarrete, Maria Schlangen, Martin Kaupp,* and Helmut Schwarz*[a]

Abstract: The thermal gas-phase reactions of methane with $[OMoH]^+$ and $[MoH]^+$ were investigated by using electrospray-ionization mass spectrometry (ESI-MS) complemented by quantum-chemical calculations. In contrast to the inertness of $[MoH]^+$ towards methane, $[OMoH]^+$ activates the C—H bond to form the ionic product $[OMo(CH_3)]^+$ concomitantly with the liberation of H_2. The origin of the varying reactivities is traced back to a different influence of the oxo ligand on the Mo—C and Mo—H bonds. While the presence of this ligand weakens both the Ti—H and the Ti—CH_3 bonds, both the Mo—H and Mo—CH_3 bonds are strengthened. The more pronounced strengthening of the Mo—CH_3 bond compared to the Mo—H bond favors the exothermicity of the reaction of $[OMoH]^+$ with CH_4.

Introduction

In gas-phase experiments, atomic Nb^+ is the only second-row transition-metal cation that mediates dehydrogenation of CH_4 at ambient conditions.[1] In contrast, its neighbor in the periodic table, atomic Mo^+ in its electronic ground state, does not react with CH_4 due to its inert $5s^0 4d^5$ configuration.[2] Furthermore, while the oxo complexes of molybdenum $[MoO_x]^+$ (x = 1,2) are not able to activate methane[3] but only cleave C—H and C—C bonds of some higher hydrocarbons,[4] $[MoO_3]^+$ shows a much higher reactivity and brings about thermal methane conversion quite efficiently ($k_{exp} = 7\times 10^{-10}\ cm^3 s^{-1} molecule^{-1}$, $\phi = 70\,\%$).[5] The reactivity of $[MoO_3]^+$ can be traced back to the presence of a terminal oxyl radical that plays a crucial role in mediating thermal hydrogen-atom transfer (HAT) from hydrocarbons.[6] Likewise, apart from these examples, the sulfide complexes of molybdenum $[MoS_x]^+$ (x = 1–3) do not react with methane. However, in the case of higher hydrocarbons such as ethane, dehydrogenation has been reported.[5]

Also, the gas-phase reactivities of diatomic transition-metal hydrides $[MH]^+$ with methane have been examined both experimentally and theoretically to elucidate the effects of adding a hydride ligand to the metal center. Thus, while naked atomic metal cations like for example, Fe^+, Co^+, Ni^+, and Pd^+ do not afford thermal C—H bond activation of methane, the corresponding $[MH]^+$ ions give rise to an efficient H/CH_3 ligand exchange.[7] Other examples include the spin-allowed reaction of the oxo-ligated hydride complexes $[OTiH]^+$ and $[OTaH]^+$ with methane.[8] In the case of the titanium complexes, according to a natural bond orbital analysis (NBO),[9] while the corresponding $[TiH]^+/CH_4$ reaction is endothermic, the presence of an oxo ligand in $[OTiH]^+$ makes the diffuse 4s orbital more available for accepting electron density from C—H bonds thus allowing the thermal activation of methane.

Herein, we describe in detail the generation of $[OMoH]^+$ as well as its spin-forbidden gas-phase reaction with CH_4; moreover, we will discuss the role of the oxygen ligand with respect to methane activation by comparing it with the $[MoH]^+/CH_4$ system. Furthermore, a comparison of the role of the oxo ligand in the activation of methane by $[OMoH]^+$ versus $[OTiH]^+$ is provided. The combination of gas-phase experiments and quantum-mechanical calculations provides insight into the fundamental steps of C—H bond activation mediated by molybdenum complexes at a molecular level.

Results and Discussion

1) Generation and structural identification of $[Mo,O,H]^+$

The ions of interest have been generated in an electrospray-ionization (ESI) source (for details, see Experimental Methods) and investigated at room temperature using a multipole-based mass spectrometer.

---

[a] M. Firouzbakht, Dr. S. Zhou, Dr. P. González-Navarrete, Dr. M. Schlangen, Prof. Dr. M. Kaupp, Prof. Dr. H. Schwarz
Institut für Chemie, Technische Universität Berlin
Straβe des 17. Juni 135, 10623 Berlin (Germany)
E-mail: Martin.Kaupp@tu-berlin.de
Helmut.Schwarz@tu-berlin.de

Supporting information and the ORCID identification number(s) for the author(s) of this article can be found under https://doi.org/10.1002/chem.201701615.

Part of a Special Issue to celebrate the 150th anniversary of the German Chemical Society (GDCh). To view the complete issue, visit https://doi.org/chem.v23.50.

© 2017 Wiley-VCH Verlag GmbH & Co. KGaA, Weinheim

ESI of a methanolic solution of $MoCl_5$ or solutions of $MoOCl_4$ in H_2O/H_2O_2 results in the formation of ions at *m/z* 115 having the elemental composition $[Mo,O,H]^+$ in line with the isotope pattern.[10] As to the structures, in addition to the ion of interest, that is, $[OMoH]^+$, the formation of an hydroxide complex $[Mo(OH)]^+$ is also conceivable. An experimental distinction of these two isomers by collision-induced dissociation (CID)[11] experiments is not possible since, according to the calculations, hydrogen-atom loss is expected in both cases to occur due to the strong molybdenum–oxygen bonds $BDE(HMo^+{-}O) = 540\ kJ\,mol^{-1}$ and $BDE(Mo^+{-}OH) = 292\ kJ\,mol^{-1}$ compared to the much smaller $BDE(OMo^+{-}H) = 248\ kJ\,mol^{-1}$ and $BDE(MoO^+{-}H) = 245\ kJ\,mol^{-1}$.[12] Similarly, the otherwise powerful method of separating and characterizing isomeric species by using traveling wave ion mobility spectrometry (TWIMS)[13] failed due to insufficient generation of $[Mo,O,H]^+$ ions. Thus, we have carried out gas-phase hydrogen–deuterium (H/D) exchange reactions[14] with D_2, as well as hydroxide–ligand exchange[15] via ion/molecule reactions with $H_2{}^{18}O$ to identify the structure(s) of $[Mo,O,H]^+$. While an H/D exchange is expected in the reactions of $[OMoH]^+$, an $^{16}O/^{18}O$ exchange with water points to the presence of $[Mo(OH)]^+$. The experiments were augmented by quantum-chemical calculations (see for details, Computational Methods).

Mass-selected $[Mo,O,H]^+$, generated from ESI of a methanolic solution of $MoCl_5$, reacts with D_2 under an H/D exchange according to Equation (1) (for mass spectra, see Figure S1a). The calculations predict that the transition states associated with the lowest energy barriers for the H/D exchange in the case of $[Mo(OH)]^+$ and $[OMoH]^+$ are located at $15.0\ kJ\,mol^{-1}$ above and $67.7\ kJ\,mol^{-1}$ below the entrance channel, respectively (see Figures S2 and S3, respectively); in the case of $[OMoH]^+$, a crossing and re-crossing from the triplet to the singlet state and back is required.

$$[Mo,O,H]^+ + D_2 \rightarrow [Mo,O,D]^+ + HD \qquad (1)$$

Thus, while the H/D exchange is kinetically less likely to occur for $[Mo(OH)]^+$, the observed reactivity, [Eq. (1)], provides circumstantial evidence that $[OMoH]^+$ is present when using a methanolic solution of $MoCl_5$ for the ion generation. However, this conclusion does not rule out the co-generation of $[Mo(OH)]^+$. To further probe the possible co-generation of isomeric $[Mo,O,H]^+$ ions, we performed a $^{16}O/^{18}O$ exchange in the reaction with $H_2{}^{18}O$, Figure 1a and 1c. Thus, ions at *m/z* 115 were independently generated from $MoCl_5$ and $MoOCl_4$ and reacted with $H_2{}^{18}O$. These reactions are more complex, as described next.

For the $[Mo,O,H]^+$ ion generated from a methanolic solution of $MoCl_5$, oxygen-atom transfer (OAT) takes place concomitant with H_2 elimination, that is, the ion $[Mo,O,{}^{18}O,H]^+$ (*m/z* 133) is generated in the reaction with $H_2{}^{18}O$. Thus, instead of an $^{16}O/^{18}O$ exchange which most likely implies a hydroxide exchange as expected for $[Mo(OH)]^+$, most probably an $H/^{18}OH$ exchange takes place, thus again pointing to the presence of $[OMoH]^+$ as the reactive species. To learn more about the reaction of $[Mo,O,H]^+$ with water, also D_2O was used as a substrate (Figure 1b and Equation (2b)). Here, an H/OD exchange concurrent with HD elimination takes place; again, this is indicative for the presence of $[OMoH]^+$ rather than $[Mo(OH)]^+$.

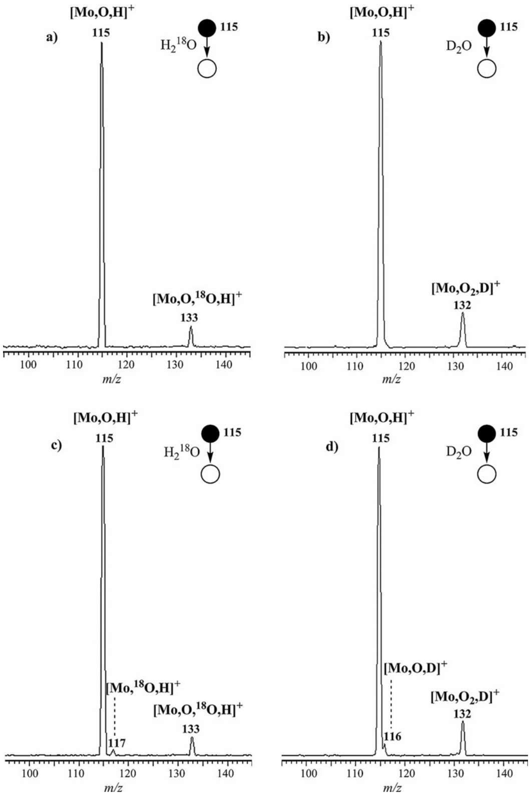

Figure 1. Mass spectra resulting from the thermal ion/molecule reaction of mass-selected $[Mo,O,H]^+$ (*m/z* 115) generated by a methanolic solution of $MoCl_5$ a) with $H_2{}^{18}O$ at a pressure of 4.8×10^{-4} mbar and b) with D_2O at a pressure of 7.4×10^{-4} mbar as well as from a solution of $MoOCl_4$ in H_2O/H_2O_2 c) with $H_2{}^{18}O$ at a pressure of 4.8×10^{-4} mbar and d) with D_2O at a pressure of 7.4×10^{-4} mbar.

$$[Mo,O,H]^+ + H_2{}^{18}O \rightarrow [Mo,O,{}^{18}O,H]^+ + H_2 \qquad (2a)$$

$$[Mo,O,H]^+ + D_2O \rightarrow [Mo,O_2,D]^+ + HD \qquad (2b)$$

The reactivity of $[Mo,O,H]^+$ ions generated from a solution of $MoOCl_4$ in H_2O/H_2O_2 towards water is different. Figures 1c and 1d detail the mass spectra for the ion/molecule reactions of *m/z* 115 ions with $H_2{}^{18}O$ and D_2O, respectively. With the former substrate, the product ions $[Mo,O,{}^{18}O,H]^+$ (*m/z* 133) and $[Mo,{}^{18}O,H]^+$ (*m/z* 117) are generated, Figure (1c), according to Equations (2a) and (3a), respectively. With the latter, $[Mo,O_2,D]^+$ (*m/z* 132), and $[Mo,O,D]^+$ (*m/z* 116), Figure (1d), are formed according to Equations (2b) and (3b). Thus, in the reactions of $[Mo,O,H]^+$ (formed from a solution of $MoOCl_4$ in H_2O/H_2O_2) with $H_2{}^{18}O$ and D_2O, $^{16}O/^{18}O$ and H/D exchanges take place, respectively, in addition to the $H/^{18}OH$ and H/OD exchanges described above. This indicates the co-generation of $[Mo(OH)]^+$ since neither $^{16}O/^{18}O$ nor H/D exchanges are observed in the reaction of $[OMoH]^+$, which is expected to be generated from a methanolic solution of $MoCl_5$ (see above). Note that these $^{16}O/^{18}O$ and H/D exchanges might be observed due to

© 2017 Wiley-VCH Verlag GmbH & Co. KGaA, Weinheim

^{16}OH/^{18}OH and OH/OD exchanges, respectively. Moreover, these results imply also that $[Mo(OH)]^+$ is not generated from a methanolic solution of $MoCl_5$. In contrast, the co-generation of $[OMoH]^+$ from $MoOCl_4$ in H_2O/H_2O_2 is not only indicated by the H/^{18}OH and H/OD exchanges but also by the H/D exchange observed for the *m/z* 115 ions from this precursor solvent in the reaction with D_2 (for mass spectra, see Figure S1b). In order to support these assumptions indicated by the experiments, quantum-chemical calculations were executed for the reactions of water with $[OMoH]^+$ and $[Mo(OH)]^+$ as reactive species.

$$[Mo,O,H]^+ + H_2{}^{18}O \rightarrow [Mo,{}^{18}O,H]^+ + H_2O \tag{3a}$$

$$[Mo,O,H]^+ + D_2O \rightarrow [Mo,O,D]^+ + DHO \tag{3b}$$

According to the DFT calculations, the $[OMoH]^+$ isomer, in its triplet ground state, is predicted to be only 4.6 kJ mol^{-1} more stable than the quintet ground state structure of $[Mo(OH)]^+$. However, the unimolecular interconversion $[OMoH]^+ \rightarrow [Mo(OH)]^+$ is inhibited by a barrier which is 201.3 kJ mol^{-1} above the $[OMoH]^+$ asymptote; thus, both species when generated by ESI are trapped in deep potential wells. The energetically lowest pathways of the degenerate oxygen exchange and the dehydrogenation reaction for the $[OMoH]^+/H_2O$ pair on the triplet potential-energy surface (PES) are shown in Figure 2a.

Starting from $[OMoH]^+$, the incoming water ligand coordinates to the metal center leading to the encounter complex ^{3}**1** (the spin state for each species is indicated by a superscript). With regard to the H/OH ligand exchange, that is, the dehydrogenation reaction observed in the experiments (Figure 1a and 1b), two different pathways have been located starting from ^{3}**1**: the multi-step sequence ^{3}**1**$\rightarrow$^{3}**3**$\rightarrow$^{3}**2**$\rightarrow$$^3[OMo(OH)]^+ + H_2$ and a σ-bond metathesis process ^{3}**1**$\rightarrow$^{3}**2**$\rightarrow$$^3[OMo(OH)]^+ + H_2$.

Dehydrogenation is exothermic by 123.5 kJ mol^{-1} (Figure 2a); however, the σ-bond metathesis reaction is kinetically much more preferred compared to the stepwise reaction (−68.2 kJ mol^{-1} for ^{3}**TS$_{1/2}$** versus −4.7 kJ mol^{-1} for ^{3}**TS$_{1/3}$**). We further probed the ability of $[OMoH]^+$ to act as precursor for the oxygen-atom exchange reaction with labeled water (Figure 1c). The two routes via ^{3}**1**$\rightarrow$^{3}**3**$\rightarrow$^{3}**1**′ and ^{3}**1**$\rightarrow$^{3}**4**$\rightarrow$^{3}**3**$\rightarrow$^{3}**1**′ are thermo-neutral, and both hydrogen atoms of the incoming water ligand are transferred to the oxo ligand of $[OMoH]^+$ (Figure 2a). The third path involves a two-state reactivity (TSR)[15] scenario and implies the isomerization $[OMoH(H_2O)]^+$ (**1**)$\rightarrow$ $[Mo(OH)(H_2O)]^+$ (**4**) via ^{3}**TS$_{1/4}$**$\rightarrow$MECP1$\rightarrow$^{5}**4**$\rightarrow$^{5}**TS$_{4/4'}$**$\rightarrow$^{5}**4**′$\rightarrow$ $^5[Mo(OH)]^+ + H_2O$ (Figure 2b). The overall process $[OMoH]^+ + H_2O \rightarrow [Mo(OH)]^+ + H_2O$ is endothermic, being 4.6 kJ mol^{-1} above the entrance channel and inhibited by a barrier (^{3}**TS$_{1/4}$**) of 9.7 kJ mol^{-1} (124.1 kJ mol^{-1} on the quintet spin surface) above the entrance channel. Altogether, the reaction pathways for the $[OMoH]^+/H_2O$ system resulting in an oxygen-atom exchange take place via ^{3}**TS$_{1/3}$** or ^{3}**TS$_{1/4}$**, and these barriers are much less favorable compared to ^{3}**TS$_{1/2}$**. Moreover, the oxygen-atom exchange reactions are thermo-neutral or endothermic by 4.6 kJ mol^{-1} relative to the entrance channel, respectively; in contrast, dehydrogenation via ^{3}**TS$_{1/2}$** is exothermic by 123.5 kJ mol^{-1}.

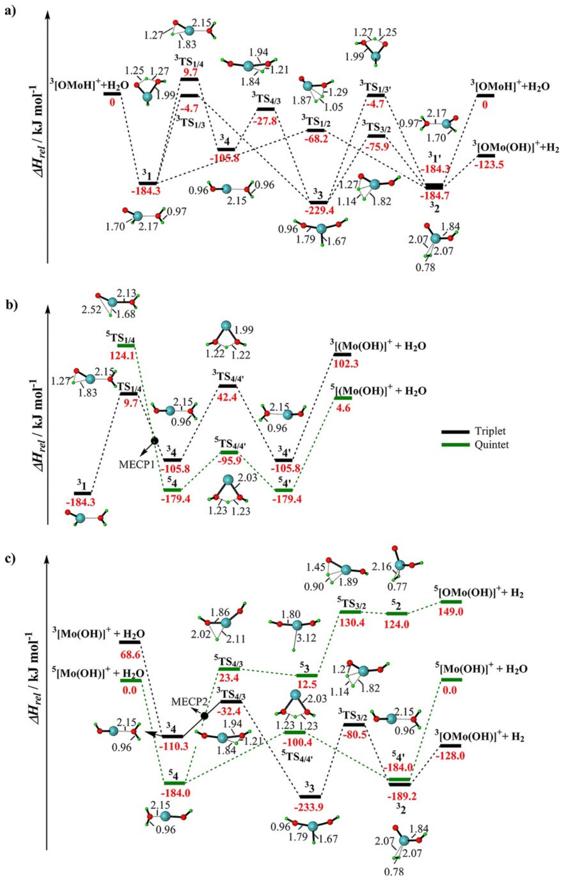
a)
ΔH_rel / kJ mol⁻¹
³[OMoH]⁺+H₂O
0
³1
-184.3
³TS1/4
9.7
-4.7
³TS1/3
³4
-105.8
³TS4/3
-27.8
³TS1/2
-68.2
³3
-229.4
³TS1/3'
-4.7
³TS3/2
-75.9
³1'
-184.3
-184.7
³2
³[OMoH]⁺+H₂O
0
³[OMo(OH)]⁺+H₂
-123.5
1.27
2.15
1.83
1.25
1.27
1.99
1.94
1.21
1.84
1.29
1.87
1.05
1.27
1.25
1.99
0.97
2.17
1.70
0.96
0.96
2.15
1.70
2.17
0.97
1.27
1.14
1.82
0.96
1.79
1.67
1.84
2.07
2.07
0.78
b)
ΔH_rel / kJ mol⁻¹
2.13
2.52
1.68
⁵TS1/4
124.1
1.27
2.15
1.83
TS1/4
9.7
MECP1
³1
-184.3
³4
-105.8
⁵4
-179.4
1.99
1.22
1.22
³TS4/4'
42.4
⁵TS4/4'
-95.9
2.03
1.23
1.23
2.15
0.96
2.15
0.96
³4'
-105.8
⁵4'
-179.4
³[(Mo(OH)]⁺ + H₂O
102.3
⁵[(Mo(OH)]⁺ + H₂O
4.6
Triplet
Quintet
c)
ΔH_rel / kJ mol⁻¹
³[Mo(OH)]⁺ + H₂O
68.6
⁵[Mo(OH)]⁺ + H₂O
0.0
2.15
0.96
³4
-110.3
⁵4
-184.0
2.15
0.96
MECP2
1.86
2.02
2.11
⁵TS4/3
23.4
³TS4/3
-32.4
1.94
1.84
1.21
1.80
3.12
⁵3
12.5
2.03
1.23
1.23
-100.4
⁵TS4/4'
³3
-233.9
0.96
1.79
1.67
1.45
0.90
1.89
2.16
0.77
⁵TS3/2
130.4
⁵2
124.0
⁵[OMo(OH)]⁺+ H₂
149.0
1.27
1.14
1.82
³TS3/2
-80.5
2.15
0.96
⁵4'
-184.0
-189.2
³2
1.84
2.07
2.07
0.78
⁵[Mo(OH)]⁺ + H₂O
0.0
³[OMo(OH)]⁺+ H₂
-128.0

Figure 2. PES for the reaction of a) and b) $[OMoH]^+$ c) $[Mo(OH)]^+$ with H_2O calculated by B3LYP/def2-TZVPD. All energies, corrected for zero-point vibrational energy (ZPVE) contributions, are given in kJ mol^{-1} and marked in red, and bond lengths in Å. Charges are omitted for the sake of brevity. H = green, O = red, Mo = blue.

Starting from $[Mo(OH)]^+$ as the reactive species, according to the computational findings, Figure 2c, the thermo-neutral, direct hydroxide-ligand exchange via σ-bond metathesis is accessible in the reaction with water via ^{5}**4**$\rightarrow$^{5}**TS$_{4/4'}$**$\rightarrow$^{5}**4**′$\rightarrow$ $^5[Mo(OH)]^+ + H_2O$ under thermal conditions (^{5}**TS$_{4/4'}$**: −100.4 kJ mol^{-1}). An alternative thermo-neutral TSR path resulting also in an oxygen exchange has been identified via ^{5}**4**$\rightarrow$MECP2$\rightarrow$^{3}**TS$_{4/3}$**$\rightarrow$^{3}**3**$\rightarrow$^{3}**TS$_{4/3'}$**$\rightarrow$MECP2$\rightarrow$^{5}**4**′$\rightarrow$$^5[Mo(OH)]^+ +$ H_2O (note that for the sake of clarity, only the first half reaction is shown in Figure 2c). In competition, dehydrogenation can take place according to a TSR scenario via ^{5}**4**$\rightarrow$MECP2$\rightarrow$^{3}**TS$_{4/3}$**$\rightarrow$^{3}**3**$\rightarrow$^{3}**TS$_{3/2}$**$\rightarrow$^{3}**2**$\rightarrow$$^3[OMo(OH)]^+ + H_2$ (Figure 2c). The relative energies of the species involved in these reaction paths are lower compared to the energy of the separated reactants, and thus thermally accessible. However, the thermo-neutral hydroxide-ligand exchange path via ^{5}**TS$_{4/4'}$** is 68.0 kJ mol^{-1} lower in energy compared to the other two pathways which both take place via ^{3}**TS$_{4/3}$**; thus, the former is kinetically favored. As a consequence, in contrast to the $[OMoH]^+$ isomer, oxygen atom exchange is preferred compared to dehydrogenation in the reaction of $[Mo(OH)]^+$ with water.

© 2017 Wiley-VCH Verlag GmbH & Co. KGaA, Weinheim

In summary, these combined experimental/computational investigations predict that when using a methanolic solution of $MoCl_5$, only a single isomer, most likely $[OMoH]^+$, is generated; in contrast, ESI of $MoOCl_4$ in H_2O/H_2O_2 presumably results in the formation of both species, $[OMoH]^+$ and $[Mo(OH)]^+$. Thus, the reactivity of clean $[OMoH]^+$ can be investigated by using a methanolic solution of $MoCl_5$.

2) C–H bond activation: reactions with methane

Figure 3a and 3b detail the mass spectra for the ion/molecule reaction of $[OMoH]^+$ (*m/z* 115), using a methanolic solution of $MoCl_5$, with methane. A fragment ion $[Mo,O,C,H_3]^+$ (*m/z* 129) is generated concomitant with the elimination of H_2, Figure 3a and Equation 4a. The relative rate constant for this reaction amounts to 3.0×10^{-10} cm^{-3} s^{-1};[16] this value corresponds to an efficiency of 30% relative to the gas-kinetic collision limit.[17]

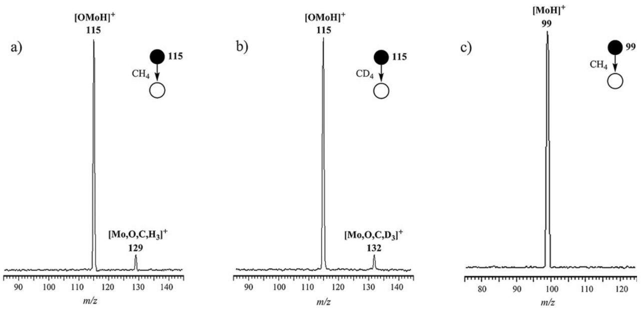

Figure 3. Mass spectra resulting from the thermal ion/molecule reaction of mass-selected $[OMoH]^+$ with a) CH_4 at a pressure of 5.1×10^{-4} mbar, with b) CD_4 at a pressure of 5.7×10^{-4} mbar and c) $[MoH]^+$ with CH_4 at a pressure of 5.4×10^{-4} mbar.

$$[OMoH]^+ + CH_4 \rightarrow [Mo,O,C,H_3]^+ + H_2 \quad (4a)$$

$$[OMoH]^+ + CD_4 \rightarrow [Mo,O,C,D_3]^+ + HD \quad (4b)$$

Labeling experiments with CD_4 result in a clean mass shift *m/z* 129→*m/z* 132, Figure 3b and Equation (4b). This is in contrast to the reaction of $[OTaH]^+$ with methane, in which eliminations of both HD and D_2 have been observed with comparable abundances; according to DFT calculations, loss of D_2 from the $[Ta,O,H]^+/CH_4$ couple is most probably due to the co-generation of $[Ta(OH)]^+$.[8b] Therefore, the exclusive elimination of HD in the reaction of $[OMoH]^+$ with CD_4 is in line with a hydride complex $[OMoH]^+$ rather than with the hydroxo complex $[Mo(OH)]^+$. We also examined the reaction of $[Mo,O,H]^+$ generated by a solution of $MoOCl_4$ in H_2O/H_2O_2 with CH_4 and CD_4 (see Figure S4). Also here, eliminations of both H_2 and HD are observed; this is in line with the assumption that both isomers $[OMoH]^+$ and $[Mo(OH)]^+$ are co-generated from $MoOCl_4$ in H_2O/H_2O_2.

DFT calculations were performed to obtain mechanistic insight into the C–H bond activation process with $[OMoH]^+$ as reactive species as well as to the origin of the non-occurrence of the methane activation by $[MoH]^+$ (Figure 4 and Figure 5). As mentioned above, the $[OMoH]^+$ species possesses a triplet ground state (with the singlet electronic state being 53.3 kJ mol^{-1} higher in energy). After the initial, barrier-free, exothermic formation of the encounter complex ^{3}**5**, the subsequent step on the triplet surface is 21.3 kJ mol^{-1} higher in energy compared to the entrance channel; therefore, a spin crossing must take place allowing the reaction to proceed thermally. Accordingly, a minimum-energy crossing point (MECP3)[18] with a relative energy of −59.5 kJ mol^{-1} has been localized prior to ^{1}**TS$_{5/6}$** (Figure 4); in the latter, a hydrogen atom is transferred to the metal center. The singlet ground state of ^{1}**TS$_{5/6}$** has been located −44.6 kJ mol^{-1} below the reactants giving rise to the intermediate ^{1}**6**. As previously demonstrated for the reaction of both $[OTiH]^+$ and $[OTaH]^+$ with CH_4, the H → CH_3 ligand-exchange corresponds mechanistically to a σ-bond metathesis process.[8] According to the calculations, molecular hydrogen cannot be eliminated in a spin-allowed process from ^{1}**6** under thermal conditions as the product pair $^1[OMo(CH_3)]^+/H_2$ is much too high in energy. In contrast, a second spin change from the singlet back to the triplet surface takes place at MECP4 (−35.4 kJ mol^{-1}); the overall process $^3[OMoH]^+ + CH_4 \rightarrow ^3[OMo(CH_3)]^+ + H_2$ is exothermic by −15.2 kJ mol^{-1}.

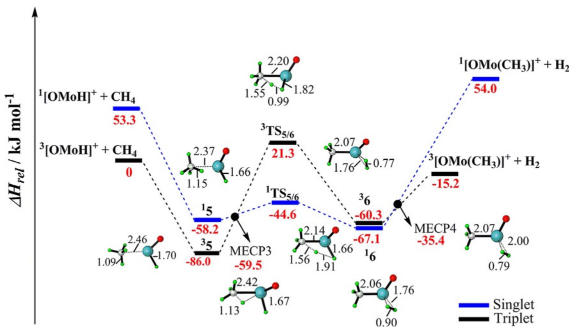

Figure 4. Simplified PESs calculated at B3LYP/def2-TZVPD level for the reaction of $[OMoH]^+$ with methane. All ZPVE-corrected energies are given in kJ mol^{-1}, and bond lengths in Å. Charges are omitted for the sake of brevity. C = gray, H = green, O = red, Mo = blue.

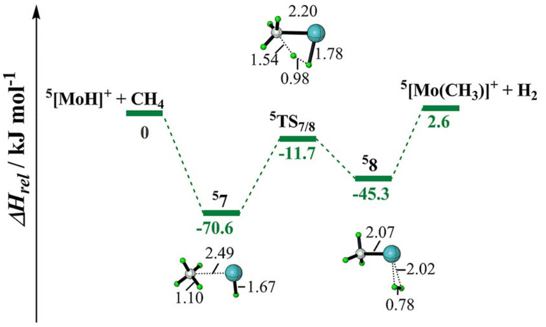

Figure 5. Simplified potential-energy surfaces calculated at B3LYP/def2-TZVPD level for the reaction of $[MoH]^+$ with methane. All ZPVE-corrected energies are given in kJ mol^{-1}, and bond lengths in Å. Charges are omitted for the sake of brevity. C = gray, H = green, Mo = blue.

The PESs for the reactions of $[MoH]^+$ with methane are shown in Figure (5). For the reaction of diatomic $[MoH]^+$ with CH_4, a reaction pathway was located on the quintet PESs. Since the singlet and triplet PESs are much higher in energy, the discussion will be confined to the quintet surface. The overall process $^5[MoH]^+ + CH_4 \rightarrow {}^5[Mo(CH_3)]^+ + H_2$ is endothermic by 2.6 kJ mol^{-1} (Figure 5).

In this context it should be mentioned that B3LYP correctly predicts the order of BDE(Mo^+–H) > BDE(Mo^+–CH_3) as compared to the experimental data (see Table S2 in the Supporting Information), but underestimates the absolute difference and thus the endothermicity of the ligand switch shown in Figure 5. However, when using the CCSD(T) method and various DFT functionals (see Computational Methods), the overall processes have in all cases been predicted to be endothermic and show qualitatively the same trend (see Figure S5). This is in line with the experimental results which show no reaction for the $[MoH]^+/CH_4$ couple (Figure (3c)).

As discussed previously,[8a] the higher reactivity of $[OTiH]^+/CH_4$ as compared to that of $[TiH]^+/CH_4$ has been attributed to a ligand effect of the oxygen atom. While the presence of the oxo ligand *weakens* both the Ti–H and the Ti–CH_3 bonds, the effect is more pronounced for the former. The situation is reversed for the analogous Mo systems. According to the B3LYP/def2-TZVPD calculations, both the Mo–H and Mo–CH_3 bonds are *strengthened* (BDE(OMo^+–H) = 259.3 kJ mol^{-1} and BDE(OMo^+–CH_3) = 267.8 kJ mol^{-1}) as compared with BDE(Mo^+–H) = 201.2 kJ mol^{-1} and BDE(Mo^+–CH_3) = 191.1 kJ mol^{-1}; thus, the more pronounced strengthening of the Mo–CH_3 bond (by 76.7 kJ mol^{-1}) than that of the Mo–H bond (by 58.1 kJ mol^{-1}) favors the exothermicity of the system $[OMoH]^+/CH_4$. Qualitatively, such differential strengthening can be explained partially by different amounts of exchange energy that are lost upon binding due to the decreasing number of unpaired nonbonding electrons ($^6Mo^+ + X \rightarrow {}^5[MoX]^+$ (X = H, CH_3) versus $^4[MoO]^+ + X \rightarrow {}^3[OMoX]^+$ (X = H, CH_3)); therefore, the Mo–H^+ and Mo–C^+ bonds are stronger in the case of $[OMoX]^+$ (X = H, CH_3) as compared to $[MoX]^+$ (X = H, CH_3).[19] Additionally, natural localized molecular orbital (NLMO) analyses[20] indicate that the Mo(5s)-contributions to the α-spin-channel Mo–X bonding NLMO are substantially enhanced by oxo substitution (Table S1 in Supporting Information; note that the trend for $[OTiX]^+$ vs. $[TiX]^+$ is just the reverse[7b]). This "spin-polarized rehybridization" appears to contribute to the strengthening of the Mo–X bonds by oxo substitution, and it is apparent also in the shapes of the relevant canonical MOs (see Figure S6 in the Supporting Information). Note the large spin polarization of the σ-bonding MOs 10 and 14 for $[OMoH]^+$ and $[OMoCH_3]^+$, respectively (no such effect is present for the corresponding Ti systems; Figure S7).

Conclusion

In summary, in this combined experimental/computational study we present mechanistic aspects of methane activation by $[OMoH]^+$ via a TSR[21] scenario; the reactivity of $[OMoH]^+$ versus the hydride $[MoH]^+$ reveals a remarkable ligand effect. According to our present study, $[MoH]^+$ does not react with CH_4 under thermal conditions. However, the introduction of an oxygen atom as a ligand to form $[OMoH]^+$ results in the generation of an active species, in that $[OMoH]^+$ activates methane spontaneously. The different reactivities are caused by the differential strengthening of the Mo–C compared to the Mo–H bond upon oxo substitution. Unlike the oxo-ligand effect in $[OTiH]^+$ reported previously, addition of oxygen to the molybdenum–hydride species does not follow a similar trend. While the presence of this ligand weakens both the Ti–H and the Ti–CH_3 bonds, the situation is different for the analogous Mo systems and both the Mo–H and Mo–CH_3 bonds are strengthened. This can be explained by different amounts of exchange energy that are lost upon binding through adding an oxo-ligand as well as the large spin polarization of and Mo(5s) admixture to the σ-bonding for $[OMoH]^+$ and $[OMoCH_3]^+$ compared to the corresponding Ti systems.

While the thermal reactions of $[OMoH]^+$ with methane have some features in common with $[OMH]^+$ (M = Ti, V, Ta), for example, σ-bond metathesis,[8] fundamental mechanistic differences exist with regard to the operation of a multi-state reactivity scenario for the molybdenum system.

Experimental and Computational Methods

The experiments were performed with a VG BIO-Q mass spectrometer of QHQ configuration (Q: quadrupole, H: hexapole) equipped with an ESI source as described in detail before.[22] Millimolar solutions of $MoCl_5$ and $MoOCl_4$ in pure methanol and in H_2O/H_2O_2 respectively, were introduced through a fused-silica capillary to the ESI source by a syringe pump (ca. 4 μL min^{-1}) to produce the metal–complex cations,$[Mo,O,H]^+$. Moreover, the cationic complex, $[MoH]^+$, was formed from a millimolar solution of $MoCl_5$ in pure methanol. Nitrogen was used as a nebulizing and drying gas at a source temperature of 80 °C. Maximal yields of the desired complexes were achieved by adjusting the cone voltage (U_c) between 70 and 100 V; U_c determines the degree of collisional activation of the incident ions in the transfer from the ESI source to the mass spectrometer. The identity of the ions was confirmed by comparison with the expected isotope patterns.[10] The ion/molecule reactions of the complexes with the substrates were probed at a collision energy (E_{lab}) set to nominally 0 eV, which in conjunction with the ca. 0.4 eV kinetic energy width of the parent ion at peak half height allows the investigation of quasi thermal reactions, as demonstrated previously.[23]

As we mentioned above, in the case of the $[MoH]^+/CH_4$ system, no signal has been observed that indicates a reaction (Figure 3 c). The upper limit for the rate coefficient, derived from the signal-to-noise ratio and the Pt+/CH4 system,[16] amounts to 9.1×10^{-12} cm^{-3}s^{-1}, corresponding to an efficiency of less than 0.1 % relative to the gas-kinetic collision limit.

The travelling-wave ion-mobility spectrometry (TWIMS) experiments were carried out with the same solutions as described above, using a Synapt G2 mass spectrometer (Waters, Manchester) fitted with a standard ESI source, as previously described.[13]

Structure optimizations were performed with the Gaussian09 program package[24] using unrestricted DFT calculations with the B3LYP[25] functional together with an def2-TZVPD including a quasirelativistic, energy-adjusted effective core potential (ECP) and an associated valence basis set for the molybdenum atom.[26] Note that previous studies achieved rather good agreement between experiment and theory for gas-phase reactions of Mo with B3LYP.[4b,27] Additional calculations with BHLYP,[28] M06[29] and TPSSH[30] functionals utilizing the same basis set, as well as CCSD(T)/aug-cc-pvtz(pp)//B3LYP/def2-TZVPD,[31] have been carried out for comparison and to probe the reliability of the results. Note that in case of single point CCSD(T) calculations, an aug-cc-pvtz-pp valence basis set for Mo including an energy-consistent, small-core pseudopotential adjusted in multiconfiguration Dirac-Hartree–Fock calculations[32] as well as aug-cc-pvtz all-electron basis sets for the remaining atoms have been used.[33] All energies are corrected for (unscaled) zero-point vibrational energy contributions. We have monitored various indicators for multi-reference character, such as total atomization energy (%TAE)[34] diagnostics. The results show that some of the species studied exhibit a %TAE above 5% (however, still less than 10%[35]), which indicates at least borderline multi-reference character for some structures. We have also found a rather large variation of certain key energy quantities with computational level (Table S2 in Supporting Information). For example, the larger effect of the oxo ligand on the $[\mathrm{OMo^+{-}CH_3}]$ BDE compared to that on the $[\mathrm{OMo^+{-}H}]$ BDE (see above) in coupled-cluster calculations is mainly due to the low CCSD(T)-level $\mathrm{Mo^+{-}CH_3}$ BDE in $[\mathrm{MoCH_3}]^+$ in comparison to the experimental data, Table S2. We therefore re-evaluated the BDEs in the simple $[\mathrm{MoH}]^+$ and $[\mathrm{MoCH_3}]^+$ cations using multi-reference perturbation theory. Single-point *N*-Electron Valence-State Perturbation Theory (NEVPT2)[36] calculations were done with the ORCA program,[37] at B3LYP/def2-TZVPD structures, using CASSCF[38] reference wave functions with active spaces of 10 electrons in 10 orbitals for $[\mathrm{MoCH_3}]^+$ and 6 electrons in 6 orbitals for $[\mathrm{MoH}]^+$. These calculations provided $\mathrm{BDE(Mo^+{-}CH_3)} = 142.5\ \mathrm{kJ\,mol^{-1}}$ and $\mathrm{BDE(Mo^+{-}H)} = 134.5\ \mathrm{kJ\,mol^{-1}}$. The former is lower and the latter is larger than the corresponding single-reference CCSD(T) value. This gives the opposite trend than the experimental results in which $\mathrm{BDE(Mo^+{-}H)}$ is larger than $\mathrm{BDE(Mo^+{-}CH_3)}$[4b] ($\mathrm{BDE(Mo^+{-}CH_3)} = 151.5 \pm 8.7\ \mathrm{kJ\,mol^{-1}}$ and $\mathrm{BDE(Mo^+{-}H)} = 166.3 \pm 5.8\ \mathrm{kJ\,mol^{-1}}$, see Table S2). Thus, while CCSD(T) is not reliable getting the relative balance between Mo-H and Mo-C BDEs as compared to the experimental BDEs, NEVPT2 with currently accessible active spaces gets the balance but undershoots the binding energies and does so in an inconsistent way. Moreover, the DFT functionals evaluated give values close to the balance, with acceptable relative magnitude compared to the experimental data, albeit in many cases they overshoot somewhat. Therefore, we resorted to using a comparison of three different hybrid DFT approaches (B3LYP, BHLYP, M06) known to usually be reliable for Mo systems,[39] and the CCSD(T) energetics, to judge the reliability of the computed energy profiles (Table S3). While the energy profiles differ to some extent for the activation of methane by $[\mathrm{OMoH}]^+$, the main feature of a larger strengthening of the $\mathrm{Mo{-}CH_3}$ compared to the Mo–H bond by oxo substitution (in line with the experimental BDEs) is retained at all levels. That is, the molybdenum carbon BDE in $[\mathrm{OMo^+{-}CH_3}]$ is strengthened compared to that in $[\mathrm{Mo^+{-}CH_3}]$ by 153.3/76.7/116.7/93.2 $\mathrm{kJ\,mol^{-1}}$ at CCSD(T)/B3LYP/M06/BHLYP levels, respectively, whereas the molybdenum–hydrogen BDE in $[\mathrm{OMo^+{-}H}]$ is strengthened compared to $[\mathrm{Mo^+{-}H}]$ by 75.8/58.1/98.8/67.9 $\mathrm{kJ\,mol^{-1}}$. As a result, the qualitative mechanisms for methane activation shown in Figure 4 using B3LYP/def2-TZVPD remain unaltered compared to the remaining three computational levels. We thus regard this level as reasonably reliable, in spite of some differences in the detailed energetics.

Intrinsic reaction coordinate (IRC) calculations were performed to link transition structures with the corresponding minima.[40] For those reactions that involve more than a single spin surface, the two-state reactivity (TSR) paradigm[21] has been considered. The minimum-energy crossing points (MECPs) were calculated by using the algorithm developed by Harvey et al.[18] Natural localized molecular orbital (NLMO) analyses[20] were carried out on the ground-state structures at B3LYP/def2-TZVPD level, using the built-in NBO3.1 module of Gaussian 09.

Acknowledgements

This work has been supported by the Fonds der Chemischen Industrie and the Deutsche Forschungsgemeinschaft (DFG), including support from the UniCat cluster of excellence. For computational resources and support, the Fakultät für Mathematik und Naturwissenschaften at the Technische Universität Berlin is acknowledged. Dr. P.G.-N. is grateful to the Alexander von Humboldt Foundation for having received a postdoctoral fellowship. Dr. Toni Maier, Dr. Robert Kretschmer and Dr. Nicole Rijs are appreciated for suggestions and comments. We are grateful to Dr. Thomas Weiske for technical assistance.

Conflict of interest

The authors declare no conflict of interest.

Keywords: bond activation · gas-phase study · ligand effect · methane · molybdenum complex

[1] A. Shayesteh, V. V. Lavrov, G. K. Koyanagi, D. K. Bohme, *J. Phys. Chem. A* **2009**, *113*, 5602 – 5611.

[2] J. B. Schilling, J. L. Beauchamp, *Organometallics* **1988**, *7*, 194 – 199.

[3] C. J. Cassady, S. W. McElvany, *Organometallics* **1992**, *11*, 2367 – 2377.

[4] a) E. F. Fialko, A. V. Kikhtenko, V. B. Goncharov, K. I. Zamaraev, *J. Phys. Chem. A* **1997**, *101*, 8607 – 8613; b) P. B. Armentrout, *J. Phys. Chem. A* **2006**, *110*, 8327 – 8338; c) P. B. Armentrout, *Organometallics* **2007**, *26*, 5473 – 5485; d) N. J. Mayhall, K. Raghavachari, *J. Phys. Chem. A* **2007**, *111*, 8211 – 8217.

[5] I. Kretzschmar, A. Fiedler, J. N. Harvey, D. Schröder, H. Schwarz, *J. Phys. Chem. A* **1997**, *101*, 6252 – 6264.

[6] For reviews, see: a) D. Schröder, H. Schwarz, *Angew. Chem. Int. Ed. Engl.* **1995**, *34*, 1973 – 1995; *Angew. Chem.* **1995**, *107*, 2126 – 2150; b) N. Dietl, M. Schlangen, H. Schwarz, *Angew. Chem. Int. Ed.* **2012**, *51*, 5544 – 5555; *Angew. Chem.* **2012**, *124*, 5638 – 5650; c) W. Lai, C. Li, H. Chen, S. Shaik, *Angew. Chem. Int. Ed.* **2012**, *51*, 5556 – 5578; *Angew. Chem.* **2012**, *124*, 5652 – 5676; d) H. Schwarz, *Isr. J. Chem.* **2014**, *54*, 1413 – 1431; e) H. Schwarz, *Chem. Phys. Lett.* **2015**, *629*, 91 – 101.

[7] a) T. J. Carlin, L. Sallans, C. J. Cassady, D. B. Jacobson, B. S. Freiser, *J. Am. Chem. Soc.* **1983**, *105*, 6320 – 6321; b) Q. Zhang, M. T. Bowers, *J. Phys. Chem. A* **2004**, *108*, 9755 – 9761; c) M. Schlangen, D. Schröder, H. Schwarz, *Angew. Chem. Int. Ed.* **2007**, *46*, 1641 – 1644; *Angew. Chem.* **2007**, *119*, 1667 – 1671; d) M. Schlangen, H. Schwarz, *Angew. Chem. Int. Ed.* **2007**, *46*, 5614 – 5617; *Angew. Chem.* **2007**, *119*, 5711 – 5715.

[8] a) R. Kretschmer, M. Schlangen, H. Schwarz, *Angew. Chem. Int. Ed.* **2013**, *52*, 6097 – 6101; *Angew. Chem.* **2013**, *125*, 6213 – 6217; b) M. Firouzbakht, N. J. Rijs, P. González-Navarrete, M. Schlangen, M. Kaupp, H. Schwarz, *Chem. Eur. J.* **2016**, *22*, 10581 – 10589.

[9] F. Weinhold, C. R. Landis, *Discovering Chemistry with Natural Bond Orbitals*, Wiley, Hoboken, **2012**.

[10] Scientific Instrument Service: Isotope Distribution Calculator and Mass Spec Plotter: http://www.sisweb.com/mstools/isotope.htm.

[11] K. Levsen, H. Schwarz, *Mass Spectrom. Rev.* **1983**, *2*, 77 – 148.

© 2017 Wiley-VCH Verlag GmbH & Co. KGaA, Weinheim

[12] The experimentally determined hydrogen-atom affinity of $[MoO]^+$ amounts to 254 kJ mol^{-1}; see: X. Zhang, H. Schwarz, *Theor. Chem. Acc.* **2011**, *129*, 389–399, and references therein.

[13] a) N. J. Rijs, T. Weiske, M. Schlangen, H. Schwarz, *Chem. Phys. Lett.* **2014**, *608*, 408–424; b) N. J. Rijs, T. Weiske, M. Schlangen, H. Schwarz, *Anal. Chem.* **2015**, *87*, 9769–9776.

[14] D. B. Jacobson, B. S. Freiser, *J. Am. Chem. Soc.* **1985**, *107*, 72–80.

[15] J. R. Khusnutdinova, P. Y. Zavalij, A. N. Vedernikov, *Organometallics* **2007**, *26*, 3466–3483.

[16] Note that the absolute rate coefficient for the reaction cannot be measured directly in our multipole setup; rather, the rate coefficient was determined by using the $[Pt]^+/CH_4$ system as a reference: a) C. Heinemann, R. Wesendrup, H. Schwarz, *Chem. Phys. Lett.* **1995**, *239*, 75–83; b) M. Pavlov, M. R. A. Blomberg, P. E. M. Siegbahn, R. Wesendrup, C. Heinemann, H. Schwarz, *J. Phys. Chem. A* **1997**, *101*, 1567–1579; c) X.-G. Zhang, R. Liyanage, P. B. Armentrout, *J. Am. Chem. Soc.* **2001**, *123*, 5563–5575; d) D. Schröder, H. Schwarz, *Can. J. Chem.* **2005**, *83*, 1936–1940.

[17] a) M. P. Langevin, *Ann. Chim. Phys* **1905**, *8*, 245–288; b) G. Gioumousis, D. P. Stevenson, *J. Chem. Phys.* **1958**, *29*, 294–299.

[18] J. N. Harvey, M. Aschi, H. Schwarz, W. Koch, *Theor. Chem. Acc.* **1998**, *99*, 95–99.

[19] G. Ohanessian, W. A. Goddard, *Acc. Chem. Res.* **1990**, *23*, 386–392.

[20] a) A. E. Reed, F. Weinhold, *J. Chem. Phys.* **1985**, *83*, 1736–1740; b) A. E. Reed, L. A. Curtiss, F. Weinhold, *Chem. Rev.* **1988**, *88*, 899–926.

[21] a) P. B. Armentrout, *Science* **1991**, *251*, 175–179; b) D. Schröder, S. Shaik, H. Schwarz, *Acc. Chem. Res.* **2000**, *33*, 139–145; c) J. N. Harvey, R. Poli, K. M. Smith, *Coord. Chem. Rev.* **2003**, *238–239*, 347–361; d) H. Schwarz, *Int. J. Mass Spectrom.* **2004**, *237*, 75–105; e) S. Shaik, *Int. J. Mass Spectrom.* **2013**, *354–355*, 5–14.

[22] C. Trage, D. Schröder, H. Schwarz, *Chem. Eur. J.* **2005**, *11*, 619–627.

[23] a) D. Schröder, H. Schwarz, S. Schenk, E. Anders, *Angew. Chem. Int. Ed.* **2003**, *42*, 5087–5090; *Angew. Chem.* **2003**, *115*, 5241–5244; b) D. Schröder, M. Engeser, H. Schwarz, E. C. E. Rosenthal, J. Döbler, J. Sauer, *Inorg. Chem.* **2006**, *45*, 6235–6245; c) N. Dietl, T. Wende, K. Chen, L. Jiang, M. Schlangen, X. Zhang, K. R. Asmis, H. Schwarz, *J. Am. Chem. Soc.* **2013**, *135*, 3711–3721.

[24] M. J. Frisch, G. W. Trucks, H. B. Schlegel, G. E. Scuseria, M. A. Robb, J. R. Cheeseman, G. Scalmani, V. Barone, B. Mennucci, G. A. Petersson, H. Nakatsuji, M. Caricato, X. Li, H. P. Hratchian, A. F. Izmaylov, J. Bloino, G. Zheng, J. L. Sonnenberg, M. Hada, M. Ehara, K. Toyota, R. Fukuda, J. Hasegawa, M. Ishida, T. Nakajima, Y. Honda, O. Kitao, H. Nakai, T. Vreven, J. A. J. Montgomery, J. E. Peralta, F. Ogliaro, M. Bearpark, J. J. Heyd, E. Brothers, K. N. Kudin, V. N. Staroverov, R. Kobayashi, J. Normand, K. Raghavachari, A. Rendell, J. C. Burant, S. S. Iyengar, J. Tomasi, M. Cossi, N. Rega, J. M. Millam, M. Klene, J. E. Knox, J. B. Cross, V. Bakken, C. Adamo, J. Jaramillo, R. Gomperts, R. E. Stratmann, O. Yazyev, A. J. Austin, R. Cammi, C. Pomelli, J. W. Ochterski, R. L. Martin, K. Morokuma, V. G. Zakrzewski, G. A. Voth, P. Salvador, J. J. Dannenberg, S. Dapprich, A. D. Daniels, Ö. Farkas, J. B. Foresman, J. V. Ortiz, J. Cioslowski, Fox, I. D. J. Gaussian, Wallingford CT, **2009**.

[25] a) A. D. Becke, *J. Chem. Phys.* **1993**, *98*, 5648–5652; b) C. Lee, W. Yang, R. G. Parr, *Phys. Rev. B* **1988**, *37*, 785–789.

[26] a) D. Andrae, U. Häußermann, M. Dolg, H. Stoll, H. Preuß, *Theor. Chim. Acta* **1990**, *77*, 123–141; b) D. Rappoport, F. Furche, *J. Chem. Phys.* **2010**, *133*, 134105.

[27] a) P. B. Armentrout, *Organometallics* **2007**, *26*, 5486–5500; b) P. González-Navarrete, M. Schlangen, X.-N. Wu, H. Schwarz, *Chem. Eur. J.* **2016**, *22*, 3077–3083; c) P. González-Navarrete, M. Schlangen, H. Schwarz, *Struct. Chem.* **2017**, *28*, 403–413.

[28] A. D. Becke, *J. Chem. Phys.* **1993**, *98*, 1372–1377.

[29] Y. Zhao, D. G. Truhlar, *Theor. Chem. Acc.* **2008**, *120*, 215–241.

[30] a) J. Tao, J. P. Perdew, V. N. Staroverov, G. E. Scuseria, *Phys. Rev. Lett.* **2003**, *91*, 146401; b) V. N. Staroverov, G. E. Scuseria, J. Tao, J. P. Perdew, *J. Chem. Phys.* **2003**, *119*, 12129–12137; c) V. N. Staroverov, G. E. Scuseria, J. Tao, J. P. Perdew, *J. Chem. Phys.* **2004**, *121*, 11507.

[31] J. A. Pople, M. Head-Gordon, K. Raghavachari, *J. Chem. Phys.* **1987**, *87*, 5968–5975.

[32] K. A. Peterson, D. Figgen, M. Dolg, H. Stoll, *J. Chem. Phys.* **2007**, *126*, 124101.

[33] T. H. Dunning, *J. Chem. Phys.* **1989**, *90*, 1007–1023.

[34] A. Karton, *WIREs Comput. Mol. Sci.* **2016**, *6*, 292–310.

[35] J. Wang, S. Manivasagam, A. K. Wilson, *J. Chem. Theory Comput.* **2015**, *11*, 5865–5872.

[36] a) C. Angeli, R. Cimiraglia, S. Evangelisti, T. Leininger, J.-P. Malrieu, *J. Chem. Phys.* **2001**, *114*, 10252–10264; b) C. Angeli, R. Cimiraglia, J.-P. Malrieu, *J. Chem. Phys.* **2002**, *117*, 9138–9153.

[37] F. Neese, *WIREs Comput. Mol. Sci.* **2012**, *2*, 73–78.

[38] B. O. Roos, P. R. Taylor, P. E. M. Siegbahn, *Chem. Phys.* **1980**, *48*, 157–173.

[39] a) L. Hu, H. Chen, *J. Chem. Theory Comput.* **2015**, *11*, 4601–4614; b) F. A. Lima, R. Bjornsson, T. Weyhermuller, P. Chandrasekaran, P. Glatzel, F. Neese, S. DeBeer, *Phys. Chem. Chem. Phys.* **2013**, *15*, 20911–20920.

[40] a) K. Fukui, *Acc. Chem. Res.* **1981**, *14*, 363–368; b) D. G. Truhlar, N. J. Kilpatrick, B. C. Garrett, *J. Chem. Phys.* **1983**, *78*, 2438–2442; c) C. Gonzalez, H. B. Schlegel, *J. Chem. Phys.* **1989**, *90*, 2154–2161.

Manuscript received: April 11, 2017
Accepted manuscript online: May 26, 2017
Version of record online: June 21, 2017

© 2017 Wiley-VCH Verlag GmbH & Co. KGaA, Weinheim

CHEMISTRY
A European Journal

Supporting Information

Metal-Dependent Strengthening and Weakening of M—H and M—C Bonds by an Oxo Ligand: Thermal Gas-Phase Activation of Methane by $[OMH]^+$ and $[MH]^+$ (M = Mo, Ti)

Marjan Firouzbakht, Shaodong Zhou, Patricio González-Navarrete, Maria Schlangen, Martin Kaupp,* and Helmut Schwarz*[a]

chem_201701615_sm_miscellaneous_information.pdf

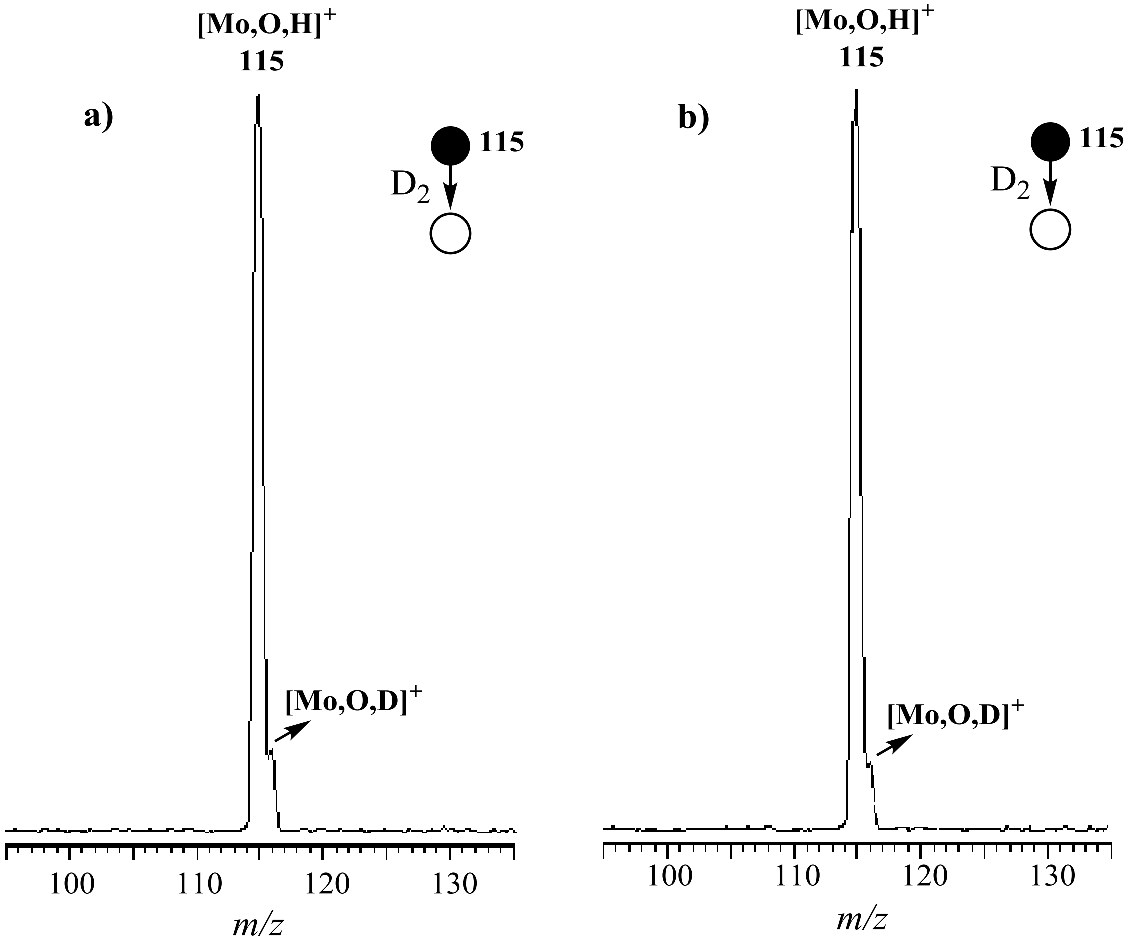

Figure S1. Mass spectra resulting from the thermal ion/molecule reaction of mass-selected $[Mo,O,H]^+$ (*m/z* 115) generated by a) a methanolic solution of $MoCl_5$ with D_2 at a pressure of 4.6×10^{-4} mbar, and b) a solution of $MoOCl_4$ in H_2O/H_2O_2 with D_2 at a pressure of 4.9×10^{-4} mbar.

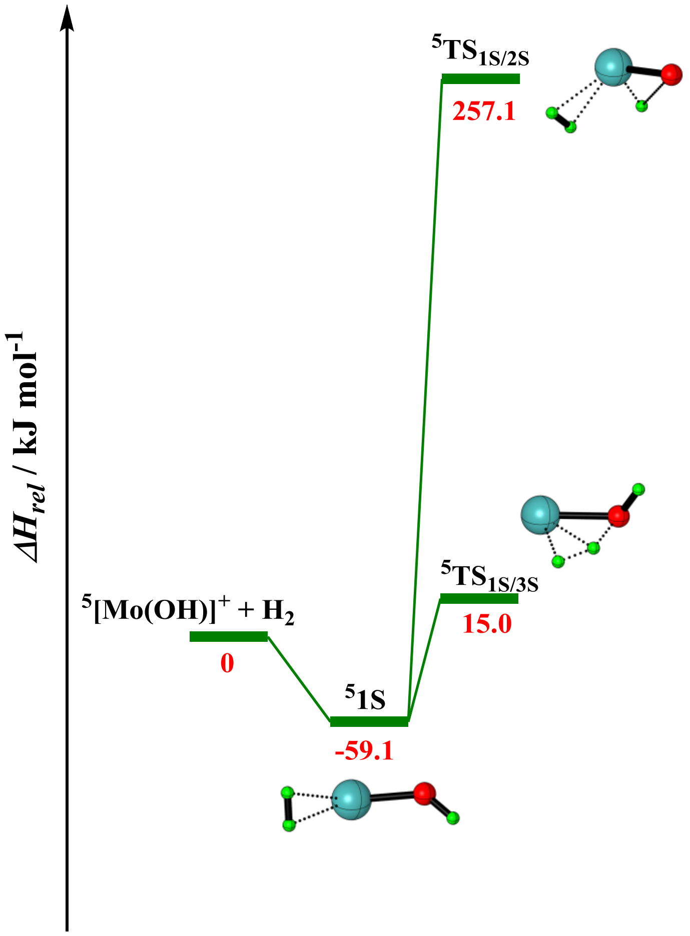

Figure S2. PESs of the reaction of $[Mo(OH)]^+$ with hydrogen (B3LYP/def2-TZVPD). All ZPVE-corrected energies are given in kJ mol^{-1} and marked in red. Note that all corresponding transition-state structures shown here in their singlet- and triplet-spin states are located well above the entrance channel; therefore, TSR is not probable for these pathways. H = green, O = red, Mo = blue.

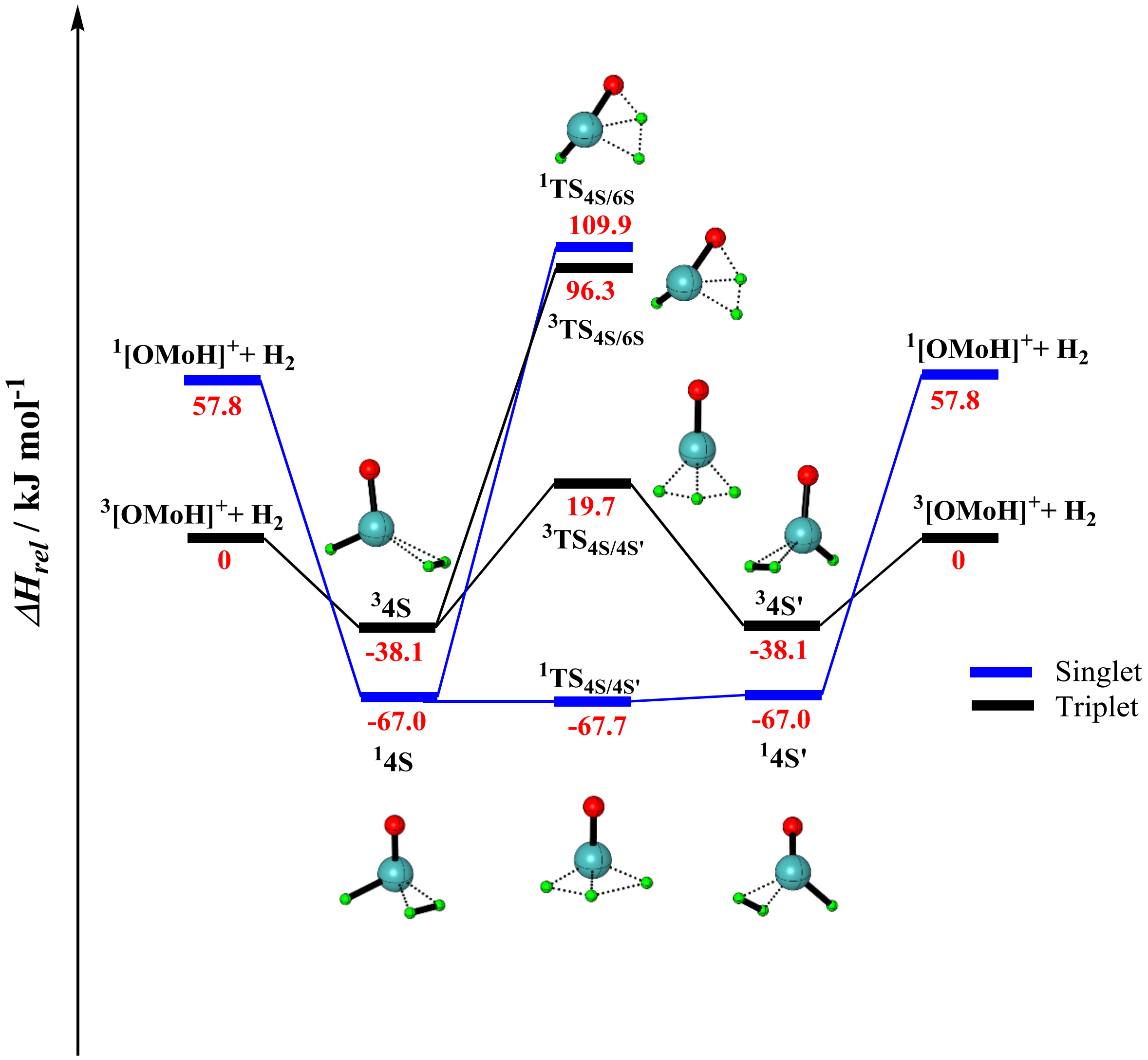

ΔH_rel / kJ mol^-1
^1[OMoH]^+ + H_2
57.8
^3[OMoH]^+ + H_2
0
^1TS_4S/6S
109.9
96.3
^3TS_4S/6S
^3TS_4S/4S'
19.7
^34S
-38.1
^34S'
-38.1
^1TS_4S/4S'
-67.0
-67.7
-67.0
^14S
^14S'
^1[OMoH]^+ + H_2
57.8
^3[OMoH]^+ + H_2
0
Singlet
Triplet

Figure S3. PESs of the reaction of $[OMoH]^+$ with hydrogen (B3LYP/def2-TZVPD). All ZPVE-corrected energies are given in kJ mol^{-1} and marked in red. H = green, O = red, Mo = blue.

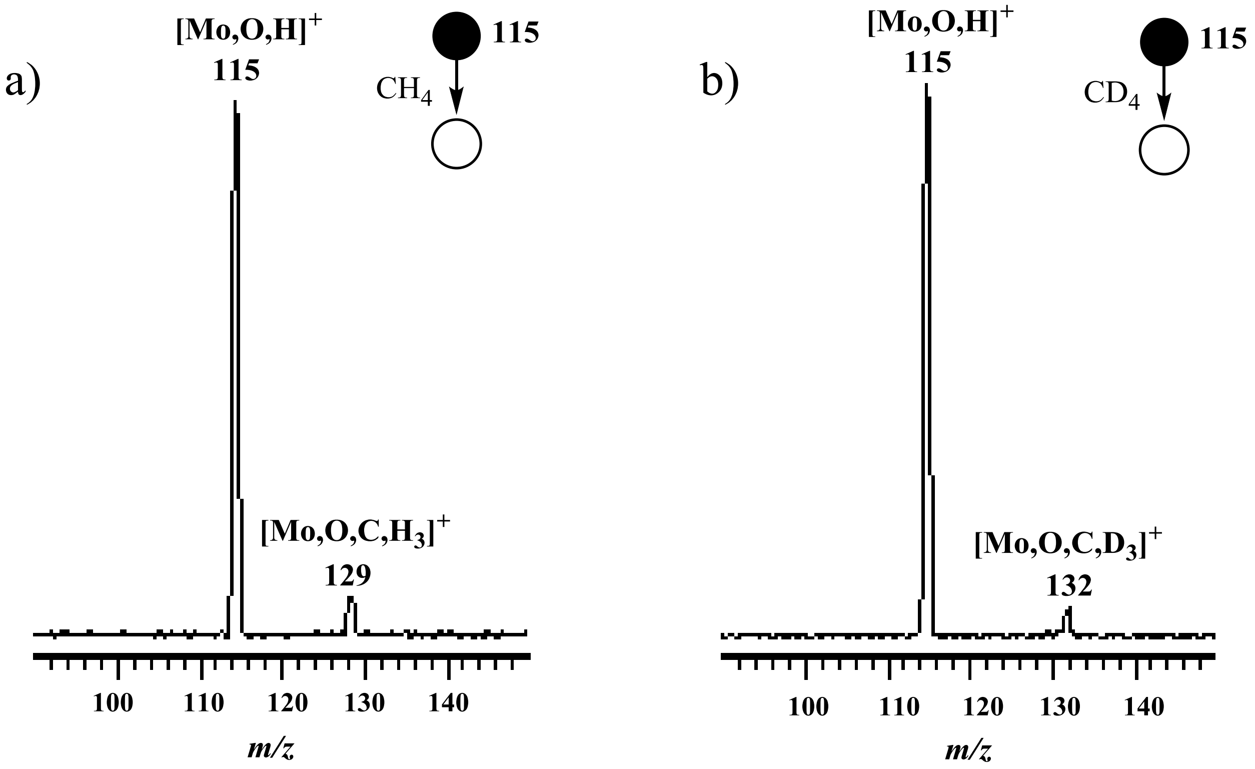

Figure S4. Mass spectra resulting from the thermal ion/molecule reaction of mass-selected [Mo,O,H]$^+$ generated from a solution of $MoOCl_4$ in H_2O/H_2O_2 with a) CH_4 at a pressure of 3.8 × 10^{-4} mbar and with b) CD_4 at a pressure of 2.9 × 10^{-4} mbar.

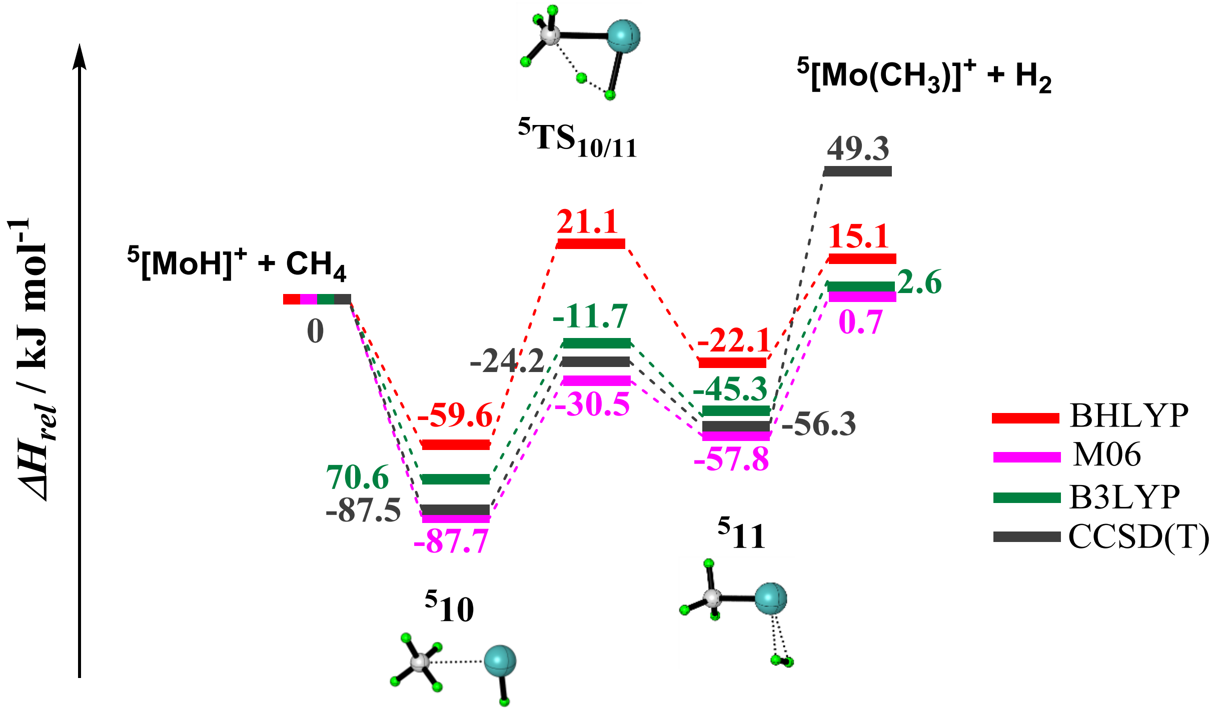

ΔH_rel / kJ mol-1
5[MoH]+ + CH4
0
5TS10/11
5[Mo(CH3)]+ + H2
49.3
21.1
15.1
2.6
0.7
-11.7
-24.2
-30.5
-22.1
-45.3
-56.3
-57.8
-59.6
70.6
-87.5
-87.7
510
511
BHLYP
M06
B3LYP
CCSD(T)

Figure S5. Simplified potential-energy surfaces (def2-TZVPD basis) for the reaction of $[MoH]^+$ with methane. All ZPVE-corrected energies are given in kJ mol^{-1}. C = gray, H= green, Mo = blue.

Table S1. Calculated s- and d-orbital contributions to the M–H-bonding natural localized molecular orbital (NLMO) for M (M = Mo,Ti) at the B3LYP/def2-TZVPD level of theory. α and β denote the spin channels of the unrestricted NLMOs.

	α		**β**	
	s%	d%	s%	d%
$[TiH]^+$	39.06	59.76	38.8	59.78
$[OTiH]^+$	19.66	75.07	19.66	75.07
$[Ti(CH_3)]^+$	23.39	76.47	29.92	69.86
$[OTi(CH_3)]^+$	12.40	85.56	12.40	85.56
$[MoH]^+$	15.32	83.94	21.72	77.17
$[OMoH]^+$	43.2	53.71	21.04	76.25
$[Mo(CH_3)]^+$	7.62	92.07	13.50	86.11
$[OMo(CH_3)]^+$	38.61	60.55	14.87	84.33

Table S2. Bond dissociation energies (BDE) obtained from different methods (computed with respect to neutral X (X = H, CH_3) and cationic Mo^+ or OMo^+ fragments).[a]

	Mo–H bond		**Mo–CH_3 bond**	
	$[OMoH]^+$	$[MoH]^+$	$[OMo(CH_3)]^+$	$[Mo(CH_3)]^+$
CCSD(T)	246.8	171.0	272.5	119.2
CCSD	235.6	161.1	248.1	95.9
B3LYP	259.3	201.2	267.8	191.1
M06	278.5	179.7	305.3	188.6
TPSSH	260.3	200.0	267.8	187.3
BHLYP	241.0	173.1	243.6	150.4
NEVPT2	-	134.5	-	142.5
Exp	-	166.3±5.8	-	151.5±8.7

[a] DFT results with def2-TZVPD basis set, CC results with aug-cc-pvtz(pp) basis at B3LYP/def2-TZVPD structure, and experimental data are taken from ref[4b] in the main text.

Table S3. Relative energies in kJ mol^{-1} of the intermediates and transition-state structures shown in Figure 1a. All energies corrected for zero-point vibrational energy contributions.[a]

	E_{rel}							
	CCSD(T)		B3LYP		BHLYP		M06	
	Singlet	Triplet	Singlet	Triplet	Singlet	Triplet	Singlet	Triplet
$[OMoH]^+ + CH_4$	41.7	0	53.3	0	56.3	0	25.9	0
5	-85.5	-106.5	-58.2	-86.0	-45.0	-86.5	-88.9	-95.7
$TS_{5/6}$	-70.2	13.9	-44.6	21.3	-1.6	35.6	-71.7	0.7
6	-89.6	-72.9	-67.1	-60.3	-34.0	-47.5	-92.6	-68.0
$[OMo(CH_3)]^+ + H_2$	89.5	-26.1	54.0	-15.2	66.0	-4.9	26.0	-18.9

[a] DFT results with def2-TZVPD basis set, CC results with aug-cc-pvtz(pp) basis at B3LYP/def2-TZVPD structure.

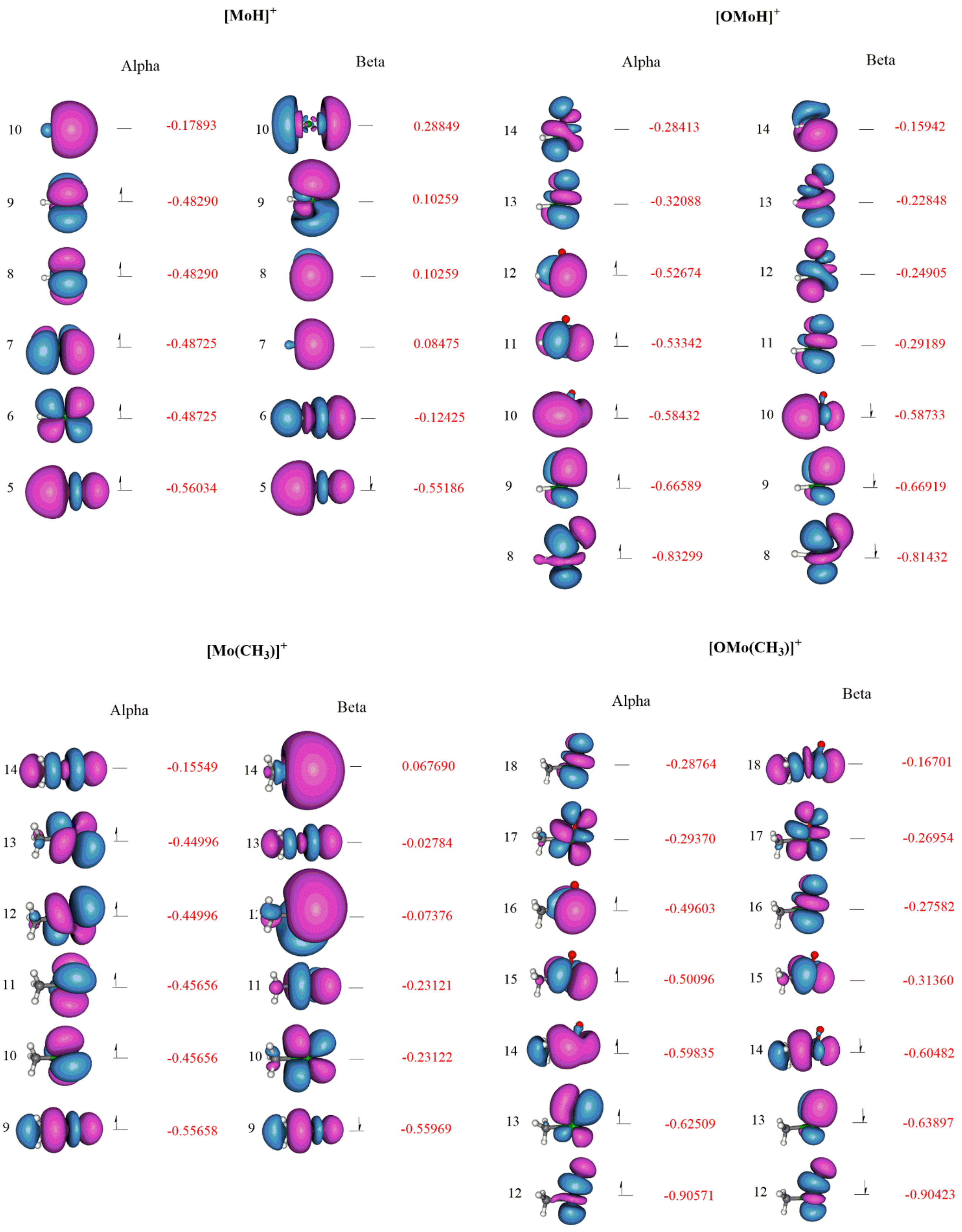
[MoH]$^+$
Alpha
Beta
10
-0.17893
9
-0.48290
8
-0.48290
7
-0.48725
6
-0.48725
5
-0.56034
10
0.28849
9
0.10259
8
0.10259
7
0.08475
6
-0.12425
5
-0.55186
[OMoH]$^+$
Alpha
Beta
14
-0.28413
13
-0.32088
12
-0.52674
11
-0.53342
10
-0.58432
9
-0.66589
8
-0.83299
14
-0.15942
13
-0.22848
12
-0.24905
11
-0.29189
10
-0.58733
9
-0.66919
8
-0.81432
[Mo(CH$_3$)]$^+$
Alpha
Beta
14
-0.15549
13
-0.44996
12
-0.44996
11
-0.45656
10
-0.45656
9
-0.55658
14
0.067690
13
-0.02784
1
-0.07376
11
-0.23121
10
-0.23122
9
-0.55969
[OMo(CH$_3$)]$^+$
Alpha
Beta
18
-0.28764
17
-0.29370
16
-0.49603
15
-0.50096
14
-0.59835
13
-0.62509
12
-0.90571
18
-0.16701
17
-0.26954
16
-0.27582
15
-0.31360
14
-0.60482
13
-0.63897
12
-0.90423

Note: All energies are in atomic units (a.u.) and marked in red

Figure S6. Molecular orbitals of [MoX]$^+$ and [OMoX]$^+$ (X = H, CH$_3$) complexes. All MO energies are in atomic units (a.u.) and marked in red. B3LYP/def2-TZVPD

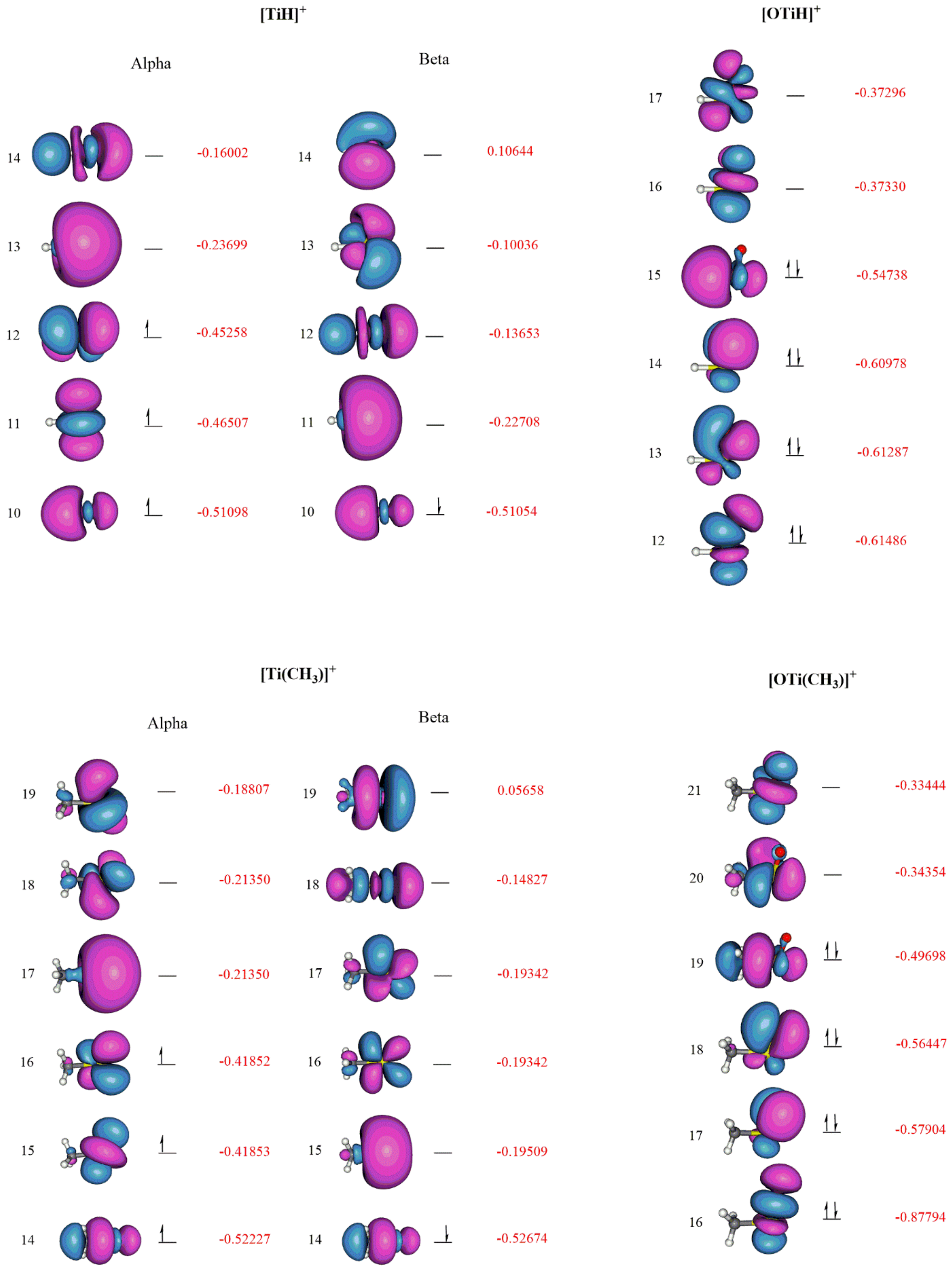

[TiH]$^+$
Alpha
Beta
14
-0.16002
14
0.10644
13
-0.23699
13
-0.10036
12
-0.45258
12
-0.13653
11
-0.46507
11
-0.22708
10
-0.51098
10
-0.51054
[OTiH]$^+$
17
-0.37296
16
-0.37330
15
-0.54738
14
-0.60978
13
-0.61287
12
-0.61486
[Ti(CH$_3$)]$^+$
Alpha
Beta
19
-0.18807
19
0.05658
18
-0.21350
18
-0.14827
17
-0.21350
17
-0.19342
16
-0.41852
16
-0.19342
15
-0.41853
15
-0.19509
14
-0.52227
14
-0.52674
[OTi(CH$_3$)]$^+$
21
-0.33444
20
-0.34354
19
-0.49698
18
-0.56447
17
-0.57904
16
-0.87794

Note: All energies are in atomic units (a.u.)

Figure S7. Molecular orbitals of [TiX]$^+$ and [OTiX]$^+$ (X = H, CH_3) complexes. All MO energies are in atomic units (a.u.) and marked in red. B3LYP/def2-TZVPD.

Paper IV

ChemPubSoc Europe
DOI: 10.1002/chem.201703767
CHEMISTRY
A European Journal
Communication

Gas-Phase Reactions

On the Electronic Origin of Remarkable Ligand Effects on the Reactivities of $[NiL]^+$ Complexes ($L=C_6H_5$, C_5H_4N, CN) towards Methane

Shaodong Zhou,[a, b] Marjan Firouzbakht,[a] Maria Schlangen,[a] Martin Kaupp,*[a] and Helmut Schwarz*[a]

Dedicated to Manuel Yáñez and Otilia Mó

Abstract: The gas-phase reactions of $[NiL]^+$ ($L=C_6H_5$, C_5H_4N, CN) with methane have been explored by using electrospray-ionization mass spectrometry (ESI-MS) complemented by quantum chemical calculations. Though the phenyl Ni complex $[Ni(C_6H_5)]^+$ exclusively abstracts one hydrogen atom from methane at ambient conditions, the cyano Ni complex $[Ni(CN)]^+$ brings about both H-atom abstraction and ligand exchange to generate $[Ni(CH_3)]^+$. In contrast, the complex 2-pyridinyl Ni $[Ni(C_5H_4N)]^+$ is inert towards this substrate. The presence of the empty 4s(Ni) orbital dominates the proton-coupled electron transfer (PCET) processes for the investigated systems.

Nickel-containing species continue to attract wide interest in gas-phase chemistry due to their various reactivities towards different kinds of small molecules[1] and, especially, nickel-mediated methane activation is in the spotlight. Although the bare nickel cation Ni^+ is not able to activate methane under thermal conditions,[2] ligation increases its reactivity. For example, by adding another atom to form $[NiX]^+$ ($X=H$, F), ligand exchange to generate $[Ni(CH_3)]^+$ and HX was observed upon thermal interaction with methane;[3] in contrast, diatomic $[NiO]^+$ brings about selective oxygen-atom transfer.[4] Ligand exchange with methane also occurs when adding the ligands L ($L=OH$, CO, H_2O) to $[NiH]^+$ to form $[Ni(H)(L)]^+$, as indicated by the generation of $[Ni(CH_3)(L)]^+$; in these cases, often H/D scrambling prevails.[5] In addition, a degenerate ligand exchange was observed upon mixing $[Ni(CH_3)]^+$ with CD_4, which is preceded/accompanied by a H/D exchange;[6] this reaction pattern also prevails for $[NiD]^+/CH_4$ to generate $[NiH]^+$.[7] Finally, with regard to nickel-containing cluster ions, Ni_n^+ ($n=2$–16) species have been reacted with methane.[8] An interesting kinetic energy dependency of the reactions on cluster size was observed; however, none of these ligand-devoid nickel clusters are capable of bringing about thermal methane activation.

Herein, we report the thermal reactions of $[NiL]^+$ ($L=C_6H_5$, C_5H_4N, CN) with methane. In contrast to the complex $[Ni(C_5H_4N)]^+$, the phenyl- and cyano-ligated complexes exhibit a strong reactivity enhancement towards CH_4. The electronic origins of the ligand effect are revealed by quantum chemical calculations.

When mass-selected, thermalized $[Ni(C_6H_5)]^+$ is exposed to CH_4, it spontaneously abstracts one hydrogen atom from this substrate with a rate constant of $6.4\times10^{-10}\,cm^{-3}\,mol^{-1}\,s^{-1}$;[9] this corresponds to an efficiency of 65%, relative to the collision rate[10] (Figure 1a, Equation (1); for technical details, see the Supporting Information). In the reaction with CH_2D_2, $[Ni(C_6H_6)]^+$ and $[Ni(C_6H_5D)]^+$ are generated in a ratio of 2.1:1, thus pointing to an intramolecular kinetic isotope effect of KIE = 2.1. In contrast, the related complex 2-pyridinyl Ni ($[Ni(C_5H_4N)]^+$) is inert towards methane under the same conditions. Furthermore, we generated another complex ion, cyano Ni ($[Ni(CN)]^+$), and examined its reactivity. As a result, this ion reacts with methane at near collision rate, and the products $[Ni(NCH)]^+$ and $[Ni(CH_3)]^+$ were generated in a ratio of 2:1 (Figure 1e, [Eqs. (2) and (3)]). In the reaction with CH_2D_2, an exact ratio in generating $[Ni(CHD_2)]^+/[Ni(CH_2D)]^+$ cannot be determined due to the interference by $[Ni(OH)]^+$; the latter ion is generated in the reaction of $[Ni(CN)]^+$ with background water. However, the H-atom transfer products $[Ni(NCH)]^+/[Ni(CHD_2)]^+$ are of much higher abundance compared to the D-atom transfer products $[Ni(NCD)]^+/[Ni(CH_2D)]^+$, even taking into account the background interference (Figure 1g,h); this finding points to an intramolecular KIE > 1.

Next, the reaction mechanisms were investigated using quantum-chemical calculations. The potential energy surfaces

$$[Ni(C_6H_5)]^+ + CH_4 \longrightarrow [Ni(C_6H_6)]^+ + CH_3^{\cdot} \qquad (1)$$

$$[Ni(CN)]^+ + CH_4 \longrightarrow [Ni(NCH)]^+ + CH_3^{\cdot} \qquad (2)$$

$$ \longrightarrow [Ni(CH_3)]^+ + HCN \qquad (3)$$

---

[a] Dr. S. Zhou, M. Firouzbakht, Dr. M. Schlangen, Prof. Dr. M. Kaupp, Prof. Dr. H. Schwarz
Institut für Chemie, Technische Universität Berlin
Strasse des 17. Juni 135, 10623 Berlin (Germany)
E-mail: martin.kaupp@tu-berlin.de
helmut.schwarz@tu-berlin.de

[b] Dr. S. Zhou
Zhejiang Provincial Key Laboratory of Advanced Chemical Engineering Manufacture Technology
College of Chemical and Biological Engineering
Zhejiang University, Hangzhou 310027 (P. R. China)

Supporting information and the ORCID identification number(s) for the author(s) of this article can be found under https://doi.org/10.1002/chem.201703767.

© 2017 Wiley-VCH Verlag GmbH & Co. KGaA, Weinheim

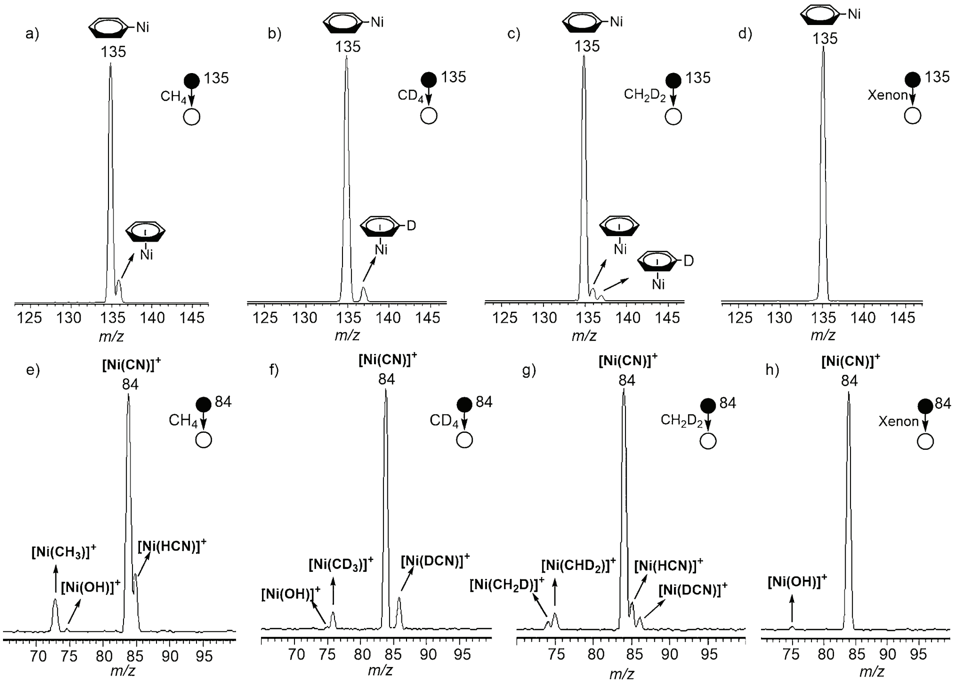

Figure 1. Mass spectra for the reactions of $[Ni(C_6H_5)]^+$ with: a) CH_4, b) CD_4, c) CH_2D_2, and d) Xe; mass spectra for the reactions of $[Ni(CN)]^+$ with: e) CH_4, f) CD_4, g) CH_2D_2, and h) Xe. The $[Ni(OH)]^+$ ions are due to the reaction of $[Ni(CN)]^+$ with background water.

(PESs) and selected structural information for the reactions of $[Ni(C_6H_5)]^+$, $[Ni(C_5H_4N)]^+$, and $[Ni(CN)]^+$ with CH_4 are shown in Figures 2, 3, and 4, respectively.

The most stable structure of $[Ni(C_6H_5)]^+$ is located on the triplet surface, in which only the *ipso* carbon of the phenyl ligand is bound to the nickel atom. As shown in Figure 2, the

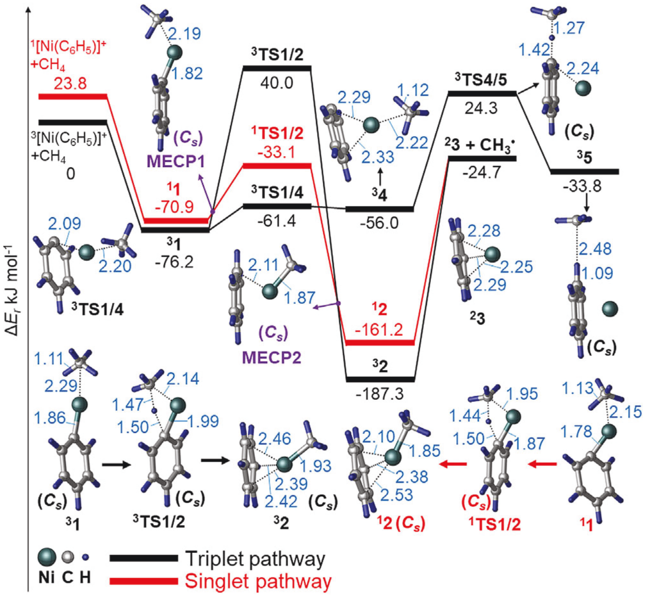
ΔEr kJ mol-1
1[Ni(C6H5)]+ +CH4
23.8
3[Ni(C6H5)]+ +CH4
0
MECP1
(Cs)
11
-70.9
31
-76.2
3TS1/2
40.0
1TS1/2
-33.1
3TS1/4
-61.4
34
-56.0
MECP2
12
-161.2
32
-187.3
3TS4/5
24.3
23 + CH3•
-24.7
35
-33.8
3TS1/4
23
1TS1/2
12 (Cs)
11
Ni C H
Triplet pathway
Singlet pathway

Figure 2. Simplified PESs and selected structural information for the reaction of $[Ni(C_6H_5)]^+$ with CH_4 as calculated at the B3LYP-D3(BJ)/def2-QZVPP//def2-TZVP level of theory. Bond lengths are given in Å, and charges are omitted for the sake of clarity.

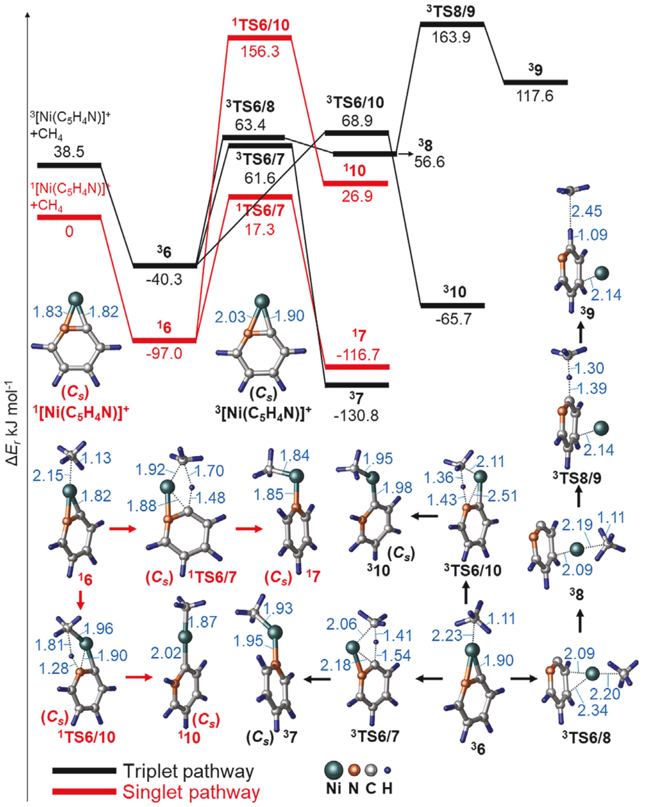
ΔEr kJ mol-1
3[Ni(C5H4N)]+ +CH4
38.5
1[Ni(C5H4N)]+ +CH4
0
36
-40.3
16
-97.0
1TS6/10
156.3
3TS6/8
63.4
3TS6/7
61.6
1TS6/7
17.3
3TS6/10
68.9
110
26.9
17
-116.7
37
-130.8
38
56.6
3TS8/9
163.9
39
117.6
310
-65.7
1[Ni(C5H4N)]+
3[Ni(C5H4N)]+
16
1TS6/7
17
310
3TS6/10
3TS8/9
39
38
1TS6/10
110
37
3TS6/7
36
3TS6/8
Triplet pathway
Singlet pathway
Ni N C H

Figure 3. Simplified PESs and selected structural information for the reaction of $[Ni(C_5H_4N)]^+$ with CH_4 as calculated at the B3LYP-D3(BJ)/def2-QZVPP//def2-TZVP level of theory. Bond lengths are given in Å, and charges are omitted for the sake of clarity.

© 2017 Wiley-VCH Verlag GmbH & Co. KGaA, Weinheim

These are not the final page numbers!

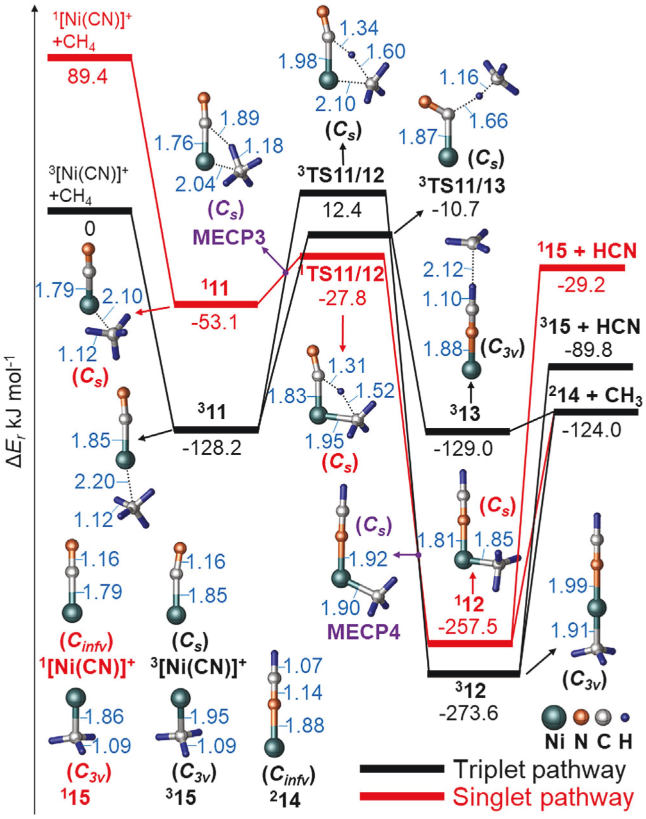

Figure 4. Simplified PESs and selected structural information for the reactions of [Ni(CN)]$^+$ with CH$_4$ as calculated at the B3LYP-D3(BJ)/def2-QZVPP//def2-TZVP level of theory. Bond lengths are given in Å, and charges are omitted for the sake of clarity.

energetically most favorable pathway for the reaction of [Ni(C$_6$H$_5$)]$^+$ with CH$_4$ proceeds via a two-state reactivity (TSR)[11] scenario. Though the transformation starts from an encounter complex ^{3}**1**, surmounting the four-center transition state ^{3}**TS1/2** in a σ-bond-metathesis process to form intermediate ^{3}**2** is thermally inaccessible; ^{3}**TS1/2** is located well above the entrance channel. Rather, a spin flip from the triplet to the singlet surface occurs at a minimum energy crossing point (MECP)[12] **MECP1**; this enables thermal access to ^{1}**TS1/2**. Next, either the intermediate ^{1}**2** is generated directly, or ^{3}**2** is formed after the system re-crosses to the triplet surface at **MECP2**. Liberation of a methyl ligand from $^{1/3}$**2** produces ^{2}**3**. In addition, ^{3}**1** can be transformed to ^{3}**4** by varying the coordination of the metal ion to an η^6 mode. From ^{3}**4**, activation of the H$_3$C–H bond may proceed via a harpoon-like transition state ^{3}**TS4/5** to form ^{3}**5**; however, this process is unavailable under thermal conditions. Considering that $^{1/3}$**2**→^{2}**3** is entropically favored, the initial H$_3$C–H bond activation via ^{1}**TS1/2** is rate limiting, in line with an intramolecular KIE 2.1, as determined experimentally.

Further, the most stable structure of [Ni(C$_5$H$_4$N)]$^+$ corresponds to an η^2-coordinated, planar complex that is located on the singlet surface, as shown in Figure 3. Five pathways, concerning transfer of a hydrogen atom from methane to the *ipso* C or the N atom of [Ni(C$_5$H$_4$N)]$^+$, have been located, that is $^{1/3}$**6**→$^{1/3}$**7**, $^{1/3}$**6**→$^{1/3}$**10**, and ^{3}**6**→^{3}**8**→^{3}**9**. However, without exception all singlet and triplet pathways explored for the [Ni(C$_5$H$_4$N)]$^+$/CH$_4$ couple involve at one stage transition states that are not accessible at ambient condition. Thus, in line with the experimental findings, the [Ni(C$_5$H$_4$N)]$^+$/CH$_4$ couple resists any C–H bond activation.

In contrast to the Ni(η^2-NC) coordination of [Ni(C$_5$H$_4$N)]$^+$, the complex [Ni(CN)]$^+$ exhibits a quasi-linear, triplet ground-state structure (Figure 4). A thermally available TSR scenario is also operative for [Ni(CN)]$^+$/CH$_4$, that is, ^{3}**11**→**MECP3**→^{1}**TS11/12**→$^{1/3}$**12**. To thermally access ^{3}**12**, **MECP4** has to be involved after surmounting ^{1}**TS11/12**. Further liberation of CH$_3^\bullet$ or HCN from $^{1/3}$**12** generates [Ni(NCH)]$^+$ or [Ni(CH$_3$)]$^+$, respectively. In addition, a single-state pathway to generate ^{3}**13** via ^{3}**TS11/13** is also available under thermal conditions. ^{3}**13** further loses CH$_3^\bullet$ to produce [Ni(NCH)]$^+$. For all thermally accessible pathways, the associated TSs are rate-limiting, in line with KIE > 1, as observed experimentally. Furthermore, irrespective of the intersystem-crossing efficiencies, the generation of [Ni(NCH)]$^+$ is always energetically more favorable than producing [Ni(CH$_3$)]$^+$, in line with the experimentally determined higher branching ratio for the former.

To obtain an even better understanding of the C–H bond activation steps, the deformation energy (ΔE_{def}), and its comparison with the respective reaction barrier ($\Delta E^{\ddagger}$) were examined and complemented by the analysis of orbitals, charges and spin distributions. These results indicate that the pathways ^{3}**4**→^{3}**5**, ^{3}**8**→^{3}**9**, and ^{3}**11**→^{3}**13** are best described as conventional hydrogen-atom transfer (HAT)[13] processes, whereas the others have PCET[14] character; more details are provided in the Supporting Information (Figures S1–S3). Thus, among all located PCET TSs, only ^{1}**TS1/2** and ^{1}**TS11/12** are thermally accessible. Notably, thermal access of these two TSs requires a spin flip from triplet to singlet, during which the associated active Ni–C sites gain increased Wiberg bond indexes (WBI) and, thus, become less ionic (see Table S2 in the Supporting Information). This is in sharp contrast to the findings obtained for the [Al$_2$Mg$_2$O$_5$]$^{\bullet+}$/CH$_4$[15] and [Al$_2$ZnO$_4$]$^{\bullet+}$/CH$_4$[16] couples for which it was demonstrated that the ionicity of the M–O pair favors heterolysis of the H$_3$C–H bond. However, the presence of an empty 4s orbital at Ni matters for the investigated PCET processes, as suggested by the NBO analysis. For example, an empty 4s(Ni) orbital is not present for ground-state ^{3}[Ni(C$_6$H$_5$)]$^+$; by crossing to the singlet surface an empty 4s(Ni) orbital is generated for accepting the methide ligand in a PCET process. The same holds true for [Ni(CN)]$^+$/CH$_4$. For ^{1}[Ni(C$_5$H$_4$N)]$^+$, however, the 4s(Ni) orbital is engaged in the dative N→Ni bond thus remaining occupied; accordingly, relatively high barriers result for the sequence **6**→**7**/**10**. This conclusion is in line with previous findings for [MH]$^+$/CH$_4$ (M = Fe, Co, Ni) in which a 3d^{n-1}4s^1→3d^n crossing is essential for the H$_3$C–H bond activation.[3d] Finally, it is also notable that ^{3}**TS11/13** is the only thermally accessible HAT TS. The low spin densities at the H-atom acceptors of the ground-state ^{3}[Ni(C$_6$H$_5$)]$^+$ (0.26), ^{1}[Ni(C$_5$H$_4$N)]$^+$ (0.00), and ^{3}[Ni(CN)]$^+$ (0.12) are responsible for the relatively high barriers for ^{3}**TS4/5**, ^{3}**TS8/9**, and ^{3}**TS11/13**. On the other hand, ^{3}**TS11/13** benefits from the excess energy released when forming ^{3}**11**, thus pulling down its relative energy well below the entrance channel.

In summary, the gas-phase reactions of $[Ni(C_6H_5)]^+$, $[Ni(C_5H_4N)]^+$, and $[Ni(CN)]^+$ with methane have been investigated both experimentally and computationally. Whereas $[Ni(C_6H_5)]^+$ exclusively abstracts one hydrogen atom from methane, $[Ni(CN)]^+$ brings about both H-atom abstraction and the ligand exchange to release HCN; in contrast, $[Ni(C_5H_4N)]^+$ is inert towards this substrate under the same conditions. A PCET pathway involving a two-state reactivity scenario[11] prevails for both $[Ni(C_6H_5)]^+/CH_4$ and $[Ni(CN)]^+/CH_4$. In addition, an alternative, single-state HAT pathway is also thermally available for $[Ni(CN)]^+/CH_4$. The presence of the empty 4s(Ni) orbital is essential for the investigated PCET pathways, whereas the HAT pathway for $[Ni(CN)]^+/CH_4$ benefits from the excess energy released when forming the encounter complex.

Acknowledgements

Generous financial support by the Fonds der Chemischen Industrie and the Deutsche Forschungsgemeinschaft ("UniCat") is appreciated. We thank Dr. Thomas Weiske and Andrea Beck for technical assistance.

Conflict of interest

The authors declare no conflict of interest.

Keywords: gas-phase reactions · ligand effects · methane activation · quantum-chemical calculations

[1] a) Y. X. Zhao, Q. Y. Liu, M. Q. Zhang, S. G. He, *Dalton Trans.* **2016**, *45*, 11471 – 11495; b) H. Schwarz, *Isr. J. Chem.* **2014**, *54*, 1413 – 1431; c) M. Schlangen, H. Schwarz, *J. Catal.* **2011**, *284*, 126 – 137; d) D. Schröder, H. Schwarz, *Proc. Natl. Acad. Sci. USA* **2008**, *105*, 18114 – 18119; e) P. B. Armentrout, *Annu. Rev. Phys. Chem.* **2001**, *52*, 423 – 461.

[2] A. Shayesteh, V. V. Lavrov, G. K. Koyanagi, D. K. Böhme, *J. Phys. Chem. A* **2009**, *113*, 5602 – 5611.

[3] a) M. Schlangen, H. Schwarz, *Helv. Chim. Acta* **2008**, *91*, 2203 – 2210; b) M. Schlangen, D. Schröder, H. Schwarz, *Chem. Eur. J.* **2007**, *13*, 6810 – 6816; c) M. Schlangen, H. Schwarz, *Angew. Chem. Int. Ed.* **2007**, *46*, 5614 – 5617; *Angew. Chem.* **2007**, *119*, 5711 – 5715; d) Q. Zhang, M. T. Bowers, *J. Phys. Chem. A* **2004**, *108*, 9755 – 9761.

[4] a) A. Božović, S. Feil, G. K. Koyanagi, A. A. Viggiano, X. H. Zhang, M. Schlangen, H. Schwarz, D. K. Bohme, *Chem. Eur. J.* **2010**, *16*, 11605 – 11610; b) D. Schröder, H. Schwarz, *Angew. Chem. Int. Ed. Engl.* **1995**, *34*, 1973 – 1995; *Angew. Chem.* **1995**, *107*, 2126 – 2150.

[5] a) O. Lakuntza, J. M. Matxain, F. Ruiperez, M. Besora, F. Maseras, J. M. Ugalde, M. Schlangen, H. Schwarz, *Phys. Chem. Chem. Phys.* **2012**, *14*, 9306 – 9310; b) Y. Dede, X. H. Zhang, M. Schlangen, H. Schwarz, M. H. Baik, *J. Am. Chem. Soc.* **2009**, *131*, 12634 – 12642; c) M. Schlangen, D. Schröder, H. Schwarz, *Angew. Chem. Int. Ed.* **2007**, *46*, 1641 – 1644; *Angew. Chem.* **2007**, *119*, 1667 – 1671; d) M. Schlangen, Ph.D. Thesis, Technische Universität Berlin, Berlin (Germany), **2008**.

[6] M. Armélin, M. Schlangen, H. Schwarz, *Chem. Eur. J.* **2008**, *14*, 5229 – 5236.

[7] T. J. Carlin, L. Sallans, C. J. Cassady, D. B. Jacobson, B. S. Freiser, *J. Am. Chem. Soc.* **1983**, *105*, 6320 – 6321.

[8] F. Y. Liu, X. G. Zhang, R. Liyanage, P. B. Armentrout, *J. Chem. Phys.* **2004**, *121*, 10976 – 10990.

[9] Note that the absolute rate coefficient for the reaction cannot be measured directly in our multipole setup; rather, the rate coefficient was determined by using the $[Pt]^+/CH_4$ system as a reference: a) C. Heinemann, R. Wesendrup, H. Schwarz, *Chem. Phys. Lett.* **1995**, *239*, 75 – 83; b) M. Pavlov, M. R. A. Blomberg, P. E. M. Siegbahn, R. Wesendrup, C. Heinemann, H. Schwarz, *J. Phys. Chem. A* **1997**, *101*, 1567 – 1579; c) X.-G. Zhang, R. Liyanage, P. B. Armentrout, *J. Am. Chem. Soc.* **2001**, *123*, 5563 – 5575; d) D. Schröder, H. Schwarz, *Can. J. Chem.* **2005**, *83*, 1936 – 1940.

[10] M. T. Bowers, J. B. Laudenslager, *J. Chem. Phys.* **1972**, *56*, 4711 – 4712.

[11] a) J. N. Harvey, *WIREs Comput. Mol. Sci.* **2014**, *4*, 1 – 14; b) S. Shaik, *Int. J. Mass Spectrom.* **2013**, *354*, 5 – 14; c) S. Shaik, H. Hirao, D. Kumar, *Acc. Chem. Res.* **2007**, *40*, 532 – 542; d) W. Nam, *Acc. Chem. Res.* **2007**, *40*, 522 – 531; e) P. E. M. Siegbahn, T. Borowski, *Acc. Chem. Res.* **2006**, *39*, 729 – 738; f) S. Shaik, D. Kumar, S. P. de Visser, A. Altun, W. Thiel, *Chem. Rev.* **2005**, *105*, 2279 – 2328; g) H. Schwarz, *Int. J. Mass Spectrom.* **2004**, *237*, 75 – 105; h) S. Shaik, S. P. de Visser, F. Ogliaro, H. Schwarz, D. Schröder, *Curr. Opin. Chem. Biol.* **2002**, *6*, 556 – 567; i) D. Schröder, S. Shaik, H. Schwarz, *Acc. Chem. Res.* **2000**, *33*, 139 – 145; j) S. Shaik, M. Filatov, D. Schröder, H. Schwarz, *Chem. Eur. J.* **1998**, *4*, 193 – 199; k) P. B. Armentrout, *Science* **1991**, *251*, 175 – 179.

[12] J. N. Harvey, M. Aschi, H. Schwarz, W. Koch, *Theor. Chem. Acc.* **1998**, *99*, 95 – 99.

[13] For recent reviews on HAT, see: a) M. Salamone, M. Bietti, *Acc. Chem. Res.* **2015**, *48*, 2895 – 2903; b) H. Schwarz, *Chem. Phys. Lett.* **2015**, *629*, 91 – 101; c) C. T. Saouma, J. M. Mayer, *Chem. Sci.* **2014**, *5*, 21 – 31; d) N. Dietl, M. Schlangen, H. Schwarz, *Angew. Chem. Int. Ed.* **2012**, *51*, 5544 – 5555; *Angew. Chem.* **2012**, *124*, 5638 – 5650; e) W. Z. Lai, C. S. Li, H. Chen, S. Shaik, *Angew. Chem. Int. Ed.* **2012**, *51*, 5556 – 5578; *Angew. Chem.* **2012**, *124*, 5652 – 5676; f) J. M. Mayer, *Acc. Chem. Res.* **2011**, *44*, 36 – 46.

[14] For recent reviews on PCET, see: a) S. Hammes-Schiffer, *J. Am. Chem. Soc.* **2015**, *137*, 8860 – 8871; b) A. Migliore, N. F. Polizzi, M. J. Therien, D. N. Beratan, *Chem. Rev.* **2014**, *114*, 3381 – 3465; c) D. R. Weinberg, C. J. Gagliardi, J. F. Hull, C. F. Murphy, C. A. Kent, B. C. Westlake, A. Paul, D. H. Ess, D. G. McCafferty, T. J. Meyer, *Chem. Rev.* **2012**, *112*, 4016 – 4093; d) J. J. Warren, T. A. Tronic, J. M. Mayer, *Chem. Rev.* **2010**, *110*, 6961 – 7001; e) P. E. M. Siegbahn, M. R. A. Blomberg, *Chem. Rev.* **2010**, *110*, 7040 – 7061; f) S. Hammes-Schiffer, *Chem. Rev.* **2010**, *110*, 6937 – 6938.

[15] J. Li, S. Zhou, J. Zhang, M. Schlangen, D. Usharani, S. Shaik, H. Schwarz, *J. Am. Chem. Soc.* **2016**, *138*, 11368 – 11377.

[16] S. Zhou, L. Yue, M. Schlangen, H. Schwarz, *Angew. Chem. Int. Ed.* **2017**, https://doi.org/10.1002/anie.201704979; *Angew. Chem.* **2017**, https://doi.org/10.1002/ange.201704979.

Manuscript received: August 11, 2017
Accepted manuscript online: September 1, 2017
Version of record online: ■■ ■■, 0000

COMMUNICATION

The gas-phase reactions of $[Ni(C_6H_5)]^+$, $[Ni(C_5H_4N)]^+$, and $[Ni(CN)]^+$ with methane have been investigated both experimentally and computationally. Whereas $[Ni(C_6H_5)]^+$ exclusively abstracts one hydrogen atom from methane, $[Ni(CN)]^+$ brings about both H-atom abstraction and the ligand exchange to release HCN; in contrast, $[Ni(C_5H_4N)]^+$ is inert towards this substrate under the same conditions.

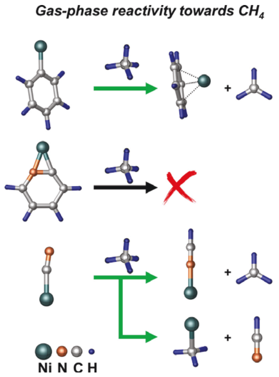

Gas-Phase Reactions

S. Zhou, M. Firouzbakht, M. Schlangen, M. Kaupp,* H. Schwarz*

■■ – ■■

On the Electronic Origin of Remarkable Ligand Effects on the Reactivities of $[NiL]^+$ Complexes ($L = C_6H_5$, C_5H_4N, CN) towards Methane

© 2017 Wiley-VCH Verlag GmbH & Co. KGaA, Weinheim

CHEMISTRY
A European Journal

Supporting Information

On the Electronic Origin of Remarkable Ligand Effects on the Reactivities of $[NiL]^+$ Complexes ($L = C_6H_5$, C_5H_4N, CN) towards Methane

Shaodong Zhou,[a, b] Marjan Firouzbakht,[a] Maria Schlangen,[a] Martin Kaupp,*[a] and Helmut Schwarz*[a]

chem_201703767_sm_miscellaneous_information.pdf

Supporting Information

Experimental and Computational Section

The experiments were performed using a VG Bio-Q mass spectrometer of QHQ configuration (Q: quadrupole; H: hexapole) equipped with an electrospray-ionization (ESI) source, as described in detail elsewhere.[1] Nickel(II) iodide, benzoic acid, picolinic acid, acetonitrile, methanol, water, CH_4, CD_4, CH_2D_2, and Xenon were obtained from Sigma-Aldrich and utilized without further purification. To generate $[Ni(C_6H_5)]^+$/$[Ni(C_5H_4N)]^+$, millimolar solutions of Nickel(II) iodide and benzoic acid/picolinic acid in a water-methanol mixture were used; the solution of Nickel(II) iodide in acetonitrile was employed to generate $[Ni(CN)]^+$. All of the samples were introduced into the mass spectrometer via a syringe pump and a fused-silica capillary connected to the ESI source with a pump rate of 4µl/min. Nitrogen was used as a nebulizing and drying gas, at a source temperature of 80 °C. The maximum intensity of the desired complex was achieved by adjusting the cone voltage (U_c) to around 50-70 V. The isotope patterns of the ions of interest have been compared with the calculated isotope patterns to confirm the identity of the ions.[2] The reaction of precursors with methane have been probed at a collision energy (E_{lab}) nominally set to 0 eV, which, in conjunction with the ca. 0.4 eV kinetic energy width of the parent ion at peak half height, allows the investigation of quasi-thermal reactions, as described previously.[3] The pressure of methane was varied between ca. 0.27×10^{-3} to 0.89×10^{-3} mbar in the hexapole. Cationic products are recorded by scanning of Q2.

The theoretical work was performed using the Gaussian 09 program.[4] The B3LYP functional,[5] including DFT-D3 dispersion correction,[6] was used for the structural optimization and frequency analysis; the def2-TZVP basis set[7] was employed for all atoms. Stationary points were optimized without symmetry constraint, and their nature was confirmed by vibrational frequency analysis. Intrinsic reaction coordinate (IRC)[8] calculations were also performed to link transition structures with the respective intermediates. Unscaled vibrational frequencies were used to correct the relative energies for zero-point vibrational energy (ZPVE) contributions. More accurate single-point energies were obtained at the (B3LYP-D3(BJ), B97-1, PBE0)/def2-QZVPP levels of theory using the B3LYP-D3(BJ)/def2-TZVP structures; note that the latter two functionals are without dispersion correction. These functionals have proven to be reliable for the calculations of Ni-containing systems.[9] Natural bond orbital (NBO)[10] calculations were performed to obtain further information on selected stationary points along the reaction coordinates.

Deformation energies (ΔE_{def}) which are required for distorting the reactants to their geometries in the TSs, were calculated as $\Delta E_{\mathrm{def}} = E(\mathrm{CH_4} + [\mathrm{NiL}]^+$ at TS geometry$) - E(\mathrm{EC})$ (L = C_6H_5, C_5H_4N, CN); ΔE_{def} and the respective reaction barrier ($\Delta E^{\ddagger}$) were calculated at the B3LYP-D3(BJ)//def2-QZVPP level.

Table S1. Energies of all relevant species as calculated at the (B97-1, PBE0)/def2-QZVPP//B3LYP-D3(BJ)/def2-TZVP levels of theory. Energies of respective entrance channels, i.e. separated reactants, were set to be 0.

Species	ΔE_r, kJ mol^{-1}	
	B97-1	PBE0
^{3}**1**	-76.7	-65.9
^{1}**1**	-62.5	-52.4
^{3}**2**	-180.0	-191.9
^{1}**2**	-156.7	-152.9
^{3}**4**	-51.5	-67.6
^{3}**5**	-36.3	-50.8
^{1}**6**	-87.7	-95.2
^{3}**6**	-33.9	-51.7
^{1}**7**	-102.3	-102.2
^{3}**7**	-118.0	-136.5
^{3}**8**	63.3	40.1
^{3}**9**	119.1	96.0
^{1}**10**	28.2	28.2
^{3}**10**	-35.0	-74.0
^{1}**11**	-50.2	-37.4
^{3}**11**	-124.5	-126.2
^{1}**12**	-247.2	-233.7
^{3}**12**	-259.5	-271.6
^{3}**13**	118.1	-118.2
^{3}**TS1/2**	45.3	37.1
^{1}**TS1/2**	-27.0	-22.7

^{3}TS1/4	-55.6	-69.4
^{3}TS4/5	18.1	3.5
^{1}TS6/7	21.5	6.8
^{3}TS6/7	67.0	46.2
^{3}TS6/8	71.9	50.5
^{3}TS8/9	160.6	141.4
^{1}TS6/10	159.8	149.0
^{3}TS6/10	75.9	49.7
^{1}TS11/12	-27.8	-18.9
^{3}TS11/12	13.4	6.8
^{3}TS11/13	-12.2	-2.2

As shown in Table S1, the PESs as calculated at the (B97-1, PBE0)/def2-QZVPP//B3LYP-D3BJ/def2-TZVP levels of theory qualitatively resemble that given by B3LYP (Figures 2 and 3 in the main text).

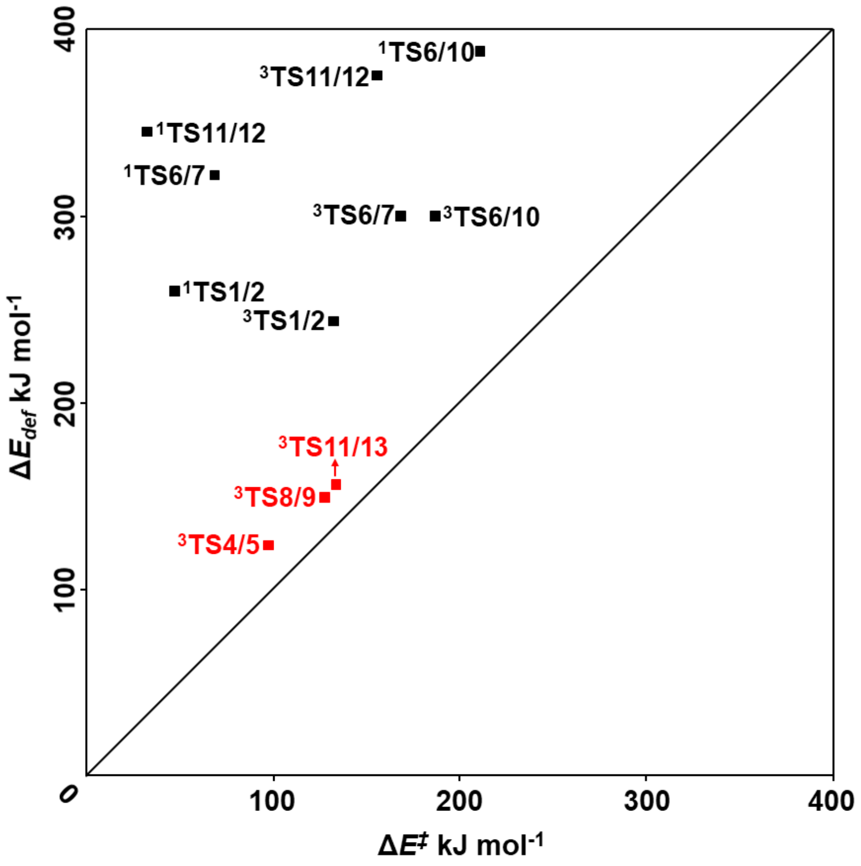

Figure S1. A plot of the sum of the deformation energies of the reactants in the TSs (ΔE_{def}) *versus* the corresponding barriers ($\Delta E^{\ddagger}$) as calculated at the B3LYP-D3(BJ)/def2-QZVPP level of theory.

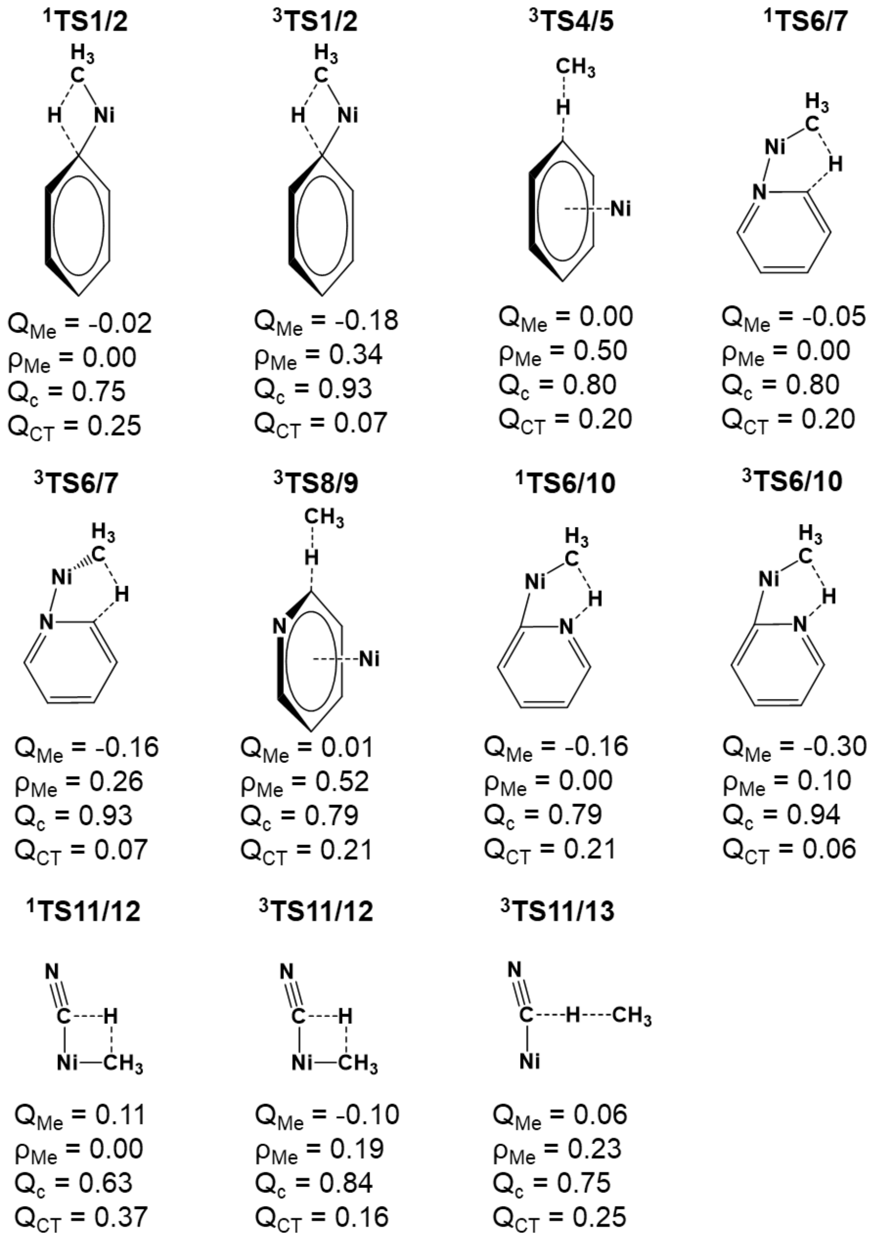

^{1}TS1/2
H$_3$
C
H
Ni
Q_{Me} = -0.02
ρ_{Me} = 0.00
Q_c = 0.75
Q_{CT} = 0.25
^{3}TS1/2
H$_3$
C
H
Ni
Q_{Me} = -0.18
ρ_{Me} = 0.34
Q_c = 0.93
Q_{CT} = 0.07
^{3}TS4/5
CH$_3$
H
Ni
Q_{Me} = 0.00
ρ_{Me} = 0.50
Q_c = 0.80
Q_{CT} = 0.20
^{1}TS6/7
H$_3$
C
Ni
H
N
Q_{Me} = -0.05
ρ_{Me} = 0.00
Q_c = 0.80
Q_{CT} = 0.20
^{3}TS6/7
H$_3$
C
Ni
H
N
Q_{Me} = -0.16
ρ_{Me} = 0.26
Q_c = 0.93
Q_{CT} = 0.07
^{3}TS8/9
CH$_3$
H
N
Ni
Q_{Me} = 0.01
ρ_{Me} = 0.52
Q_c = 0.79
Q_{CT} = 0.21
^{1}TS6/10
H$_3$
C
Ni
H
N
Q_{Me} = -0.16
ρ_{Me} = 0.00
Q_c = 0.79
Q_{CT} = 0.21
^{3}TS6/10
H$_3$
C
Ni
H
N
Q_{Me} = -0.30
ρ_{Me} = 0.10
Q_c = 0.94
Q_{CT} = 0.06
^{1}TS11/12
N
C
H
Ni
CH$_3$
Q_{Me} = 0.11
ρ_{Me} = 0.00
Q_c = 0.63
Q_{CT} = 0.37
^{3}TS11/12
N
C
H
Ni
CH$_3$
Q_{Me} = -0.10
ρ_{Me} = 0.19
Q_c = 0.84
Q_{CT} = 0.16
^{3}TS11/13
N
C
H
CH$_3$
Ni
Q_{Me} = 0.06
ρ_{Me} = 0.23
Q_c = 0.75
Q_{CT} = 0.25

Figure S2. Schematic representations of the TSs together with NBO charges (Q) and spin densities (ρ) on the methyl group (Me), the charges on the complex (Q_c), and the amount of charge transferred (Q_{CT}) from methane to the complex ion as calculated at the B3LYP-D3(BJ)/def2-TZVP level of theory.

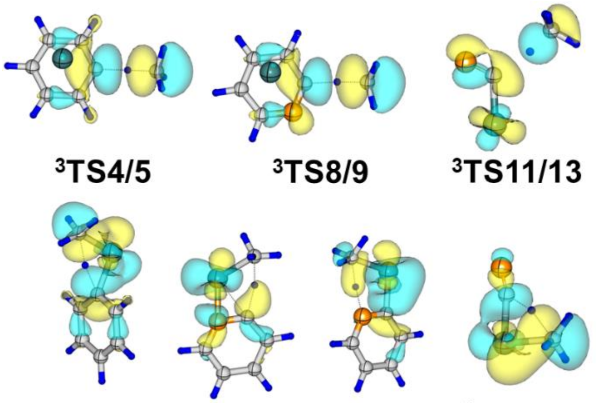

^{3}**TS4/5** ^{3}**TS8/9** ^{3}**TS11/13**

^{3}**TS1/2** ^{3}**TS6/7** ^{3}**TS6/10** ^{3}**TS11/12**

Figure S3. SNOs in TSs: the ϕ_{HAT} type SNOs in ^{3}**TS4/5**, ^{3}**TS8/9** and ^{3}**TS11/13** *versus* the ϕ_{PCET} type ones in other TSs as calculated at the B3LYP-D3(BJ)/def2-TZVP level of theory.

As shown in Figure S1, for ^{3}**TS4/5**, ^{3}**TS8/9** and ^{3}**TS11/13**, $\Delta E_{\mathrm{def}} \approx \Delta E^{\ddagger}$, is indicative for HAT; for all the other pathways, however, $\Delta E_{\mathrm{def}} >> \Delta E^{\ddagger}$; this large stabilizing interaction is indicative for a PCET character.[11] Further, as shown in Figure S2, for ^{3}**TS4/5** and ^{3}**TS8/9** considerable spin densities are located on the methyl groups thus pointing to the HAT character; however, ^{1}**TS1/2**, ^{1}**TS6/7**, ^{1}**TS11/12** and ^{1}**TS6/10** have a PCET character, and the former three TSs exhibit discrete ET events; ^{3}**TS1/2**, ^{3}**TS6/7**, ^{3}**TS11/12** and ^{3}**TS6/10** have a PCET character with a hybrid HAT feature as reflected by the low spin densities located at the respective methyl groups; ^{3}**TS11/13** has a HAT character with a hybrid PCET feature as reflected by the charge already transferred from methane to the NiCN moiety.[11] Finally, as shown in Figure S3, ^{3}**TS4/5**, ^{3}**TS8/9** and ^{3}**TS11/13** possess the singly occupied spin natural orbitals (SNOs) with a node on H in transit between two σ-type lobes on the two C atoms; this is typical for a HAT character. Combining all these features, one arrives at the conclusion that the pathways ^{3}**4** → ^{3}**5**, ^{3}**8** → ^{3}**9** and ^{3}**11** → ^{3}**13** are genuine HAT processes while the others have PCET character.

Table S2. WBIs for relevant species on PESs.

Species	WBI	
	Ni–C	Ni–N
$^3[Ni(C_6H_5)]^+$	0.26	-
$^1[Ni(C_6H_5)]^+$	0.91	-
$^3[Ni(C_5H_4N)]^+$	0.18	0.12
$^1[Ni(C_5H_4N)]^+$	0.75	0.44
$^3[Ni(CN)]^+$	0.21	-
$^1[Ni(CN)]^+$	0.85	-
^{1}MECP1	0.94	
^{3}MECP1	0.23	
^{1}MECP3	0.84	
^{3}MECP3	0.22	

That an empty *4s*(Ni) orbital is indeed essential for the reactions of $[NiL]^+$ (L = C_6H_5, C_5H_4N, CN) with methane via PCET is suggested by NBO analysis. For example, for the electronic ground states of $^3[Ni(C_6H_5)]^+$ and $^3[Ni(CN)]^+$, the electronic configuration at the metal center is $3d^8 4s^1$; an empty *4s*(Ni) orbital is not present, which disfavors accepting the methide in a PCET process. By crossing to the singlet surface a $3d^9 4s^0$(Ni) configuration is formed thus generating an empty *4s*(Ni) orbital, facilitating accepting the methide; subsequent electronic rearrangements as well as a spin-re-crossing to the triplet surface generate a new σ(Ni–CH_3) bond in which the *sd*(Ni) hybrid orbital is involved; accordingly, a new σ(L–H) (L = C_6H_5 or CN) bond is also formed. For the ground-state $^1[Ni(C_5H_4N)]^+$, however, the *4s*(Ni) orbital is engaged in the dative N→Ni bond thus remaining occupied; to accept the methide in a PCET process, the electron pair of the N→Ni bond has to be shifted to the *2p*(N) orbital thus presenting the empty *4s*(Ni) orbital. The afterward electronic rearrangements generate the new σ(Ni–CH_3) and σ(NC–H) bonds; in the former, the *sd*(Ni) hybrid orbital is involved.

References

[1] C. Trage, D. Schröder, H. Schwarz, *Chem. Eur. J.* **2005**, *11*, 619-627.

[2] V. G. Solomonik, A. N. Smirnov, *Russ. J. Coord. Chem.* **2008**, *34*, 706-711.

[3] a) D. Schröder, H. Schwarz, S. Schenk, E. Anders, *Angew. Chem. Int. Ed.* **2003**, *42*, 5087-5090; b) D. Schröder, M. Engeser, H. Schwarz, E. C. E. Rosenthal, J. Döbler, J. Sauer, *Inorg. Chem.* **2006**, *45*, 6235-6245; c) N. Dietl, T. Wende, K. Chen, L. Jiang, M. Schlangen, X. Zhang, K. R. Asmis, H. Schwarz, *J. Am. Chem. Soc.* **2013**, *135*, 3711-3721.

[4] M. J. Frisch, G. W. Trucks, H. B. Schlegel, G. E. Scuseria, M. A. Robb, J. R. Cheeseman, G. Scalmani, V. Barone, B. Mennucci, G. A. Petersson, H. Nakatsuji, M. Caricato, X. Li, H. P. Hratchian, A. F. Izmaylov, J. Bloino, G. Zheng, J. L. Sonnenberg, M. Hada, M. Ehara, K. Toyota, R. Fukuda, J. Hasegawa, M. Ishida, T. Nakajima, Y. Honda, O. Kitao, H. Nakai, T. Vreven, J. A. Montgomery, Jr., J. E. Peralta, F. Ogliaro, M. Bearpark, J. J. Heyd, E. Brothers, K. N. Kudin, V. N. Staroverov, R. Kobayashi, J. Normand, K. Raghavachari, A. Rendell, J. C. Burant, S. S. Iyengar, J. Tomasi, M. Cossi, N. Rega, J. M. Millam, M. Klene, J. E. Knox, J. B. Cross, V. Bakken, C. Adamo, J. Jaramillo, R. Gomperts, R. E. Stratmann, O. Yazyev, A. J. Austin, R. Cammi, C. Pomelli, J. W. Ochterski, R. L. Martin, K. Morokuma, V. G. Zakrzewski, G. A. Voth, P. Salvador, J. J. Dannenberg, S. Dapprich, A. D. Daniels, O. Farkas, J. B. Foresman, J. V. Ortiz, J. Cioslowski, D. J. Fox, Gaussian 09, Revision D.01, Gaussian, Inc., Wallingford CT, 2009.

[5] a) A. D. Becke, *J. Chem. Phys.* **1993**, *98*, 5648-5652; b) A. D. Becke, *J. Chem. Phys.* **1993**, *98*, 1372-1377; c) C. T. Lee, W. T. Yang, R. G. Parr, *Phys. Rev. B* **1988**, *37*, 785-789; d) B. Miehlich, A. Savin, H. Stoll, H. Preuss, *Chem. Phys. Lett.* **1989**, *157*, 200-206.

[6] a) S. Grimme, S. Ehrlich, L. Goerigk, *J. Comput. Chem.* **2011**, *32*, 1456-1465; b) S. Grimme, J. Antony, S. Ehrlich, H. Krieg, *J. Chem. Phys.* **2010**, *132*, 154104.

[7] F. Weigend, R. Ahlrichs, *Phys. Chem. Chem. Phys.* **2005**, *7*, 3297-3305.

[8] a) H. P. Hratchian, H. B. Schlegel, *J. Chem. Theory Comput.* **2005**, *1*, 61-69; b) D. G. Truhlar, N. J. Kilpatrick, B. C. Garrett, *J. Chem. Phys.* **1983**, *78*, 2438-2442; c) K. Fukui, *Acc. Chem. Res.* **1981**, *14*, 363-368.

[9] a) M. Steinmetz, S. Grimme, *ChemistryOpen* **2013**, *2*, 115-124; b) X. F. Xu, D. G. Truhlar, *J. Chem. Theory Comput.* **2012**, *8*, 80-90; c) S. M. Tekarli, M. L. Drummond, T. G. Williams, T. R. Cundari, A. K. Wilson, *J. Phys. Chem. A* **2009**, *113*, 8607-8614.

[10] a) A. E. Reed, L. A. Curtiss, F. Weinhold, *Chem. Rev.* **1988**, *88*, 899-926; b) J. E. Carpenter, F. Weinhold, *J. Mol. Struct. Theochem* **1988**, *46*, 41-62; c) A. E. Reed, R. B. Weinstock, F. Weinhold, *J. Chem. Phys.* **1985**, *83*, 735-746; d) A. E. Reed, F. Weinhold, *J. Chem. Phys.* **1985**, *83*, 1736-1740; e) A. E. Reed, F. Weinhold, *J. Chem. Phys.* **1983**, *78*, 4066-4073; f) J. P. Foster, F. Weinhold, *J. Am. Chem. Soc.* **1980**, *102*, 7211-7218.

[11] D. Usharani, D. C. Lacy, A. S. Borovik, S. Shaik, *J. Am. Chem. Soc.* **2013**, *135*, 17090-17104.

Paper V

JACS
JOURNAL OF THE AMERICAN CHEMICAL SOCIETY
Article
pubs.acs.org/JACS

Sequential Gas-Phase Activation of Carbon Dioxide and Methane by $[Re(CO)_2]^+$: The Sequence of Events Matters!

Shaodong Zhou,[†] Jilai Li,[†,‡] Marjan Firouzbakht,[†] Maria Schlangen,[†] and Helmut Schwarz*[,†]

[†]Institut für Chemie, Technische Universität Berlin, Straße des 17. Juni 135, 10623 Berlin, Germany
[‡]Institute of Theoretical Chemistry, Jilin University, Changchun 130023, People's Republic of China

Supporting Information

ABSTRACT: The potential of carbonyl rhenium complexes in activating and coupling carbon dioxide and methane has been explored by using a combination of gas-phase experiments (FT-ICR mass spectrometry) and high-level quantum chemical calculations. While the complexes $[Re(CO)_x]^+$ (x = 0, 1, 3) are thermally unreactive toward CO_2, $[Re(CO)_2]^+$ abstracts one oxygen atom from this substrate spontaneously at ambient conditions. Based on ^{13}C and ^{18}O labeling experiments, the newly generated CO ligand is preferentially eliminated, and two mechanistic scenarios are considered to account for this unexpected finding. The oxo complex $[ORe(CO)_2]^+$ reacts further with CH_4 to produce the dihydridomethylene complex $[ORe(CO)(CH_2)(H)_2]^+$. However, coupling of the CO and CH_2 ligands to form $CH_2{=}C{=}O$ does not take place. Further, the complexes $[Re(CO)_x(CH_2)]^+$ (x = 1, 2), generated in the thermal reaction of $[Re(CO)_x]^+$ (x = 1, 2) with CH_4, are inert toward CO_2. Mechanistic insight on the origin of this remarkable reactivity pattern has been derived from detailed quantum chemical calculations.

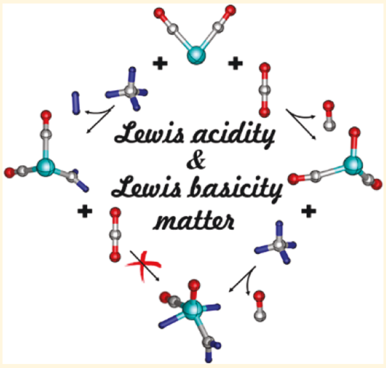

■ INTRODUCTION

Activation of CH_4[1−5] and CO_2[6−13] and their use as C1 building blocks have attracted wide research interest, and coupling of these two inert molecules[14−16] constitutes an enormous challenge. The endothermicity of 37.7 kJ mol^{-1} for the direct coupling of CH_4 and CO_2 to CH_3CO_2H and the high barriers involved in the various steps prohibit an entire catalytic cycle under liberation of the product in the gas phase under thermal conditions.[17−21] In contrast to the vast number of gas-phase studies on CH_4 activation,[1,5,22−26] there are only a few reports dealing with thermal activation of CO_2.[6] For example, some bare metal cations M^+ and metal-containing clusters give rise to oxygen-atom transfer (OAT) from CO_2;[6,27−33] this reaction is driven by the high oxophilicities of these species.[34] In addition to OAT, charge transfer accompanied by coulomb explosion can occur in the thermal reactions of CO_2 with some doubly charged cations,[35,36] and a coupled oxygen−sulfur ligand-transfer mechanism is operative in the reactions of CO_2 with diatomic $[MS]^+$ (M = Y, Zr, Nb, Sc, Ti), generating COS and MO^+.[37−39] Further, C−X bond formation is accessible under ambient conditions by the insertion of CO_2 in an $Y^+{-}X$ bond (Y = metal or non-metal atoms; X = H,[40−42] C,[28] OH[43,44]). In addition, η^2-coordinated CO_2 on $[MgOH]^+$ undergoes C−C coupling with CH_3Cl to produce an acetyl unit.[45] With regard to the direct coupling of CH_4 and CO_2 in the gas phase, however, mutually orthogonal electronic properties of the active species are required to activate and couple these two substrates.[34] So far, only Ta species were found to promote, though stoichiometrically, the activation of both molecules.[29,46,47]

In this work, we report our recent attempts to activate sequentially CH_4 and CO_2 by employing rhenium carbonyl complexes. As will be shown, while neither $[Re(CO)]^+$ nor $[Re(CO)_3]^+$ is able to activate CO_2, $[Re(CO)_2]^+$ gives rise to OAT from this substrate to generate $[ORe(CO)_2]^+$. Further, this OAT product activates two C−H bonds of methane under the elimination of CO, forming a dihydrido carbene complex. In contrast, the methylene complexes $[Re(CO)_x(CH_2)]^+$ (x = 1, 2), generated in the reaction of $[Re(CO)_x]^+$ with CH_4 under H_2 elimination,[48] are unreactive toward CO_2. Also, coupling of the CH_2 and CO ligands in the various product ions generated to produce $CH_2{=}C{=}O$ has not been achieved. Mechanistic insight and the root causes of the unexpected experimental results are revealed by using high-level quantum chemical calculations.

■ RESULTS AND DISCUSSION

Activation of CO_2. When mass-selected and thermalized $[Re(CO)_x]^+$ (x = 0−3) ions are exposed to CO_2, only $[Re(CO)_2]^+$ reacts to form $[Re,C_2,O_3]^+$; Figure 1a and eq 1.

$$[Re(CO)_2]^+ + CO_2 \rightarrow [Re, C_2, O_3]^+ + CO \tag{1}$$

The efficiency amounts to 6%, relative to the collision rate,[49] with a rate constant $k = 3.9 \times 10^{-11}$ cm^3 molecule^{-1} s^{-1}. In the reaction with $C^{18}O_2$, $[Re,C_2,O_2,^{18}O]^+$ and $[Re,C_2,O,^{18}O_2]^+$ are generated in a ratio of 1:1.7; if $^{13}CO_2$ is employed as a

Received: February 6, 2017
Published: April 12, 2017

© 2017 American Chemical Society

DOI: 10.1021/jacs.7b01255
J. Am. Chem. Soc. 2017, 139, 6169−6176

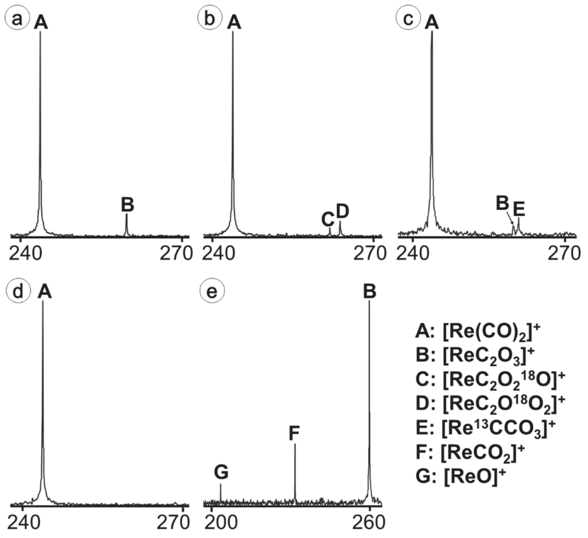

Figure 1. Mass spectra for the thermal reactions of $[Re(CO)_2]^+$ with (a) CO_2, (b) $C^{18}O_2$, (c) $^{13}CO_2$, and (d) Ar ($p = 1 \times 10^{-8}$ mbar; reaction delay 1.5s). (e) CA mass spectrum of $[Re,C_2,O_3]^+$ with Ar at E_{coll} = 5.2 eV.

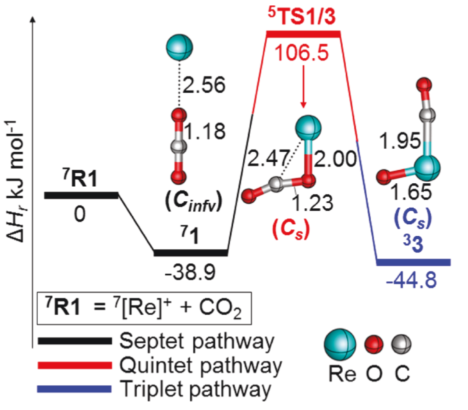

Figure 2. Simplified PES and selected structural information for the reaction of atomic $[Re]^+$ with CO_2 as calculated at the CCSD(T)/def2-TZVPP//B2GP-PLYP/def2-TZVP level of theory. Zero-point-corrected energies are given in kJ mol^{-1}, and bond lengths in Å; charges are omitted for the sake of clarity.

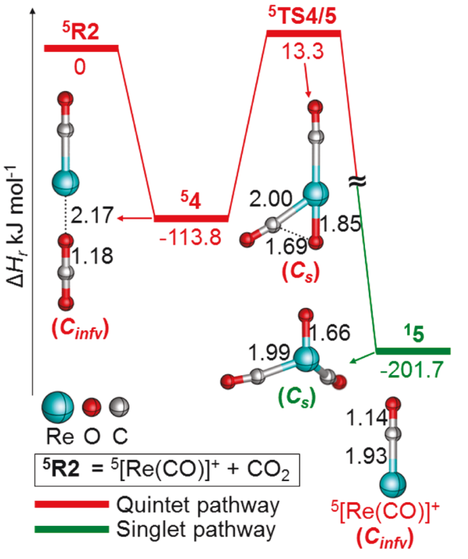

Figure 3. Simplified PES and selected structural information for the reaction of $[Re(CO)]^+$ with CO_2 as calculated at the CCSD(T)/def2-TZVPP//B2GP-PLYP/def2-TZVP level of theory. Zero-point-corrected energies are given in kJ mol^{-1}, and bond lengths in Å; charges are omitted for the sake of clarity.

substrate, within detection limit, the same ratio was obtained for the products $[Re,C_2,O_3]^+$ versus $[Re,^{13}C,C,O_3]^+$. When the mass-selected product ion $[Re,C_2,O_3]^+$ is subjected to collisional activation (CA),[50,51] up to a collision energy of E_{coll} = 5.2 eV, only $[Re,C,O_2]^+$ and $[ReO]^+$ are generated upon the losses of one and two CO molecules, respectively (Figure 1d); this observation is indicative of the presence of an oxo complex $[ORe(CO)_2]^+$. Further, the previously generated methylene complexes $[Re(CO)_x(CH_2)]^+$ (x = 1, 2)[48] were also employed in the reactions with CO_2 to check if sequential activation of CH_4 and CO_2 by carbonyl rhenium complexes can be accomplished. However, neither of them thermally reacts with CO_2.

Next, the reaction mechanisms were interrogated by high-level quantum chemical calculations. The potential-energy surfaces (PESs) of the most favorable reaction pathways, as well as some structural information on relevant intermediates involved in the reactions with CO_2, are shown in Figures 2−7. Details of alternative pathways considered as well as the total energies of all species discussed are available in the Supporting Information (SI).

As shown in Figure 2, in addition to the septet $[Re]^+$ ground state, the quintet and triplet states are also involved in the energetically most favorable PES to bring about OAT. The transformations proceed via one-step insertion of the rhenium atom into the C−O bond, i.e., ^{7}**1** → ^{5}**TS1/3** → ^{3}**3**. However, for all three spin states, this process is hindered by significant kinetic barriers located well above the entrance channel of $^7[Re]^+/CO_2$. More details are shown in the SI (Figure S1).

A one-step insertion path is also operative for the reaction of $[Re(CO)]^+$ with CO_2: as shown in Figure 3, the energetically most favorable pathway starts from an encounter complex ^{5}**4**, which is directly converted to the intermediate ^{1}**5**. While the transition state ^{5}**TS4/5** is pulled down in energy as compared to the ones for $^7[Re]^+/CO_2$, it is still energetically above the ground-state entrance channel ^{5}**R2** and thus inaccessible under thermal conditions. For the energetically highly unfavorable triplet and singlet PESs of $[Re(CO)]^+/CO_2$, more details are shown in the SI (Figure S2). These results agree with the experimental finding that neither $[Re]^+$ nor $[Re(CO)]^+$ are thermally reactive toward CO_2.

For the reaction of $[Re(CO)_2]^+$ with CO_2, eq 1, according to the calculations a two-state reactivity (TSR)[52−62] scenario may prevail. As shown in Figure 4, the triplet state $^3[Re(CO)_2]^+$ corresponds to the ground state, and the transformation starts from an encounter complex ^{3}**6**. However, the initial insertion of the rhenium atom into the OC−O bond on the triplet surface involves a transition state ^{3}**TS6/7** which is located slightly above the ground-state entrance channel ^{3}**R3**. While the thermal energy of the system may suffice to drive OAT, a spin crossing from ^{3}**6** to ^{1}**6** via a minimum energy crossing point (MECP)[63] seems to be favored, as **MECP1** is with −66 kJ mol^{-1} located well below ^{3}**R3**. From ^{1}**6**, the above-mentioned insertion step can take place by surmounting ^{1}**TS6/7** to generate the global minimum ^{1}**7**.[64] All these steps are available under ambient conditions. Subsequent liberation of a CO molecule produces $^1[ORe(CO)_2]^+$. As the three CO ligands of

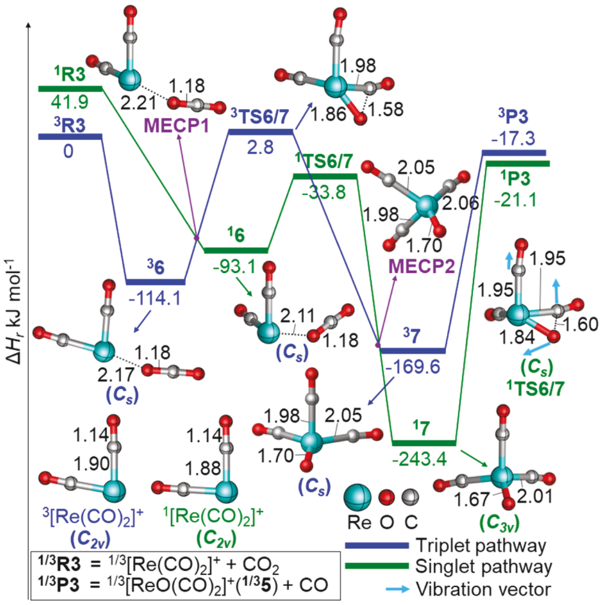

Figure 4. Simplified PES and selected structural information for the reactions of triplet and singlet spin states of $[Re(CO)_2]^+$ with CO_2 as calculated at the CCSD(T)/def2-TZVPP//B2GP-PLYP/def2-TZVP level of theory.[72] Zero-point-corrected energies are given in kJ mol^{-1}, and bond lengths in Å; charges are omitted for the sake of clarity.

^{1}7 are structurally equivalent, in the absence of kinetic isotope effects (KIEs), the branching ratio of products generated in the experiment with $C^{18}O_2$, i.e., $[^{18}ORe(CO)_2]^+$ versus $[^{18}ORe(CO)(C^{18}O)]^+$, as well as $[ORe(CO)_2]^+$ versus $[ORe(^{13}CO)(CO)]^+$ in the experiment with $^{13}CO_2$, should amount to 1:2. As "heavy-element" KIEs can be ruled out,[65] the experimentally observed ratio of 1:1.7 for both the ^{13}C and the ^{18}O labeling experiments requires different explanations.[66] One possibility invokes the operation of dynamic effects.[67] This may be indicated by the vectors for the vibrational modes of the CO ligands of ^{1}**TS6/7** (Figure 4). We note that the two Re−C bonds for the original CO ligands are of the same length as the one of the newly generated ligand (1.95 Å) in ^{1}**TS6/7**; further, all three Re−C bonds are elongated from 1.88 to 2.01 Å in the course of forming ^{1}7. However, while only a relatively minor vibration corresponds to the stretching of the original Re−C bonds, the newly generated CO ligand exhibits a much larger amplitude. Thus, this newly generated CO ligand is more prone to be liberated from the metal center provided the intramolecular energy distribution of the rovibrationally hot intermediate ^{1}7 is not complete (non-ergodic behavior[66−71]). However, this interpretation has been questioned by a reviewer, who suggested an alternative explanation: (i) the kinetic energy of the $[Re(CO)_2]^+/CO_2$ system may be sufficient to traverse ^{3}**TS6**/7, and (ii) the uncertainties of the calculations cannot guarantee that this transition state is indeed located above ^{3}**R3**.[72] Further, if spin−orbit coupling may not be efficient enough to bring about the triplet-singlet switch at **MECP1**, some fraction of the reactive ensemble may well stay on its triplet surface throughout the OAT from CO_2 to $[Re(CO)_2]^+$, or provided spin−orbit coupling is efficient ^{3}7 may be accessed via **MECP2**.[64] As the three CO ligands will never become equivalent on the triplet surface, the newly generated CO ligand will be evaporated preferentially, in line with the labeling experiments. A conclusive distinction between these two (and possibly other mechanistic variants) cannot be made for the time being.

Upon ligation of the rhenium center with a third CO ligand, a rather inert closed-shell complex $^1[Re(CO)_3]^+$ is formed. As shown in Figure 5, on energetic ground CO_2 activation via insertion of the rhenium atom into the OC−O bond is not possible for the singlet state of $[Re(CO)_3]^+$ at ambient conditions. The triplet pathway is even higher in energy, as shown in the SI (Figure S3).

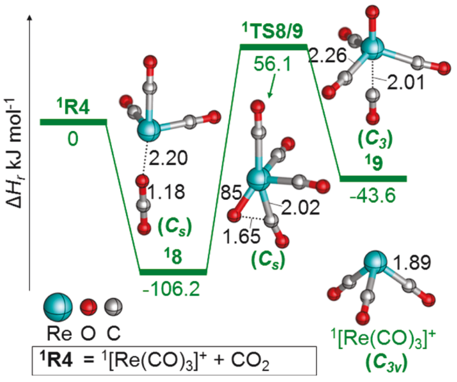

Figure 5. Simplified PES and selected structural information for the reactions of singlet $[Re(CO)_3]^+$ with CO_2 as calculated at the CCSD(T)/def2-TZVPP//B2GP-PLYP/def2-TZVP level of theory. Zero-point-corrected energies are given in kJ mol^{-1}, and bond lengths in Å; charges are omitted for the sake of clarity.

Next, we will present the computational findings for the $[Re(CO)_x(CH_2)]^+/CO_2$ (x = 1, 2) couples. In addition to the OAT via insertion of Re into a C−O bond of CO_2 (**10** → **11**, Figure 6; **13** → **14**, Figure 7), we also considered the C−C coupling via insertion of the $ReCH_2$ unit into the O−CO bond (**10** → **12**, Figure 6; **13** → **15**, Figure 7). However, none of these thermochemically exothermic transformations is accessible under thermal conditions for either spin state, as all associated transition states are located above the respective entrance channel. More details are shown in the SI (Figures S4 and S5).

To obtain further insight into the above-described processes, an analysis of the associated molecular orbitals (MOs) was performed. To allow for CO_2 activation at a transition-metal center, the Lewis-pair interaction between the two reactants is crucial:[73,74] a low-lying empty π-type orbital at the metal center favors accepting electrons from the highest occupied molecular orbital (HOMO) of CO_2 ($1\pi_u(CO_2)$), while a high-lying occupied π-type orbital of the metal facilitates electron back-donating to the lowest unoccupied molecular orbital (LUMO) of CO_2 ($2\pi^*{}_u(CO_2)$). Thus, the inertness of bare $[Re]^+$ toward CO_2 is attributed to its septet, high-spin ground state ($6s^15d^5$) with a stable half-filled valence shell that provides neither a low-lying empty orbital nor a high-lying doubly occupied orbital; spin-pairing by lifting the degeneracy requires too much energy.[75] The orbital diagrams for the interaction of CO_2 with the various rhenium complexes investigated are shown in Figure 8. According to the calculations, the energy gap between the HOMO of $[Re]^+$ and the LUMO of CO_2 amounts to 18.3 eV, and the one between the HOMO of CO_2 and the LUMO of $[Re]^+$ is 7.6 eV. Upon CO coordination, the former gap does not change much, while the latter shrinks considerably since the CO-ligation lowers the energy of the empty $6p$(Re) orbitals.[48] Thus, while the energy gaps between the HOMOs of

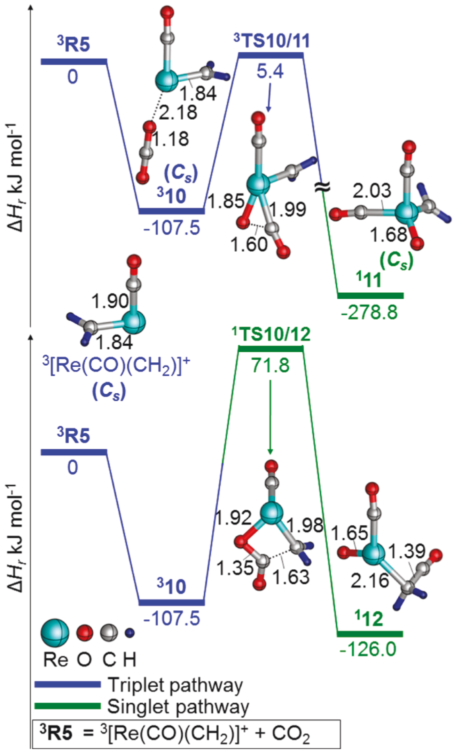
ΔHr kJ mol-1
3R5
0
3TS10/11
5.4
1.84
2.18
1.18
(Cs)
310
-107.5
1.85
1.99
1.60
≈
2.03
1.68
(Cs)
111
-278.8
1.90
1.84
3[Re(CO)(CH2)]+
(Cs)
1TS10/12
71.8
ΔHr kJ mol-1
3R5
0
1.92
1.98
1.35
1.63
1.65
1.39
2.16
310
-107.5
112
-126.0
Re O C H
Triplet pathway
Singlet pathway
3R5 = 3[Re(CO)(CH2)]+ + CO2

Figure 6. Simplified PES and selected structural information for the reactions of $[Re(CO)(CH_2)]^+$ with CO_2 as calculated at the CCSD(T)/def2-TZVPP//B2GP-PLYP/def2-TZVP level of theory. Zero-point-corrected energies are given in kJ mol^{-1}, and bond lengths in Å; charges are omitted for the sake of clarity.

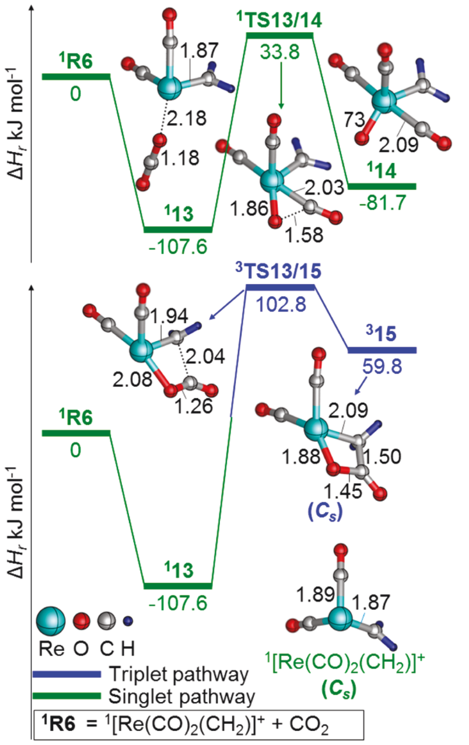
ΔHr kJ mol-1
1R6
0
1.87
2.18
1.18
113
-107.6
1TS13/14
33.8
1.86
2.03
1.58
73
2.09
114
-81.7
3TS13/15
102.8
ΔHr kJ mol-1
1.94
2.04
2.08
1.26
1R6
0
315
59.8
2.09
1.88
1.50
1.45
(Cs)
113
-107.6
1.89
1.87
1[Re(CO)2(CH2)]+
(Cs)
Re O C H
Triplet pathway
Singlet pathway
1R6 = 1[Re(CO)2(CH2)]+ + CO2

Figure 7. Simplified PES and selected structural information for the reactions of $[Re(CO)_2(CH_2)]^+$ with CO_2 as calculated at the CCSD(T)/def2-TZVPP//B2GP-PLYP/def2-TZVP level of theory. Zero-point-corrected energies are given in kJ mol^{-1}, and bond lengths in Å; charges are omitted for the sake of clarity.

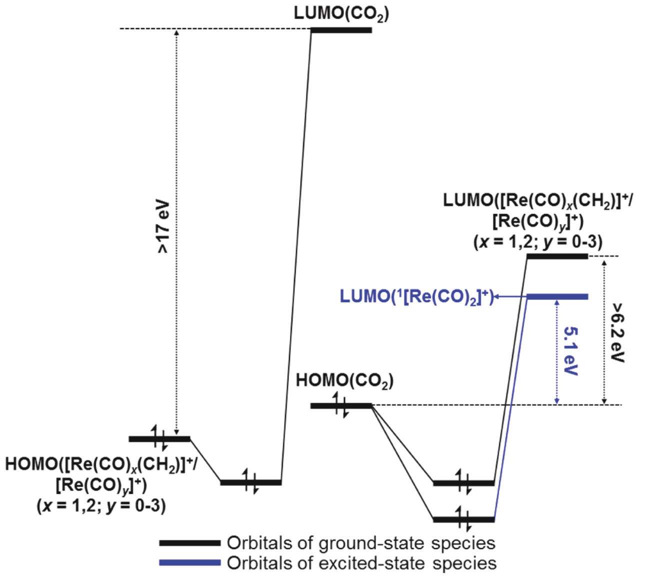
LUMO(CO2)
>17 eV
LUMO([Re(CO)x(CH2)]+/
[Re(CO)y]+)
(x = 1,2; y = 0-3)
LUMO(1[Re(CO)2]+)
5.1 eV
>6.2 eV
HOMO(CO2)
HOMO([Re(CO)x(CH2)]+/
[Re(CO)y]+)
(x = 1,2; y = 0-3)
Orbitals of ground-state species
Orbitals of excited-state species

Figure 8. Orbital diagrams for the interaction of CO_2 with selected Re complexes.

$[Re(CO)]^+$, $[Re(CO)_2]^+$, and $[Re(CO)_3]^+$ and the LUMO of CO_2 remain in the range of 18.0−18.3 eV, the splittings between the HOMO of CO_2 and the LUMOs of $[Re(CO)]^+$, $[Re(CO)_2]^+$, and $[Re(CO)_3]^+$) decrease to 6.2−6.4 eV. However, given the fact that $[Re(CO)]^+$ and $[Re(CO)_3]^+$ remain inert toward CO_2, the latter energy gaps are obviously still too high to afford thermal activation of CO_2. The distinctive behavior of $[Re(CO)_2]^+$ is related to the relatively low excitation energy necessary for promotion of the triplet ground state to the singlet state (42 kJ mol^{-1}), such that a spin-crossing for $[Re(CO)_2]^+/CO_2$ is energetically accessible under thermal conditions. One of the 5*d* orbitals of the excited $^1[Re(CO)_2]^+$ is empty, resulting in an even lower HOMO-(CO_2)−LUMO($^1[Re(CO)_2]^+$) gap of 5.1 eV; thus, CO_2 activation via such a donor−acceptor interaction is facilitated. As to the methylene complexes $[Re(CO)_x(CH_2)]^+$ (x = 1, 2), for their ground states the HOMO($[Re(CO)_x(CH_2)]^+$)−LUMO(CO_2) and HOMO(CO_2)−LUMO($[Re(CO)_x(CH_2)]^+$) energy gaps are with >17 eV and >6.2 eV, respectively, again much too large to engage in CO_2 activation. While excited $^1[Re(CO)(CH_2)]^+$ has an empty 5*d*(Re) orbital resulting in a relatively low HOMO(CO_2)−LUMO($^1[Re(CO)(CH_2)]^+$ gap of 5.2 eV, the rather high excitation energy $^3[Re(CO)(CH_2)]^+ \rightarrow {}^1[Re(CO)(CH_2)]^+$ (68 kJ mol^{-1}) pushes up energetically the singlet pathways in the PES, thus making it inaccessible under ambient conditions.

Obviously, for the rhenium complexes considered here, their reactivities toward CO_2 via insertion of the metal atom into the OC−O bond depends crucially on the energy required to generate an empty 5*d*(Re) orbital.

Attempted Methane Activation and Its Coupling with CO To Form $CH_2{=}C{=}O$. When mass-selected and thermalized $[ORe(CO)_2]^+$ ions are exposed to CH_4, only $[Re,C_2,H_4,O_2]^+$ is generated; this process corresponds to a formal CO/CH_4 ligand exchange (Figure 9a and eq 2; note that

$$[ORe(CO)_2]^+ + CH_4 \rightarrow [Re, C_2, H_4, O_2]^+ + CO \qquad (2)$$

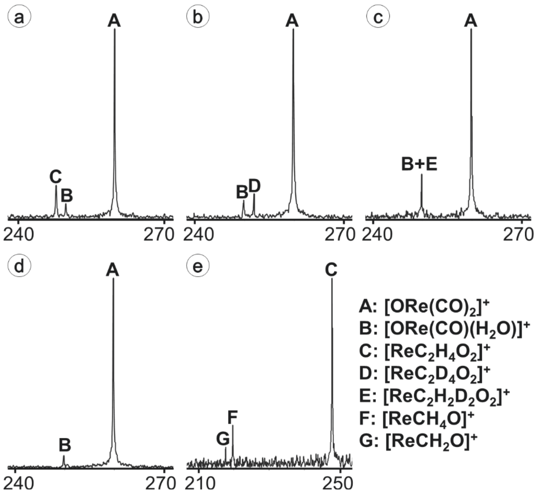

Figure 9. Mass spectra for the thermal reactions of $[ORe(CO)_2]^+$ with (a) CH_4, (b) CD_4, (c) CH_2D_2, and (d) Ar ($p = 2 \times 10^{-9}$ mbar; reaction delay 2 s). (e) CA mass spectrum of $[Re,C_2,H_4,O_2]^+$ with Ar at $E_{coll} = 5.1$ eV.

the formation of $[ORe(CO)(H_2O)]^+$ is due to the reaction of $[Re(CO)_2]^+$ with background H_2O as revealed by the reference spectrum shown in Figure 9d). After considering the contribution of the reaction with background water, the efficiency amounts to 26%, with a rate constant $k = 2.6 \times 10^{-10}$ cm^3 molecule^{-1} s^{-1}. In the reaction with CD_4, the rate constant decreases to $k = 2.0 \times 10^{-10}$ cm^3 molecule^{-1} s^{-1}; thus, an overall intermolecular kinetic isotope effect, KIE = 1.3, is operative. When mass-selected $[Re,C_2,H_4,O_2]^+$ is subjected to CA, only $[Re,C,H_4,O]^+$ is generated upon elimination of CO at low collision energy (e.g., $E_{coll} = 3.5$ eV); at a collision energy of up to $E_{coll} = 5.1$ eV another ionic product $[Re,C,H_2,O]^+$ corresponding to the loss of (C,H_2,O) appears (Figures 9e). These findings are compatible with structural assignments of the product ion as $[ORe(CO)(CH_2)(H)_2]^+$, $[Re(CO)(CH_2O)(H)_2]^+$, or $[Re(CO)(OH)(CH)(H)_2]^+$, respectively.

Mechanistic aspects of the reaction were addressed in high-level quantum chemical calculations. The PESs of the most favorable reaction pathways, as well as some structural information on relevant coordinates, are shown in Figure 10. All transformations are confined to the singlet surface; while the triplet $^3[ORe(CO)_2]^+$ is only 4 kJ mol^{-1} above the ground-state $^1[ORe(CO)_2]^+$ (obtained at CCSD(T)/def2-QZVPP//B2GP-PLYP/def2-TZVP level of theory), all the other conceivable triplet species along the reaction coordinate are much higher in energy as compared to the corresponding singlet ones (see SI, Table S8) and therefore not further considered here. Starting from an encounter complex **^{1}16**, oxidative insertion of the rhenium atom into the $H_3C{-}H$ bond via **^{1}TS16/17** takes place to generate **^{1}17**. Next, by surmounting **^{1}TS17/18** and **^{1}TS18/19**, another C−H bond is cleaved, thus transfering a second hydrogen atom to the metal center to form **^{1}19**. The latter liberates a CO molecule to produce $^1[ORe(CO)(CH_2)(H)_2]^+$. While the production of **^{1}P7a** is higher in enthalpy as compared to **^{1}TS18/19**, the former is entropically much more favorable.[76−78] Accordingly, the hydrogen-transfer step **^{1}18** → **^{1}19** is rate-limiting for the whole reaction process, in line with an experimentally observed KIE > 1.

For the initial $H_3C{-}H$ bond activation, in addition to an oxidative addition of CH_4 to the Re center as described above, insertion of the Re−O moiety into the $H_3C{-}H$ bond has also been considered. However, this process is kinetically impeded as the associated transition state (**^{1}TS16/20**, Figure 10) is energetically located well above the entrance channel **^{1}R7**. Further, the energetics for the conceivable formation of $^1[Re(CO)(OH)(CH)H_2]^+$ + CO (**^{1}P7b**) has also been calculated;

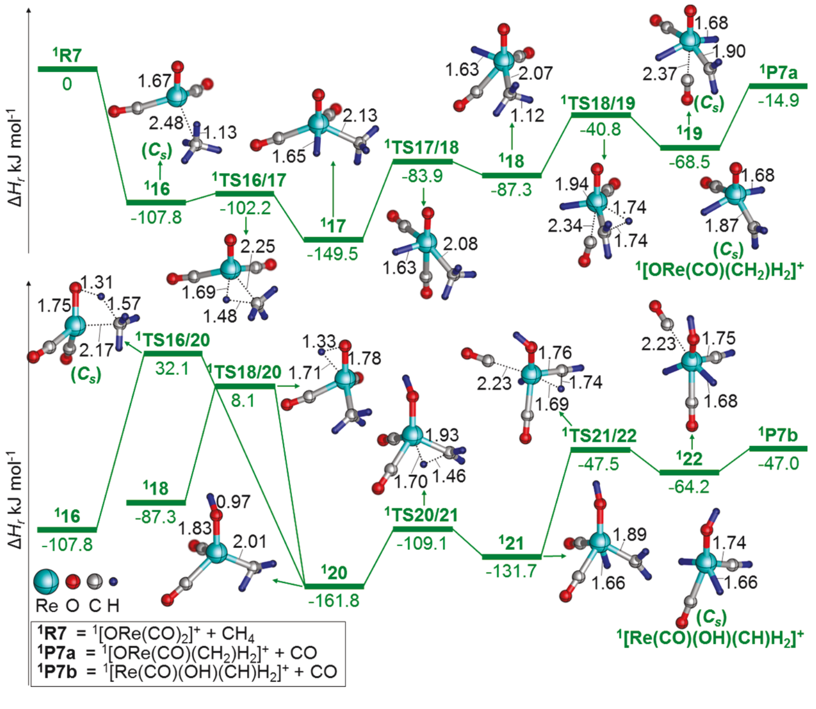
ΔH_f kJ mol^{-1}
^{1}R7
0
^{1}16
-107.8
^{1}TS16/17
-102.2
^{1}17
-149.5
^{1}TS17/18
-83.9
^{1}18
-87.3
^{1}TS18/19
-40.8
^{1}19
-68.5
^{1}P7a
-14.9
(C$_s$)
1.67
2.48
1.13
2.13
1.65
2.25
1.69
1.48
2.08
1.63
1.63
2.07
1.12
1.68
1.90
2.37
1.94
1.74
2.34
1.74
1.68
1.87
^{1}[ORe(CO)(CH$_2$)H$_2$]$^+$
ΔH_f kJ mol^{-1}
^{1}16
-107.8
^{1}TS16/20
32.1
^{1}18
-87.3
^{1}TS18/20
8.1
^{1}20
-161.8
^{1}TS20/21
-109.1
^{1}21
-131.7
^{1}TS21/22
-47.5
^{1}22
-64.2
^{1}P7b
-47.0
1.31
1.75
1.57
2.17
1.33
1.71
1.78
0.97
1.83
2.01
1.93
1.70
1.46
1.76
2.23
1.74
1.69
1.89
1.66
2.23
1.75
1.68
1.74
1.66
^{1}[Re(CO)(OH)(CH)H$_2$]$^+$
Re O C H
^{1}R7 = ^{1}[ORe(CO)$_2$]$^+$ + CH$_4$
^{1}P7a = ^{1}[ORe(CO)(CH$_2$)H$_2$]$^+$ + CO
^{1}P7b = ^{1}[Re(CO)(OH)(CH)H$_2$]$^+$ + CO

Figure 10. PES and selected structural information for the reaction of $[ORe(CO)_2]^+$ with CH_4 as calculated at the CCSD(T)/def2-TZVPP//B2GP-PLYP/def2-TZVP level of theory. Zero-point-corrected energies are given in kJ mol^{-1}, and bond lengths in Å; charges are omitted for the sake of clarity.

here, the energetically most favorable pathway corresponds to ^{1}**16** → ^{1}**17** → ^{1}**18** → ^{1}**20** → ^{1}**21** → ^{1}**22**. Although the generation of ^{1}**P7b** is more exothermic than that of ^{1}[ORe(CO)(CH$_2$)H$_2$]$^+$ + CO (^{1}**P7a**), the former is kinetically much less favorable as the transition state ^{1}**TS18/20** is 8 kJ mol^{-1} higher in energy as compared to ^{1}**R7** not to speak of the entropic advantage of the step ^{1}**19** → ^{1}**P7a**; thus, the path leading to ^{1}**P7b** is hardly accessible under thermal conditions. Finally, the generation of the other conceivable product ^{1}[Re(CO)(CH$_2$O)H$_2$]$^+$ has also been considered; however, this process is endothermic by 143 kJ mol^{-1}. In conclusion, the product ion generated in Equation 2 most likely corresponds to the complex [ORe(CO)(CH$_2$)(H)$_2$]$^+$, which upon CA gives rise to the consecutive elimination of CO and H$_2$.

Next, a Natural Bond Orbital (NBO) analysis was performed to gain further insight into the initial H$_3$C−H bond activation steps. Figure 11 shows those orbitals that participate in the steps ^{1}**16** → ^{1}**17**/^{1}**20**; as will be shown, both reactions have the characteristic features of a proton-coupled electron transfer (PCET)[79,80] process. For example, in the step ^{1}**16** → ^{1}**20** a proton is abstracted from methane by an oxygen atom via conversion of an electron pair from the doubly occupied π(Re−O) orbital to the σ(O−H) orbital to make the new O−H bond in ^{1}**TS16/20**; accordingly, the electron pair of the original σ(H$_3$C−H) bond is donated to the empty n(Re) orbital to form a Re−C bond. For the energetically clearly favored path ^{1}**16** → ^{1}**17**, by donation of the electron pair of the original σ(H$_3$C−H) bond to the empty n(Re) orbital, a three-center-two-electron bond (σ(Re−H−C)) is formed in ^{1}**TS16/17**. A proton is stripped from the three-center unit at a point adjacent to ^{1}**TS16/17** in the forward IRC path (**IRC1**). Next, the proton is transfered and accepted by the 5d(Re) orbital to form a σ(Re−H) bond; simultaneously, the σ(Re−C) bond is generated. All these processes are followed by subsequent reorganization of the electronic structures. The higher barrier for the step ^{1}**16** → ^{1}**20** as compared to ^{1}**16** → ^{1}**17** is due to the weaker Lewis basicity of the oxygen atom in the complex. This is reflected by the finding that the doubly occupied π(Re−O) orbital, which is formed from the electron pair of the 2p(O) orbital, is lower in energy than the highest, doubly occupied 5d(Re) orbital by 4.0 eV. Interestingly, during the H$_3$C−H bond activation step, rhenium serves as both a Lewis base and acid. Thus, it is this amphoteric character, strongly enhanced by ligation, that enables the thermal activation of CO$_2$ and CH$_4$ by the rhenium center.

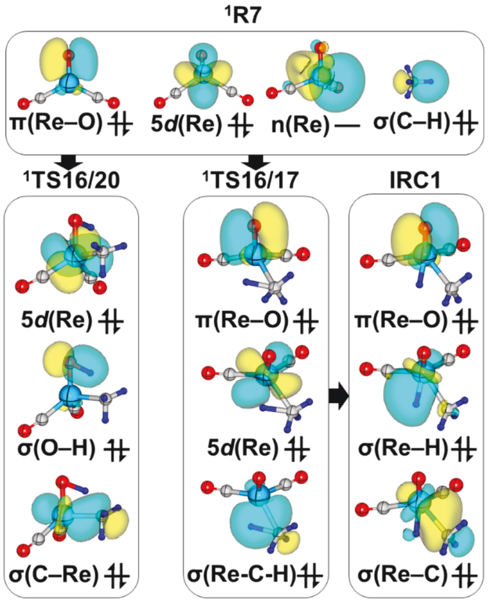

Figure 11. Schematic orbital diagrams represented by natural bond orbitals for the separated reactant ^{1}**R7** and the transition states in the steps ^{1}**16** → ^{1}**17**/^{1}**20**. The cyan and yellow surfaces represent positive and negative phases of the wave functions, respectively.

Finally, while the carbonyl complex [Re(CO)$_2$]$^+$ activates sequentially both CO$_2$ and CH$_4$, the coupling of these two inert molecules is not possible under thermal conditions. To reform CO$_2$ with CH$_4$, the utilization of the hydrido, oxo, and methylene ligands in [ORe(CO)(CH$_2$)H$_2$]$^+$ may matter; it remains to be studied whether or not this hydrido methylene complex can be isomerized to more reactive intermediates at elevated temperatures, or may serve as a reactive partner to bring about thermal activation of other small, inert molecules.

■ CONCLUSION

We have presented a combined experimental/computational investigation on the thermal activation of carbon dioxide and methane by carbonyl rhenium complexes in the gas phase. In the thermal interaction of [Re(CO)$_x$]$^+$ (x = 0−3) with CO$_2$, only [Re(CO)$_2$]$^+$ is capable of abstracting one oxygen atom from this substrate; next, the ionic product [ORe(CO)$_2$]$^+$ activates C−H bonds of methane to produce a hydrido methylene complex [ORe(CO)(CH$_2$)(H)$_2$]$^+$. Reversing the activation steps, i.e., sequential activation of first CH$_4$ and then CO$_2$, is not possible under thermal conditions. The unique reactivity of [Re(CO)$_2$]$^+$ toward CO$_2$ among all investigated rhenium complexes is attributed to its rather low excitation energy from the triplet ground state to a reactive singlet state; the existence of one empty 5d orbital in ^{1}[Re(CO)$_2$]$^+$ exhibits strong Lewis acid character, thus facilitating thermal CO$_2$ activation. For the activation of CH$_4$ by [ORe(CO)$_2$]$^+$, both the Lewis base and acid characters of the rhenium center are crucial in the initial insertion of the rhenium atom into the H$_3$C−H bond via PECT. Thus, it is the amphoteric character of rhenium, enhanced by ligation, that enables the thermal reactivities of this complex toward both CO$_2$ and CH$_4$. Coupling of the C1 fragments CO and CH$_2$ to form CH$_2$CO does not take place.

■ ASSOCIATED CONTENT

Supporting Information

The Supporting Information is available free of charge on the ACS Publications website at DOI: 10.1021/jacs.7b01255.

> Experimental and computational details, additional potential energy surfaces, Cartesian coordinates, and absolute energies for key calculated species (PDF)

■ AUTHOR INFORMATION

Corresponding Author

*helmut.schwarz@tu-berlin.de

ORCID

Jilai Li: 0000-0002-3363-9164

Helmut Schwarz: 0000-0002-3369-7997

Notes

The authors declare no competing financial interest.

■ ACKNOWLEDGMENTS

Generous financial support by the Fonds der Chemischen Industrie and the Deutsche Forschungsgemeinschaft ("UniCat") is appreciated. We thank Dr. Thomas Weiske for technical assistance and an anonymous reviewer for persistent and insightful comments on the reaction of $[Re(CO)_2]^+$ with CO_2. This article is dedicated to Prof. Itamar Willner, The Hebrew University of Jerusalem, on the occasion of his 70th birthday.

■ REFERENCES

(1) Schwarz, H. *Isr. J. Chem.* **2014**, *54*, 1413−1431.
(2) Tang, P.; Zhu, Q. J.; Wu, Z. X.; Ma, D. *Energy Environ. Sci.* **2014**, *7*, 2580−2591.
(3) Ding, X. L.; Wu, X. N.; Zhao, Y. X.; He, S. G. *Acc. Chem. Res.* **2012**, *45*, 382−390.
(4) Cavaliere, V. N.; Mindiola, D. J. *Chem. Sci.* **2012**, *3*, 3356−3365.
(5) Schwarz, H. *Angew. Chem., Int. Ed.* **2011**, *50*, 10096−10115.
(6) Schwarz, H. *Coord. Chem. Rev.* **2017**, *334*, 112−123.
(7) Bontemps, S. *Coord. Chem. Rev.* **2016**, *308*, 117−130.
(8) Fiorani, G.; Guo, W. S.; Kleij, A. W. *Green Chem.* **2015**, *17*, 1375−1389.
(9) Yang, L. H.; Wang, H. M. *ChemSusChem* **2014**, *7*, 962−998.
(10) Wang, W.; Wang, S. P.; Ma, X. B.; Gong, J. L. *Chem. Soc. Rev.* **2011**, *40*, 3703−3727.
(11) Mikkelsen, M.; Jorgensen, M.; Krebs, F. C. *Energy Environ. Sci.* **2010**, *3*, 43−81.
(12) Morris, A. J.; Meyer, G. J.; Fujita, E. *Acc. Chem. Res.* **2009**, *42*, 1983−1994.
(13) Yin, X. L.; Moss, J. R. *Coord. Chem. Rev.* **1999**, *181*, 27−59.
(14) Huang, W.; Sun, W. Z.; Li, F. *AIChE J.* **2010**, *56*, 1279−1284.
(15) Sellers, H.; Spiteri, R. J.; Perrone, M. *J. Phys. Chem. C* **2009**, *113*, 2340−2346.
(16) Shi, D. X.; Feng, Y. Q.; Zhong, S. H. *Catal. Today* **2004**, *98*, 505−509.
(17) *Thermodynamic Properties of Individual Substances*; Gurvich, L. V., Veyts, I. V., Alcock, C. B., Eds.; Hemisphere Publ. Corp.: New York, 1991.
(18) In *CODATA Key Values for Thermodynamics*, 4th ed.; Cox, J. D., Wagman, D. D., Medvedev, V. A., Eds.; Hemisphere Publ. Corp.: New York, 1984; Vol. 2.
(19) For a recent review, see: Schwarz, H. *Angew. Chem., Int. Ed.* **2015**, *54*, 10090−10100.
(20) *Catalytic Activation of Carbon Dioxide*; ACS Symposium Series; Ayers, W. M., Ed.; American Chemical Society: Washington, DC, 1988.
(21) Behr, A. *Carbon Dioxide Activation by Metal Complexes*; VCH: Weinheim, 1988.
(22) Armentrout, P. B. *Chem. - Eur. J.* **2017**, *23*, 10−18.
(23) Schwarz, H. *Chem. Phys. Lett.* **2015**, *629*, 91−101.
(24) Dietl, N.; Schlangen, M.; Schwarz, H. *Angew. Chem., Int. Ed.* **2012**, *51*, 5544−5555.
(25) Schröder, D. *Angew. Chem., Int. Ed.* **2010**, *49*, 850−851.
(26) Schröder, D.; Schwarz, H. *Proc. Natl. Acad. Sci. U. S. A.* **2008**, *105*, 18114−18119.
(27) Canale, V.; Robinson, R.; Zavras, A.; Khairallah, G. N.; d'Alessandro, N.; Yates, B. F.; O'Hair, R. A. J. *J. Phys. Chem. Lett.* **2016**, *7*, 1934−1938.
(28) Firouzbakht, M.; Schlangen, M.; Kaupp, M.; Schwarz, H. *J. Catal.* **2016**, *343*, 68−74.
(29) Firouzbakht, M.; Rijs, N. J.; Gonzalez-Navarrete, P.; Schlangen, M.; Kaupp, M.; Schwarz, H. *Chem. - Eur. J.* **2016**, *22*, 10581−10589.
(30) Ricks, A. M.; Brathwaite, A. D.; Duncan, M. A. *J. Phys. Chem. A* **2013**, *117*, 11490−11498.
(31) Hossain, E.; Rothgeb, D. W.; Jarrold, C. C. *J. Chem. Phys.* **2010**, *133*, 024305.
(32) Koyanagi, G. K.; Bohme, D. K. *J. Phys. Chem. A* **2006**, *110*, 1232−1241.
(33) Kappes, M. M.; Staley, R. H. *J. Phys. Chem.* **1981**, *85*, 942−944.
(34) Li, J.; Gonzalez-Navarrete, P.; Schlangen, M.; Schwarz, H. *Chem. - Eur. J.* **2015**, *21*, 7780−7789.
(35) Lourenco, C.; Michelini, M. D.; Marcalo, J.; Gibson, J. K.; Oliveira, M. C. *J. Phys. Chem. A* **2012**, *116*, 12399−12405.
(36) Santos, M.; Michelini, M. D.; Lourenco, C.; Marcalo, J.; Gibson, J. K.; Oliveira, M. C. *J. Phys. Chem. A* **2012**, *116*, 3534−3540.
(37) Kretzschmar, I.; Schröder, D.; Schwarz, H.; Armentrout, P. B. *Int. J. Mass Spectrom.* **2006**, *249*, 263−278.
(38) Kretzschmar, I.; Schröder, D.; Schwarz, H.; Rue, C.; Armentrout, P. B. *J. Phys. Chem. A* **2000**, *104*, 5046−5058.
(39) Kretzschmar, I.; Schröder, D.; Schwarz, H.; Rue, C.; Armentrout, P. B. *J. Phys. Chem. A* **1998**, *102*, 10060−10073.
(40) Zhang, X. X.; Liu, G. X.; Meiwes-Broer, K. H.; Gantefor, G.; Bowen, K. *Angew. Chem., Int. Ed.* **2016**, *55*, 9644−9647.
(41) Tang, S. Y.; Rijs, N. J.; Li, J.; Schlangen, M.; Schwarz, H. *Chem. - Eur. J.* **2015**, *21*, 8483−8490.
(42) Hajdasz, D. J.; Ho, Y. H.; Squires, R. R. *J. Am. Chem. Soc.* **1994**, *116*, 10751−10760.
(43) Petrie, S. *Int. J. Mass Spectrom.* **2006**, *254*, 136−144.
(44) Schröder, D.; Schwarz, H.; Schenk, S.; Anders, E. *Angew. Chem., Int. Ed.* **2003**, *42*, 5087−5090.
(45) Dossmann Soldi-Lose, H.; Afonso, C.; Lesage, D.; Tabet, J. C.; Uggerud, E. *Angew. Chem., Int. Ed.* **2012**, *51*, 6938−6941.
(46) Wesendrup, R.; Schwarz, H. *Angew. Chem., Int. Ed. Engl.* **1995**, *34*, 2033−2035.
(47) Sändig, N.; Koch, W. *Organometallics* **1998**, *17*, 2344−2351.
(48) Zhou, S.; Li, J.; Schlangen, M.; Schwarz, H. *Angew. Chem., Int. Ed.* **2017**, *56*, 2951−2954.
(49) Bowers, M. T.; Laudenslager, J. B. *J. Chem. Phys.* **1972**, *56*, 4711−4712.
(50) Levsen, K.; Schwarz, H. *Mass Spectrom. Rev.* **1983**, *2*, 77−148.
(51) Levsen, K.; Schwarz, H. *Angew. Chem., Int. Ed. Engl.* **1976**, *15*, 509−519.
(52) Harvey, J. N. *WIREs Comput. Mol. Sci.* **2014**, *4*, 1−14.
(53) Shaik, S. *Int. J. Mass Spectrom.* **2013**, *354*, 5−14.
(54) Shaik, S.; Hirao, H.; Kumar, D. *Acc. Chem. Res.* **2007**, *40*, 532−542.
(55) Nam, W. *Acc. Chem. Res.* **2007**, *40*, 522−531.
(56) Siegbahn, P. E. M.; Borowski, T. *Acc. Chem. Res.* **2006**, *39*, 729−738.
(57) Shaik, S.; Kumar, D.; de Visser, S. P.; Altun, A.; Thiel, W. *Chem. Rev.* **2005**, *105*, 2279−2328.
(58) Schwarz, H. *Int. J. Mass Spectrom.* **2004**, *237*, 75−105.
(59) Shaik, S.; de Visser, S. P.; Ogliaro, F.; Schwarz, H.; Schröder, D. *Curr. Opin. Chem. Biol.* **2002**, *6*, 556−567.
(60) Schröder, D.; Shaik, S.; Schwarz, H. *Acc. Chem. Res.* **2000**, *33*, 139−145.
(61) Shaik, S.; Filatov, M.; Schröder, D.; Schwarz, H. *Chem. - Eur. J.* **1998**, *4*, 193−199.
(62) Armentrout, P. B. *Science* **1991**, *251*, 175−179.
(63) Harvey, J. N.; Aschi, M.; Schwarz, H.; Koch, W. *Theor. Chem. Acc.* **1998**, *99*, 95−99.
(64) As shown in Figure 4, after having traversed ^{1}**TS6/7**, a further spin change via **MECP2** is possible.
(65) According to the calculations, the zero-point vibrational energies of the various ^{18}O- and ^{13}C-labeled isotopologues generated along the singlet surface differ by <0.1 kJ mol^{-1}. Thus, significant KIEs can be ruled out.
(66) A similar non-statistical behavior was recently reported for the generation of CH_3OH from the couple $[OSi(OH)]^+/CH_4$: Sun, X.; Zhou, S.; Schlangen, M.; Schwarz, H. *Chem. - Eur. J.* **2016**, *22*, 14257−14263.
(67) For a recent Perspective article on this topic, see: Carpenter, B. K.; Harvey, J. N.; Orr-Ewing, A. J. *J. Am. Chem. Soc.* **2016**, *138*, 4695−4705 and numerous references therein.
(68) Carpenter, B. K. *Annu. Rev. Phys. Chem.* **2005**, *56*, 57−89.

(69) Hase, W. L. *Science* **1994**, *266*, 998−1002.

(70) Depke, G.; Lifshitz, C.; Schwarz, H.; Tzidony, E. *Angew. Chem., Int. Ed. Engl.* **1981**, *20*, 792−793.

(71) Oref, I.; Rabinovitch, B. S. *Acc. Chem. Res.* **1979**, *12*, 166−175.

(72) According to more advanced calculations performed at the relativistic CCSD(T)/cc-pVTZ-dk level of theory, ^{3}**TS6/7** is located 1.1 kJ mol^{-1} above the entrance channel.

(73) Schneider, J.; Jia, H. F.; Muckerman, J. T.; Fujita, E. *Chem. Soc. Rev.* **2012**, *41*, 2036−2051.

(74) Drees, M.; Cokoja, M.; Kuhn, F. E. *ChemCatChem* **2012**, *4*, 1703−1712.

(75) Armentrout, M. M.; Li, F. X.; Armentrout, P. B. *J. Phys. Chem. A* **2004**, *108*, 9660−9672.

(76) There is extensive experimental evidence that adsorption of CO is accompanied by a significant entropy loss (refs 77 and 78). Consequently, liberation of CO lowers the free energy of ^{1}**P7a** by ca. 30 kJ mol^{-1} relative to that of ^{1}**TS18/19**.

(77) Pursell, C. J.; Hartshorn, H.; Ward, T.; Chandler, B. D.; Boccuzzi, F. *J. Phys. Chem. C* **2011**, *115*, 23880−23892.

(78) Garrone, E.; Bonelli, B.; Tsyganenko, A. A.; Dalgado, M. R.; Palomino, G. T.; Manoilova, O. V.; Arean, C. O. *J. Phys. Chem. B* **2003**, *107*, 2537−2542.

(79) For recent reviews on PCET, see: (a) Hammes-Schiffer, S. *J. Am. Chem. Soc.* **2015**, *137*, 8860−8871. (b) Migliore, A.; Polizzi, N. F.; Therien, M. J.; Beratan, D. N. *Chem. Rev.* **2014**, *114*, 3381−3465. (c) Weinberg, D. R.; Gagliardi, C. J.; Hull, J. F.; Murphy, C. F.; Kent, C. A.; Westlake, B. C.; Paul, A.; Ess, D. H.; McCafferty, D. G.; Meyer, T. J. *Chem. Rev.* **2012**, *112*, 4016−4093. (d) Warren, J. J.; Tronic, T. A.; Mayer, J. M. *Chem. Rev.* **2010**, *110*, 6961−7001. (e) Siegbahn, P. E. M.; Blomberg, M. R. A. *Chem. Rev.* **2010**, *110*, 7040−7061. (f) Hammes-Schiffer, S. *Chem. Rev.* **2010**, *110*, 6937−6938.

(80) For recent examples of gas-phase PCET processes, see: (a) Schwarz, H.; González-Navarrete, P.; Li, J.; Schlangen, M.; Sun, X.; Weiske, T.; Zhou, S. *Organometallics* **2017**, *36*, 8−17. (b) Li, J.; Zhou, S.; Zhang, J.; Schlangen, M.; Usharani, D.; Shaik, S.; Schwarz, H. *J. Am. Chem. Soc.* **2016**, *138*, 11368−11377. (c) Li, J.; Zhou, S.; Zhang, J.; Schlangen, M.; Weiske, T.; Usharani, D.; Shaik, S.; Schwarz, H. *J. Am. Chem. Soc.* **2016**, *138*, 7973−7981. (d) Li, J.; Wu, X.-N.; Zhou, S.; Tang, S.; Schlangen, M.; Schwarz, H. *Angew. Chem., Int. Ed.* **2015**, *54*, 12298−12302.

Supporting Information

Sequential Gas-Phase Activation of Carbon Dioxide and Methane by $[Re(CO)_2]^+$: The Sequence of Events Matters!

Shaodong Zhou[†], Jilai Li[†‡], Marjan Firouzbakht[†], Maria Schlangen[†], and Helmut Schwarz[†*orcid.org/0000-0002-3369-7997]

[†]*Institut für Chemie, Technische Universität Berlin, Straße des 17. Juni 135, 10623 Berlin, Germany*

[‡]*Institute of Theoretical Chemistry, Jilin University, Changchun, 130023, People's Republic of China*

Email: helmut.schwarz@tu-berlin.de

Experimental and Computational Section

The experiments were carried out using a Spectrospin-CMS-47X Fourier-transform ion cyclotron resonance (FT-ICR) mass spectrometer as described elsewhere.[1-3] $[Re(CO)_x]^+$ (x = 1 – 3) ions were generated by laser ablation of a Re target using a Nd:YAG laser (λ=1064 nm); helium, mixed with CO, served as a carrier gas. The ions were transferred from the external ion source into the cylindrical ICR-cell, which is located in a superconducting magnetic field (7.05 T), by using a system of electrostatic potentials and lenses. Thermalization of the ions of interest has been achieved by collisions with repeatedly pulsed-in argon. Collisional activation (CA) experiments were performed for structural investigations via introducing argon into the ICR cell for collisions with the ion of interest; the latter has been translationally excited to increase its kinetic energy.

The theoretical work was performed using the Gaussian 09 program.[4] The B2GP-PLYP functional,[5] including DFT-D3 dispersion correction,[6-7] was used for the structural optimization and frequency analysis. The reliability of this functional in calculating rhenium containing systems has been demonstrated previously.[8] The def2-TZVP basis set[9] was employed, and the ECP-60 pseudopotential[10] was used for the Re atom. Stationary points were optimized without symmetry constraint, and their nature was confirmed by vibrational frequency analysis. Intrinsic reaction coordinate (IRC)[11-13] calculations were also performed to link transition structures with the respective intermediates. Unscaled vibrational frequencies were used to correct the relative energies for zero-point vibrational energy (ZPVE) contributions. Single-point energies were obtained at the CCSD(T)[14-17]/def2-TZVPP level of theory. Natural bond orbital (NBO)[18-23] calculations were performed to obtain further information on selected stationary points along the reaction paths. The minimum energy crossing points (MECPs) were identified by means of the algorithm developed by Harvey et al.[24] The T1 diagnostics in the CCSD(T) calculations are given, together with the cartesian coordinates and the absolute energies.

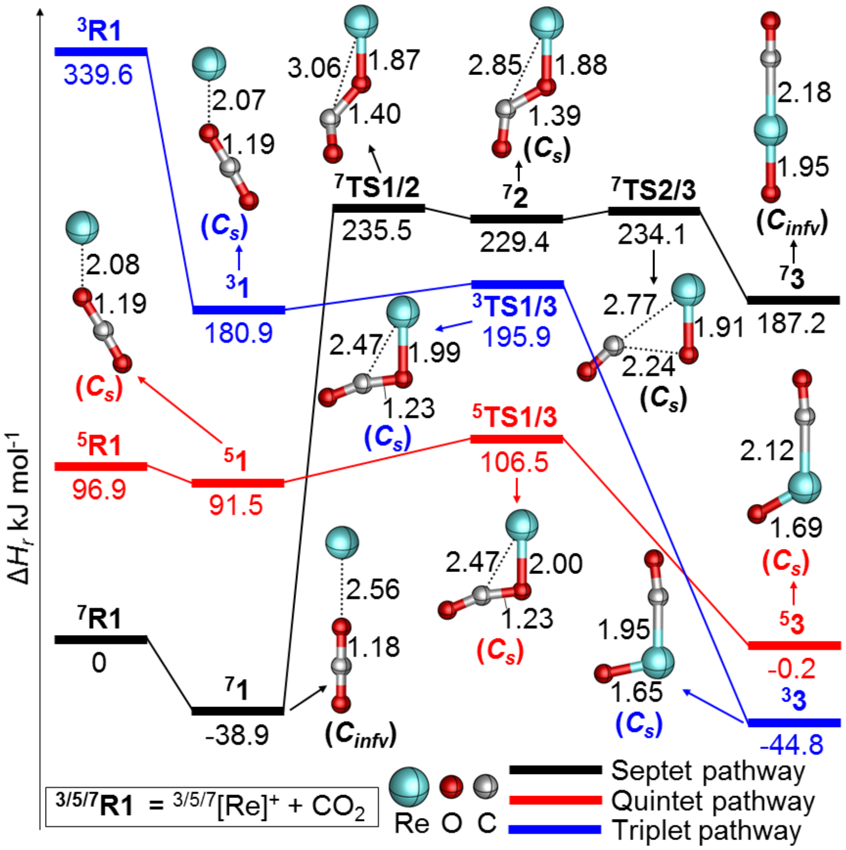
ΔH_r kJ mol^-1
^3R1
339.6
^5R1
96.9
^7R1
0
^31
180.9
^51
91.5
^71
-38.9
^7TS1/2
235.5
^72
229.4
^7TS2/3
234.1
^73
187.2
^3TS1/3
195.9
^5TS1/3
106.5
^53
-0.2
^33
-44.8
2.07
1.19
(C_s)
2.08
1.19
(C_s)
3.06
1.87
1.40
2.85
1.88
1.39
(C_s)
2.18
1.95
(C_infv)
2.47
1.99
1.23
(C_s)
2.77
1.91
2.24
(C_s)
2.12
1.69
(C_s)
2.56
1.18
(C_infv)
2.47
2.00
1.23
(C_s)
1.95
1.65
(C_s)
^3/5/7R1 = ^3/5/7[Re]^+ + CO_2
Re O C
Septet pathway
Quintet pathway
Triplet pathway

Figure S1. PES and selected structural information for the reaction of atomic $[Re]^+$ in three different spin states with CO_2 as calculated at the CCSD(T)/def2-TZVPP//B2GP-PLYP/def2-TZVP level of theory. Zero-point corrected energies are given in kJ mol^{-1}, and bond lengths in Å; charges are omitted for the sake of clarity.

Table S1. Energetics for the reaction of atomic $[Re]^+$ with CO_2 as calculated at the B2GP-PLYP/def2-TZVP level of theory.

Species	ΔH_r, kJ mol^{-1}
^{7}**1**	-43.4
^{7}**TS1/2**	223.5
^{7}**2**	218.4
^{7}**TS2/3**	298.2
^{7}**3**	190.6
^{5}**R1**	159.9
^{5}**1**	79.1
^{5}**TS1/3**	91.1
^{5}**3**	-19.6
^{3}**R1**	332.0
^{3}**1**	321.2
^{3}**TS1/3**	263.3
^{3}**3**	-72.1

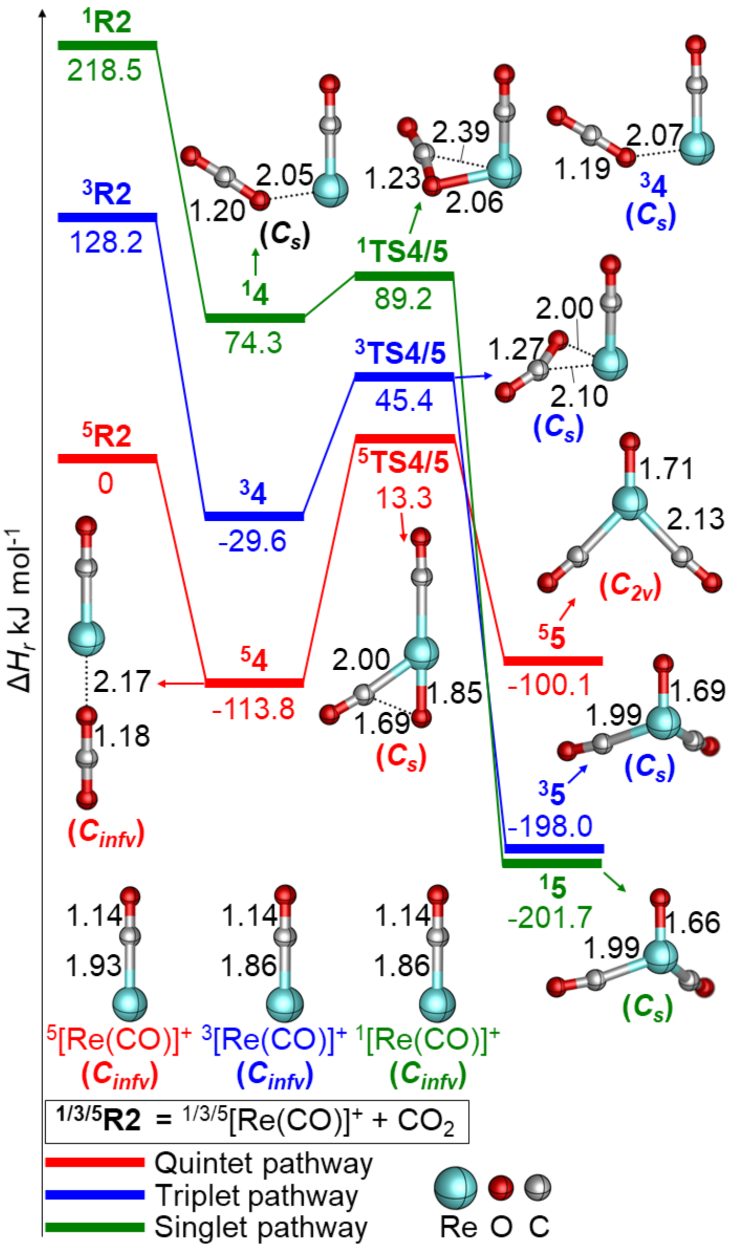
^{1}R2
218.5
^{3}R2
128.2
^{5}R2
0
^{1}4
74.3
^{3}4
-29.6
^{5}4
-113.8
^{1}TS4/5
89.2
^{3}TS4/5
45.4
^{5}TS4/5
13.3
^{5}5
-100.1
^{3}5
-198.0
^{1}5
-201.7
ΔH$_r$ kJ mol^{-1}
2.05
1.20
(C$_s$)
2.39
1.23
2.06
2.07
1.19
(C$_s$)
2.00
1.27
2.10
(C$_s$)
1.71
2.13
(C$_{2v}$)
2.17
1.18
(C$_{infv}$)
2.00
1.85
1.69
(C$_s$)
1.99
1.69
(C$_s$)
1.99
1.66
(C$_s$)
1.14
1.93
1.14
1.86
1.14
1.86
^{5}[Re(CO)]$^+$
(C$_{infv}$)
^{3}[Re(CO)]$^+$
(C$_{infv}$)
^{1}[Re(CO)]$^+$
(C$_{infv}$)
$^{1/3/5}$R2 = $^{1/3/5}$[Re(CO)]$^+$ + CO$_2$
Quintet pathway
Triplet pathway
Singlet pathway
Re O C

Figure S2. PES and selected structural information for the reaction of $[Re(CO)]^+$ in three different spin states with CO_2 as calculated at the CCSD(T)/def2-TZVPP//B2GP-PLYP/def2-TZVP level of theory. Zero-point corrected energies are given in kJ mol^{-1}, and bond lengths in Å; charges are omitted for the sake of clarity.

Table S2. Energetics for the reaction of $[Re(CO)]^+$ with CO_2 as calculated at the B2GP-PLYP/def2-TZVP level of theory.

Species	ΔH_r, kJ mol^{-1}
^{5}**4**	-115.7
^{5}**TS4/5**	14.7
^{5}**5**	-103.9
^{3}**R2**	121.8
^{3}**4**	-41.2
^{3}**TS4/5**	41.0
^{3}**5**	-209.1
^{1}**R2**	141.0
^{1}**4**	81.0
^{1}**TS4/5**	83.0
^{1}**5**	-209.1

Table S3. Energetics for the reaction of $[Re(CO)_2]^+$ with CO_2 as calculated at the B2GP-PLYP/def2-TZVP level of theory.

Species	ΔH_r, kJ mol^{-1}
^{3}**6**	-117.0
^{3}**TS6/7**	12.0
^{3}**7**	-170.7
^{1}**R3**	43.3
^{1}**6**	-98.6
^{1}**TS6/7**	-28.2
^{1}**7**	-245.1

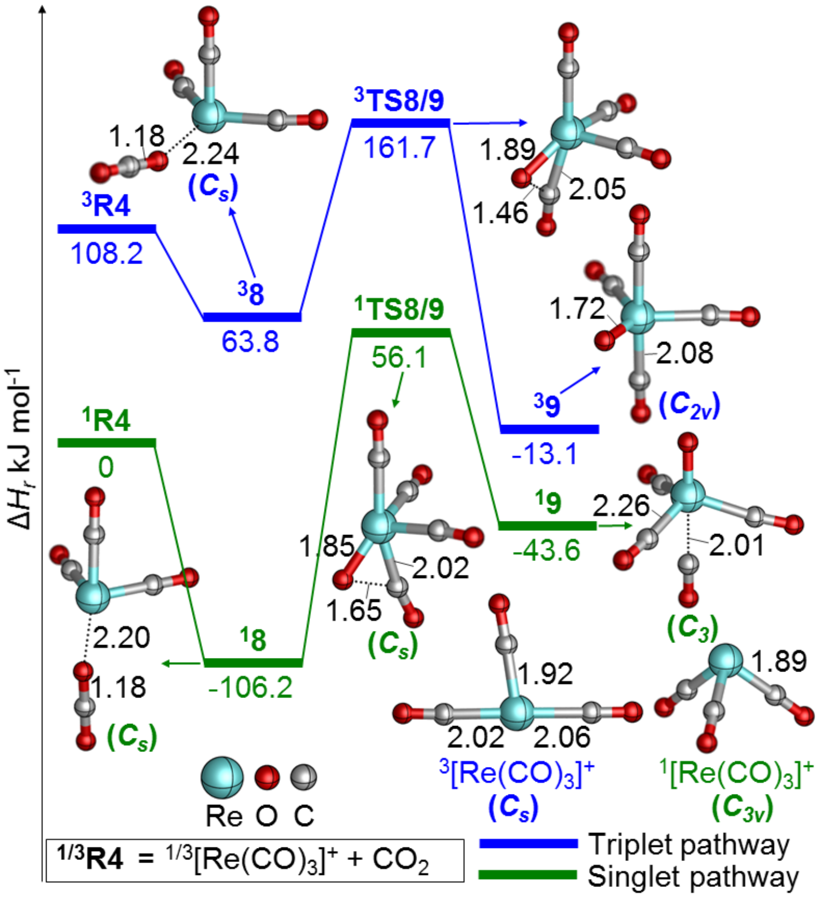
ΔH_r kJ mol-1
3R4
108.2
38
63.8
3TS8/9
161.7
39
-13.1
1R4
0
18
-106.2
1TS8/9
56.1
19
-43.6
1.18
2.24
(Cs)
1.89
2.05
1.46
1.72
2.08
(C2v)
1.85
2.02
1.65
(Cs)
2.26
2.01
(C3)
2.20
1.18
(Cs)
1.92
2.02
2.06
3[Re(CO)3]+
(Cs)
1.89
1[Re(CO)3]+
(C3v)
Re O C
1/3R4 = 1/3[Re(CO)3]+ + CO2
Triplet pathway
Singlet pathway

Figure S3. PES and selected structural information for the reactions of singlet and triplet $[Re(CO)_3]^+$ with CO_2 as calculated at the CCSD(T)/def2-TZVPP//B2GP-PLYP/def2-TZVP level of theory. Zero-point corrected energies are given in kJ mol^{-1}, and bond lengths in Å; charges are omitted for the sake of clarity.

Table S4. Energetics for the reaction of $[Re(CO)_3]^+$ with CO_2 as calculated at the B2GP-PLYP/def2-TZVP level of theory.

Species	ΔH_r, kJ mol^{-1}
^{1}8	-112.1
^{1}TS8/9	63.9
^{1}9	-40.7
^{3}R4	114.7
^{3}8	64.6
^{3}TS8/9	175.9
^{3}9	4.0

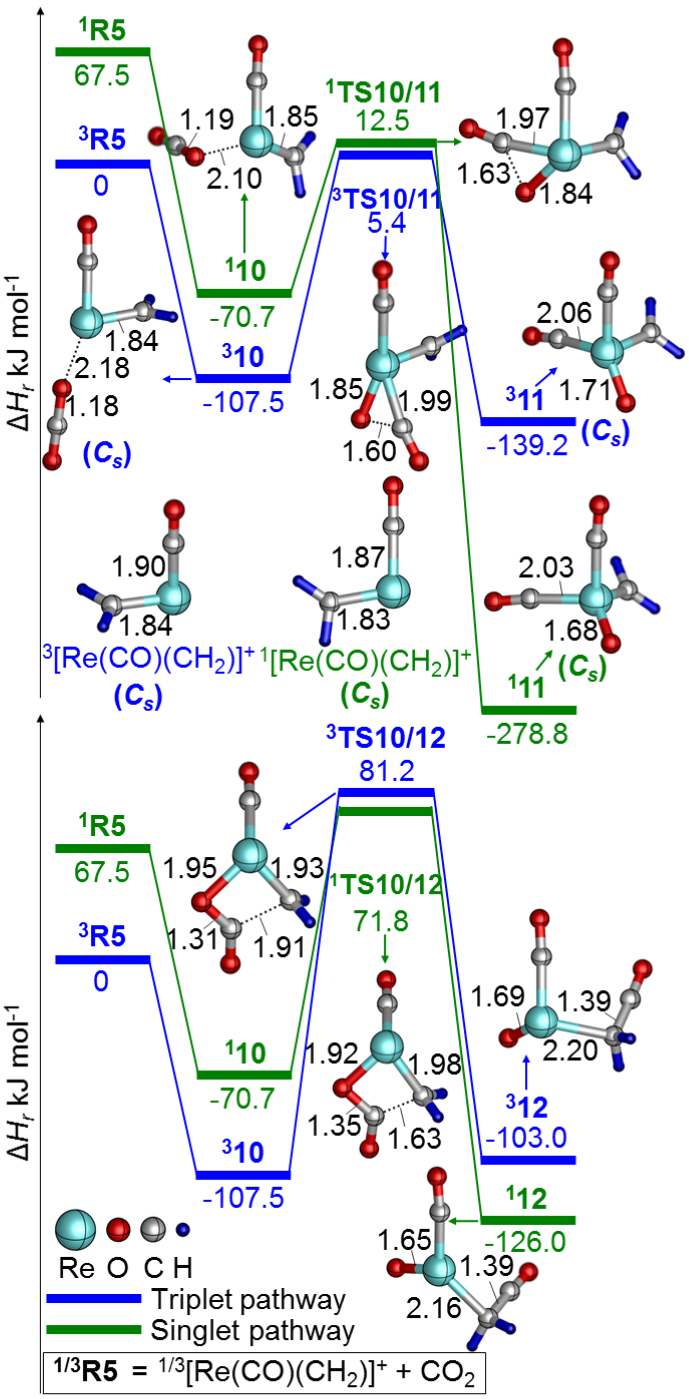
ΔH_r kJ mol^-1
¹R5
67.5
³R5
0
1.19
1.85
2.10
¹10
-70.7
³10
-107.5
1.84
2.18
1.18
(C_s)
¹TS10/11
12.5
³TS10/11
5.4
1.85
1.99
1.60
1.97
1.63
1.84
2.06
1.71
³11
-139.2
(C_s)
1.90
1.84
³[Re(CO)(CH₂)]⁺
(C_s)
1.87
1.83
¹[Re(CO)(CH₂)]⁺
(C_s)
2.03
1.68
(C_s)
¹11
-278.8
ΔH_r kJ mol^-1
³TS10/12
81.2
¹R5
67.5
³R5
0
1.95
1.93
1.31
1.91
¹TS10/12
71.8
¹10
-70.7
³10
-107.5
1.92
1.98
1.35
1.63
1.69
1.39
2.20
³12
-103.0
¹12
-126.0
1.65
1.39
2.16
Re O C H
Triplet pathway
Singlet pathway
^1/3R5 = ^1/3[Re(CO)(CH₂)]⁺ + CO₂

Figure S4. PES and selected structural information for the reactions of triplet and singlet $[Re(CO)(CH_2)]^+$ with CO_2 as calculated at the CCSD(T)/def2-TZVPP//B2GP-PLYP/def2-TZVP level of theory. Zero-point corrected energies are given in kJ mol^{-1}, and bond lengths in Å; charges are omitted for the sake of clarity.

Table S5. Energetics for the reaction of $[Re(CO)(CH_2)]^+$ with CO_2 as calculated at the B2GP-PLYP/def2-TZVP level of theory.

Species	ΔH_r, kJ mol^{-1}
^{3}**10**	-110.6
^{3}**TS10/11**	12.8
^{3}**11**	-150.8
^{1}**R5**	64.0
^{1}**10**	-81.4
^{1}**TS10/11**	12.7
^{1}**11**	-287.8
^{3}**TS10/12**	85.2
^{3}**12**	-118.0
^{1}**TS10/12**	81.9
^{1}**12**	-132.9

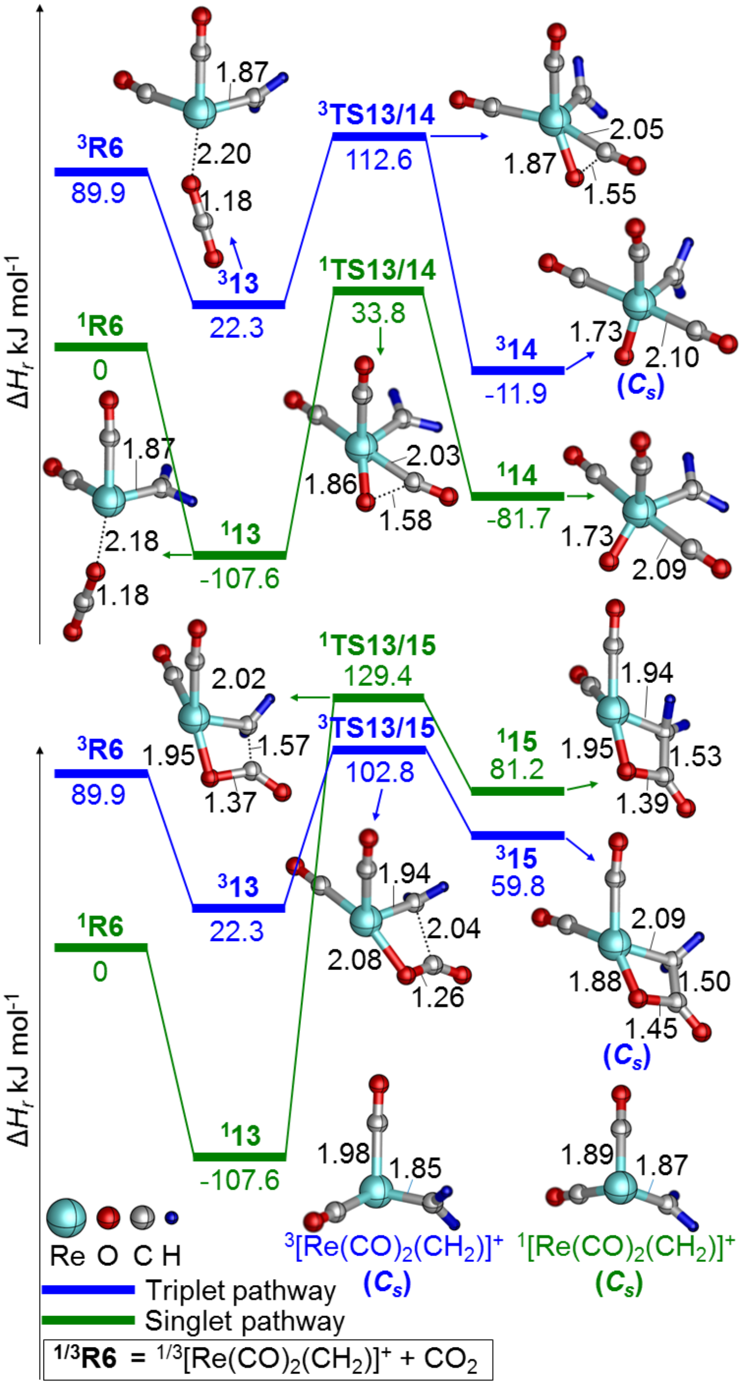
ΔHr kJ mol-1
3R6
89.9
1R6
0
313
22.3
113
-107.6
3TS13/14
112.6
1TS13/14
33.8
314
-11.9
114
-81.7
(Cs)
1.87
2.20
1.18
2.18
2.05
1.87
1.55
1.73
2.10
2.03
1.86
1.58
1.73
2.09
1TS13/15
129.4
3TS13/15
102.8
115
81.2
315
59.8
2.02
1.95
1.57
1.37
1.94
2.04
2.08
1.26
1.94
1.95
1.53
1.39
2.09
1.88
1.50
1.45
1.98
1.85
1.89
1.87
Re O C H
Triplet pathway
Singlet pathway
3[Re(CO)2(CH2)]+
1[Re(CO)2(CH2)]+
1/3R6 = 1/3[Re(CO)2(CH2)]+ + CO2

Figure S5. PES and selected structural information for the reactions of the singlet and triplet states of $[Re(CO)_2(CH_2)]^+$ with CO_2 as calculated at the CCSD(T)/def2-TZVPP//B2GP-PLYP/def2-TZVP level of theory. Zero-point corrected energies are given in kJ mol^{-1}, and bond lengths in Å; charges are omitted for the sake of clarity.

Table S6. Energetics for the reaction of $[Re(CO)_2(CH_2)]^+$ with CO_2 as calculated at the B2GP-PLYP/def2-TZVP level of theory.

Species	ΔH_r, kJ mol^{-1}
^{1}**13**	-112.4
^{1}**TS13/14**	43.7
^{1}**14**	-71.4
^{3}**R6**	92.7
^{3}**13**	17.8
^{3}**TS13/14**	127.5
^{3}**14**	6.4
^{1}**TS13/15**	144.6
^{1}**15**	96.3
^{3}**TS13/15**	105.8
^{3}**15**	74.3

Table S7. Energetics for the reaction of $[ORe(CO)_2]^+$ with CH_4 on the singlet surface as calculated at the B2GP-PLYP/def2-TZVP level of theory.

Species	ΔH_r, kJ mol^{-1}
^{1}**16**	-111.5
^{1}**TS16/17**	-104.6
^{1}**17**	-148.0
^{1}**TS16/20**	34.9
^{1}**20**	-160.0
^{1}**17/18**	-82.4
^{1}**18**	-87.9
^{1}**TS18/19**	-29.0
^{1}**19**	-55.3
^{1}**TS18/20**	14.1
^{1}**TS20/21**	-103.0
^{1}**21**	-127.4
^{1}**TS21/22**	-25.4
^{1}**22**	-49.4

^{1}**P7a**	3.8
^{1}**P7b**	-30.4

Table S8. Energetics for the reaction of $[ORe(CO)_2]^+$ with CH_4 on the triplet surface as calculated at the CCSD(T)/def2-TZVPP//B2GP-PLYP/def2-TZVP and B2GP-PLYP/def2-TZVP levels of theory, respectively.

Species	$\Delta H_{r(\mathrm{CCSD(T)})}$, kJ mol^{-1}	$\Delta H_{r(\mathrm{B2GP\text{-}PLYP})}$, kJ mol^{-1}
^{3}**R7**	3.9	0.0
^{3}**16**	-66.1	-72.6
^{3}**TS16/17**	-0.5	-3.0
^{3}**17**	-13.9	-14.3
^{3}**TS16/20**	80.2	83.4
^{3}**20**	-125.6	-159.7
^{3}**17/18**	7.9	7.4
^{3}**18**	-22.4	-24.6
^{3}**TS18/19**	125.8	137.5
^{3}**19**	131.6	135.2
^{3}**TS18/20**	98.9	111.6
^{3}**TS20/21**	12.7	29.2
^{3}**21**	-29.6	-18.5
^{3}**TS21/22**	Not located	Not located
^{3}**22**	Not located	Not located
^{3}**P7a**	181.0	194.1
^{3}**P7b**	212.1	229.8

Cartesian coordinates

^{3}1

1 3 (charge mutiplicity)

$E_{CCSD(T)}$ = -265.953241 (in Hatree); T1 = 0.026

Re	0.70843000	-0.02632500	0.00000000
C	-2.42663100	0.06797500	0.00000100
O	-3.51957100	-0.24959700	0.00000000
O	-1.30199100	0.44541300	-0.00000100

^{5}1

1 5

$E_{CCSD(T)}$ = -265.9860117; T1 = 0.024

Re	0.71109400	-0.02670000	0.00000000
C	-2.43636100	0.07115500	0.00000000
O	-3.52609200	-0.25605600	0.00000000
O	-1.31314600	0.45300400	0.00000100

^{7}1

1 7

$E_{CCSD(T)}$ = -266.0356823; T1 = 0.013

Re	-0.00121700	-0.03195900	0.84526600
C	0.00407400	0.10931700	-2.89250500
O	0.00585500	0.15231000	-4.03763600
O	0.00250100	0.06531700	-1.71735200

^{7}2

1 7

$E_{CCSD(T)}$ = -265.9312431; T1 = 0.022

Re	0.64850500	-0.02603600	0.00000200
C	-2.17900000	-0.34111900	-0.00004400
O	-3.31211200	-0.07684500	0.00003000
O	-1.13337500	0.57677400	-0.00001500

^{3}3

1 3

$E_{CCSD(T)}$ = -266.0369518; T1 = 0.051

Re	-0.33141700	-0.17378100	-0.00001300
C	1.60977900	-0.00346200	0.00000200
O	2.71839000	0.22622400	0.00001900
O	-0.81869000	1.40557400	0.00010500

^{5}3

1 5

$E_{CCSD(T)}$ = -266.0194167; T1 = 0.051

Re	-0.30728600	-0.16735200	-0.00000900
C	1.79161400	0.10012300	-0.00001400
O	2.88846600	0.33069000	0.00000200
O	-1.35136800	1.16314100	0.00009400

^{7}3

1 7

$E_{CCSD(T)}$ = -265.9474251; T1 = 0.021

Re	-0.20594800	-0.05743400	0.12090400
C	1.61934000	0.45121800	-0.95084100
O	2.55820900	0.71264500	-1.50219100
O	-1.84195100	-0.51261900	1.08184300

^{1}4

1 1

$E_{CCSD(T)}$ = -379.2075864; T1 = 0.019

Re	0.61145400	-0.34545100	-0.00004400
C	0.54117400	1.49182200	0.00027100
O	0.48392400	2.64368900	-0.00001000
O	-1.39201900	-0.77658300	0.00031600
C	-2.41771300	-0.16333700	0.00033700
O	-3.41688600	0.37513200	-0.00035100

^{3}4

1 3

$E_{CCSD(T)}$ = -379.2472969; T1 = 0.028

Re	0.62709700	-0.34078900	0.00003300
C	-2.44316900	-0.18274300	-0.00003600
O	-3.46177900	0.32365500	0.00013400
O	-1.40446200	-0.76080400	-0.00022700
C	0.52009200	1.49667800	-0.00045500
O	0.42951400	2.64659600	0.00015000

^{5}4

1 5

$E_{CCSD(T)}$ = -379.2792557; T1 = 0.018

Re	0.33373900	-0.00007700	-0.00000100
C	2.28463500	-0.00003900	0.00000400
O	3.42173800	0.00062500	0.00000100
O	-1.84048600	-0.00055600	0.00000300
C	-3.01814600	-0.00001100	0.00000200
O	-4.15992500	0.00069200	0.00000000

^{1}5

1 1

$E_{CCSD(T)}$ = -379.3107671; T1 = 0.027

Re	0.00000000	0.25577100	-0.17738500
C	-1.65781100	-0.82118900	0.04709800
O	-2.62394700	-1.33577100	0.33686300
O	0.00030300	1.50575300	0.91871100
C	1.65783300	-0.82098900	0.04696800
O	2.62362500	-1.33619900	0.33685900

^{3}5

1 3

$E_{CCSD(T)}$ = -379.3094846; T1 = 0.028

Re	-0.00005200	-0.38323900	-0.18482900
C	1.41340800	1.00128700	0.02100300
O	2.23138900	1.74165700	0.26716000
O	-0.00041300	-1.39345200	1.16706000
C	-1.41302400	1.00175500	0.02094600
O	-2.23077900	1.74238300	0.26708700

^{5}**5**

1 5

$E_{CCSD(T)}$ = -379.2717081; T1 = 0.042

Re	0.36757400	0.00039400	-0.00000900
C	-1.16032200	1.47809000	0.00001900
O	-1.89606000	2.32829600	0.00000700
O	2.08017900	0.00152800	0.00004400
C	-1.15765500	-1.48022600	0.00002800
O	-1.89164600	-2.33191500	0.00000200

^{1}**6**

1 1

$E_{CCSD(T)}$ = -492.5398012; T1 = 0.021

Re	-0.48451800	0.00001000	-0.49247300
C	-0.67567300	1.28249300	0.84381800
O	-0.77368400	2.06135300	1.68232800
O	1.61956900	0.00009400	-0.66570200
C	2.58770100	0.00001100	0.01747300
O	3.54267900	0.00003500	0.63938400
C	-0.67566600	-1.28259900	0.84369500
O	-0.77348100	-2.06151000	1.68218200

^{3}**6**

1 3

$E_{CCSD(T)}$ = -492.5475652; T1 = 0.020

Re	-0.20744500	-0.29136300	0.00008700
C	-2.13846500	-0.48007300	-0.00017600
O	-3.27301100	-0.55534800	-0.00036100
O	1.96325900	-0.36955400	-0.00003100
C	-0.74626100	1.50325000	0.00003600
O	-1.08405800	2.59854100	-0.00000500
C	3.08992900	-0.01694100	-0.00012400
O	4.18470500	0.30321200	-0.00022200

^{1}**7**

1 1

$E_{CCSD(T)}$ = -492.5946342; T1 = 0.023

Re	0.00011500	-0.00002700	0.23459300
C	-0.64800600	1.71804100	-0.58715300
O	-1.02809300	2.72654800	-0.92970200
O	-0.00019000	0.00092500	1.90932600
C	-1.16484400	-1.42017100	-0.58631400
O	-1.84845400	-2.25315400	-0.92925200

C	1.81259300	-0.29892600	-0.58654000
O	2.87585100	-0.47327500	-0.92967400

^{3}7

1 3

$E_{CCSD(T)}$ = -492.5666305; T1 = 0.026

Re	-0.00004700	-0.24086700	0.25540600
C	-1.64831100	-0.29854300	-0.96188900
O	-2.63440300	-0.37483500	-1.50632200
O	-0.00954900	-0.71158900	1.88696100
C	1.65604700	-0.29512500	-0.95511100
O	2.64505300	-0.37068100	-1.49425500
C	-0.00247500	1.73028600	0.08841100
O	-0.00460900	2.86277300	0.09062900

^{1}8

1 1

$E_{CCSD(T)}$ = -605.6797694; T1 = 0.023

Re	0.16940700	-0.00013600	0.33374800
C	-3.14148800	0.00012800	0.18018700
O	-4.23364600	-0.00074500	-0.14972600
O	-2.01776900	-0.00031100	0.54329800
C	0.53187400	-1.29726200	-0.97969400
O	0.75136100	-2.07726000	-1.78710200
C	0.53198300	1.29913800	-0.97748400
O	0.75150300	2.08054200	-1.78347900
C	2.05510900	-0.00107300	0.67329300
O	3.17724900	-0.00164500	0.87589600

^{3}8

1 3

$E_{CCSD(T)}$ = -605.6137669; T1 = 0.023

Re	-0.22476900	0.00000400	-0.26177900
C	3.09813800	0.00006800	-0.02569400
O	4.15784500	0.00007500	0.40047700
O	2.00898600	0.00006200	-0.48210300
C	-1.08552500	-1.80592400	-0.35345300
O	-1.70246800	-2.75739500	-0.38968600
C	-0.64000400	-0.00001800	1.56658400
O	-0.86963300	-0.00003000	2.68967000
C	-1.08568500	1.80585200	-0.35344400
O	-1.70271200	2.75727000	-0.38967400

^{1}9

1 1

$E_{CCSD(T)}$ = -605.6527465; T1 = 0.025

Re	0.03154600	-0.01597000	0.40287500
C	1.90264500	0.06953400	-0.32762500
O	2.99887900	0.11317200	-0.60289200
O	0.16431700	-0.08326900	2.10155000
C	-1.02126700	1.63926600	-0.03715500

O	-1.62007000	2.59288600	-0.14426300
C	-0.14475000	0.07345000	-1.85116300
O	-0.23267600	0.11796200	-2.97278800
C	-0.92366800	-1.68740100	-0.17648900
O	-1.46591800	-2.66216600	-0.36423900

^{3}9

1 3

$E_{CCSD(T)}$ = -605.6415346; T1 = 0.034

Re	-0.00004700	-0.00013500	-0.21856200
C	2.07529900	0.00045800	-0.17611300
O	3.19895000	0.00053600	-0.11552500
O	-0.00030200	-0.00035900	-1.93535500
C	-2.07620700	0.00080100	-0.17542900
O	-3.19977000	0.00080100	-0.11458100
C	0.00038300	-1.66253300	0.97818800
O	0.00061800	-2.66241700	1.50536700
C	0.00006900	1.66208900	0.97839200
O	0.00128300	2.66209100	1.50533400

^{1}10

1 1

$E_{CCSD(T)}$ = -418.5379614; T1 = 0.022

Re	-0.56294700	0.29824800	0.17643800
C	-0.67428000	0.58145800	-1.65322200
H	-0.73171300	-0.13779400	-2.46602500
H	-0.67905100	1.64222400	-1.95096100
C	-0.52111600	-1.53306800	0.05864800
O	-0.48046900	-2.67829300	-0.09695700
O	1.48993300	0.61169000	0.47469800
C	2.48990600	0.12812600	0.05580100
O	3.47362900	-0.29991000	-0.32564300

^{3}10

1 3

$E_{CCSD(T)}$ = -418.5517355; T1 = 0.032

Re	-0.27822800	-0.02371400	-0.00000600
C	-0.83503200	1.72565200	0.00000800
H	-1.01119100	2.27450400	0.92776100
H	-1.01121000	2.27451100	-0.92773700
C	-2.15199700	-0.44786700	0.00001300
O	-3.25905600	-0.72783100	0.00002500
O	1.88090700	-0.32137100	-0.00002800
C	3.05249600	-0.20370000	0.00000400
O	4.19023900	-0.10267000	0.00003300

^{1}11

1 1

$E_{CCSD(T)}$ = -418.6148315; T1 = 0.024

Re	0.00000100	-0.28140900	-0.04668600
C	0.00001300	-1.13154500	1.63052300

H	0.00000600	-0.43479800	2.47997800
H	0.00003000	-2.18764800	1.88407600
C	1.51995600	1.05692900	0.03298100
O	2.41858300	1.73994000	0.02211700
O	0.00000800	-1.25055800	-1.42442600
C	-1.51996900	1.05691300	0.03298400
O	-2.41860300	1.73991500	0.02212100

^{3}**11**

1 3

$E_{CCSD(T)}$ = -418.5617255; T1 = 0.038

Re	-0.00002900	-0.28333900	-0.09545400
C	-0.00017900	-0.37149700	1.79466900
H	0.00034600	0.47516800	2.47934800
H	-0.00081000	-1.34773700	2.28074300
C	1.56130300	1.05565300	-0.09738100
O	2.49469300	1.69025600	-0.15107000
O	-0.00055000	-1.92127700	-0.59783800
C	-1.56086400	1.05618800	-0.09746000
O	-2.49401300	1.69114200	-0.15109100

^{1}**12**

1 1

$E_{CCSD(T)}$ = -418.5098996; T1 = 0.027

Re	0.21044600	-0.29669400	-0.09767600
C	-1.81357200	-0.28838900	-0.84214600
H	-2.27752400	-1.25950600	-0.64730100
H	-1.91715500	0.02433300	-1.88432200
C	1.71432700	0.98816400	-0.12629700
O	2.60290700	1.68330800	0.00559300
O	-2.73789900	1.47302100	0.71449700
O	0.47042100	-1.26458600	1.21399300
C	-2.27946100	0.69243900	0.03255000

^{3}**12**

1 3

$E_{CCSD(T)}$ = -418.5500302; T1 = 0.026

Re	0.57648500	-0.14645800	-0.13401400
C	-1.18662600	-1.43230600	-0.42786900
H	-1.07218200	-2.38294400	0.09637800
H	-1.35637600	-1.59215700	-1.49825000
C	-0.22544100	1.61583200	-0.17405800
O	-0.67201700	2.66170400	-0.06665100
O	-3.07711800	-0.08145900	0.53872400
O	1.38972200	-0.32025000	1.33529700
C	-2.24335300	-0.70360900	0.10092300

^{1}**13**

1 1

$E_{CCSD(T)}$ = -531.6878988; T1 = 0.024

Re	-0.22056400	-0.28871300	-0.07965600

C	-0.65716600	-0.63069900	1.70813100
H	-1.03761000	0.03567900	2.47751700
H	-0.52452000	-1.67726600	2.02465800
C	-0.33679300	1.55419900	0.07977400
O	-0.42221200	2.69130100	0.24418500
C	3.02555600	-0.08633800	-0.18401800
O	4.09174200	0.29662000	-0.05112100
C	-2.14248700	-0.17294500	-0.39040200
O	-3.25633300	-0.06358300	-0.58402600
O	1.93302300	-0.51061700	-0.33514800

^{3}**13**

1 3

$E_{CCSD(T)}$ = -531.6370492; T1 = 0.039

Re	-0.17849900	-0.15441700	-0.04307200
C	-0.38666600	-1.18470500	1.50028200
H	-0.92731200	-2.09308200	1.75199800
H	-0.02281300	-0.61086000	2.36895800
C	-2.00376200	-0.66098500	-0.44375800
O	-3.06628700	-0.97861400	-0.69745700
C	-0.83409300	1.74685400	0.05464100
O	-1.26992200	2.75215100	0.35650600
C	3.11895300	0.02038300	-0.21620600
O	4.23977900	-0.19361500	-0.16330400
O	1.96779600	0.26456900	-0.27828600

^{1}**14**

1 1

$E_{CCSD(T)}$ = -531.6751991; T1 = 0.026

Re	0.05117400	-0.16646000	-0.07441700
C	-0.15313500	-0.47214600	1.83046900
H	0.68025700	-0.13792400	2.45912000
H	-0.87993400	-1.05851400	2.38313000
C	-0.17265100	1.85119500	-0.08133000
O	-0.31900600	2.96604100	-0.19132000
C	2.14577600	-0.18383400	0.08770400
O	3.26406000	-0.23905900	0.17551100
C	-2.02834400	-0.36605300	0.04715700
O	-3.13779300	-0.47913900	0.18236600
O	-0.10579300	-1.15959400	-1.48718200

^{3}**14**

1 3

$E_{CCSD(T)}$ = -531.6485122; T1 = 0.043

Re	0.00000700	-0.20022000	-0.03690900
C	0.00001300	-0.56144000	1.83848700
H	-0.00012700	0.17511400	2.64110000
H	0.00013500	-1.59636900	2.18059500
C	-0.00007200	1.90991700	0.00020700
O	-0.00012100	3.03090000	-0.16639200
C	2.09524000	-0.12317000	-0.14228900

O	3.21586000	-0.05370800	-0.17332900
C	-2.09521300	-0.12326900	-0.14229500
O	-3.21583700	-0.05385200	-0.17333400
O	0.00005600	-1.69515100	-0.90922200

^{1}**15**

1 1

$E_{CCSD(T)}$ = -531.6136338; T1 = 0.025

Re	-0.10467400	-0.18119200	-0.26739000
C	1.07198200	0.47399500	1.13081100
H	0.32391900	-0.50971900	1.43172700
H	1.04577900	1.10832500	2.01115800
C	-1.84460800	-0.86072300	0.44314900
O	-2.79948800	-1.29835300	0.87023500
C	-1.25365000	1.38158300	-0.10572900
O	-1.85509500	2.34264900	-0.01414500
O	1.75713800	-0.45359800	-0.77525200
C	2.33689500	0.07499100	0.36831600
O	3.47459200	0.23076600	0.61817300

^{3}**15**

1 3

$E_{CCSD(T)}$ = -531.6232179; T1 = 0.027

Re	-0.12918900	-0.00000600	-0.21507800
C	1.30406700	0.00000700	1.31229900
H	1.26398800	-0.90312200	1.92141400
H	1.26399400	0.90314000	1.92140500
C	-1.58666800	-1.33327400	0.17431000
O	-2.32795600	-2.16516600	0.37256200
C	-1.58663200	1.33330100	0.17429600
O	-2.32789900	2.16521400	0.37254100
O	1.60530000	-0.00001900	-0.95110900
C	2.38768900	-0.00000300	0.27407900
O	3.55685900	0.00000100	0.29077300

^{1}**16**

1 1

$E_{CCSD(T)}$ = -419.6958319; T1 = 0.026

Re	0.00000700	-0.10756400	0.22456800
C	1.59611600	0.74850900	-0.57489900
O	2.54664700	1.29757900	-0.86500300
O	-0.00002600	0.02979300	1.89365100
C	-1.59608300	0.74857400	-0.57489200
O	-2.54660200	1.29766900	-0.86498200
C	-0.00010300	-2.18444400	-1.13134700
H	0.90334200	-2.73482100	-1.36791900
H	-0.90374500	-2.73464600	-1.36754900
H	-0.00016100	-1.25381200	-1.72282600
H	0.00028000	-2.08561400	-0.00681500

^{3}**16**

1 3

$E_{CCSD(T)}$ = -419.679883; T1 = 0.029

Re	-0.21443400	0.13088300	-0.20499100
C	1.40365900	0.88974800	0.59967100
O	2.38732100	1.34587600	0.93806200
O	-0.18685000	0.40596800	-1.88189800
C	0.50686100	-1.65629800	0.20694800
O	0.96684200	-2.68800000	0.31118000
C	-2.07113800	0.23334300	1.53889000
H	-2.42127800	-0.18389700	2.48193500
H	-2.29762600	-0.53385900	0.78636100
H	-0.99519700	0.42282600	1.77200700
H	-2.57813900	1.16722400	1.32224300

^{1}17

1 1

$E_{CCSD(T)}$ = -419.7092379; T1 = 0.023

Re	-0.00216200	-0.29008200	-0.03825500
C	-0.97079500	1.53002600	-0.19238900
O	-1.54937300	2.48791700	-0.31448600
C	1.84269800	0.54650800	0.29788400
O	2.89921600	0.91700500	0.42186200
C	-1.65949700	-0.77495800	1.21677500
H	-2.60032400	-0.49652500	0.74864900
H	-1.65793200	-1.81709800	1.51300300
H	-1.51048400	-0.15714900	2.11266800
O	-0.08716700	-1.19527500	-1.43538600
H	0.55507800	-1.25973900	1.18527600

^{3}17

1 3

$E_{CCSD(T)}$ = -419.6565745; T1 = 0.027

Re	-0.24099100	-0.17390600	-0.09096900
C	0.62661900	1.79321500	-0.18370200
O	1.01705100	2.82692200	-0.40763500
C	1.65762200	-0.82598800	0.27322400
O	2.67328600	-1.25279800	0.51243200
C	-1.68203900	0.61243500	1.23292300
H	-2.28679700	1.13274400	0.47161600
H	-2.28172100	-0.15562900	1.71199600
H	-1.29716000	1.31276600	1.96638900
O	-1.14738800	-1.33231100	-0.94670200
H	-0.01677100	-0.65938200	1.47324300

^{1}18

1 1

$E_{CCSD(T)}$ = -419.6846066; T1 = 0.025

Re	-0.04634100	-0.32061900	-0.04344400
C	-1.55091200	0.99386600	0.30371800
O	-2.43699100	1.66479300	0.50170600
C	1.23450900	1.37980000	-0.23677800

O	1.96646200	2.18963400	-0.51113600
C	1.51853300	-0.86244500	1.19558900
H	2.49713200	-0.40376300	1.23979200
H	1.57871200	-1.95109500	1.20724500
O	-0.62582800	-1.66512500	-0.90473100
H	0.04572500	0.34843100	-1.53011800
H	0.91205200	-0.52888600	2.07946500

^{3}**18**

1 3

$E_{CCSD(T)}$ = -419.6596751; T1 = 0.031

Re	-0.01994400	-0.31521200	-0.10481600
C	-1.78280600	0.84754100	-0.01426200
O	-2.80109600	1.32860200	-0.02111100
C	1.36765800	1.15923500	-0.32207600
O	2.23596100	1.86356000	-0.47196600
C	0.61712500	0.15448700	1.88028900
H	0.41091000	1.17044800	2.20325100
H	1.65630200	-0.10224000	2.07177600
O	0.34325100	-1.96506200	-0.31130500
H	0.03013400	0.34720200	-1.63877800
H	-0.03835800	-0.55890300	2.39627700

^{1}**19**

1 1

$E_{CCSD(T)}$ = -419.6740458; T1 = 0.028

Re	0.40625000	0.02703400	-0.00001200
C	-1.62495800	-1.19038100	0.00002100
O	-2.53478800	-1.84441900	0.00003300
C	-1.20591700	1.49740800	0.00006900
O	-2.01580200	2.27041700	0.00011300
C	1.06876200	-1.75811200	-0.00006800
H	0.52400900	-2.69505300	-0.00008200
H	2.15138500	-1.88789800	-0.00008500
O	1.77725000	1.00752900	-0.00002600
H	-0.19234400	-0.10318800	1.56416600
H	-0.19243900	-0.10311900	-1.56416000

^{3}**19**

1 3

$E_{CCSD(T)}$ = -419.5969462; T1 = 0.032

Re	0.06925800	-0.29555700	-0.05261700
C	-1.41620200	1.17639300	-0.27268300
O	-2.28735600	1.86097700	-0.48520400
C	1.60158400	1.02120400	0.19898400
O	2.52393800	1.65830200	0.31535400
C	-1.44801700	-0.60883900	1.33936400
H	-2.32314900	-1.12651700	0.95304800
H	-1.50041200	-0.23591900	2.35119000
O	0.41480600	-1.82471900	-0.70504000
H	0.66390100	-0.18739900	1.49871000

H	0.33000600	0.62760000	-1.45150500

^{1}20

1 1

$E_{CCSD(T)}$ = -419.7159442; T1 = 0.024

Re	-0.26159300	-0.23741300	0.00352100
C	0.41150500	1.48151700	-0.23891600
O	0.78323000	2.55495700	-0.40217200
O	-1.49538300	-0.43828800	-1.33289100
C	1.70040700	-0.67744200	0.01417300
O	2.81191900	-0.87877500	-0.04280800
C	-0.91526700	0.34547400	1.81531600
H	-0.81504600	1.33282300	2.25164300
H	-1.78746900	-0.20069700	2.17720600
H	0.03567600	-0.26824300	2.03773600
H	-1.79171500	0.14164300	-2.05110100

^{3}20

1 3

$E_{CCSD(T)}$ = -419.7014378; T1 = 0.025

Re	0.30084900	0.00000300	-0.07573800
C	-1.16312500	-1.30533100	-0.14474400
O	-1.97050200	-2.10011200	-0.22993700
O	1.99260400	0.00000500	-0.77776500
C	-1.16315000	1.30531200	-0.14475200
O	-1.97054100	2.10007800	-0.22995300
C	0.45438800	0.00001500	1.96955700
H	1.03428000	-0.89423300	2.22525700
H	1.03426900	0.89427200	2.22524600
H	-0.49156600	0.00001200	2.50800400
H	2.67818800	-0.00000900	-1.45726000

^{1}21

1 1

$E_{CCSD(T)}$ = -419.7016895; T1 = 0.025

Re	-0.19489400	-0.20691800	-0.01352200
C	-0.25057000	1.71902400	0.20646100
O	-0.30066500	2.84513000	0.35669600
O	-1.67738100	-0.63346000	-1.03019800
C	1.75869500	-0.10781600	-0.36993000
O	2.85674200	-0.07021500	-0.64053400
C	0.08544600	-1.31644000	1.49393700
H	0.40192100	-1.24756800	2.52386900
H	-0.25904400	-2.31358200	1.16731200
H	0.37963100	0.58101200	1.33602200
H	-2.49646200	-0.40126300	-1.48353700

^{3}21

1 3

$E_{CCSD(T)}$ = -419.6606198; T1 = 0.031

Re	0.00446400	0.05071700	-0.01838400

C	2.04936700	-0.17769900	-0.31959900
O	3.12766900	-0.39694300	-0.55129000
O	-0.03101400	1.86305600	0.48543400
C	-2.01488000	-0.20367000	-0.32957600
O	-3.09669600	-0.41274300	-0.55961100
C	-0.01110600	-1.36543100	1.22663400
H	0.53126500	-1.26037300	2.16974500
H	-0.60488600	-2.27674500	1.14500200
H	-0.02633000	-0.72797400	-1.50538500
H	-0.37482000	2.51517000	1.10840900

^{1}22

1 1

$E_{CCSD(T)}$ = -419.6726637; T1 = 0.022

Re	-0.06906600	0.15651800	0.02624100
C	1.93244600	-0.76606500	-0.28149000
O	2.93130700	-1.25197500	-0.42606700
O	0.92720400	1.78056300	-0.17623600
C	-1.95281500	-0.42549500	-0.36029600
O	-3.01949200	-0.71644400	-0.57859900
C	-0.25020000	-0.66533200	1.56158800
H	-0.27639500	-1.05159700	2.57481500
H	-1.29961000	1.26177200	0.34554700
H	-0.20367100	-1.25458200	-0.86829100
H	1.87090400	1.94977800	-0.09170800

MECP1

$E_{B2GP-PLYP}$ = -492.9110748

Re	0.24504000	-0.03341000	-0.44789700
C	1.34040900	-1.16458800	0.58917700
O	1.99261500	-1.83372200	1.24976100
O	-1.95481600	-0.01558100	-0.25568000
C	-2.93505500	0.00183400	0.40932000
O	-3.88615000	0.01611900	1.03693800
C	1.23017800	1.27751100	0.47540900
O	1.82444800	2.06033100	1.06258300

MECP2

$E_{B2GP-PLYP}$ = -492.9227245

Re	0.00052600	-0.31875900	-0.18165700
C	1.66854100	-0.00343300	0.98071400
O	2.66680500	0.09688900	1.49754600
O	-0.02333300	-1.14357500	-1.66548000
C	-1.64733000	-0.01058900	1.00112600
O	-2.63935500	0.08785200	1.53041400
C	-0.00946100	1.63264800	-0.50309500
O	-0.01786300	2.73322600	-0.76850400

^{1}[Re(CO)]$^+$

1 1

$E_{CCSD(T)}$ = -190.7678466; T1 = 0.020

Re	0.00000000	0.00000000	0.39458300
C	0.00000000	0.00000000	-1.46448700
O	0.00000000	0.00000000	-2.60085400

^{1}[Re(CO)]$^+$

1 3

$E_{CCSD(T)}$ = -190.7927081; T1 = 0.019

Re	0.00000000	0.00000000	0.00000000
C	0.00000000	0.00000000	1.86190000
O	0.00000000	0.00000000	3.00341000

^{5}[Re(CO)]$^+$

1 5

$E_{CCSD(T)}$ = -190.841404; T1 = 0.020

Re	0.00000000	0.00000000	0.00000000
C	0.00000000	0.00000000	1.92936800
O	0.00000000	0.00000000	3.06461100

^{1}[Re(CO)$_2$]$^+$

1 1

$E_{CCSD(T)}$ = -304.0933152; T1 = 0.022

Re	0.00000000	0.00000000	0.50035300
C	0.00000000	1.29355900	-0.85927900
O	0.00000000	2.06572500	-1.70094400
C	0.00000000	-1.29355900	-0.85927900
O	0.00000000	-2.06572500	-1.70094400

^{3}[Re(CO)$_2$]$^+$

1 3

$E_{CCSD(T)}$ = -304.1091077; T1 = 0.023

Re	0.00000000	0.00000000	0.53534700
C	0.00000000	1.21490500	-0.92177600
O	0.00000000	1.91762600	-1.81810600
C	0.00000000	-1.21490500	-0.92177600
O	0.00000000	-1.91762600	-1.81810600

^{1}[Re(CO)$_3$]$^+$

1 1

$E_{CCSD(T)}$ = -417.302644; T1 = 0.025

Re	0.00009500	-0.00002700	-0.55014600
C	-0.89577800	-1.21988000	0.58300900
O	-1.42909800	-1.94580400	1.28176900
C	1.50426600	-0.16567400	0.58329700
O	2.39949000	-0.26434900	1.28222300
C	-0.60868700	1.38567000	0.58294000
O	-0.97113000	2.21031600	1.28169200

^{3}[Re(CO)$_3$]$^+$

1 3

$E_{CCSD(T)}$ = -417.2603366; T1 = 0.023

Re	-0.07166500	-0.29694300	-0.00002600

C	-2.12507600	-0.09765500	0.00001200
O	-3.24654400	0.02315100	0.00012000
C	1.93471800	-0.52285100	0.00001800
O	3.06318600	-0.60279700	0.00011800
C	0.39806300	1.56127700	-0.00004700
O	0.69944200	2.65791100	0.00002200

^{1}[Re(CO)(CH$_2$)]$^+$
1 1
$E_{CCSD(T)}$ = -230.0896549; T1 = 0.047

Re	0.00000000	0.36857900	0.00000000
C	1.76654500	-0.11485100	0.00000000
H	2.31492100	-1.05118200	0.00000000
H	2.37086100	0.81803000	0.00000000
C	-0.81586000	-1.31513300	0.00000000
O	-1.29873600	-2.35379300	0.00000000

^{3}[Re(CO)(CH$_2$)]$^+$
1 3
$E_{CCSD(T)}$ = -230.1157155; T1 = 0.040

Re	-0.37059400	-0.18727300	-0.00001000
C	-0.33871200	1.65149800	-0.00007100
H	-0.31299100	2.22766600	-0.92819900
H	-0.31240800	2.22590600	0.92921200
C	1.52403500	-0.05680100	0.00017400
O	2.66349700	0.00296400	-0.00010600

^{1}[Re(CO)$_2$(CH$_2$)]$^+$
1 1
$E_{CCSD(T)}$ = -343.3101298; T1 = 0.028

Re	-0.45658000	-0.00000700	-0.21786100
C	-0.82064000	0.00000600	1.61392600
H	-0.13899400	0.00000600	2.45980400
H	-1.89120900	0.00002200	1.87700200
C	0.96850700	1.22549400	-0.00863500
O	1.84843400	1.93414800	0.15141700
C	0.96853300	-1.22547500	-0.00862900
O	1.84847800	-1.93410900	0.15143200

^{3}[Re(CO)$_2$(CH$_2$)]$^+$
1 3
$E_{CCSD(T)}$ = -343.2742572; T1 = 0.033

Re	0.00000000	-0.32056400	-0.24139800
C	0.00000000	-1.21167900	1.37525400
H	-0.00000100	-0.81466700	2.38805000
H	0.00000100	-2.30296800	1.23472800
C	-1.58123300	0.83475600	0.06308900
O	-2.43552900	1.52580800	0.34209200
C	1.58123400	0.83475600	0.06308900
O	2.43553000	1.52580700	0.34209200

^{1}[ORe(CO)(CH$_2$)H$_2$]$^+$

1 1

$E_{CCSD(T)}$ = -306.4923247; T1 = 0.029

Re	-0.21282800	-0.02926100	0.00000000
C	1.92312600	0.10314300	0.00001800
O	3.04089700	0.17048100	0.00003400
C	-1.50335200	1.32696000	-0.00024300
H	0.27191900	0.43088900	1.53838100
H	-1.14071500	2.35793100	-0.00040700
H	-2.58267500	1.19979300	-0.00024400
H	0.27197300	0.43039700	-1.53851100
O	-0.96302400	-1.52111600	0.00022800

^{3}[ORe(CO)(CH$_2$)H$_2$]$^+$

1 3

$E_{CCSD(T)}$ = -306.416331; T1 = 0.027

Re	-0.20543300	-0.04301900	0.02294100
C	1.93365900	0.16010900	-0.01198700
O	3.04975800	0.24384600	-0.04778600
C	-1.59633600	1.39394700	-0.05873600
H	0.32708600	0.51001400	-1.46453200
H	-1.95683700	1.84843100	-0.97662700
H	-2.08206000	1.71872600	0.86139000
O	-0.95897900	-1.54225800	-0.11402400
H	0.36912300	0.21218500	1.57801000

^{7}TS1/2

1 7

$E_{CCSD(T)}$ = -265.9277438; T1 = 0.026

Re	-0.66362500	-0.02785900	0.00024100
C	2.36406300	0.05682400	-0.41485300
O	3.31412000	-0.23947000	0.17739600
O	1.13431700	0.45803300	0.13148400

^{3}TS1/3

1 3

$E_{CCSD(T)}$ = -265.9445066; T1 = 0.022

Re	0.56968900	-0.05832200	-0.00000100
C	-1.89144000	0.09770200	0.00001300
O	-2.82515700	-0.56106500	0.00000600
O	-1.09709200	1.03456200	-0.00000600

^{5}TS1/3

1 5

$E_{CCSD(T)}$ = -265.9785244; T1 = 0.027

Re	0.57319300	-0.05766200	0.00000000
C	-1.89538000	0.08525800	0.00001700
O	-2.84579500	-0.55097900	0.00000200
O	-1.10635800	1.02762000	-0.00001600

^{7}TS2/3

1 7

$E_{CCSD(T)}$ = -265.9277069; T1 = 0.028

Re	-0.59476100	-0.08995500	0.00000200
C	2.16709900	-0.31400500	-0.00008400
O	3.28643500	-0.26987400	0.00004600
O	0.66412500	1.34870400	-0.00000400

^{1}TS4/5

1 1

$E_{CCSD(T)}$ = -379.2001336; T1 = 0.058

Re	0.33139500	-0.46616300	-0.07744000
C	1.07712600	1.23852000	0.06934000
O	1.52516500	2.29379700	0.17221800
O	-1.41467000	-0.23940300	0.99334700
C	-1.88188400	0.42980500	0.07713900
O	-2.61375300	1.06464000	-0.54942100

^{3}TS4/5

1 3

$E_{CCSD(T)}$ = -379.2164177; T1 = 0.051

Re	-0.12912900	-0.49047000	-0.02218900
C	1.58013400	0.72701200	0.01585100
O	2.50824900	0.99113500	-0.63225300
O	0.91786300	0.79876700	1.09644700
C	-1.48859300	0.82886700	-0.13152200
O	-2.28418000	1.64134600	-0.16941500

^{5}TS4/5

1 5

$E_{CCSD(T)}$ = -379.2275021; T1 = 0.042

Re	0.06395500	-0.29864400	-0.00001700
C	2.08597300	0.49797000	-0.00014700
O	3.11290700	0.95030600	0.00014200
O	-1.70919100	-0.82335900	0.00013200
C	-1.57059700	0.86191600	0.00000500
O	-2.38982500	1.65292700	-0.00001200

^{1}TS6/7

1 1

$E_{CCSD(T)}$ = -492.5140546; T1 = 0.025

Re	-0.00009800	-0.07287500	-0.49727100
C	-1.45708100	-0.93381900	0.48031200
O	-2.33111600	-1.32233200	1.08999200
O	0.00069600	1.75581100	-0.68701800
C	0.00080300	1.33893300	0.85379900
O	0.00131400	1.97184400	1.80881500
C	1.45626200	-0.93521200	0.48000600
O	2.33003500	-1.32454900	1.08953700

^{3}TS6/7

1 3

$E_{CCSD(T)}$ = -492.4996645; T1 = 0.026

Re	0.02697000	-0.08915600	0.43518500
C	-1.31404800	1.36481500	-0.08095400
O	-1.93696000	2.23010400	-0.45045200
O	1.84575700	-0.46494400	0.45953800
C	-1.06666000	-1.31392400	-0.62854600
O	-1.62665500	-2.06043000	-1.27186900
C	1.48616900	0.39349900	-0.81718100
O	2.13591700	0.79781500	-1.67206600

^{1}TS8/9

1 1

$E_{CCSD(T)}$ = -605.6143637; T1 = 0.026

Re	-0.00263500	0.00008300	-0.35664600
C	1.95092600	-0.00015400	0.14808500
O	2.99076900	-0.00029100	0.61409300
O	1.49271800	0.00039100	-1.43878300
C	-0.29306700	-1.44223200	0.92404700
O	-0.35725100	-2.32267200	1.63822100
C	-0.29307300	1.44196200	0.92445000
O	-0.35724500	2.32220800	1.63887300
C	-2.08060200	-0.00001700	-0.33364500
O	-3.20742800	-0.00007900	-0.35604900

^{3}TS8/9

1 3

$E_{CCSD(T)}$ = -605.573247; T1 = 0.030

Re	-0.01660600	-0.21126800	-0.13529500
C	2.03454000	-0.29661000	-0.05771500
O	3.17227800	-0.06723600	-0.02093300
O	1.30855400	-1.56516600	-0.11190400
C	-2.03840300	-0.62220600	-0.46586300
O	-3.13082300	-0.84484300	-0.63637300
C	-0.48049800	0.41097300	1.65408100
O	-0.70818800	0.73707600	2.71552600
C	-0.12318500	1.72703600	-0.68957200
O	-0.03047700	2.80640800	-1.00861900

^{1}TS10/11

1 1

$E_{CCSD(T)}$ = -418.5031896; T1 = 0.027

Re	-0.08204900	-0.41587900	-0.21303600
C	-1.24431300	-0.92420900	1.16762900
H	-1.29511400	-2.02674000	1.18079200
H	-1.76724700	-0.40788400	1.96332300
C	-1.18449700	1.24837700	-0.13198100
O	-1.72146800	2.23144100	0.01039900
O	1.64123800	-0.71306700	0.35395300
C	1.36384700	0.87721200	0.14021200
O	2.03095600	1.78378600	0.35795100

^{3}TS10/11

1 3

$E_{CCSD(T)}$ = -418.5052814; T1 = 0.040

Re	0.05922600	-0.11681900	-0.17798500
C	0.25239900	-1.46866500	1.07800600
H	0.72284200	-1.36585700	2.05729600
H	-0.24136400	-2.42907200	0.90836200
C	2.07792800	0.53836800	0.11658000
O	3.12781200	0.92040900	0.23768400
O	-1.59451500	-0.21652400	-0.99321500
C	-1.70778500	0.61552200	0.37459000
O	-2.61563500	1.10173800	0.87655400

^{1}TS10/12

1 1

$E_{CCSD(T)}$ = -418.4820498; T1 = 0.029

Re	-0.33132700	-0.45416300	-0.02821500
C	1.07618500	0.02474100	1.27732800
H	1.59752800	-0.86066500	1.65658500
H	1.01430000	0.85360200	1.97357100
C	-1.53612700	0.96541600	0.04876000
O	-2.22540700	1.87876700	0.07314200
O	2.89793300	1.03128700	-0.05233700
O	1.06742400	0.23263600	-1.14917000
C	1.84628600	0.49780000	-0.07393800

^{3}TS10/12

1 3

$E_{CCSD(T)}$ = -418.4776254; T1 = 0.027

Re	-0.27179800	-0.41570600	0.01723600
C	0.87457200	0.32322700	1.37775100
H	1.42088800	-0.45444200	1.93050400
H	0.88874800	1.30464900	1.83882400
C	-1.80200700	0.77770500	-0.09309400
O	-2.62901500	1.55319200	-0.17308300
O	2.93962400	1.04984000	-0.08461900
O	1.21667700	-0.03385200	-1.17771800
C	1.90358700	0.52811700	-0.21443700

^{1}TS13/14

1 1

$E_{CCSD(T)}$ = -531.6313504; T1 = 0.029

Re	0.01254400	-0.18166100	-0.13548600
C	0.18604100	-0.19256600	1.78526000
H	1.14085400	-0.19618000	2.30668600
H	-0.66949700	-0.20420400	2.45213600
C	0.47001100	1.72426200	-0.12511900
O	0.64177800	2.84417100	-0.15298500
C	2.04697600	-0.61334300	0.00294100
O	3.13450600	-0.90514200	0.04581000
C	-1.98970800	-0.13804200	0.17927500

O	-3.06080600	-0.06020700	0.58166800
O	-1.42698800	-0.71093400	-1.18093600

^{3}**TS13/14**

1 3

$E_{CCSD(T)}$ = -531.6000508; T1 = 0.040

Re	0.00771800	-0.15929600	0.00543800
C	0.16736000	-0.17037700	1.86547900
H	0.86083400	0.41778200	2.46647500
H	-0.49153500	-0.83005500	2.43388300
C	0.58412100	1.81636900	-0.10543900
O	0.76759400	2.92461100	-0.21175400
C	1.98306400	-0.70748200	-0.36113900
O	3.05717200	-0.98983300	-0.55640600
C	-2.01436200	0.01522500	-0.25750200
O	-3.13136100	0.27909000	-0.38862900
O	-1.35205800	-1.38423700	-0.36278800

^{1}**TS13/15**

1 1

$E_{CCSD(T)}$ = -531.5946601; T1 = 0.037

Re	-0.09013900	-0.07374300	-0.33053700
C	1.05280700	0.57806000	1.19836100
H	0.70234400	0.20895300	2.16631600
H	1.27113000	1.64895100	1.27887300
C	-1.61817800	-1.14238000	0.36070300
O	-2.44381000	-1.79218300	0.79062900
C	-1.49111700	1.18650900	0.12850500
O	-2.26272200	1.98034100	0.39510000
O	1.77535200	0.04272000	-0.87383200
C	2.29334200	0.04293500	0.39730500
O	3.35190900	-0.27062200	0.79258500

^{3}**TS13/15**

1 3

$E_{CCSD(T)}$ = -531.6047003; T1 = 0.030

Re	0.11090300	-0.03981800	-0.29928000
C	-0.80470300	-0.11356900	1.40876900
H	-1.02363900	0.77687500	1.99720900
H	-0.79403800	-1.04598100	1.97482900
C	1.36937300	1.30757400	0.22412200
O	2.07980200	2.13286400	0.55849000
C	1.66212000	-1.14365900	0.17140200
O	2.53572600	-1.81397100	0.44937000
O	-1.85586600	0.25326500	-0.91731000
C	-2.42520200	-0.01317100	0.17167800
O	-3.42335900	-0.19310400	0.73671900

^{1}**TS16/17**

1 1

$E_{CCSD(T)}$ = -419.6898877; T1 = 0.025

Re	0.01369300	-0.22238200	-0.10074900
C	-1.18496000	1.39577600	-0.01657200
O	-1.89959300	2.27072600	-0.07931100
C	1.78222900	0.60055800	0.38078600
O	2.83087000	0.99045700	0.54589800
C	-1.28974600	-1.28785900	1.38634700
H	-2.07724000	-1.53128100	0.67099000
H	-1.01939100	-2.19606400	1.92120100
H	-1.63880500	-0.53922200	2.09336000
O	0.02903200	-1.01826300	-1.57431500
H	0.18086100	-1.24902100	1.22904900

^{3}TS16/17

1 3

$E_{CCSD(T)}$ = -419.6503688; T1 = 0.029

Re	0.27207700	-0.03147900	-0.13088300
C	-1.54889800	-1.08852500	-0.09950300
O	-2.50074900	-1.67138800	-0.27533800
C	-0.77322600	1.59741600	0.31896500
O	-1.30188300	2.57149700	0.55156100
C	1.17038400	-1.09533800	1.56360800
H	1.30480400	-1.98901300	0.93450000
H	2.14306000	-0.74511500	1.89621700
H	0.52764700	-1.32430500	2.40701300
O	1.53669000	0.29360700	-1.22176400
H	0.65669200	0.38827100	1.44438700

^{1}TS16/20

1 1

$E_{CCSD(T)}$ = -419.6371066; T1 = 0.025

Re	-0.00000100	-0.15809300	-0.08576100
C	-1.50140300	1.09952900	0.15336700
O	-2.42835000	1.75614900	0.18336800
O	-0.00000600	-1.34212100	-1.37645700
C	1.50141600	1.09951200	0.15336900
O	2.42837000	1.75612200	0.18337000
C	-0.00001400	-1.81160900	1.31850700
H	-0.90734200	-2.39758800	1.44451900
H	0.90730300	-2.39760500	1.44452000
H	-0.00000700	-1.03827900	2.10719300
H	-0.00001100	-1.99532300	-0.23783800

^{3}TS16/20

1 3

$E_{CCSD(T)}$ = -419.6185189; T1 = 0.029

Re	-0.17487200	-0.15596800	-0.14213100
C	0.55501000	1.66530400	-0.00553300
O	0.86903600	2.75710300	0.03344300
O	-1.66414700	-0.48325600	-1.05655100
C	1.75748000	-0.80295800	0.20379200
O	2.79751000	-1.23746900	0.29168700

C	-1.57834200	-0.16376700	1.56468300
H	-2.68185900	-0.19154700	1.51023300
H	-1.27860400	-1.07597600	2.07935000
H	-1.33819400	0.74207500	2.10880500
H	-2.01004500	-0.25942900	0.23515000

^{1}TS17/18

1 1

$E_{CCSD(T)}$ = -419.6818553; T1 = 0.025

Re	0.39480400	-0.04694200	0.03160900
C	-0.69843000	1.65351900	-0.03879400
O	-1.24402800	2.64078000	-0.09835100
C	-1.89637800	-0.69113800	-0.00301800
O	-2.95162200	-1.06597800	-0.01960700
C	0.40531800	-2.12417100	-0.13870200
H	-0.16417300	-2.69662700	0.59218100
H	1.47255400	-2.34300000	-0.02469100
O	1.91042700	0.64576100	-0.17584500
H	0.41479100	0.18274100	1.64329200
H	0.08526000	-2.41623600	-1.14792600

^{3}TS17/18

1 3

$E_{CCSD(T)}$ = -419.6466807; T1 = 0.046

Re	-0.32120900	-0.20177000	0.03125800
C	1.68785500	-0.99153800	-0.01158800
O	2.70368200	-1.46551400	-0.00729300
C	1.05900100	1.59307300	-0.03548100
O	1.62947600	2.55436300	-0.15354400
C	-1.59147200	1.48510900	0.02324700
H	-1.25042700	2.34577800	0.58793300
H	-2.48918300	1.07402900	0.49221000
O	-1.47260000	-1.39194800	-0.33222900
H	-0.18100800	-0.14225500	1.67472000
H	-1.80546100	1.76016900	-1.01177000

^{1}TS18/19

1 1

$E_{CCSD(T)}$ = -419.6623118; T1 = 0.027

Re	-0.39888600	-0.03743200	-0.06269700
C	1.77845100	-0.90087300	-0.11476200
O	2.78708500	-1.36497400	-0.27107000
C	0.89007100	1.58343400	0.19082500
O	1.54726900	2.47488400	0.38442000
C	-0.70294800	-1.81903300	0.63002000
H	-0.03575400	-2.59294300	0.98775000
H	-1.75714900	-2.04453300	0.80912600
O	-1.86580900	0.76947700	-0.27395500
H	0.19578000	-0.25333700	-1.61090900
H	-0.02819000	-0.51803200	1.56461800

^{3}TS18/19

1 3

$E_{CCSD(T)}$ = -419.5983599; T1 = 0.036

Re	-0.20831200	-0.25665700	-0.11595200
C	2.01663600	0.39036500	-0.13868900
O	3.09575200	0.68213200	-0.23036400
C	-0.70320300	1.70848800	0.25644300
O	-0.97679500	2.76452000	0.52759800
C	0.53273100	-1.75168300	1.04815200
H	-0.13406900	-2.24093700	1.75038200
H	1.57137600	-2.05658400	1.09085900
O	-1.78080200	-0.81528200	-0.42910800
H	0.24957600	0.38082200	-1.60887200
H	0.15428900	0.03202800	1.52360300

^{1}TS18/20

1 1

$E_{CCSD(T)}$ = -419.6459025; T1 = 0.027

Re	0.16100400	-0.27917400	-0.00537000
C	-1.84992000	-0.12629500	0.25105400
O	-2.97140500	-0.06218600	0.35639400
C	0.16814700	1.63411600	-0.29895300
O	0.23502800	2.72969700	-0.60052700
C	1.46474300	0.15050800	1.51330300
H	2.01092600	1.07804900	1.63213300
H	2.03644100	-0.72828700	1.80912700
O	0.77650800	-1.34297900	-1.28780200
H	0.34920200	-0.14822800	-1.69859700
H	0.50927300	0.19031300	2.12314700

^{3}TS18/20

1 3

$E_{CCSD(T)}$ = -419.6104553; T1 = 0.037

Re	0.01136700	-0.31496200	-0.02057800
C	-1.74864700	0.69513500	0.06023600
O	-2.76854900	1.17462000	-0.02701100
C	1.13228100	1.27305800	-0.35163200
O	1.82128600	2.13762400	-0.58951500
C	0.76470800	-0.12701600	1.94542100
H	1.78449000	-0.50943200	2.00578600
H	0.09228900	-0.78417100	2.51324800
O	0.40332400	-1.64062300	-1.06643500
H	0.00028700	-0.38036900	-1.80507300
H	0.73184300	0.87606900	2.36894500

^{1}TS20/21

1 1

$E_{CCSD(T)}$ = -419.6917639; T1 = 0.026

Re	-0.17494100	-0.22487100	-0.03206400
C	-0.27531600	1.66252900	0.08213500
O	-0.37969600	2.79861600	0.14854100

O	-1.55622500	-0.77457700	-1.13432300
C	1.81941900	-0.15026500	-0.27354800
O	2.93300100	-0.12321500	-0.46235900
C	-0.26812500	-0.83566900	1.80160800
H	-0.43881100	-0.41199500	2.78679000
H	-0.26865500	-1.93604700	1.79581100
H	0.46950100	0.37169200	1.42356700
H	-2.27398500	-0.42445900	-1.67739600

^{3}TS20/21
1 3
$E_{CCSD(T)}$ = -419.643337; T1 = 0.029

Re	0.00035900	0.01869800	-0.04830600
C	2.07653900	-0.02090200	-0.14262500
O	3.19877200	-0.07174000	-0.20194800
O	-0.04131000	1.86349500	0.39189600
C	-2.08236900	-0.05779800	-0.12298300
O	-3.20112000	-0.13326900	-0.20686900
C	0.09593300	-1.78598500	0.60805600
H	-0.66143300	-2.20486000	1.27324100
H	0.89800000	-2.49278500	0.40500100
H	-0.40048500	-1.30221200	-1.07259100
H	-0.05433200	2.51775800	1.09796600

^{1}TS21/22
1 1
$E_{CCSD(T)}$ = -419.6644922; T1 = 0.025

Re	0.06454000	-0.26334800	0.00244900
C	-1.69984400	1.09284400	0.17421100
O	-2.57096100	1.76860700	0.37485900
O	-1.12750500	-1.39465400	-0.95522800
C	1.53888200	1.09821600	-0.24866600
O	2.37118700	1.83831900	-0.43096800
C	0.94599100	-1.25548100	1.15620900
H	1.48195100	-1.90478700	1.83684500
H	1.40218300	-1.15668300	-0.51846400
H	0.23221800	0.76858400	1.30349800
H	-2.04882900	-1.26764100	-1.20535700

References

(1) Engeser, M.; Weiske, T.; Schröder, D.; Schwarz, H. *J. Phys. Chem. A* **2003,** *107*, 2855-2859.
(2) Eller, K.; Zummack, W.; Schwarz, H. *J. Am. Chem. Soc.* **1990,** *112*, 621-627.
(3) Eller, K.; Schwarz, H. *Int. J. Mass Spectrom. Ion Processes* **1989,** *93*, 243-257.
(4) Frisch, M. J.; Trucks, G. W.; Schlegel, H. B.; Scuseria, G. E.; Robb, M. A.; Cheeseman, J. R.; Scalmani, G.; Barone, V.; Mennucci, B.; Petersson, G. A.; Nakatsuji, H.; Caricato, M.; Li, X.; Hratchian, H. P.; Izmaylov, A. F.; Bloino, J.; Zheng, G.; Sonnenberg, J. L.; Hada, M.; Ehara, M.; Toyota, K.; Fukuda, R.; Hasegawa, J.; Ishida, M.; Nakajima, T.; Honda, Y.; Kitao, O.; Nakai, H.; Vreven, T.; Montgomery, J. A.; Jr.; Peralta, J. E.; Ogliaro, F.; Bearpark, M.; Heyd, J. J.; Brothers,

E.; Kudin, K. N.; Staroverov, V. N.; Kobayashi, R.; Normand, J.; Raghavachari, K.; Rendell, A.; Burant, J. C.; Iyengar, S. S.; Tomasi, J.; Cossi, M.; Rega, N.; Millam, J. M.; Klene, M.; Knox, J. E.; Cross, J. B.; Bakken, V.; Adamo, C.; Jaramillo, J.; Gomperts, R.; Stratmann, R. E.; Yazyev, O.; Austin, A. J.; Cammi, R.; Pomelli, C.; Ochterski, J. W.; Martin, R. L.; Morokuma, K.; Zakrzewski, V. G.; Voth, G. A.; Salvador, P.; Dannenberg, J. J.; Dapprich, S.; Daniels, A. D.; Farkas, O.; Foresman, J. B.; Ortiz, J. V.; Cioslowski, J.; Fox, D. J., Gaussian 09, Revision D.01, Gaussian, Inc., Wallingford CT, 2009.
(5) Karton, A.; Tarnopolsky, A.; Lamère, J.-F.; Schatz, G. C.; Martin, J. M. L. *J. Phys. Chem. A* **2008,** *112*, 12868-12886.
(6) Grimme, S.; Ehrlich, S.; Goerigk, L. *J. Comput. Chem.* **2011,** *32*, 1456-1465.
(7) Grimme, S.; Antony, J.; Ehrlich, S.; Krieg, H. *J. Chem. Phys.* **2010,** *132*, 154104.
(8) Sun, Y. H.; Chen, H. *J. Chem. Theory Comput.* **2014,** *10*, 579-588.
(9) Weigend, F.; Ahlrichs, R. *Phys. Chem. Chem. Phys.* **2005,** *7*, 3297-3305.
(10) Andrae, D.; Haussermann, U.; Dolg, M.; Stoll, H.; Preuss, H. *Theor. Chim. Acta* **1990,** *77*, 123-141.
(11) Hratchian, H. P.; Schlegel, H. B. *J. Chem. Theory Comput.* **2005,** *1*, 61-69.
(12) Truhlar, D. G.; Kilpatrick, N. J.; Garrett, B. C. *J. Chem. Phys.* **1983,** *78*, 2438-2442.
(13) Fukui, K. *Acc. Chem. Res.* **1981,** *14*, 363-368.
(14) Scuseria, G. E.; Schaefer, H. F. *J. Chem. Phys.* **1989,** *90*, 3700-3703.
(15) Scuseria, G. E.; Janssen, C. L.; Schaefer, H. F. *J. Chem. Phys.* **1988,** *89*, 7382-7387.
(16) Pople, J. A.; Headgordon, M.; Raghavachari, K. *J. Chem. Phys.* **1987,** *87*, 5968-5975.
(17) Purvis, G. D.; Bartlett, R. J. *J. Chem. Phys.* **1982,** *76*, 1910-1918.
(18) Reed, A. E.; Curtiss, L. A.; Weinhold, F. *Chem. Rev.* **1988,** *88*, 899-926.
(19) Carpenter, J. E.; Weinhold, F. *J. Mol. Struct. Theochem* **1988,** *46*, 41-62.
(20) Reed, A. E.; Weinstock, R. B.; Weinhold, F. *J. Chem. Phys.* **1985,** *83*, 735-746.
(21) Reed, A. E.; Weinhold, F. *J. Chem. Phys.* **1985,** *83*, 1736-1740.
(22) Reed, A. E.; Weinhold, F. *J. Chem. Phys.* **1983,** *78*, 4066-4073.
(23) Foster, J. P.; Weinhold, F. *J. Am. Chem. Soc.* **1980,** *102*, 7211-7218.
(24) Harvey, J. N.; Aschi, M.; Schwarz, H.; Koch, W. *Theor. Chem. Acc.* **1998,** *99*, 95-99.

Paper VI

ChemPubSoc Europe
DOI: 10.1002/chem.201601339
CHEMISTRY
A European Journal
Full Paper

Two-State Reactivity

On the Activation of Methane and Carbon Dioxide by $[HTaO]^+$ and $[TaOH]^+$ in the Gas Phase: A Mechanistic Study

Marjan Firouzbakht,[a] Nicole J. Rijs,[b] Patricio González-Navarrete,[a] Maria Schlangen,[a] Martin Kaupp,*[a] and Helmut Schwarz*[a]

Dedicated to Professor Paul Knochel on the occasion of his 60th birthday

Abstract: The thermal reactions of $[Ta,O,H]^+$ with methane and carbon dioxide have been investigated experimentally and theoretically by using electrospray ionization mass spectrometry (ESI MS) and density functional theory calculations. Although the activation of methane proceeds by liberation of H_2, the activation of CO_2 gives rise to the formation of $[OTa(OH)]^+$ under the elimination of CO. Computational studies of the reactions of methane and carbon dioxide with the two isomers of $[Ta,O,H]^+$, namely, $[HTaO]^+$ and $[Ta(OH)]^+$, have been performed to elucidate mechanistic aspects and to explain characteristic reaction patterns.

Introduction

The efficient conversion of C-1 compounds (e.g., CO_2, CO, and CH_4) into value-added chemicals and fuels is currently receiving considerable attention.[1] Natural gas is an abundant C-1 resource, of which methane is the major component by volume ($\approx$87 %).[1b] In addition to methane, carbon dioxide is also rightly viewed as an optimal C-1 source in organic synthesis, due to its high abundance and availability (e.g., as an industrial byproduct of combustion and of respiration), low cost, and being practically nontoxic compared with alternative reagents.[2] However, due to the inert nature of methane (as indicated by the high C—H bond dissociation energy (BDE) (H_3C—H) of 434 kJ mol^{-1}, the negative electron affinity, and an extremely high pK_a value) the development of conversion processes is still a challenging issue.[3] Likewise, CO_2 is also known for its kinetic inertness; moreover, with a standard enthalpy of formation of -394 kJ mol^{-1}, it is thermodynamically very stable.[3a,4]

A possible answer to these challenges is given by the ability of some transition-metal (TM) complexes to activate the unreactive C—H and C—O bonds of methane and carbon dioxide, respectively, making them useful catalysts in many important chemical reactions.[5] Recently, SiO_2-supported tantalum complexes have been used as catalysts to activate the C—H bonds of short alkanes, thus transforming them into longer-chain analogues.[6] Likewise, the activation of carbon dioxide by tantalum-hydride complexes through the migratory insertion into a Ta—H bond has been reported.[7]

Gas-phase experiments have proven useful to systematically study catalytic reactions, because they are not obscured by ill-defined conditions, such as the role of solvents, aggregation phenomena, or counterion effects.[3b] To date, several studies on the activation of CH_4 and CO_2 mediated by TM complexes in the gas phase have been performed.[8] In particular, metal-mediated dehydrogenation of methane was observed to occur in the thermal reaction with some of the third-row TM ions, according to Equation (1) (M = Ta, W, Os, Ir, and Pt).[8d,9]

$$[M]^+ + CH_4 \rightarrow [M,C,H_2]^+ + H_2 \qquad (1)$$

Furthermore, oxygen-atom transfer (OAT) from CO_2 to bare TM cations, including 5d cations, has been observed in the gas phase, reflecting the high oxophilicity of these species, as shown in Equation (2) (M = Sc, Ti, Y, Zr, Nb, La, Hf, Ta, and W).[10]

$$[M]^+ + CO_2 \rightarrow [MO]^+ + CO \qquad (2)$$

Intriguingly, the stoichiometric coupling of methane to carbon dioxide by atomic Ta^+ has been observed through the intermediate carbene complex, $[Ta(CH_2)]^{+}$.[11] Thus, Ta complexes are promising candidates to carry out both C—H and C—O bond activations for the generation of value-added chemi-

---

[a] M. Firouzbakht, Dr. P. González-Navarrete, Dr. M. Schlangen,
Prof. Dr. M. Kaupp, Prof. Dr. H. Schwarz
Institut für Chemie
Technische Universität Berlin
Strasse des 17. Juni 135
10623 Berlin (Germany)
E-mail: Martin.Kaupp@tu-berlin.de
Helmut.Schwarz@tu-berlin.de

[b] Dr. N. J. Rijs
Institute of Nanotechnology
Karlsruhe Institute of Technology
Hermann-von-Helmholtz-Platz 1
76344 Eggenstein-Leopoldshafen (Germany)

Supporting information for this article can be found under http://dx.doi.org/10.1002/chem.201601339.

© 2016 Wiley-VCH Verlag GmbH & Co. KGaA, Weinheim

cals. It has been shown previously that finding a “simple” reagent to simultaneously mediate both the activation of CH_4 and CO_2 with high efficiency can be extremely daunting.[8e] As such, herein we aim to understand and describe in detail the activation of CH_4 and CO_2 promoted by the tantalum oxo and hydroxo complexes, $[HTaO]^+$ and $[Ta(OH)]^+$, respectively, at a strictly molecular level.

Results and Discussion

Generation of $[Ta,H,O]^+$ and attempts to experimentally distinguish isomeric $[HTaO]^+$ and $[Ta(OH)]^+$

ESI of a methanolic solution of $TaCl_5$ results in the formation of ions with *m/z* 198, which contain tantalum, as indicated by the isotope pattern, and correspond to $[Ta,O,H]^+$. As has been shown for related Ta complexes,[12] this $[Ta,O,H]^+$ species may contain two possible isomers, that is, structures **1** and **2** (Scheme 1), which are inseparable by standard MS based on their mass-to-charge ratio alone.

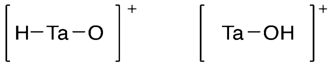

1 2

Scheme 1. Isomers of the tantalum complex with *m/z* 198.

Unfortunately, unambiguously identifying structures **1**, that is, $[HTaO]^+$, or **2**, that is, $[Ta(OH)]^+$, through collision-induced dissociation (CID) experiments is not instructive. Due to the strong tantalum–oxygen bond[13] and the less pronounced hydrogen-atom affinity of $[TaO]^+$,[14] hydrogen-atom loss is expected in both cases; thus, the predicted fragmentation patterns are the same. Further, parent ion scans for structural identification are also inconclusive (for details, see the Supporting Information). DFT calculations predict that the generation of structure **1**, $[HTaO]^+$, is energetically favored compared to that of structure **2**, $[Ta(OH)]^+$ (the latter being 30.9 $kJ\,mol^{-1}$ higher in energy); thus the formation of structure **1** is thermodynamically preferred in the gas phase (see Figure S1 in the Supporting Information, path I and path II, respectively). However, the relatively harsh conditions in the ESI source can presumably result in the formation of both species.

To obtain further information of the structure of the ions with *m/z* 198, we have carried out a time-honored hydrogen–deuterium (H/D) exchange reaction with D_2 in order to identify the structure in directly through the reactivity.[15] As mentioned in the Experimental Section, however, in all spectra that have been recorded after isolation of $[Ta,O,H]^+$ (*m/z* 198), a signal at *m/z* 199 is observed, most likely resulting from a reaction with background molecules. Notwithstanding this, the intensity of the signal at *m/z* 199 is considerably higher in intensity when D_2 is introduced into the reaction cell instead of Xe only (see Figure S2 in the Supporting Information). Thus, mass-selected $[Ta,O,H]^+$ reacts with D_2 according to Equation (3).

$$[Ta,O,H]^+ + D_2 \rightarrow [Ta,O,D]^+ + HD \quad (3)$$

The lowest kinetic barrier for an H/D exchange in the case of $[Ta(OH)]^+$ has been located through DFT calculations at 74.9 $kJ\,mol^{-1}$ above the entrance channel, whereas the formation of $[DTaO]^+$ proceeds through a transition state, which is located 32.8 $kJ\,mol^{-1}$ below the entrance channel (for details, see Figure S3 in the Supporting Information). Thus, although the H/D exchange is not kinetically possible for the $[Ta(OH)]^+$ isomer **2**, the observed reactivity [Eq. (3)] provides circumstantial evidence that structure **1** is present. However, this conclusion does not rule out the co-generation and presence of unreactive isomer **2**.

Finally, in terms of separating isomeric species based on their shape and size, as has been previously achieved for isomeric copper species formed through ESI,[16] the collisional cross sections (CCS) in N_2 of structure **1**, in its doublet spin state, and of structure **2**, in the quartet spin state, have been calculated to 119.0 and 109.6 $Å^2$, respectively. This is a moderate difference (≈8%), which may result in structural resolvability. Further, metal complexes with an open coordination site are known to have a reduced mobility in N_2 compared to their more coordinatively saturated counterparts.[16a, 17] Thus, we explored the feasibility of separating the species through ion mobility experiments, specifically, travelling wave ion mobility (TWIMS).[16a, 17] As such, the mass selected *m/z* 198 ion was subjected to the TWIMS cell in order to separate any isomers present. Unfortunately, despite several efforts, the ion is prone to destruction during TWIMS, and it is therefore not possible to obtain a satisfactory arrival time distribution due to signal loss. Thus, we are unable to directly separate any isomers, nor structurally identify them by using TWIMS.

In summary, although we cannot exclude the presence of the $[Ta(OH)]^+$ species **2**, the $[HTaO]^+$ species has certainly been generated in the course of the ESI process. However, owing to the probability of having produced a mixture of two isomers, we henceforth considered the reactivity toward CH_4 and CO_2 of both isomers. Indeed, the fact that structure **2** is generated concomitantly with structure **1** is indicated by the labeling experiment by using CD_4 as substrate, and by the associated potential energy surfaces (PESs), respectively (see further below).

C–H bond activation

Reactions with methane

We thus tested the ability of the $[Ta,O,H]^+$ ions formed (Scheme 1) to activate a C–H bond of methane. Figure 1 details the mass spectra for the ion/molecule reaction of *m/z* 198 ions with methane; a fragment ion $[Ta,O,C,H_3]^+$ (*m/z* 212) is generated concomitant with the elimination of H_2 (Figure 1 a and [Eq. (4)]).

$$[Ta,O,H]^+ + CH_4 \rightarrow [Ta,O,C,H_3]^+ + H_2 \quad (4)$$

Labeling experiments with CD_4 result in shifts, that is, *m/z* 212→214, and *m/z* 212→215 (Figure 1 b). Therefore, not only the expected labeled complex $[Ta,O,C,D_3]^+$ (*m/z* 215), formed by ligand exchange to generate HD, is observed [Eq. (5 a)], but also the unexpected complex $[Ta,O,C,H,D_2]^+$ (*m/z* 214) is gener-

© 2016 Wiley-VCH Verlag GmbH & Co. KGaA, Weinheim

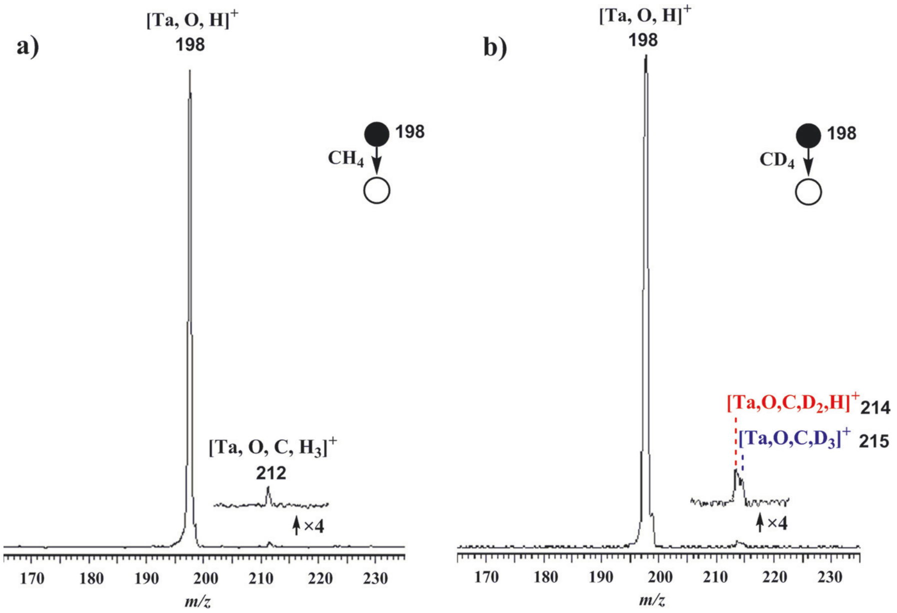

Figure 1. Mass spectra resulting from the thermal ion/molecule reaction of mass-selected $[Ta,O,H]^+$ with a) CH_4 at a pressure of 6.7×10^{-4} mbar and b) CD_4 at a pressure of 7.2×10^{-4} mbar. Steps of the multistep MS experiment are described with the mass of the isolated complex indicated in the insert.

ated under D_2 elimination with comparable abundance [Eq. (5 b)].

$$[Ta,O,H]^+ + CD_4 \rightarrow [Ta,O,C,D_3]^+ + HD \tag{5a}$$

$$\rightarrow [Ta,O,C,D_2H]^+ + D_2 \tag{5b}$$

DFT calculations were executed in order to obtain mechanistic insight into the C–H bond activation process with structures **1** and **2** as reactive species. Relevant stationary points on the PESs of the low-spin ground state for the reaction of structure ^{2}**1** with methane are shown in Figure 2; note that the related processes on the high-spin quartet surface are much higher in energy and are therefore not considered here for the thermal process.

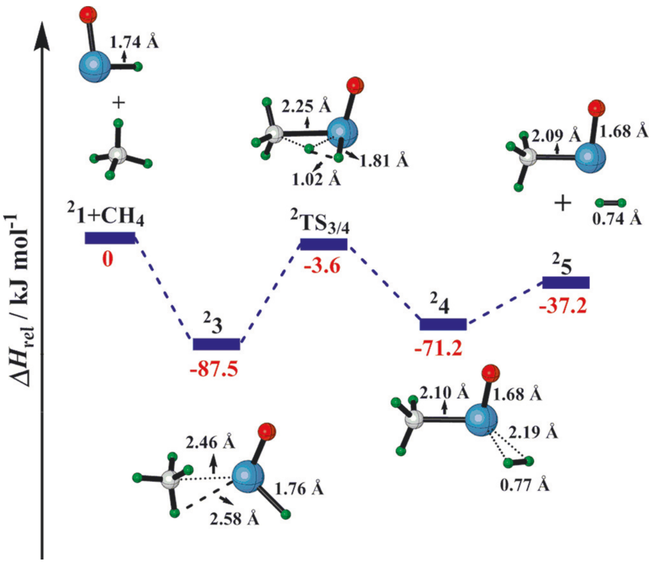

Figure 2. Potential-energy surfaces for the reaction of structure ^{2}**1** with CH_4 on the doublet spin surface. All energies are given in [kJ mol^{-1}]. Charges are omitted for the sake of brevity (C = gray, H = green, O = red, Ta = blue).

Starting from structure ^{2}**1**, the incoming methane coordinates to the metal center leading to the exothermic and barrier-free formation of complex ^{2}**3**. Then, a hydrogen atom from methane is transferred to the hydride ligand in a concerted manner through $^2TS_{3/4}$, giving rise to the intermediate $[(CH_3)Ta(H_2)]^+$ (^{2}**4**). As previously demonstrated for the reaction of $[HTiO]^+$ with CH_4, this corresponds to a σ-bond metathesis process,[18] with a coplanar arrangement of the two hydrogen, the carbon, and the tantalum atoms. Subsequently, the elimination of H_2 from complex ^{2}**4** results in the corresponding $[(CH_3)TaO]^+$ complex; the overall process is exothermic by 37.2 kJ mol^{-1}. An alternative pathway for the H_2 formation may proceed through a stepwise mechanism (Figure S4 in the Supporting Information). However, the first step corresponding to an oxidative addition is hampered by a barrier of 60.5 kJ mol^{-1} relative to $[HTaO]^+/CH_4$ and, therefore, is kinetically hindered under ambient conditions. It should be noted that the dehydrogenation according to Figure 2 results in the elimination of HD when CD_4 is used as substrate; scrambling processes through the back reaction $[(CD_3)Ta(HD)]^+$ (**4**$_{D4}$)$\rightarrow[(CD_3H)Ta(D)]^+$ (**3**$_{D4}$) are very unlikely according to the calculations. A possible explanation for the occurrence of Equation (5 b) will be given in the next paragraph.

The PESs of the reactions of $[Ta(OH)]^+$ (**2**) with methane are shown in Figure 3. In contrast to the doublet ground state of complex **1**, the reactive species **2** possesses a quartet ground state (with the doublet electronic state being 35.7 kJ mol^{-1} higher in energy). However, the ground state of the product ions of dehydrogenation, that is, $[Ta(O)(CH_3)]^+$ or $[Ta(OH)(CH_2)]^+$ (**5** and **9**, respectively, Figure 3), corresponds to the doublet state. Moreover, aside from the initial barrier-free

© 2016 Wiley-VCH Verlag GmbH & Co. KGaA, Weinheim

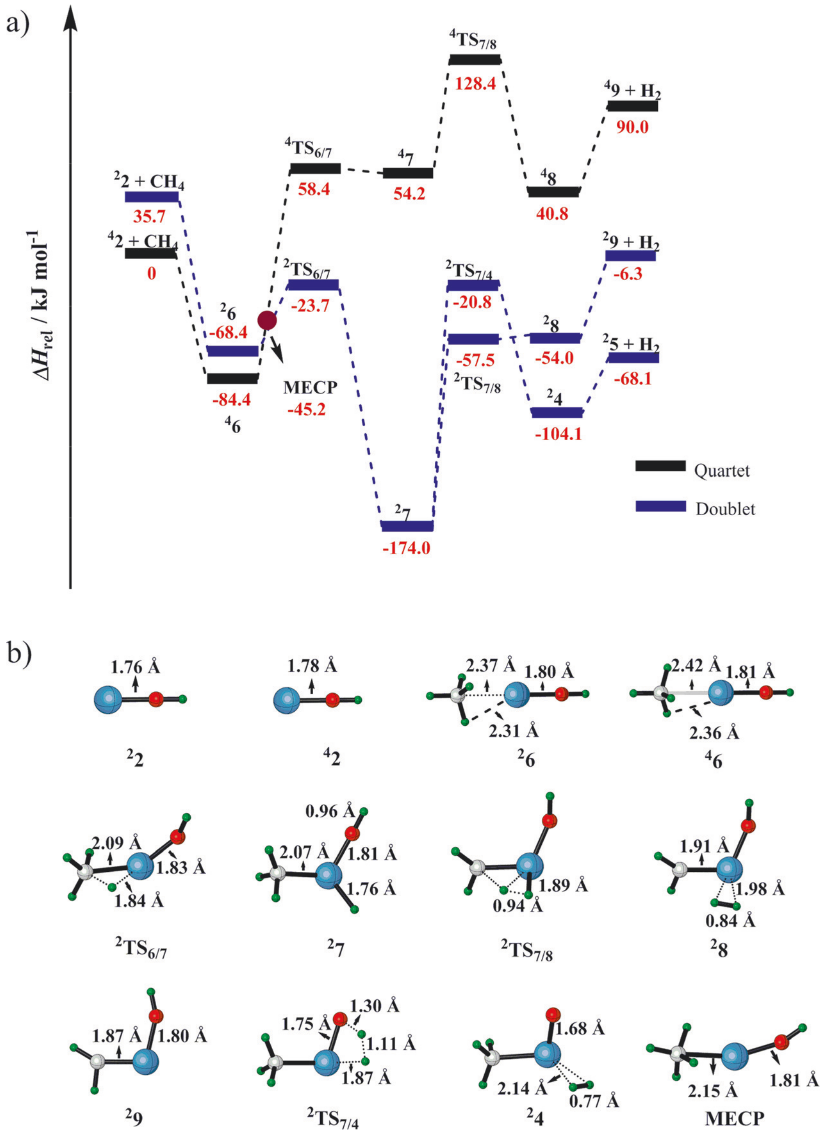
a)
ΔH_rel / kJ mol^-1
⁴TS7/8
128.4
⁴9 + H2
90.0
⁴TS6/7
58.4
⁴7
54.2
⁴8
40.8
²2 + CH4
35.7
⁴2 + CH4
0
²9 + H2
-6.3
²TS6/7
-23.7
²TS7/4
-20.8
²6
-68.4
²8
-54.0
-57.5
²TS7/8
²5 + H2
-68.1
-84.4
⁴6
MECP
-45.2
²4
-104.1
²7
-174.0
Quartet
Doublet
b)
1.76 Å
²2
1.78 Å
⁴2
2.37 Å
1.80 Å
2.31 Å
²6
2.42 Å
1.81 Å
2.36 Å
⁴6
2.09 Å
1.83 Å
1.84 Å
²TS6/7
0.96 Å
2.07 Å
1.81 Å
1.76 Å
²7
1.89 Å
0.94 Å
²TS7/8
1.91 Å
1.98 Å
0.84 Å
²8
1.87 Å
1.80 Å
²9
1.30 Å
1.75 Å
1.11 Å
1.87 Å
²TS7/4
1.68 Å
2.14 Å
0.77 Å
²4
2.15 Å
1.81 Å
MECP

Figure 3. a) Potential-energy surfaces for the reaction of structure **2** with methane for the low-spin (blue) and high-spin (black) states. All energies are given in [kJ mol^{-1}]. Charges are omitted for the sake of brevity. b) Structures of the species involved with selected geometric parameters indicated (C = gray, H = green, O = red, Ta = blue).

formation of the encounter complex ^{4}**6**, which is exothermic by 84.4 kJ mol^{-1}, the subsequent steps on the quartet surface are all considerably higher in energy compared to the entrance channel. Therefore, a spin crossing must take place to allow the reaction to proceed through a thermally accessible pathway. A minimum energy crossing point (MECP) with a relative energy of −45.2 kJ mol^{-1} has been localized prior to $^2TS_{6/7}$ (Figure 3); in $^2TS_{6/7}$ a hydrogen atom is transferred from CH_4 to the metal center. The lower doublet state of the latter, $^2TS_{6/7}$, has been located −23.7 kJ mol^{-1} below the reactants giving rise to the hydride intermediate $[HTa(OH)(CH_3)]^+$ (^{2}**7**), whose formation constitutes a driving force for the processes shown in Figure 3 a.

From structure ^{2}**7**, two different reaction pathways toward the elimination of H_2 are possible on the doublet PES. The first one takes place through σ-bond metathesis ($^2TS_{7/8}$) to generate the intermediate ^{2}**8**, from which H_2 is eliminated under the formation of structure ^{2}**9**. In intermediate ^{2}**8**, the H–H bond length of 0.83 Å is larger compared to the one calculated for intermediate ^{2}**4** (0.77 Å) and free H_2 (0.74 Å); nevertheless, complex ^{2}**8** can be characterized as a genuine H_2 complex rather than a dihydride intermediate.[19] The stronger interaction of the dihydrogen ligand with the metal center in structure ^{2}**8** compared to intermediate ^{2}**4** is further indicated by the shorter H–Ta bond lengths (1.96 and 1.98 Å vs. 2.14 and 2.19 Å, respectively) and the higher desorption energy (47.7 vs. 34.0 kJ mol^{-1}, respectively). This may be attributed to the presence of the strong (σ- and π-) donor carbene ligand in intermediate ^{2}**8**, which together with the hydroxo ligand, ensures more electron density at the metal center. Thus, structure ^{2}**8** has a more pronounced synergistic $H_2 \rightarrow Ta$ donation and $Ta \rightarrow H_2$ π-back-donation compared to the oxo/methyl ligand framework in structure ^{2}**4**. These considerations are confirmed by natural population analysis (NPA) charges, which indicate a less

© 2016 Wiley-VCH Verlag GmbH & Co. KGaA, Weinheim

positive metal center in intermediate ^{2}**8** compared to structure ^{2}**4** (see Table S1 in Supporting Information). Alternative to the formation of intermediate ^{2}**8**, the hydrogen-atom transfer from the OH moiety to the hydride ligand can take place through $^2TS_{7/4,}$ giving rise to complex ^{2}**4**. This step is exothermic by 104.1 $kJ\,mol^{-1}$, relative to the energy of the reactant pair. As described above, from intermediate ^{2}**4**, molecular hydrogen can be eliminated yielding the cationic isomer ^{2}**5** under thermal conditions. An interconversion of the two isomeric product ions, $^2\mathbf{5} \rightleftharpoons {}^2TS_{5/9} \rightleftharpoons {}^2\mathbf{9}$, is inhibited by a kinetic barrier of 138.3 $kJ\,mol^{-1}$. Finally, the formation of $[Ta(CH_3)]^+$ and H_2O is endothermic by 169.6 or 194.6 $kJ\,mol^{-1}$ on the quartet or doublet spin surfaces, respectively. This is in line with the experimental findings according to which water elimination does not take place.

Regarding the reactions of $[Ta,O,H]^+$ with CD_4, the loss of HD [Eq. (5 a)] can only be explained by the formation of structure ^{2}**5** (Figures 2 and 3 a), whereas the formation of structure ^{2}**9** (Figure 3 a) results in the elimination of D_2 [Eq. (5 b)]. Thus, the occurrence of D_2 elimination implies the co-generation of $[Ta(OH)]^+$ (**2**) under the ESI conditions together with its isomer $[HTaO)]^+$ (**1**).

Reactions with carbon dioxide

Next, we explored the possibility to activate the C–O bonds of CO_2 by the two $[Ta,O,H]^+$ species **1** and **2**. Figures 4 a and b detail the mass spectra for the thermal ion/molecule reactions of the mass-selected ions $[Ta,O,H]^+$ (*m/z* 198) with CO_2 and $C^{18}O_2$, respectively. The reaction results in an oxygen-atom transfer (OAT) from CO_2, yielding the complex $[Ta,O_2,H]^+$ (*m/z* 214) concomitant with the elimination of carbon monoxide [Eq. (6)].

$$[Ta,O,H]^+ + CO_2 \rightarrow [Ta,O_2,H]^+ + CO \qquad (6)$$

Experiments with $C^{18}O_2$ result in a quantitative shift, that is, *m/z* 214→216. Thus, the oxygen atom that is transferred to the ionic product originates exclusively from carbon dioxide, according to Equation (7). At higher pressures of the labeled substrate, however, not only the expected labeled complex $[Ta,^{18}O,O,H]^+$ at *m/z* 216 is observed, but also unlabeled $[Ta,O_2,H]^+$ at *m/z* 214. The latter product is most likely generated in reactions with residual gases containing oxygen, such as H_2O, present as background gas in the mass spectrometer (see Figure S5 in Supporting Information).[20]

$$[Ta,O,H]^+ + C^{18}O_2 \rightarrow [Ta,^{18}O,O,H]^+ + C^{18}O \qquad (7)$$

For the reaction of $[Ta,O,H]^+$ with carbon dioxide, four different mechanistic pathways were considered, depending on the structure of the precursor ion (A–D, Scheme 2). In path A (Scheme 2), a hydrogen-atom transfer from the metal center of $[HTaO]^+$ to an oxygen atom of CO_2 concomitant with the C–O bond cleavage and the oxygen-atom transfer to the metal center takes place simultaneously, followed by decarbonylation, yielding $[OTa(OH)]^+$. Path B (Scheme 2) also starts with $[HTaO]^+$ as a parent ion and corresponds to an insertion/decarbonylation mechanism. This is a common scenario for CO_2 activation observed in many reactions, which commences with the insertion of a CO unit of CO_2 into a metal–hydrogen bond (i.e., carboxylation resulting in the generation of a formate ligand).[8h,21] The higher oxophilicity of early transition metals can accelerate this reaction step due to the driving force of a stronger M–OCO interaction.[20,21b–d] A direct oxygen-atom transfer from CO_2 to the metal center of both isomers of $[Ta,O,H]^+$ (Scheme 1) is also possible, concurrent with the generation of $[HTa(O)_2]^+$ or $[OTa(OH)]^+$ (path C or D in Scheme 2,

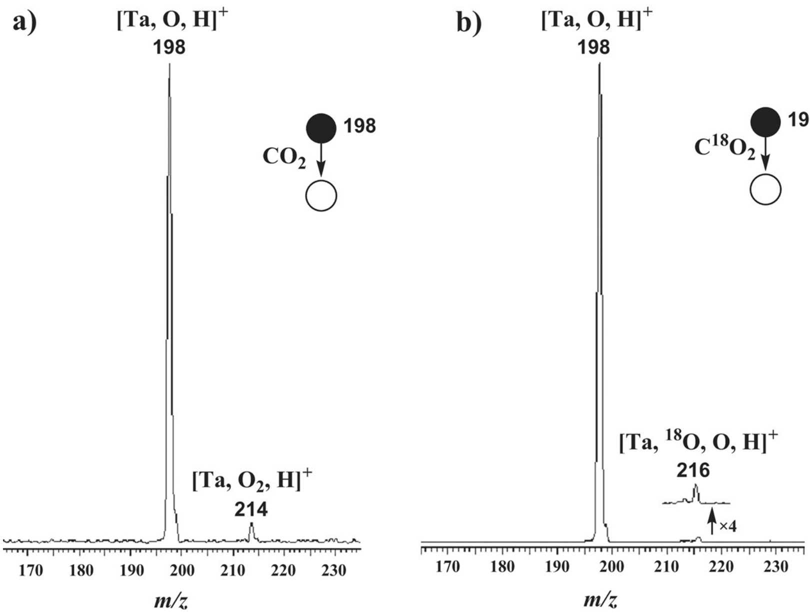

Figure 4. Mass spectra resulting from the thermal ion/molecule reaction of mass-selected $[Ta,O,H]^+$ with a) CO_2 at a pressure of 8.1×10^{-4} mbar and b) $C^{18}O_2$ at a pressure of 11.2×10^{-4} mbar. Steps of the multistep MS experiment are described with the mass of the isolated complex indicated in the insert.

© 2016 Wiley-VCH Verlag GmbH & Co. KGaA, Weinheim

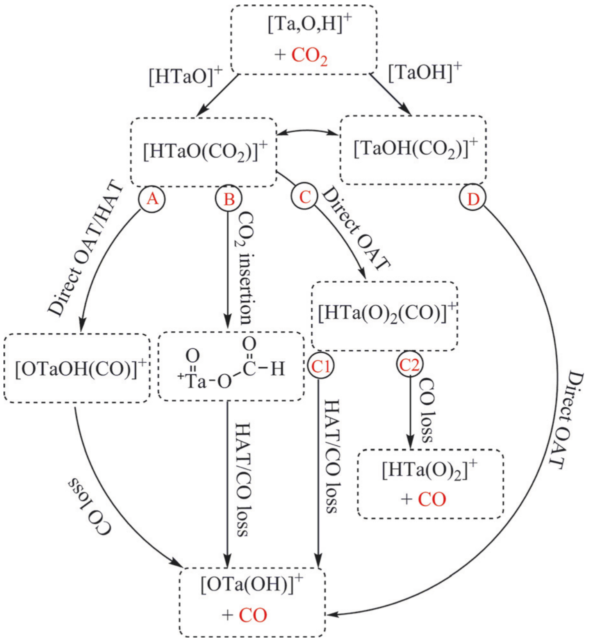

Scheme 2. Possible routes for the reaction of $[Ta,O,H]^+$ with carbon dioxide

respectively). Note that one of the oxygen ligands in $[HTa(O)_2]^+$ (path C2 in Scheme 2) corresponds to an oxyl radical, such that the oxidation state of Ta does not exceed the maximum number of five. Further, a hydrogen-atom transfer from the metal center of $[HTa(O)_2]^+$ to an oxygen atom takes place, followed by decarbonylation yielding $[OTa(OH)]^+$ (path C1 in Scheme 2). Finally, an interconversion $[HTaO(CO_2)]^+ \rightleftharpoons [Ta(OH)(CO_2)]^+$ might be possible by using the energy provided by forming the encounter complexes.

All these pathways have been investigated by means of DFT calculations. Starting from $[HTaO(CO_2)]^+$, path A (Scheme 2) is hindered by a barrier of 77.6 kJ mol^{-1} above the entrance channel; thus, path A is not accessible under thermal conditions.[22] Likewise, the interconversion $[HTaO(CO_2)]^+ \rightleftharpoons [Ta(OH)(CO_2)]^+$ is hampered by a kinetic barrier amounting to 69.4 kJ mol^{-1} on the doublet spin surface. Further, the direct OAT from CO_2 to the Ta atom of $[HTaO]^+$, path C (Scheme 2), is hindered by a barrier of 61.7 kJ mol^{-1} in the low-spin ground state; thus, both paths C1 and C2 are inaccessible under thermal conditions. Therefore, only paths B and D (Scheme 2) constitute plausible alternatives, as described in the following.

The mechanistic scenario for path B (Scheme 2), that is, the elimination of CO through the insertion of CO_2 into the Ta–H bond of $[HTaO]^+$, is shown for the low-spin state (doublet) in Figure 5 (note that the related high-spin state is much higher in energy and is thus not considered here).

Starting from structure ^{2}**1**, the incoming carbon dioxide coordinates in an end-on fashion to the metal center leading to complex ^{2}**10** (Figure 5). A CO_2 insertion process of the CO unit into the Ta–H bond occurs through a four-centered transition state, that is, $^2TS_{10/11}$, generating the formate intermediate ^{2}**12**. This step is kinetically and thermodynamically possible as $^2TS_{10/11}$ and intermediate ^{2}**11** are located below the entrance channel. Then, from structure ^{2}**11**, hydrogen-atom migration from the carbon atom to the Ta-bound oxygen atom of the OCHO unit takes place through $^2TS_{11/12}$ resulting in the decarbonylated complex ^{2}**12**, in which CO is loosely coordinated to the hydrogen atom of the newly formed OH ligand. A barrier-less elimination of carbon monoxide from intermediate ^{2}**12** gives rise to structure ^{2}**13**.

Relevant stationary points on the PESs for the reaction of $[Ta(OH)]^+$ with carbon dioxide through path D (Scheme 2) are shown in Figure 6. After having formed the quartet adduct ^{4}**14**, a continuation on the spin-allowed quartet surface is prohibited by a high barrier that is 69.5 kJ mol^{-1} above the entrance channel (i.e., $^4TS_{14/15}$). Therefore, in order to allow for a process that is thermally viable, the system must undergo an intersystem crossing (ISC) to access the lower-energy doublet surface. Thus, after spin crossing in the vicinity of intermediate $^2TS_{14/15}$, the migration of an oxygen atom of CO_2 to the metal center through $^2TS_{14/15}$ eventually leads, under the elimination of CO, to the highly exothermic formation of $[OTa(OH)]^+$ (^{2}**13**).

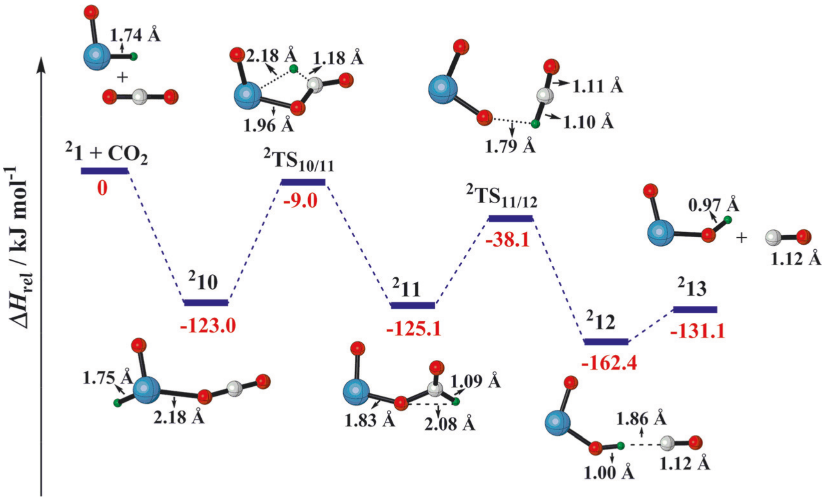

Figure 5. Potential-energy surfaces for the reaction of structure ^{2}**1** with CO_2 in the doublet spin state through path B (Scheme 2). All energies are given in [kJ mol^{-1}]. Charges are omitted for the sake of brevity (C = gray, H = green, O = red, Ta = blue).

© 2016 Wiley-VCH Verlag GmbH & Co. KGaA, Weinheim

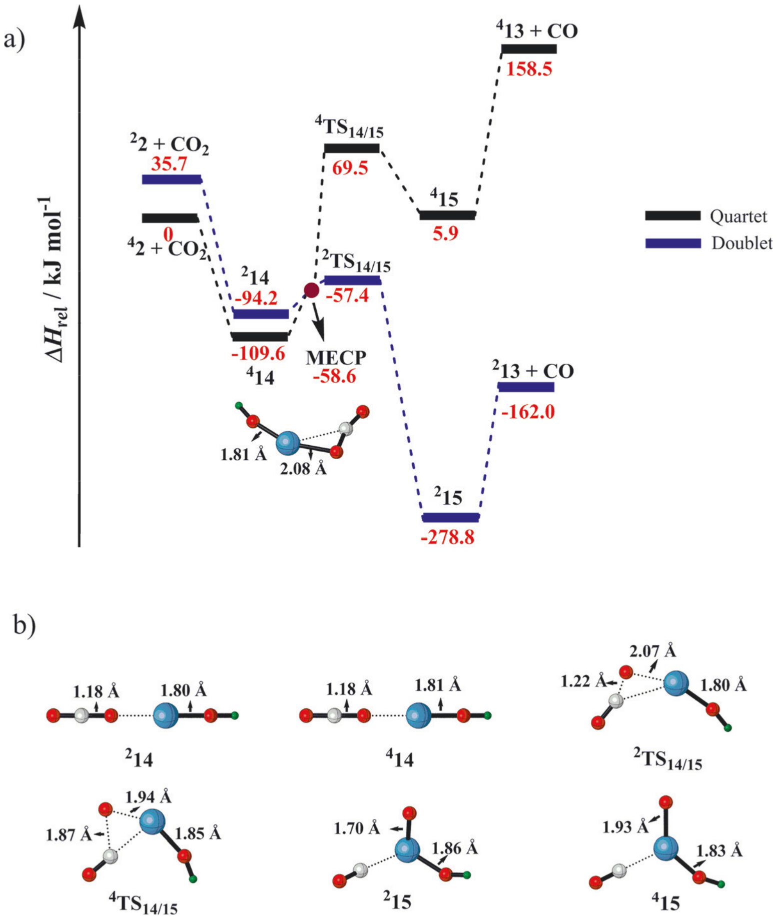

Figure 6. a) Potential-energy surfaces for the reaction of structure ^{4}**2** with carbon dioxide for the low-spin (blue) and high-spin (black) states through path D (Scheme 2). All energies are given in [kJ mol^{-1}]. Charges are omitted for the sake of brevity. b) Structures of the species involved and selected geometric parameters are indicated (C = gray, H = green, O = red, Ta = blue).

Two plausible pathways were found for the activation of CO$_2$, revealing that both structures ^{2}**1** and ^{4}**2** are able to activate the C–O bonds of CO$_2$. Similar to the reaction with methane, although structure ^{2}**1** mediates the reaction on a spin-allowed doublet surface through a step-wise carboxylation/decarbonylation mechanism, the process through structure ^{4}**2** must undergo an ISC from the quartet to the doublet surface according to a TSR scenario. The relative energies of the species involved in these reaction paths are lower compared to the energy of the separated reactants, and thus thermally allowed, which shows that both species (Scheme 1) can account for the CO$_2$ activation products observed (Figures 5 and 6).

Conclusion

In this combined experimental/computational study, we have investigated the mechanistic aspects of the activation of both methane and carbon dioxide by two isomers of [Ta,O,H]$^{+}$ (*m/z* 198), that is, [HTaO]$^{+}$ and [TaOH]$^{+}$.

Although we were able to confidently identify [HTaO]$^{+}$ through H/D exchange as being present, evidence for the cogeneration of [Ta(OH)]$^{+}$ is more indirect. As such, both isomers were considered as precursor species in the thermal ion/molecule reactions carried out. These experiments revealed that [Ta,O,H]$^{+}$ (*m/z* 198) reacting with CH$_4$ and CO$_2$ resulted in the ionic products [CH$_3$TaO]$^{+}$ (*m/z* 212) and [OTaOH]$^{+}$ (*m/z* 214), respectively. Isotopic labeling experiments with CD$_4$ revealed the formations of [Ta,O,C,D$_3$]$^{+}$ and [Ta,O,C,D$_2$H]$^{+}$, and a clean reaction in the case of reaction with C^{18}O$_2$.

DFT calculations reveal that although [HTaO]$^{+}$ possesses a doublet ground state, the ground state of [Ta(OH)]$^{+}$ corresponds to the quartet state. This has mechanistic implications for the observed reactivity. The calculated PESs indicate that both isomers are able to thermally activate a C–H bond of methane: whereas in the spin-allowed activation of CH$_4$ by [HTaO]$^{+}$ the rate-limiting step proceeds through a transition state located only 3.6 kJ mol^{-1} below the entrance channel, the activation of a C–H bond in case of the CH$_4$/[TaOH]$^{+}$ system requires an ISC and is associated with a rate-limiting barrier located 20 kJ mol^{-1} below the entrance channel. The activation of CO$_2$ follows a similar trend: the rate-limiting transition-state structure of the spin-allowed C–O activation mediated by [HTaO]$^{+}$ is -9.0 kJ mol^{-1} below the separated reactants, whereas for the [Ta(OH)]$^{+}$ system a spin crossing is necessary to access the transition structure of the C–O bond activation with a relative energy of -57.4 kJ mol^{-1}.

© 2016 Wiley-VCH Verlag GmbH & Co. KGaA, Weinheim

These findings may represent a significant step forward to realizing a single metal-oxo and metal-hydroxo catalyst capable of both C–H and C–O activations; tantalum metal centers are thus suggested to form such catalysts. As the products of the reactions described above are also oxo and hydroxo species, it is of course also of interest to see if a catalytic cycle can be closed involving both CH_4 and CO_2.

Experimental Section

The experiments were performed by using a VG Bio-Q mass spectrometer of QHQ configuration (Q = quadrupole; H = hexapole) equipped with an electrospray ionization (ESI) source, as described in detail elsewhere.[23] CH_3OH, $TaCl_5$, CH_4, CD_4, CO_2, and $C^{18}O_2$ were obtained from Sigma–Aldrich and utilized without further purification. To generate $[Ta,O,H]^+$, a methanolic millimolar solution of tantalum(V) chloride was introduced into the mass spectrometer by using a syringe pump and a fused-silica capillary connected to the ESI source, with a pump rate of 4 $\mu l\,min^{-1}$. Nitrogen was used as a nebulizing and drying gas, at a source temperature of 80 °C. The maximum intensity of the desired complex was achieved by adjusting the cone voltage (U_c) to around 110–120 V. The isotope patterns of the ions of interest have been compared with the calculated isotope patterns to confirm the identity of the ions.[24] The reactions of $[Ta,O,H]^+$ with methane and carbon dioxide have been probed at a collision energy (E_{lab}) nominally set to 0 eV, which, in conjunction with the approximately 0.4 eV kinetic energy width of the parent ion at peak half height, allows the investigation of quasi-thermal reactions, as described previously.[8a,25] The pressure of methane or carbon dioxide was varied between approximately 0.45×10^{-3} to 1.27×10^{-3} mbar in the hexapole. Cationic products are recorded by scanning of Q2. Note that in all the mass spectra in which the precursor ion $[Ta,O,H]^+$ (*m/z* 198) has been isolated for ion/molecule reactions, a minor signal at *m/z* 199 was also observed. The formation of ions with $\Delta m = +1$ relative to the precursor ion can in this case generally be explained by 1) an H/D exchange between the $[Ta,O,H]^+$ precursor and deuterated substrates, which are not completely removed from the mass spectrometer, 2) a ligand exchange of the hydroxo ligand of $[Ta(OH)]^+$ with water, or 3) hydrogen-atom abstraction from hydrocarbons present as residual gases in the reaction cell. However, we rule out the presence of deuterated substrates, like CD_4, in the mass spectrometer after more than two days, and preliminary DFT calculations indicate that the ligand exchange $[Ta(OH)]^+ + H_2O \rightarrow [Ta(H_2O)]^+ + OH^{\cdot}$ is endothermic by 384.6 $kJ\,mol^{-1}$. Hydrogen-atom abstraction from propene by $[Ta(OH)]^+$ or by $[HTaO]^+$ has been calculated to also be, but less, endothermic by 66.1 and 97.0 $kJ\,mol^{-1}$, respectively. Therefore a clear explanation for the formation of ions with *m/z* 199 in the thermal conditions has to be explored in further studies. The travelling-wave ion-mobility spectrometry (TWIMS) experiments were carried out with the same solutions described above, on a Synapt G2 mass spectrometer (Waters, Manchester) fitted with a standard ESI source, as previously described.[16a,17] Even with extensive tuning of the instrument parameters, it was not possible to retain a signal satisfactory for measuring an arrival time distribution.

Computational Details

For the computational studies we employed the Gaussian 09 program package[26] by using unrestricted DFT calculations with the B3LYP functional[27] and the def2-QZVP basis sets of Weigend and Ahlrichs, including a quasi-relativistic, energy-adjusted effective core potential (ECP) and an associated valence basis set for the tantalum atom.[28] The satisfying performance of the B3LYP functional for energetic and structural aspects of 5d block transition metals has been confirmed previously in benchmark studies.[14,29] Likewise, the nature of local minima and transition states (TSs) has been verified by harmonic vibrational frequency analysis of the respective optimized structures. Intrinsic reaction coordinate (IRC) calculations[30] have been performed in order to confirm the connection between TSs and minima. All energies (given in [$kJ\,mol^{-1}$]) are corrected for (unscaled) zero-point vibrational energy contributions. For those reactions that involve more than a single spin surface, the two-state reactivity (TSR) paradigm has been considered.[31] It was thus necessary to not only locate and characterize the stationary points on each potential energy surface (PES), but to also identify the regions where the relevant spin states lie close in energy (minimum energy crossing point, MECP). We located MECPs through the structures having identical geometry and energy in the doublet and quartet states. The MECPs were calculated by using the algorithm developed by Harvey et al.[32] Natural population analyses[33] (NPA) were carried out on the ground-state structures by using the built-in NBO3.1 module of Gaussian 09.[26]

Collisional cross sections were calculated by using the trajectory method within the Mobcal program.[34] N_2 parameters[35] were added to the trajectory method by the Bush group.[36]

Acknowledgements

This work has been supported by the Fonds der Chemischen Industrie, the Deutsche Forschungsgemeinschaft (DFG), and the Cluster of Excellence “Unifying Concepts in Catalysis” (coordinated by the Technische Universität Berlin and funded by the DFG). For computational resources, the Institut für Mathematik at the Technische Universität Berlin is acknowledged. N.J.R. and P.G.-N. thank the Alexander von Humboldt Foundation for support in the form of postdoctoral fellowships. Dr. Robert Kretschmer and Dr. Shaodong Zhou are appreciated for suggestions and comments. We thank Dr. Thomas Weiske for technical assistance.

Keywords: bond activation · carbon dioxide · decarbonylation · H_2 liberation · methane · tantalum

[1] a) G. A. Olah, *Angew. Chem. Int. Ed.* **2005**, *44*, 2636 – 2639; *Angew. Chem.* **2005**, *117*, 2692 – 2696; b) J. R. Webb, T. Bolaño, T. B. Gunnoe, *ChemSusChem* **2011**, *4*, 37 – 49; c) W. Wang, S. Wang, X. Ma, J. Gong, *Chem. Soc. Rev.* **2011**, *40*, 3703 – 3727; d) M. Cokoja, C. Bruckmeier, B. Rieger, W. A. Herrmann, F. E. Kühn, *Angew. Chem. Int. Ed.* **2011**, *50*, 8510 – 8537; *Angew. Chem.* **2011**, *123*, 8662 – 8690; e) G. A. Olah, *Angew. Chem. Int. Ed.* **2013**, *52*, 104 – 107; *Angew. Chem.* **2013**, *125*, 112 – 116; f) P. V. L. Reddy, K.-H. Kim, H. Song, *Renewable Sustainable Energy Rev.* **2013**, *24*, 578 – 585; g) M. Aresta, A. Dibenedetto, A. Angelini, *Chem. Rev.* **2014**, *114*, 1709 – 1742; h) J. M. Weber, *Int. Rev. Phys. Chem.* **2014**, *33*, 489 – 519.

[2] a) H. Arakawa, M. Aresta, J. N. Armor, M. A. Barteau, E. J. Beckman, A. T. Bell, J. E. Bercaw, C. Creutz, E. Dinjus, D. A. Dixon, K. Domen, D. L. DuBois, J. Eckert, E. Fujita, D. H. Gibson, W. A. Goddard, D. W. Goodman, J. Keller, G. J. Kubas, H. H. Kung, J. E. Lyons, L. E. Manzer, T. J. Marks, K. Morokuma, K. M. Nicholas, R. Periana, L. Que, J. Rostrup-Nielson, W. M. H. Sachtler, L. D. Schmidt, A. Sen, G. A. Somorjai, P. C. Stair, B. R. Stults, W. Tumas, *Chem. Rev.* **2001**, *101*, 953 – 996; b) M. Aresta, A. Dibenedetto, *Dalton Trans.* **2007**, 2975 – 2992.

© 2016 Wiley-VCH Verlag GmbH & Co. KGaA, Weinheim

[3] a) V. Havran, M. P. Duduković, C. S. Lo, *Ind. Eng. Chem. Res.* **2011**, *50*, 7089 – 7100; b) H. Schwarz, *Chem. Phys. Lett.* **2015**, *629*, 91 – 101.

[4] C. Maeda, Y. Miyazaki, T. Ema, *Catal. Sci. Technol.* **2014**, *4*, 1482 – 1497.

[5] a) I. Hermans, *Angew. Chem. Int. Ed.* **2013**, *52*, 4522 – 4523; *Angew. Chem.* **2013**, *125*, 4618 – 4619; b) W. B. Tolman, *Activation of Small Molecules: Organometallic and Bioinorganic Perspectives*, Wiley, New York, **2006**.

[6] a) V. Vidal, A. Théolier, J. Thivolle-Cazat, J.-M. Basset, J. Corker, *J. Am. Chem. Soc.* **1996**, *118*, 4595 – 4602; b) D. Soulivong, S. Norsic, M. Taoufik, C. Coperet, J. Thivolle-Cazat, S. Chakka, J.-M. Basset, *J. Am. Chem. Soc.* **2008**, *130*, 5044 – 5045; c) Y. Chen, E. Abou-hamad, A. Hamieh, B. Hamzaoui, L. Emsley, J.-M. Basset, *J. Am. Chem. Soc.* **2015**, *137*, 588 – 591.

[7] a) M. A. Rankin, C. C. Cummins, *J. Am. Chem. Soc.* **2010**, *132*, 10021 – 10023; b) J. Ballmann, F. Pick, L. Castro, M. D. Fryzuk, L. Maron, *Inorg. Chem.* **2013**, *52*, 1685 – 1687.

[8] a) D. Schröder, H. Schwarz, S. Schenk, E. Anders, *Angew. Chem. Int. Ed.* **2003**, *42*, 5087 – 5090; *Angew. Chem.* **2003**, *115*, 5241 – 5244; b) N. Dietl, C. van der Linde, M. Schlangen, M. K. Beyer, H. Schwarz, *Angew. Chem. Int. Ed.* **2011**, *50*, 4966 – 4969; *Angew. Chem.* **2011**, *123*, 5068 – 5072; c) N. Dietl, M. Schlangen, H. Schwarz, *Chem. Eur. J.* **2011**, *17*, 1783 – 1788; d) H. Schwarz, *Isr. J. Chem.* **2014**, *54*, 1413 – 1431; e) J. Li, P. González-Navarrete, M. Schlangen, H. Schwarz, *Chem. Eur. J.* **2015**, *21*, 7780 – 7789; f) S. Zhou, J. Li, X.-N. Wu, M. Schlangen, H. Schwarz, *Angew. Chem. Int. Ed.* **2016**, *55*, 441 – 444; *Angew. Chem.* **2016**, *128*, 452 – 455; g) M. Firouzbakht, M. Schlangen, M. Kaupp, H. Schwarz, *J. Catal.* **2016**, DOI: 10.1016/j.jcat.2015.09.012; h) H. Schwarz, *Coord. Chem. Rev.* **2016**, DOI: 10.1016/j.ccr.2016.03.009; i) S. Ramakrishnan, K. M. Waldie, I. Warnke, A. G. De Crisci, V. S. Batista, R. M. Waymouth, C. E. D. Chidsey, *Inorg. Chem.* **2016**, *55*, 1623 – 1632; j) P. D. Dau, P. B. Armentrout, M. C. Michelini, J. K. Gibson, *Phys. Chem. Chem. Phys.* **2016**, *18*, 7334 – 7340.

[9] a) K. K. Irikura, J. L. Beauchamp, *J. Am. Chem. Soc.* **1991**, *113*, 2769 – 2770; b) K. K. Irikura, J. L. Beauchamp, *J. Phys. Chem.* **1991**, *95*, 8344 – 8351; c) M. Pavlov, M. R. A. Blomberg, P. E. M. Siegbahn, R. Wesendrup, C. Heinemann, H. Schwarz, *J. Phys. Chem. A* **1997**, *101*, 1567 – 1579; d) X.-G. Zhang, R. Liyanage, P. B. Armentrout, *J. Am. Chem. Soc.* **2001**, *123*, 5563 – 5575; e) A. Shayesteh, V. V. Lavrov, G. K. Koyanagi, D. K. Bohme, *J. Phys. Chem. A* **2009**, *113*, 5602 – 5611.

[10] G. K. Koyanagi, D. K. Bohme, *J. Phys. Chem. A* **2006**, *110*, 1232 – 1241.

[11] R. Wesendrup, H. Schwarz, *Angew. Chem. Int. Ed. Engl.* **1995**, *34*, 2033 – 2035; *Angew. Chem.* **1995**, *107*, 2176 – 2179.

[12] a) G. Wang, J. Zhuang, M. Zhou, *J. Phys. Chem. A* **2011**, *115*, 8623 – 8629; b) M. Santos, M. d. C. Michelini, C. Lourenço, J. Marçalo, J. K. Gibson, M. C. Oliveira, *J. Phys. Chem. A* **2012**, *116*, 3534 – 3540.

[13] a) D. Schröder, H. Schwarz, S. Shaik in *Characterization, Orbital Description, and Reactivity Patterns of Transition-Metal Oxo Species in the Gas Phase, Vol. 97* (Ed. B. Meunier), Springer, Heidelberg, **2000**, pp. 91 – 123; b) C. S. Hinton, F. Li, P. B. Armentrout, *Int. J. Mass Spectrom.* **2009**, *280*, 226 – 234; c) C. S. Hinton, M. Citir, M. Manard, P. B. Armentrout, *Int. J. Mass Spectrom.* **2011**, *308*, 265 – 274.

[14] X. Zhang, H. Schwarz, *Theor. Chem. Acc.* **2011**, *129*, 389 – 399.

[15] D. B. Jacobson, B. S. Freiser, *J. Am. Chem. Soc.* **1985**, *107*, 72 – 80.

[16] a) N. J. Rijs, T. Weiske, M. Schlangen, H. Schwarz, *Chem. Phys. Lett.* **2014**, *608*, 408 – 424; b) N. J. Rijs, P. González-Navarrete, M. Schlangen, H. Schwarz, *J. Am. Chem. Soc.* **2016**, *138*, 3125 – 3135.

[17] N. J. Rijs, T. Weiske, M. Schlangen, H. Schwarz, *Anal. Chem.* **2015**, *87*, 9769 – 9776.

[18] R. Kretschmer, M. Schlangen, H. Schwarz, *Angew. Chem. Int. Ed.* **2013**, *52*, 6097 – 6101; *Angew. Chem.* **2013**, *125*, 6213 – 6217.

[19] G. J. Kubas, *Catal. Lett.* **2005**, *104*, 79 – 101.

[20] S.-Y. Tang, N. J. Rijs, J. Li, M. Schlangen, H. Schwarz, *Chem. Eur. J.* **2015**, *21*, 8483 – 8490.

[21] a) C. Federsel, A. Boddien, R. Jackstell, R. Jennerjahn, P. J. Dyson, R. Scopelliti, G. Laurenczy, M. Beller, *Angew. Chem. Int. Ed.* **2010**, *49*, 9777 – 9780; *Angew. Chem.* **2010**, *122*, 9971 – 9974; b) W. Sattler, G. Parkin, *J. Am. Chem. Soc.* **2012**, *134*, 17462 – 17465; c) Y. Jiang, O. Blacque, T. Fox, H. Berke, *J. Am. Chem. Soc.* **2013**, *135*, 7751 – 7760; d) C. Dong, X. Yang, J. Yao, H. Chen, *Organometallics* **2015**, *34*, 121 – 126; e) H. Fong, J. C. Peters, *Inorg. Chem.* **2015**, *54*, 5124 – 5135.

[22] Note that despite several efforts, the optimization of this transition state at the B3LYP/def2-QZVP level of theory was not achieved; therefore, the transition state was calculated by using a smaller basis set (i.e., def2-TZVP). The structure obtained by this method was then used for a single-point energy calculation at the B3LYP/def2-QZVP level of theory.

[23] C. Trage, D. Schröder, H. Schwarz, *Chem. Eur. J.* **2005**, *11*, 619 – 627.

[24] Scientific Instrument Service: Isotope Distribution Calculator and Mass Spec Plotter: http://www.sisweb.com/mstools/isotope.htm.

[25] a) D. Schröder, M. Engeser, H. Schwarz, E. C. E. Rosenthal, J. Döbler, J. Sauer, *Inorg. Chem.* **2006**, *45*, 6235 – 6245; b) N. Dietl, T. Wende, K. Chen, L. Jiang, M. Schlangen, X. Zhang, K. R. Asmis, H. Schwarz, *J. Am. Chem. Soc.* **2013**, *135*, 3711 – 3721.

[26] Gaussian 09, Revision A.02, M. J. Frisch, G. W. Trucks, H. B. Schlegel, G. E. Scuseria, M. A. Robb, J. R. Cheeseman, G. Scalmani, V. Barone, B. Mennucci, G. A. Petersson, H. Nakatsuji, M. Caricato, X. Li, H. P. Hratchian, A. F. Izmaylov, J. Bloino, G. Zheng, J. L. Sonnenberg, M. Hada, M. Ehara, K. Toyota, R. Fukuda, J. Hasegawa, M. Ishida, T. Nakajima, Y. Honda, O. Kitao, H. Nakai, T. Vreven, J. A. Montgomery, Jr., J. E. Peralta, F. Ogliaro, M. Bearpark, J. J. Heyd, E. Brothers, K. N. Kudin, V. N. Staroverov, R. Kobayashi, J. Normand, K. Raghavachari, A. Rendell, J. C. Burant, S. S. Iyengar, J. Tomasi, M. Cossi, N. Rega, J. M. Millam, M. Klene, J. E. Knox, J. B. Cross, V. Bakken, C. Adamo, J. Jaramillo, R. Gomperts, R. E. Stratmann, O. Yazyev, A. J. Austin, R. Cammi, C. Pomelli, J. W. Ochterski, R. L. Martin, K. Morokuma, V. G. Zakrzewski, G. A. Voth, P. Salvador, J. J. Dannenberg, S. Dapprich, A. D. Daniels, O. Farkas, J. B. Foresman, J. V. Ortiz, J. Cioslowski, D. J. Fox, Gaussian Inc., Wallingford CT, **2009**.

[27] a) A. D. Becke, *J. Chem. Phys.* **1993**, *98*, 5648 – 5652; b) C. Lee, W. Yang, R. G. Parr, *Phys. Rev. B* **1988**, *37*, 785 – 789.

[28] a) F. Weigend, R. Ahlrichs, *Phys. Chem. Chem. Phys.* **2005**, *7*, 3297 – 3305; b) D. Andrae, U. Häußermann, M. Dolg, H. Stoll, H. Preuß, *Theor. Chem. Acc.* **1990**, *77*, 123 – 141.

[29] X. Zhang, H. Schwarz, *Chem. Eur. J.* **2010**, *16*, 5882 – 5888.

[30] a) K. Fukui, *Acc. Chem. Res.* **1981**, *14*, 363 – 368; b) D. G. Truhlar, N. J. Kilpatrick, B. C. Garrett, *J. Chem. Phys.* **1983**, *78*, 2438 – 2442; c) C. Gonzalez, H. B. Schlegel, *J. Chem. Phys.* **1989**, *90*, 2154 – 2161.

[31] a) P. B. Armentrout, *Science* **1991**, *251*, 175 – 179; b) D. Schröder, S. Shaik, H. Schwarz, *Acc. Chem. Res.* **2000**, *33*, 139 – 145; c) J. N. Harvey, R. Poli, K. M. Smith, *Coord. Chem. Rev.* **2003**, *238 – 239*, 347 – 361; d) H. Schwarz, *Int. J. Mass Spectrom.* **2004**, *237*, 75 – 105; e) S. Shaik, *Int. J. Mass Spectrom.* **2013**, *354 – 355*, 5 – 14.

[32] J. N. Harvey, M. Aschi, H. Schwarz, W. Koch, *Theor. Chem. Acc.* **1998**, *99*, 95 – 99.

[33] A. E. Reed, R. B. Weinstock, F. Weinhold, *J. Chem. Phys.* **1985**, *83*, 735 – 746.

[34] a) M. F. Mesleh, J. M. Hunter, A. A. Shvartsburg, G. C. Schatz, M. F. Jarrold, *J. Phys. Chem.* **1996**, *100*, 16082 – 16086; b) A. A. Shvartsburg, M. F. Jarrold, *Chem. Phys. Lett.* **1996**, *261*, 86 – 91; c) M. F. Mesleh, J. M. Hunter, A. A. Shvartsburg, G. C. Schatz, M. F. Jarrold, *J. Phys. Chem. A* **1997**, *101*, 968 – 968.

[35] A. K. Rappe, C. J. Casewit, K. S. Colwell, W. A. Goddard, W. M. Skiff, *J. Am. Chem. Soc.* **1992**, *114*, 10024 – 10035.

[36] I. Campuzano, M. F. Bush, C. V. Robinson, C. Beaumont, K. Richardson, H. Kim, H. I. Kim, *Anal. Chem.* **2012**, *84*, 1026 – 1033.

Received: March 21, 2016
Published online on June 29, 2016

CHEMISTRY
A European Journal

Supporting Information

On the Activation of Methane and Carbon Dioxide by $[HTaO]^+$ and $[TaOH]^+$ in the Gas Phase: A Mechanistic Study

Marjan Firouzbakht,[a] Nicole J. Rijs,[b] Patricio González-Navarrete,[a] Maria Schlangen,[a] Martin Kaupp,*[a] and Helmut Schwarz*[a]

chem_201601339_sm_miscellaneous_information.pdf

Structural information of the [Ta,O,H]$^+$ ions investigated in this study can be obtained by using the parent-ion scan mode available for the QqQ mass spectrometer. [Ta,O_2,C,H_3]$^+$ has been identified as the precursor for the [Ta,O,H]$^+$ ions formed during ESI from methanolic solution of $TaCl_5$. Three reasonable structural isomers for [Ta,O_2,C,H_3] are conceivable (Structures **1S** – **3S**).

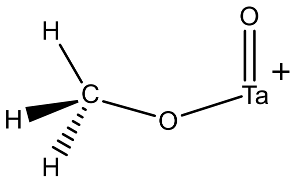

1S

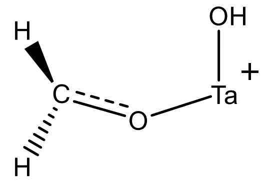

2S

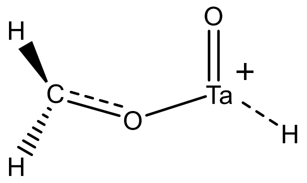

3S

CID experiments of [Ta,O_2,C,H_3] result in two different species, *m/z* 198 and *m/z* 213, corresponding to the elimination of CH_2O and CH_3, respectively. While the loss of a methyl radical is indicative for **1S**, [OTa(OCH_3)]$^+$, and prevails over that of CH_2O at higher collision energies, elimination of CH_2O is conceivable for intermediate **2S** and **3S**.[1] Thus, either two of the isomers (**1S** and **2S** or **1S** and **3S**, respectively) are concomitantly generated or only the **1S** isomer that interconverts to another isomer during the CID process. To get further hints, DFT-based potential energy surfaces (PESs) have been considered (Figure S1). The doublet (low spin) state of [OTa(OCH_3)]$^+$ (**1S**) is the energetic minimum of the PESs. Starting from **1S**, the interconversions **1S** → **2S** and **1S** → **3S** can occur by hydrogen-atom transfer to the oxygen-atom, resulting in complex **2S** (path I, Figure S1), or to the metal center, leading to complex **3S** (path II, Figure S1), respectively. The generation of [HTaO]$^+$ (path II, Figure S1) is energetically favored compared to that of [Ta(OH)]$^+$ (path I, Figure S1) and $\mathbf{TS_{1S/3S}}$ to generate the former requires less energy than $\mathbf{TS_{1S/2S}}$ for the latter complex; thus, the formation of [HTaO]$^+$ is kinetically and thermodynamically preferred. That CH_2O loss is favored at lower collision energies while the elimination of CH_3 is more pronounced at higher energies is indicative of two different types of fragmentations, i.e. rearrangement processes precede most likely the elimination of CH_2O while the CH_3 loss is probably achieved by simple bond cleavage. Thus, the CID fragmentation pattern at different collision energies points to the exclusive existence of isomer **1S**. This is to some extent not in line with the calculations according to which the elimination of CH_3 should be favored also at lower collision energies since it requires only 301.1 kJ mol^{-1} compared to 323.5 kJ mol^{-1} for the loss of CH_2O; obviously, the theoretical method applied cannot describe these fragmentations quantitatively. Nevertheless, we assume that the rearrangement to **2S** and **3S** is possible since both processes are much lower in energy compared to the fragmentation processes. Moreover, the cone voltage applied in the experiments is U_c = 110-120 V. This is relatively high, resulting in quite harsh conditions in the ESI source; thus, the exclusive formation of either $[HTaO]^+$ or $[Ta(OH)]^+$ cannot be inferred from these investigations.

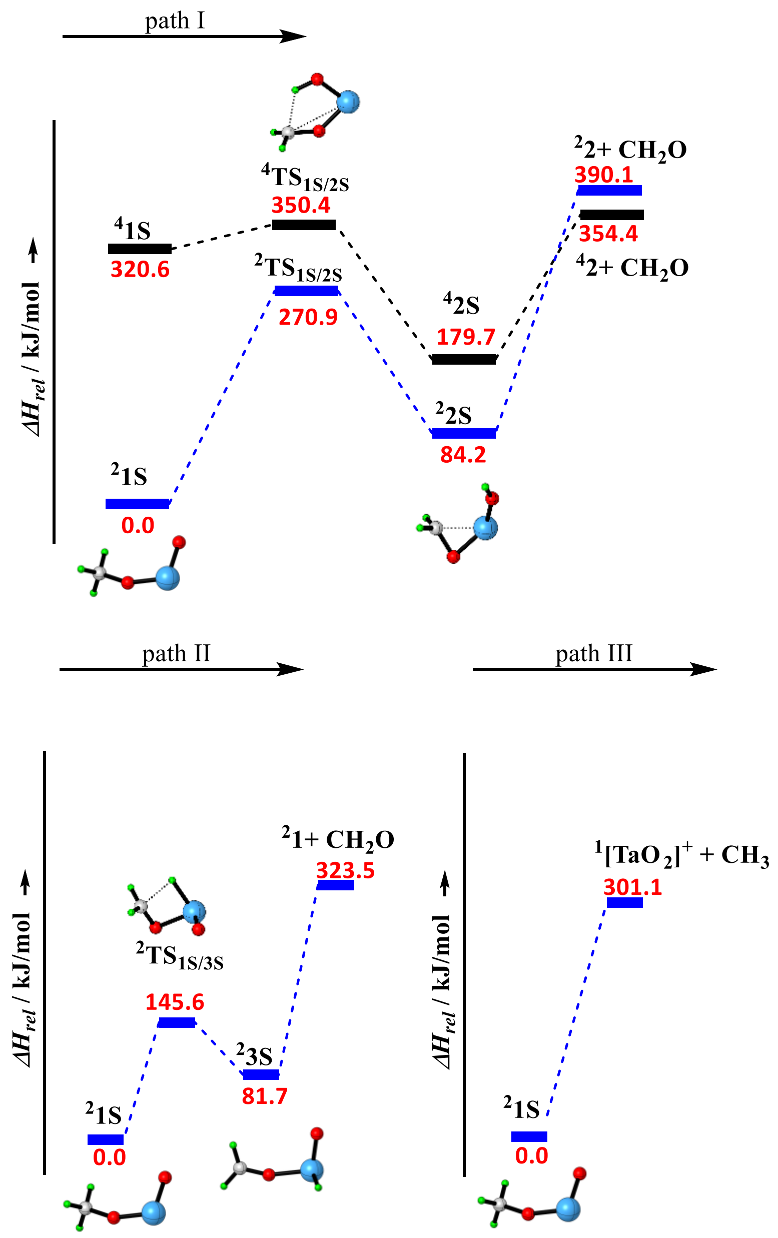
path I
ΔH_rel / kJ/mol
⁴1S
320.6
⁴TS1S/2S
350.4
²TS1S/2S
270.9
²2+ CH₂O
390.1
354.4
⁴2+ CH₂O
⁴2S
179.7
²2S
84.2
²1S
0.0
path II
ΔH_rel / kJ/mol
²TS1S/3S
145.6
²1+ CH₂O
323.5
²3S
81.7
²1S
0.0
path III
ΔH_rel / kJ/mol
¹[TaO₂]⁺ + CH₃
301.1
²1S
0.0

Figure S1. Potential-energy surfaces for the dissociation pathways of $[TaO(OCH_3)]^+$ for the low-spin (blue, doublet) and high-spin (black, quartet) states. All energies are given in kJ mol^{-1} and marked in red (B3LYP/def2-QZVP). Charges are omitted for the sake of brevity. C= gray, H= green, O= red, Ta= blue.

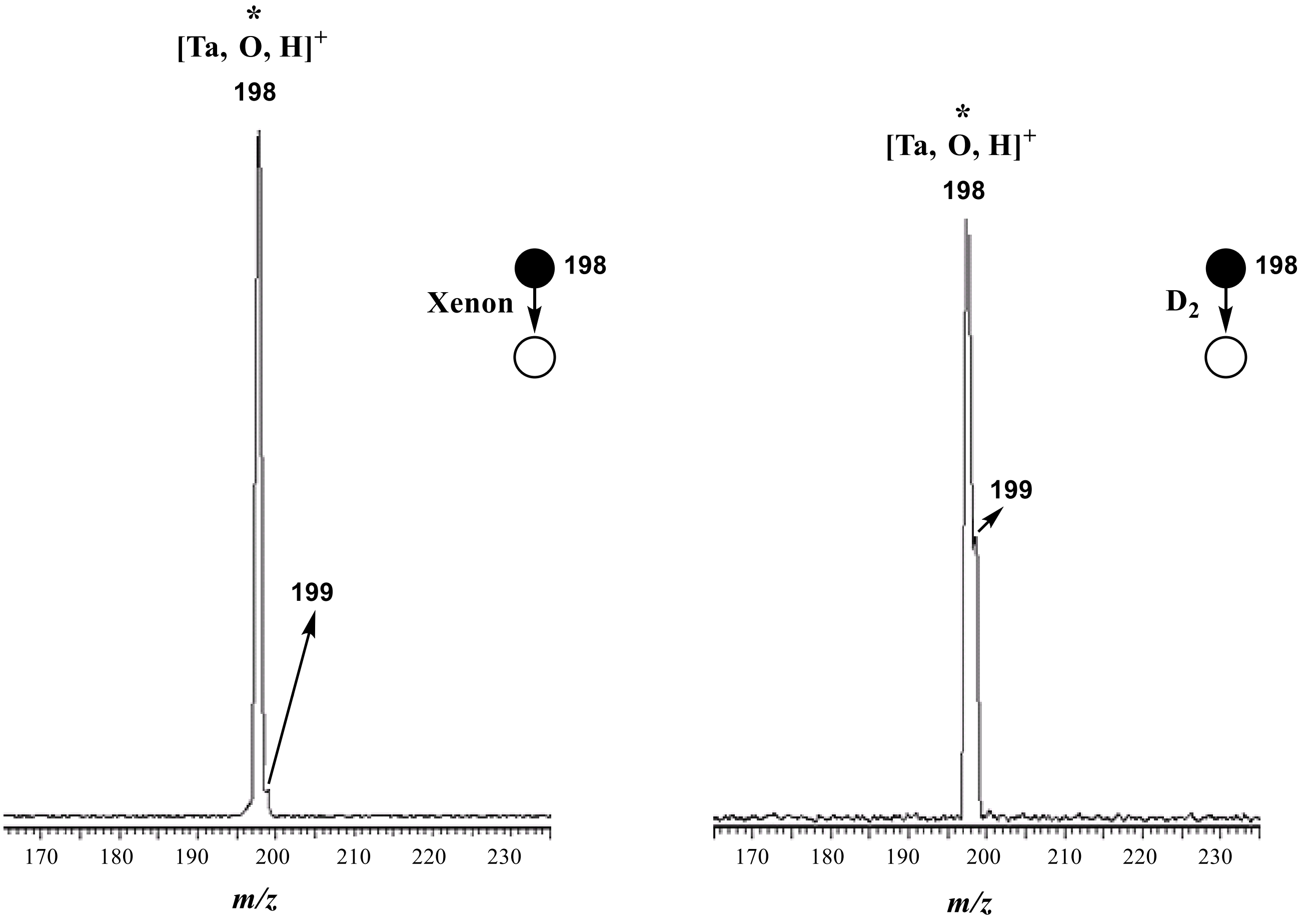

Figure S2. Mass spectrum resulting from the thermal ion/molecule reaction of mass-selected $[Ta,O,H]^+$ with a) xenon at a pressure of 10.2×10^{-4} mbar and b) D_2 at a pressure of 10.0×10^{-4} mbar. Steps of the multistep MS experiment are described with the mass of the isolated complex indicated in the insert.

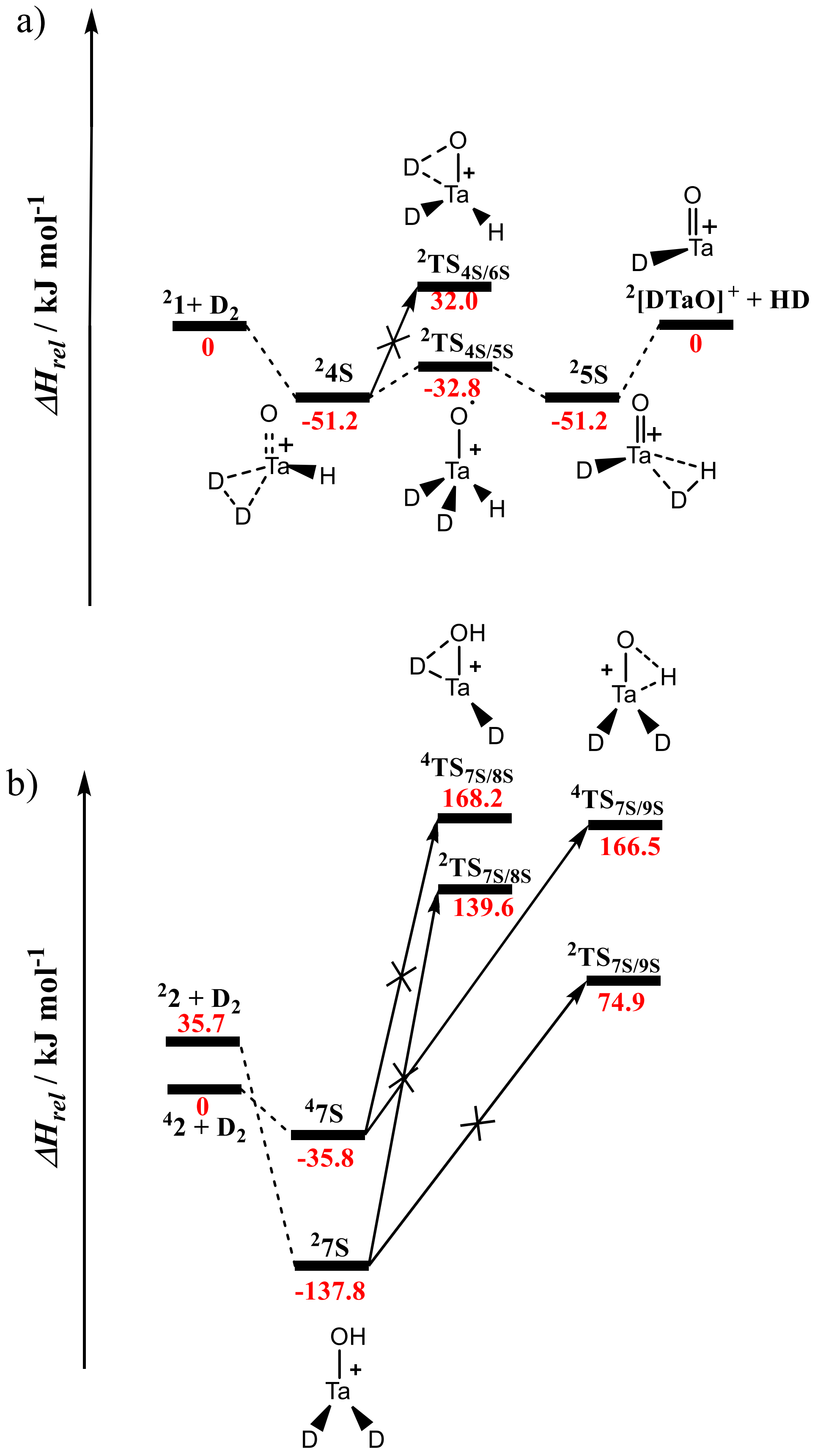
a)
ΔH_rel / kJ mol-1
2 1+ D2
0
2 4S
-51.2
2 TS4S/6S
32.0
2 TS4S/5S
-32.8
2 5S
-51.2
2 [DTaO]+ + HD
0
b)
ΔH_rel / kJ mol-1
2 2 + D2
35.7
0
4 2 + D2
4 7S
-35.8
2 7S
-137.8
4 TS7S/8S
168.2
2 TS7S/8S
139.6
4 TS7S/9S
166.5
2 TS7S/9S
74.9

Figure S3. PESs of the reaction of a) $[HTaO]^+$ and b) $[Ta(OH)]^+$ with D_2. All energies are given in kJ mol^{-1} and marked in red (B3LYP/def2-QZVP).

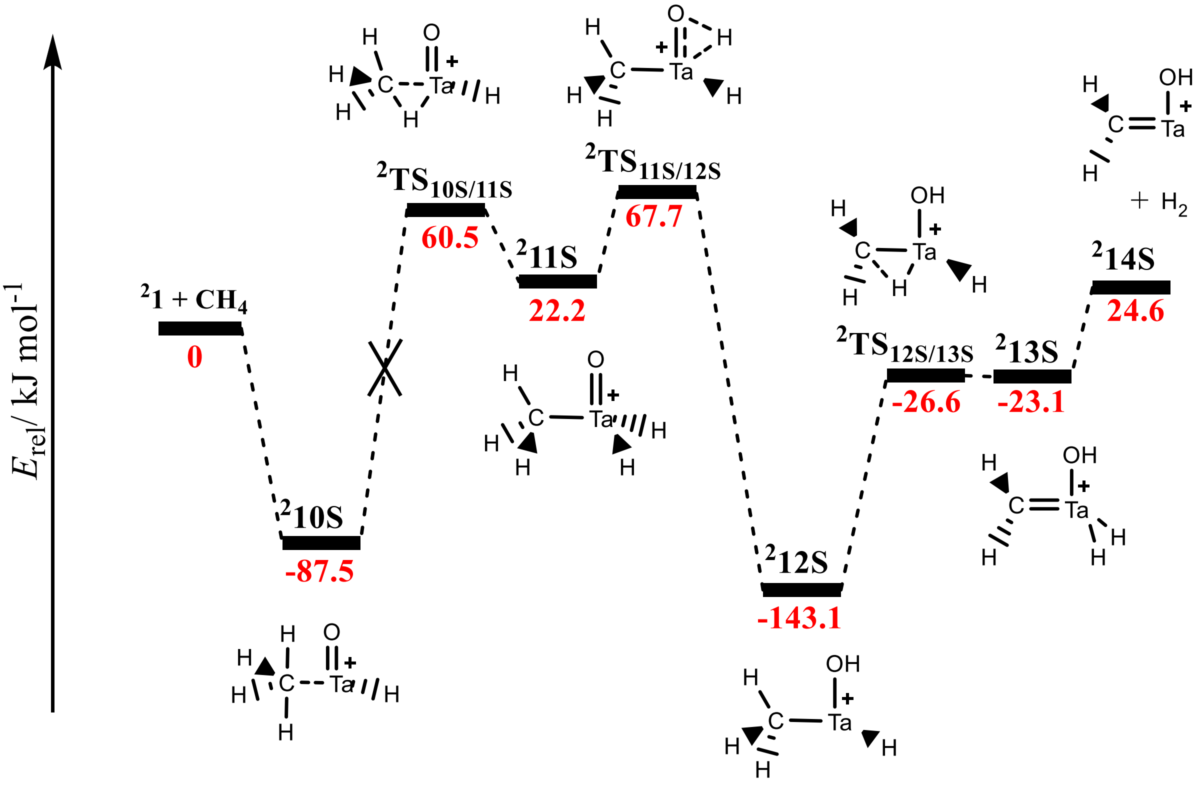
E_{rel}/ kJ mol^{-1}
^{2}1 + CH$_4$
0
^{2}10S
-87.5
^{2}TS$_{10S/11S}$
60.5
^{2}11S
22.2
^{2}TS$_{11S/12S}$
67.7
^{2}12S
-143.1
^{2}TS$_{12S/13S}$
-26.6
^{2}13S
-23.1
^{2}14S
24.6
+ H$_2$

Figure S4. PESs of the reaction of $[HTaO]^+$ with CH_4. All energies are given in kJ mol^{-1} and marked in red (B3LYP/def2-QZVP).

		Q, ^{2}**4**			Q, ^{2}**8**
CH_2	C	-0.72154	CH_3	C	-0.53952
	H	0.24707		H	0.13280
	H	0.26791		H	0.13363
Ta	Ta	1.38796		H	0.14429
OH	O	-0.86732	Ta	Ta	1.35265
	H	0.54855	O	O	-0.31466
H_2	H	0.12233	H_2	H	0.03470
	H	0.01502		H	0.04610

Table S1. Natural population analysis (NPA) atomic charges (BLYP/def2/QZVP) for ^{2}**4** and ^{2}**8**.

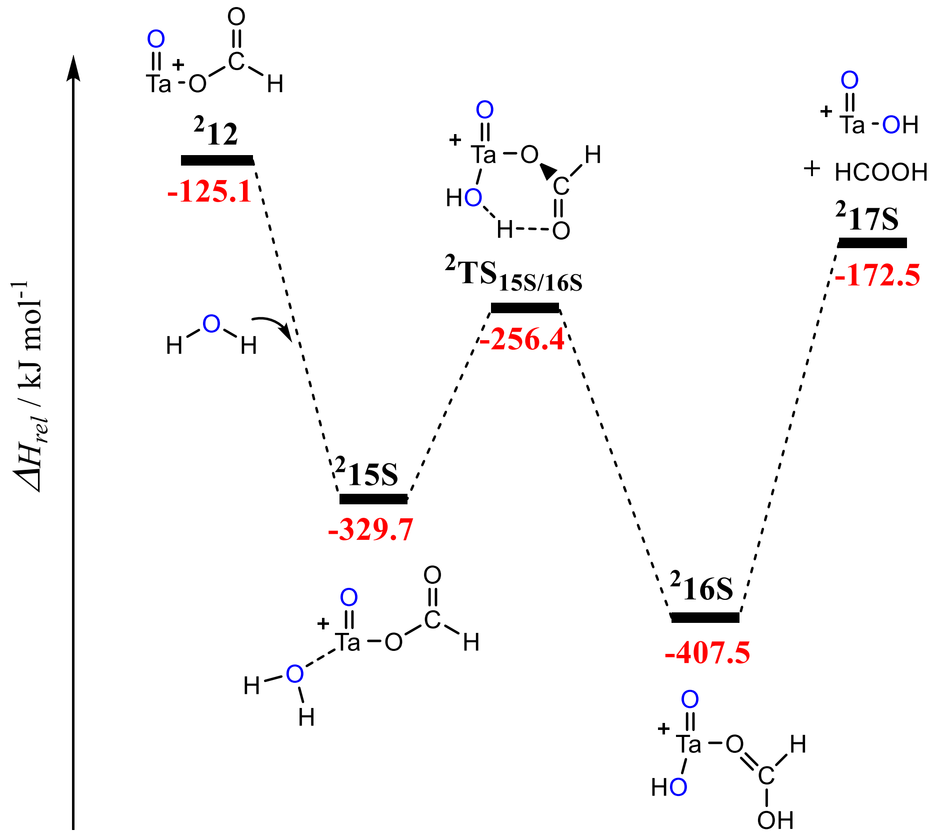
ΔH_rel / kJ mol-1
212
-125.1
215S
-329.7
2TS15S/16S
-256.4
216S
-407.5
217S
-172.5
+ HCOOH

Figure S5. PESs of the reaction of $[OTa(O_2CH)]^+$ (^{2}**12**) with H_2O. This process might be the reason for the formation of unlabeled $[Ta,O_2,H)]^+$ *m/z* 214 in the reaction of $[Ta,O,H]^+$ with $C^{18}O_2$ at a higher pressures, at which intermediate ^{2}**12** might be stabilized by collisions (see also Figure 5 in the manuscript). Oxygen atom shown in blue corresponds to ^{16}O. All energies are given in kJ mol^{-1} and marked in red (B3LYP/def2-QZVP).

References

[1] a) A. Fiedler, D. Schröder, H. Schwarz, B. L. Tjelta, P. B. Armentrout, *J. Am. Chem. Soc.* **1996**, *118*, 5047-5055; b) D. Schröder, H. Schwarz, S. Polarz, M. Driess, *Phys. Chem. Chem. Phys.* **2005**, *7*, 1049-1053; c) M. Schlangen, H. Schwarz, *ChemCatChem* **2010**, *2*, 799-802.

Paper VII

Journal of Catalysis 343 (2016) 68–74

Contents lists available at ScienceDirect

Journal of Catalysis

journal homepage: www.elsevier.com/locate/jcat

Mechanistic aspects of CO_2 activation mediated by phenyl yttrium cation: A combined experimental/theoretical study

Marjan Firouzbakht, Maria Schlangen, Martin Kaupp, Helmut Schwarz *

Institut für Chemie, Technische Universität Berlin, Straße des 17. Juni 135, 10623 Berlin, Germany

A R T I C L E I N F O

Article history:
Received 14 August 2015
Revised 10 September 2015
Accepted 16 September 2015
Available online 17 October 2015

Keywords:
Bond activation
Carbon dioxide
Yttrium phenyl cation
C—C bond formation
Decarbonylation
ESI-MS

A B S T R A C T

The thermal reactions of the per-deuterated yttrium phenyl cation with carbon dioxide have been investigated experimentally by using electrospray-ionization mass spectrometry and computationally by means of density functional theory. The process proceeds by migratory insertion under C—C bond formation followed, to some extent, by decarbonylation. Labeling experiments with $C^{18}O_2$ confirm the origin of the oxygen incorporated in both productions. With regard to the mechanisms, the calculations reveal that the benzoate salt of yttrium corresponds to the most stable isomer. While extrusion of CO starting from this ion, or from two isomeric encounter complexes, is hampered by kinetic barriers, decarbonylation is accessible under thermal conditions from other intermediates which are generated after insertion of CO_2 into the Y—C bond of $[YC_6D_5]^+$.

© 2015 Elsevier Inc. All rights reserved.

1. Introduction

Owing to human activities, the anthropogenic component in atmospheric CO_2 is steadily increasing. One way to make sensible use of the CO_2 emissions is to explore and employ efficient methods by which CO_2 is converted into more valuable chemicals [1–3]. Not surprisingly, carbon dioxide is rightly viewed as an optimal C1 source in organic synthesis due to its abundance, low cost, and nontoxicity [4,5], in contrast to other C1 carbon sources such as phosgene or carbon monoxide [6]. Although carbon dioxide is thermodynamically very stable and kinetically rather inert, CO_2 activation with suitably reactive reagents is feasible [3], and there exist quite a few methodologies to activate and transform CO_2 into value-added chemicals. One of them employs high-energy starting materials such as organometallics or highly-strained ring compounds [6,7]. Also, transition-metal complexes have served as appropriate candidates for the activation of CO_2 [8–10] on the ground that some of these metals are capable to change easily their valence state and mode of coordination and are thus capable to initiate insertion reactions [11]. With regard to the elucidation of strictly molecular-level based reaction mechanisms, gas-phase experiments proved useful as they are not obscured by ill-defined effects such as the role of solvents, aggregation phenomena, or counter-ion effects. In recent years, both bare and ligated-metal ions have been investigated and probed with respect to the activation of CO_2. For instance, oxygen-atom transfer from CO_2 to bare, early transition-metal cations has been observed in the gas phase reflecting the high oxophilicity of these species [12,13]; for the same reason, a favorable interaction of CO_2 with heteronuclear oxide clusters $[MMgO]^{+/0/-}$ (M = Sc–Zn) possessing early transition metals has been predicted in a recent theoretical study [14]. Further, the ligand-controlled CO_2 activation by $[LTiH]^+$ (L = Cp_2, O) proceeds via CO_2 insertion and, in the case of $[OTiH]^+$, subsequent CO extrusion occurs [15]. Likewise, the carbene complex $[Ta(CH_2)]^+$ in its reaction with carbon dioxide forms the acetic acid equivalent CH_2CO, thus providing a rare example for the stoichiometric coupling of methane and carbon dioxide [16].

A prominent strategy for CO_2 activation involves the insertion of CO_2 into a metal–hydrogen or metal–carbon bond [15,17–25], and the greater oxophilicity of early transition metals can accelerate this reaction by providing a stronger M–OCO interaction [23]. Here, we describe the reactivity of the cationic yttrium phenyl complex toward carbon dioxide in the gas phase as investigated by using electrospray ionization mass spectrometry (ESI-MS) in conjunction with density functional theory (DFT); we aim at understanding mechanistic aspects of the CO_2 activation promoted by an insertion process of an early transition-metal complex at a strictly molecular level. Although yttrium exists mainly in the +3 oxidation state, also Y^{2+} complexes have been isolated [26]; these complexes are supposed to be highly reactive. Ligated group 3 transition-metal ions LM^+, with L corresponding to an anionic

---

* Corresponding author.
E-mail addresses: Martin.Kaupp@tu-berlin.de (M. Kaupp), Helmut.Schwarz@tu-berlin.de (H. Schwarz).

http://dx.doi.org/10.1016/j.jcat.2015.09.012
0021-9517/© 2015 Elsevier Inc. All rights reserved.

ligand, possess only one unpaired valence electron at the metal center; thus, the traditional oxidative addition pathway will be disfavored as compared with, e.g., migratory insertion processes [27–29].

2. Experimental section and computational details

The experiments were performed using a VG Bio-Q mass spectrometer of QHQ configuration (Q: quadrupole; H: hexapole) equipped with an electrospray-ionization (ESI) source, as described in detail previously [30]. To avoid the mass overlap between the yttrium phenyl cation $[Y(C_6H_5)]^+$ and the isobaric ^{13}C signal of the yttrium benzyne cation $[Y(C_6H_4)]^+$, deuterated $[Y(C_6D_5)]^+$ has been utilized instead of $[Y(C_6H_5)]^+$. To generate $[Y(C_6D_5)]^+$, a millimolar solution of yttrium(III) acetate hydrate and perdeuterated benzoic acid in a methanol/water mixture was used for ESI; the precursor ion is formed presumably by endothermic decarboxylation in the ion source. Methanol, water, deuterated benzoic acid, yttrium(III) acetate hydrate, CO_2, and $C^{18}O_2$ were obtained from Sigma–Aldrich and utilized without further purification. The solution has been introduced into the mass spectrometer

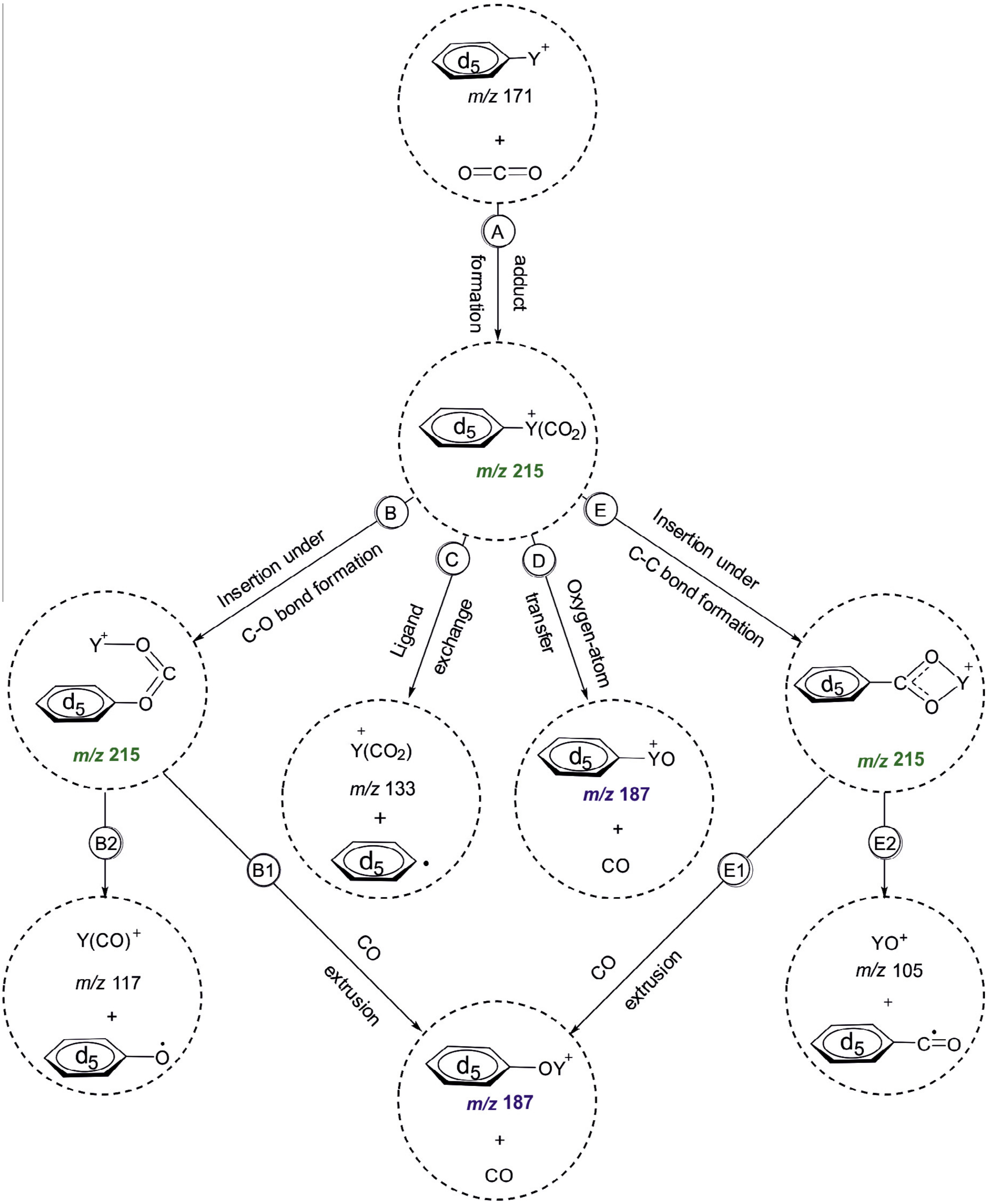
d5
Y+
m/z 171
+
O=C=O
A
adduct formation
d5
Y(CO2)+
m/z 215
B
Insertion under C-O bond formation
C
Ligand exchange
D
Oxygen-atom transfer
E
Insertion under C-C bond formation
Y+—O
C
O
d5
m/z 215
Y(CO2)+
m/z 133
+
d5
d5
YO+
m/z 187
+
CO
d5
C
O
O
Y+
m/z 215
B2
B1
E1
E2
CO extrusion
CO extrusion
Y(CO)+
m/z 117
+
d5
O
d5
OY+
m/z 187
+
CO
YO+
m/z 105
+
d5
C=O

Scheme 1. Possible routes for the reaction of $[Y(C_6D_5)]^+$ with carbon dioxide.

via a syringe pump and a fused-silica capillary connected to the ESI source with a pump rate of 4 µl/min. Nitrogen was used as a nebulizing and drying gas at a source temperature of 80 °C. The maximum intensity of the desired complex was achieved by adjusting the cone voltage (U_c) to around 100–110 V. The isotope patterns of the ions of interest have been compared with the calculated isotope patterns to confirm the identity of the ions [31]. The thermal reactions of $[Y(C_6D_5)]^+$ with carbon dioxide have been probed at a collision energy (E_{lab}) nominally set to 0 eV in the hexapole at a stationary pressure ranging from ca 0.75×10^{-3} to 1.27×10^{-3} mbar. Cationic products are recorded by scanning of Q2.

For the computational studies we employed the Gaussian 09 program package [32] using unrestricted calculations with the B3LYP functional [33,34] and the def2-QZVP basis sets of Weigend and Ahlrichs [35] including a quasirelativistic, energy-adjusted ECP [36] and associated valence basis set for yttrium [35]. The satisfying performance of the B3LYP functional for energetic and structural aspects of 4d-block transition metals has been confirmed previously in benchmark studies [37,38]. The nature of local minima and transition states (TSs) was verified by harmonic vibrational frequency analysis of the respective optimized structures. IRC calculations [39–41] were performed in order to confirm the connection between transition states and minima. Further structure optimizations starting from the last point of IRC were performed when no local minima have been located in the IRC calculations. In case of a flat potential-energy surface (PES) in the immediate vicinity of a transition state, frozen-scan calculations were carried out instead of IRC calculations. While all systems were optimized with the default grids (FineGrid keyword) of the Gaussian 09 program, some key stationary points on flat sections of the PES were checked with larger grids (UltraFine grid option). Natural population analyses [42] (NPA) were carried out on the ground-state structures, using the built-in NBO3.1 module of Gaussian 09. All energies (given in kJ mol^{-1}) are corrected for (unscaled) zero-point vibrational energy contributions.

3. Results and discussion

In principle, several pathways are conceivable for the reaction of the yttrium phenyl cation with CO_2 (Scheme 1).

$$[Y(C_6D_5)]^+ + CO_2 \longrightarrow [Y,C_7,D_5,O_2]^+ \qquad 71\% \qquad (1)$$

$$[Y(C_6D_5)]^+ + CO_2 \longrightarrow [Y,C_6,D_5,O]^+ + CO \qquad 29\% \qquad (2)$$

In the present study, two product ions, m/z 215 and m/z 187, respectively, are observed in the reaction of mass-selected $[Y(C_6D_5)]^+$ (m/z 171) with carbon dioxide, Eqs. (1) and (2); the corresponding mass spectrum is shown in Fig. 1. The main process gives rise to the formation of ions at m/z 215 which may correspond to a simple adduct (path A) or to insertion intermediates; the latter may be accessible via either C—O or C—C bond formation, respectively (paths B and E, Scheme 1).

In addition to an ion at m/z 215, a fragment ion $[Y,C_6,D_5,O]^+$ (m/z 187) is generated concomitant with the elimination of carbon monoxide, according to Eqn (2). While direct O-atom transfer from CO_2 to the metal (Scheme 1, path D) has often been observed in the reactions of early transition metals due to their high oxophilicity [12–14,16], CO can also be eliminated from any of the insertion intermediates generated according to paths B1 and E1, respectively. Therefore a mechanistic clarification is warranted.

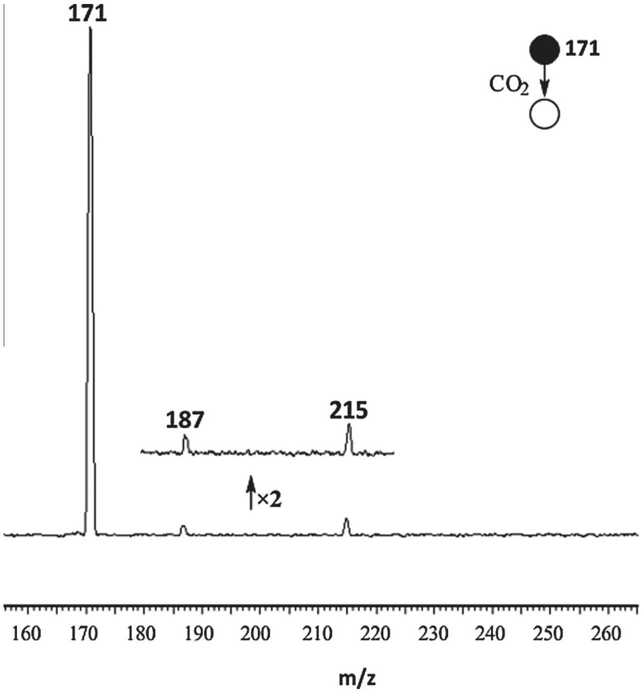

Fig. 1. Mass spectrum resulting from the thermal ion/molecule reaction of mass-selected $[Y(C_6D_5)]^+$ with CO_2 at a pressure of 1.01×10^{-3} mbar.

Experiments with $C^{18}O_2$ result in quantitative shifts i.e. m/z 187 → 189 and m/z 215 → 219. Thus, the oxygen atoms in both ionic products originate exclusively from carbon dioxide. Structural information of the complex at m/z 215 and the product ion at m/z 187 was sought by performing traveling wave ion mobility spectrometry-mass spectrometry (TWIMS-MS) [43], which proved insightful to structurally identify the reaction of $[LTiH]^+$ (L = Cp_2, O) with CO_2 [15]. However, despite several efforts it was not possible to generate sufficient intensities of $[Y(C_6D_5)]^+$ to perform a TWIMS-MS analysis. Thus, DFT calculations were executed in order to obtain the relative energies of conceivable encounter complexes and insertion intermediates as well as the energetic profiles of the respective processes, including the loss of CO. Relevant stationary points on the PESs are shown in Figs. 2 and 3, and their relative energies are summarized in Table 1. The calculation accuracy of stationary points on the flat sections of the PESs was checked with larger grids, and by and large, the energy differences compared to the default grid were negligible.

Starting from $[Y(C_6D_5)]^+$, the incoming carbon dioxide coordinates to the metal center of the educt ion with either both oxygen atoms, leading to the complex **1**, or with one of its oxygen atoms, giving rise to **2**. An alternative encounter complex has been considered in which the metal center coordinates side-on to the C═O unit of CO_2. However, this complex is energetically less favorable compared to **2** by 16 kJ mol^{-1}. An interconversion $\mathbf{1} \rightleftharpoons \mathbf{TS_{1/2}} \rightleftharpoons \mathbf{2}$ is thermodynamically possible as $\mathbf{TS_{1/2}}$ is located below the entrance channel. Starting from **2**, the insertion process under C—C bond formation, to eventually lead to the global minimum **6**, commences via the four-centered transition structure $\mathbf{TS_{2/3}}$ to produce interme-

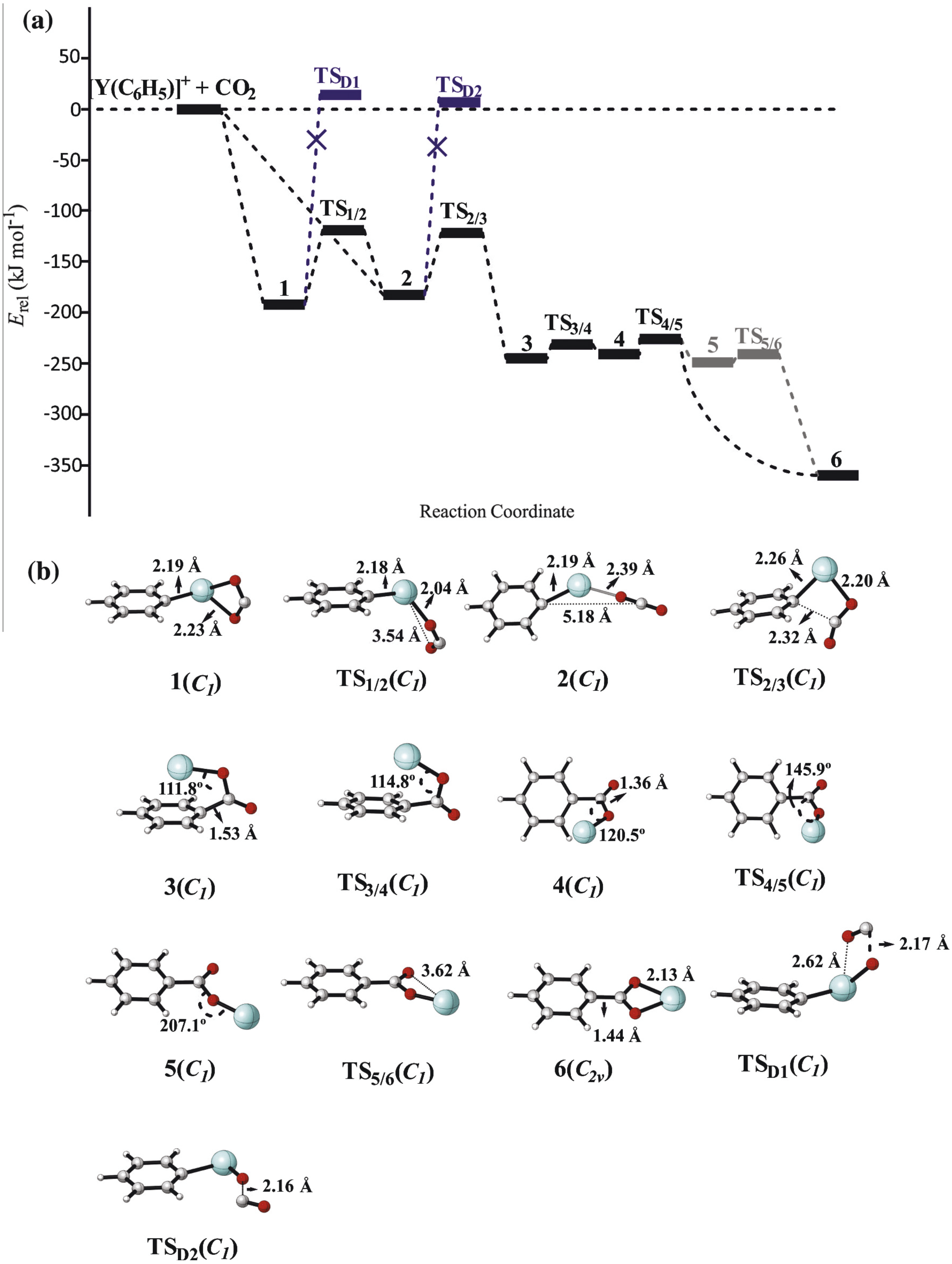
(a)
50
0
-50
-100
-150
-200
-250
-300
-350
E_rel (kJ mol^-1)
[Y(C6H5)]+ + CO2
TSD1
TSD2
TS1/2
TS2/3
1
2
3
TS3/4
4
TS4/5
5
TS5/6
6
Reaction Coordinate
(b)
2.19 Å
2.23 Å
1(C1)
2.18 Å
2.04 Å
3.54 Å
TS1/2(C1)
2.19 Å
2.39 Å
5.18 Å
2(C1)
2.26 Å
2.20 Å
2.32 Å
TS2/3(C1)
111.8°
1.53 Å
3(C1)
114.8°
TS3/4(C1)
1.36 Å
120.5°
4(C1)
145.9°
TS4/5(C1)
207.1°
5(C1)
3.62 Å
TS5/6(C1)
2.13 Å
1.44 Å
6(C2v)
2.62 Å
2.17 Å
TSD1(C1)
2.16 Å
TSD2(C1)

Fig. 2. (a) Simplified potential-energy surface (stationary points) for the insertion reaction of $[Y(C_6D_5)]^+$ with CO_2. The energies are given relative to the doublet ground state of the educts. For the sake of clarity, charges are omitted. Y●, O●, C● and H●. (b) Structures of the species involved; symmetries are given in parentheses, and selected geometric parameters are indicated. For all species, the spin is located at the Y atom, and the NPA charge at Y varies from 1.417 to 2.043. Structures **5** and $\mathbf{TS_{5/6}}$ are marked in gray, as they are artifacts of the standard grid and vanish with larger grids; see footnote to Table 1.

diate **3**. While in $\mathbf{TS_{3/4}}$ the yttrium atom is η^6 coordinated to the phenyl ring with bond lengths ranging from 2.519 to 2.923 Å, in the following step **4** → **6** the coordination changes to an η^2 coordination of Y to both oxygen atoms of the carboxylate group. We note in passing, that a monodentate-bound minimum **5**, found in the optimization with the standard grid, vanishes when enlargening the grid to UltraFine (cf. footnote to Table 1, Fig. 2). Isomer **6**, with its planar bidentate structure, is predicted to correspond to the species *m/z* 215 (Scheme 1, path E). The overall step $[Y(C_6D_5)]^+ + CO_2 \rightarrow$ **6** is exothermic by 360.9 kJ mol^{-1}. Regarding the insertion resulting in C—O bond formation, i.e. path B in Scheme 1, two different variants have been considered, starting

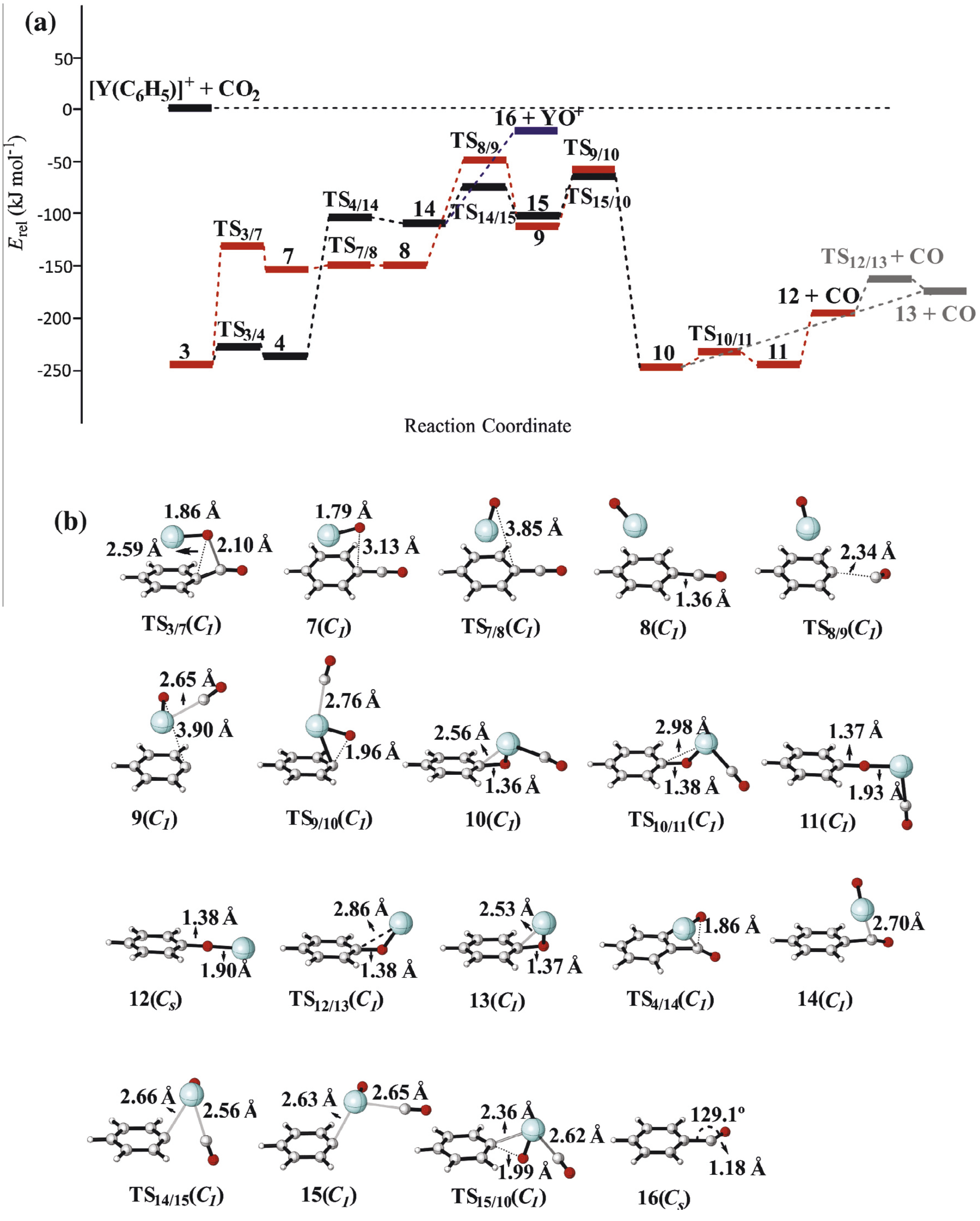
(a)
E_{rel} (kJ mol^{-1})
50
0
-50
-100
-150
-200
-250
$[Y(C_6H_5)]^+ + CO_2$
16 + YO$^+$
$TS_{8/9}$
$TS_{9/10}$
$TS_{4/14}$
14
$TS_{14/15}$
15
$TS_{15/10}$
9
$TS_{3/7}$
7
$TS_{7/8}$
8
$TS_{3/4}$
4
3
10
$TS_{10/11}$
11
12 + CO
$TS_{12/13}$ + CO
13 + CO
Reaction Coordinate
(b)
1.86 Å
2.59 Å
2.10 Å
$TS_{3/7}(C_1)$
1.79 Å
3.13 Å
$7(C_1)$
3.85 Å
$TS_{7/8}(C_1)$
1.36 Å
$8(C_1)$
2.34 Å
$TS_{8/9}(C_1)$
2.65 Å
3.90 Å
$9(C_1)$
2.76 Å
1.96 Å
$TS_{9/10}(C_1)$
2.56 Å
1.36 Å
$10(C_1)$
2.98 Å
1.38 Å
$TS_{10/11}(C_1)$
1.37 Å
1.93 Å
$11(C_1)$
1.38 Å
1.90Å
$12(C_s)$
2.86 Å
1.38 Å
$TS_{12/13}(C_1)$
2.53 Å
1.37 Å
$13(C_1)$
1.86 Å
$TS_{4/14}(C_1)$
2.70Å
$14(C_1)$
2.66 Å
2.56 Å
$TS_{14/15}(C_1)$
2.63 Å
2.65 Å
$15(C_1)$
2.36 Å
2.62 Å
1.99 Å
$TS_{15/10}(C_1)$
129.1°
1.18 Å
$16(C_s)$

Fig. 3. (a) Simplified potential-energy surface (stationary points) for the decarbonylation reaction of $[Y(C_6D_5)]^+$ with CO_2. The energies are given relative to the doublet ground state of the educts. For the sake of brevity, charges are omitted. Y●, O●, C● and H●. (b) Structures of the species involved. Symmetries are given in parentheses and selected geometric parameters are indicated. For all species, the spin is located at the Y atom, and the NPA charge at Y varies from 1.537 to 1.892. Structures **13** and $\mathbf{TS_{12/13}}$ are marked in gray, as they are artifacts of the standard grid and vanish with larger grids; see footnote to Table 1.

either from encounter complex **2** or from intermediate **3**. However, both paths are inhibited by kinetic barriers amounting to 23.5 and 50.1 kJ mol^{-1} above the entrance channel, respectively (Fig. S1 in Supporting Information).

As mentioned, in addition to the formation of the *m*/*z* 215 ions, a product corresponding to decarbonylation is observed, Eq. (2). Conceivable pathways of this reaction have also been investigated by means of DFT calculations, Fig. 3. As pointed out above, three different reaction routes, D, B1, or E1 (Scheme 1), have to be considered. The direct O atom transfer from CO_2 to the Y atom of $[Y(C_6D_5)]^+$, path D, can take place via the adduct complexes **1** and **2**, respectively. However, both paths are hampered by barriers of 9.2 ($\mathbf{TS_{D1}}$, Fig. 2) and 1.1 kJ mol^{-1} ($\mathbf{TS_{D2}}$, Fig. 2) above the entrance channel, respectively. Principally, CO can be eliminated from any of the insertion intermediates. However, as the insertion process under C—O bond formation, path B in Scheme 1, is not accessible under thermal conditions, we investigated the expulsion of CO only from those insertion intermediates which have been formed via C—C bond coupling (path E1), i.e. the complexes **3**, **4**, and **6**. A pathway starting from the benzoate complex **6** is endothermic

Table 1
Relative energies in kJ mol^{-1} of the intermediates and transition-state structures shown in Figs. 2 and 3.

	E_{rel}		E_{rel}		E_{rel}
$Y(C_6H_5)^+ + CO_2$	0	**TS**$_{3/7}$	−129.9	**13**[a] + CO	−173.1
1	−197.6	**7**	−158.6	**TS**$_{4/14}$	−105.4
TS$_{1/2}$	−126.7	**TS**$_{7/8}$	−151.8	**14**	−148.3
2	−182.9	**8**	−153.8	**TS**$_{14/15}$	−79.8
TS$_{2/3}$	−132.7	**TS**$_{8/9}$	−55.2	**15**	−107.4
3	−246.2	**9**	−116.8	**TS**$_{15/10}$	−69.1
TS$_{3/4}$	−231.9	**TS**$_{9/10}$	−62.2	**16** + YO^+	−26.2
4	−237.9	**10**	−244.9	**TS**$_{D1}$	9.2
TS$_{4/5}$	−224.8	**TS**$_{10/11}$	−229.3	**TS**$_{D2}$	1.1
5[a]	−243.7	**11**	−244.3		
TS$_{5/6}$	−243.5	**12** + CO	−191.1		
6	−360.9	**TS**$_{12/13}$ + CO	−165.8		

[a] Optimization with UltraFine grids made structures **5** and **13** converge to **6** and **12**, respectively. That is, these minima and the associated transition states are artifacts of the standard Fine grid.

and inhibited by a barrier of 54.4 kJ mol^{-1} above the entrance channel. It is thus not accessible under thermal conditions (Fig. S2 in Supporting Information). The two alternative mechanistic scenarios for the elimination of CO, involving intermediates **3** and **4**, are shown in Fig. 3. Starting from **3**, a C—O bond is cleaved via transition-state structure **TS**$_{3/7}$. In the resulting intermediate **7**, the YO moiety is located above the aromatic ring to which yttrium is still η^6 coordinated with Y—C bond lengths ranging from 2.884 to 3.003 Å. After rotation of the YO axis relative to the ring plane via the low-lying transition-state structure **TS**$_{7/8}$, complex **8** is formed which isomerizes to **9** via transition state **TS**$_{8/9}$. In this rather energy-demanding step, the C_{ipso}—CO bond is cleaved, and the resulting CO ligand coordinates to Y. Subsequently, the oxo ligand of the YO moiety migrates to C_{ipso}, giving rise to isomer **10**. This step is energetically exothermic by 244.9 kJ mol^{-1} relative to the reactant pairs. According to the initial calculations, from **10** carbon monoxide can be eliminated either directly, yielding the cationic isomer **13**, or the reaction proceeds via transition state **TS**$_{10/11}$ to generate intermediate **11** from which CO is liberated under the formation of **12**. However, intermediate **13** appears to be an artifact of the standard grid used and vanishes when enlargening the grid to UltraFine. That is, isomer **12** likely corresponds to the product ion of decarbonylation.

Alternatively, decarbonylation can commence from complex **4**. Starting from this intermediate, the first step corresponds to a C—O bond cleavage via **TS**$_{4/14}$ to produce **14**. Next, C—C bond cleavage is achieved via **TS**$_{14/15}$ to generate intermediate **15**, in which the phenyl group and the CO ligand are loosely coordinated to the YO moiety. As described for **TS**$_{9/10}$, C—O bond formation between the oxo ligand of YO and C_{ipso} can take place via **TS**$_{15/10}$ to form **10**. All these steps are thermodynamically and kinetically accessible. Thus, both **9** and **15** can serve as intermediates en route to **10**.

Finally, the formation of YO^+, path E2 in Scheme 1, has also been considered computationally. This reaction is energetically accessible when $[C_7,D_5,O]^{\cdot}$ is not eliminated as separated C_6D_5 and CO moieties but as a benzoyl radical $C_6D_5CO^{\cdot}$. The enthalpy of the overall reaction $[Y(C_6D_5)]^+ + CO_2 \rightarrow YO^+ + C_6D_5CO^{\cdot}$, via intermediates **7**, **8**, or **14**, has been calculated to −26.2 kJ mol^{-1} (**16**, Fig. 3). However, the decarbonylation paths via **TS**$_{7/8}$, **TS**$_{8/9}$, and **TS**$_{14/15}$ are 125.6 kJ mol^{-1}, 29.0 kJ mol^{-1}, and 53.6 kJ mol^{-1}, respectively, lower in energy compared to the formation of YO^+ + **16** (Fig. 3). This may explain why YO^+ is not observed experimentally as a product ion.

4. Conclusion

In a combined experimental/computational study, we have investigated mechanistic aspects of the thermal gas-phase reaction of the yttrium phenyl cation $[Y(C_6D_5)]^+$ with carbon dioxide. We demonstrate the feasibility of carbon dioxide activation under carbon–carbon bond formation to generate an yttrium benzoate complex. According to DFT calculations, the most stable structure of this system corresponds to a benzoate complex in which the yttrium atom is η^2 coordinated to both oxygen atoms of the carboxylate group. This product ion is 360.9 kJ mol^{-1} below the separated reactants. Various pathways have been considered for the decarbonylation process, starting from different intermediates. If loss of CO was to take place from the encounter complex **1** or **2**, formation of high valent $[(C_6D_5)YO]^+$ would be hampered by kinetic barriers that are too high in energy to be accessible under thermal conditions. In contrast, CO can be eliminated from other intermediates, which are formed in the course of insertion of CO_2 into the Y—C bond of $[YC_6D_5]^+$.

Acknowledgments

This work is supported by the Fonds der Chemischen Industrie, the Deutsche Forschungsgemeinschaft (DFG), and the Cluster of Excellence “Unifying Concepts in Catalysis” (coordinated by the Technische Universität Berlin and funded by the DFG). For computational resources, the Institut für Mathematik at the Technische Universität Berlin is acknowledged. Dr. Nicole Rijs, Dr. Patricio González-Navarrete, Dr. Robert Kretschmer, Dr. Shaodong Zhou, Dr. Shiya Tang, and Dr. Xiao-Nan Wu are appreciated for suggestions and comments. We thank Dr. Thomas Weiske for technical assistance.

Appendix A. Supplementary material

Supplementary data associated with this article can be found, in the online version, at http://dx.doi.org/10.1016/j.jcat.2015.09.012.

References

[1] X. Yin, J.R. Moss, Coord. Chem. Rev. 181 (1999) 27.
[2] W. Wang, S. Wang, X. Ma, J. Gong, Chem. Soc. Rev. 40 (2011) 3703.
[3] K. Huang, C.-L. Sun, Z.-J. Shi, Chem. Soc. Rev. 40 (2011) 2435.
[4] H. Arakawa, M. Aresta, J.N. Armor, M.A. Barteau, E.J. Beckman, A.T. Bell, J.E. Bercaw, C. Creutz, E. Dinjus, D.A. Dixon, K. Domen, D.L. DuBois, J. Eckert, E. Fujita, D.H. Gibson, W.A. Goddard, D.W. Goodman, J. Keller, G.J. Kubas, H.H. Kung, J.E. Lyons, L.E. Manzer, T.J. Marks, K. Morokuma, K.M. Nicholas, R. Periana, L. Que, J. Rostrup-Nielson, W.M.H. Sachtler, L.D. Schmidt, A. Sen, G.A. Somorjai, P.C. Stair, B.R. Stults, W. Tumas, Chem. Rev. 101 (2001) 953.
[5] M. Aresta, A. Dibenedetto, Dalton Trans. (2007) 2975.
[6] M. Aresta, A. Dibenedetto, A. Angelini, Chem. Rev. 114 (2014) 1709.
[7] T. Sakakura, J.-C. Choi, H. Yasuda, Chem. Rev. 107 (2007) 2365.
[8] D. Schröder, H. Schwarz, S. Schenk, E. Anders, Angew. Chem. Int. Ed. 42 (2003) 5087.
[9] P.G. Jessop, F. Joó, C.-C. Tai, Coord. Chem. Rev. 248 (2004) 2425.
[10] T. Fan, X. Chen, Z. Lin, Chem. Comm. 48 (2012) 10808.
[11] D. Schröder, H. Schwarz, Proc. Natl. Acad. Sci. 105 (2008) 18114.
[12] M.R. Sievers, P.B. Armentrout, Inorg. Chem. 38 (1999) 397.
[13] G.K. Koyanagi, D.K. Bohme, J. Phys. Chem. A 110 (2006) 1232.
[14] J. Li, P. González-Navarrete, M. Schlangen, H. Schwarz, Chem. Eur. J. 21 (2015) 7780.
[15] S.-Y. Tang, N.J. Rijs, J. Li, M. Schlangen, H. Schwarz, Chem. Eur. J. 21 (2015) 8483.
[16] R. Wesendrup, H. Schwarz, Angew. Chem. Int. Ed. 34 (1995) 2033.
[17] W.J. Evans, D.B. Rego, J.W. Ziller, A.G. DiPasquale, A.L. Rheingold, Organometallics 26 (2007) 4737.
[18] C. Federsel, A. Boddien, R. Jackstell, R. Jennerjahn, P.J. Dyson, R. Scopelliti, G. Laurenczy, M. Beller, Angew. Chem. Int. Ed. 49 (2010) 9777.
[19] L. Dang, Z. Lin, T.B. Marder, Organometallics 29 (2010) 917.
[20] W. Sattler, G. Parkin, J. Am. Chem. Soc. 134 (2012) 17462.
[21] R. Zhang, L. Song, H. Liu, B. Wang, Appl. Catal. A 443–444 (2012) 50.
[22] Y. Jiang, O. Blacque, T. Fox, H. Berke, J. Am. Chem. Soc. 135 (2013) 7751.
[23] K.-C. Lau, B.J. Petro, S. Bontemps, R.F. Jordan, Organometallics 32 (2013) 6895.
[24] C. Dong, X. Yang, J. Yao, H. Chen, Organometallics 34 (2015) 121.
[25] H. Fong, J.C. Peters, Inorg. Chem. 54 (2015) 5124.
[26] M.R. MacDonald, J.W. Ziller, W.J. Evans, J. Am. Chem. Soc. 133 (2011) 15914.
[27] M.A. Tolbert, J.L. Beauchamp, J. Am. Chem. Soc. 106 (1984) 8117.
[28] Y. Huang, M.B. Wise, D.B. Jacobson, B.S. Freiser, Organometallics 6 (1987) 346.
[29] Y. Huang, Y.D. Hill, B.S. Freiser, J. Am. Chem. Soc. 113 (1991) 840.

[30] C. Trage, D. Schröder, H. Schwarz, Chem. Eur. J. 11 (2005) 619.
[31] Scientific Instrument Service: Isotope Distribution Calculator and Mass Spec Plotter: <http://www.sisweb.com/mstools/isotope.htm>.
[32] M.J.T.G.W. Frisch, H.B. Schlegel, G.E. Scuseria, M.A. Robb, J.R. Cheeseman, G. Scalmani, V. Barone, B. Mennucci, G.A. Petersson, H. Nakatsuji, M. Caricato, X. Li, H.P. Hratchian, A.F. Izmaylov, J. Bloino, G. Zheng, J.L. Sonnenberg, M. Hada, M. Ehara, K. Toyota, R. Fukuda, J. Hasegawa, M. Ishida, T. Nakajima, Y. Honda, O. Kitao, H. Nakai, T. Vreven, J.A. Montgomery Jr., J.E. Peralta, F. Ogliaro, M. Bearpark, J.J. Heyd, E. Brothers, K.N. Kudin, V.N. Staroverov, R. Kobayashi, J. Normand, K. Raghavachari, A. Rendell, J.C. Burant, S.S. Iyengar, J. Tomasi, M. Cossi, N. Rega, J.M. Millam, M. Klene, J.E. Knox, J.B. Cross, V. Bakken, C. Adamo, J. Jaramillo, R. Gomperts, R.E. Stratmann, O. Yazyev, A.J. Austin, R. Cammi, C. Pomelli, J.W. Ochterski, R.L. Martin, K. Morokuma, V.G. Zakrzewski, G.A. Voth, P. Salvador, J.J. Dannenberg, S. Dapprich, A.D. Daniels, Ö. Farkas, J.B. Foresman, J.V. Ortiz, J. Cioslowski, D.J. Fox, Gaussian Inc., Wallingford, CT, 2009.
[33] A.D. Becke, J. Chem. Phys. 98 (1993) 5648.
[34] C. Lee, W. Yang, R.G. Parr, Phys. Rev. B 37 (1988) 785.
[35] F. Weigend, R. Ahlrichs, Phys. Chem. Chem. Phys. 7 (2005) 3297.
[36] D. Andrae, U. Häußermann, M. Dolg, H. Stoll, H. Preuß, Theor. Chem. Acc. 77 (1990) 123.
[37] X. Zhang, H. Schwarz, Chem. Eur. J. 16 (2010) 5882.
[38] X. Zhang, H. Schwarz, Theor. Chem. Acc. 129 (2011) 389.
[39] K. Fukui, Acc. Chem. Res. 14 (1981) 363.
[40] D.G. Truhlar, N.J. Kilpatrick, B.C. Garrett, J. Chem. Phys. 78 (1983) 2438.
[41] C. Gonzalez, H.B. Schlegel, J. Chem. Phys. 90 (1989) 2154.
[42] A.E. Reed, R.B. Weinstock, F.A. Weinhold, J. Chem. Phys. 83 (1985) 735.
[43] N.J. Rijs, T. Weiske, M. Schlangen, H. Schwarz, Chem. Phys. Lett. 608 (2014) 408.

Supporting information

Mechanistic aspects of CO_2 activation mediated by phenyl yttrium cation: a combined experimental/theoretical study

Marjan Firouzbakht, Maria Schlangen, Martin Kaupp,* Helmut Schwarz*

Institut für Chemie, Technische Universität Berlin, Straße des 17. Juni 135, 10623 Berlin, Germany

Email: Helmut.Schwarz@tu-berlin.de
Martin.Kaupp@tu-berlin.de

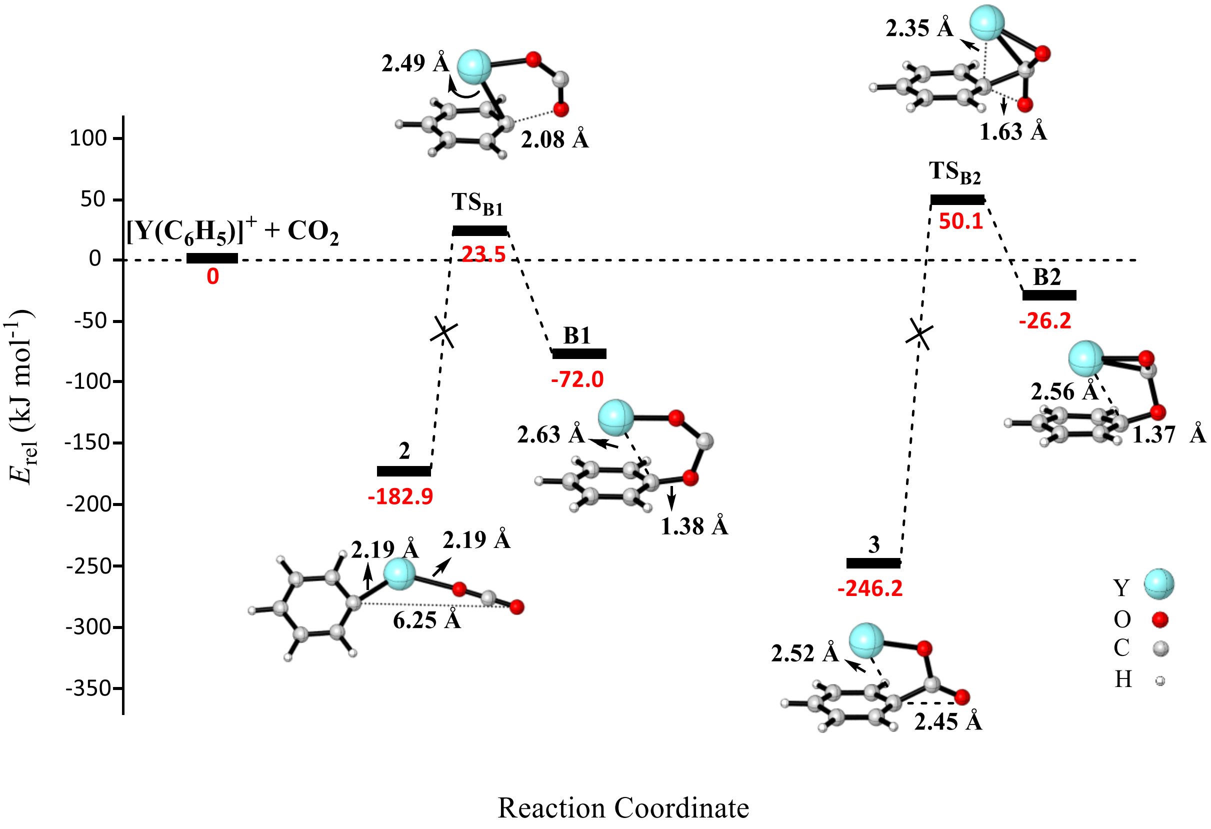

Figure S1: Simplified potential-energy surface (stationary points) for the CO$_2$ insertion under C–O bond formation in the reaction of [Y(C$_6$D$_5$)]$^+$ with CO$_2$. The energies are given relative to the doublet ground state of the educts and are marked in red. For the sake of brevity, charges are omitted.

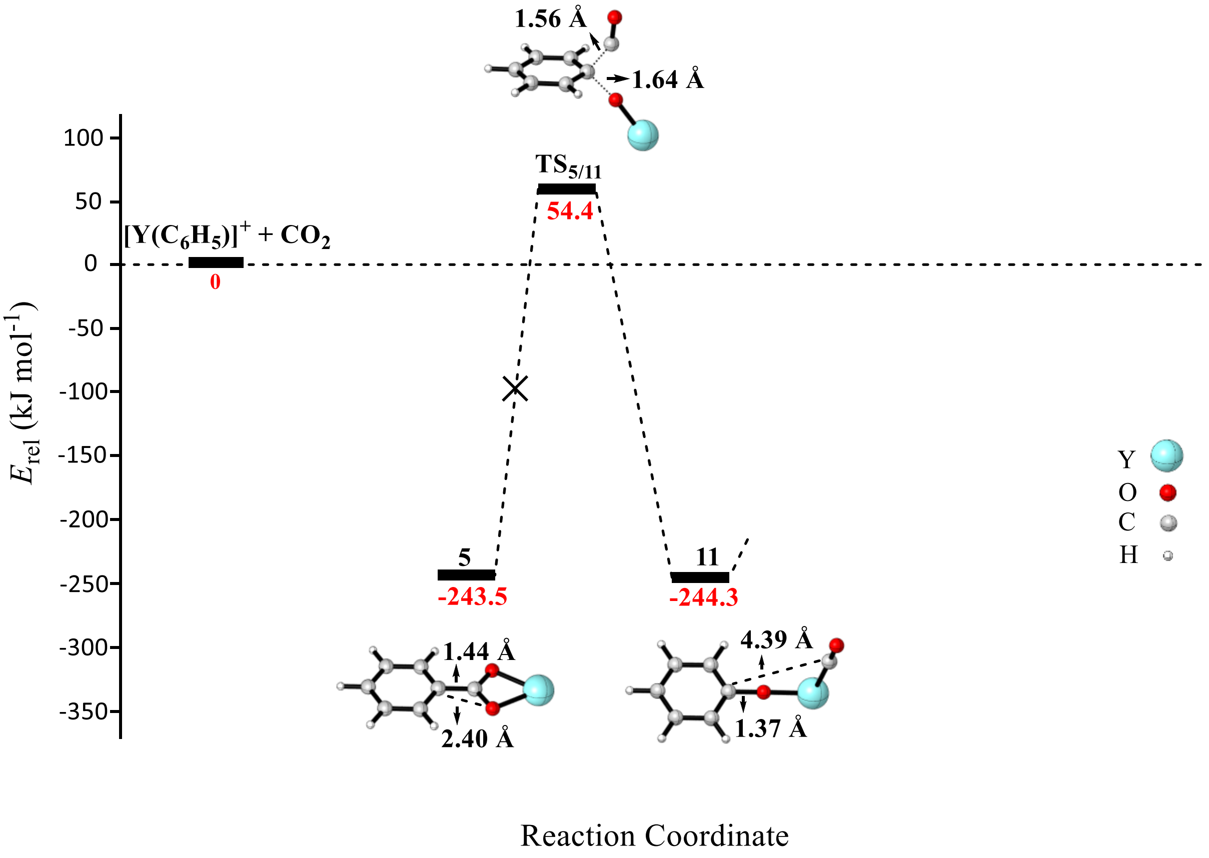

Figure S2: Simplified potential-energy surface (stationary points) for the decarbonylation path of the reaction of $[Y(C_6D_5)]^+$ with CO_2. The energies are given relative to the doublet ground state of the educts and are marked in red. For the sake of brevity, charges are omitted.

Cartesian coordinates of key complexes

1

C	-1.12157800	-5.52588400	0.02267100
O	-1.93842600	-6.47603800	0.02609300
O	-0.54725700	-5.05308200	1.03089500
C	-1.18773300	-8.43356000	4.06199900
C	-0.93098200	-9.40758900	5.02555100
C	0.15633800	-10.24451200	4.83073900
C	0.96477700	-10.10873700	3.69866500
C	0.69537800	-9.13585300	2.74940400
C	-0.39483700	-8.27134500	2.91378500
H	-2.07069400	-7.79397200	4.26787400
H	-1.55943000	-9.50929800	5.89828600
H	0.37993100	-11.00850500	5.56145300
H	1.80866800	-10.77093500	3.56513000
H	1.33283500	-9.04714700	1.88061000
Y	-1.63160700	-6.59456400	2.24055000

2

C	0.03791200	0.25153900	-0.03780000
O	-0.12140600	0.03855500	1.10921100
O	0.19398100	0.45623200	-1.14779700
C	0.10177900	-1.55086100	5.75438700
C	0.33724100	-2.13429400	6.99943600
C	1.39852000	-3.01666900	7.11492200
C	2.20382000	-3.30717100	6.00933500
C	1.95440500	-2.71846500	4.78018300
C	0.88847700	-1.82138300	4.62785800
H	-0.75933200	-0.85433400	5.71917900
H	-0.28797900	-1.90556300	7.85040800
H	1.60536700	-3.48391100	8.06711500
H	3.02793500	-3.99834300	6.11888000
H	2.59063400	-2.95833700	3.93875600
Y	-0.35797800	-0.47321000	3.43066500

6

C	-0.00018300	-0.00183600	-0.00921100
C	0.00041800	-0.00161700	1.37270600
C	1.22328000	-0.00017900	2.06288400
C	2.43854100	0.00106800	1.35942600
C	2.42399700	0.00084500	-0.02245200
C	1.20814200	-0.00061700	-0.70390900
H	-0.93525800	-0.00296200	-0.54951400
H	-0.92676600	-0.00254900	1.92549300
H	3.37172000	0.00219300	1.90204800
H	3.35306600	0.00179500	-0.57301300
H	1.20220100	-0.00082000	-1.78485500
C	1.23064900	-0.00008400	3.50343200
O	0.13723000	-0.00091400	4.20764200
O	2.33051800	0.00118000	4.19740800
Y	1.24190900	-0.00024700	6.02432800

12

C	0.00419500	-0.05183900	0.01184300
C	-0.01838200	0.02386700	1.39813500
C	1.18764600	0.07830000	2.08441400
C	2.40712500	0.06122700	1.42020500
C	2.41223900	-0.01471600	0.03383100
C	1.21513400	-0.07184900	-0.67113700
H	-0.92754300	-0.09577400	-0.53319500
H	-0.95357900	0.03998500	1.93936400
H	3.33138800	0.10604700	1.97836800
H	3.35469300	-0.02964800	-0.49408600
H	1.22592400	-0.13175600	-1.74945600
O	1.17432500	0.14722400	3.46537900
Y	1.16450700	0.20024100	5.36303500

13

C	-0.00904800	-0.04224200	-0.03393600
C	-0.04063100	-0.01732300	1.36796700
C	1.16390600	0.01266300	2.09971300
C	2.39084400	0.01722000	1.42842500
C	2.39935300	-0.03159100	0.04525000
C	1.20734400	-0.04692300	-0.68888500
H	-0.93355900	-0.09809000	-0.59018000
H	-0.97873400	-0.20853400	1.88780700
H	3.30655700	0.04665000	2.00073000
H	3.34576500	-0.04766000	-0.47644800
H	1.24133500	-0.08084000	-1.76767900
O	1.07987300	0.20320100	3.44905400
Y	-0.01640000	1.86613100	3.34933600